Instability, coherent structures and turbulent mixing in cross sheared flow in stratified environments

Yuan Xiao

College of Science and Engineering
James Cook Univiersity
Australia

This dissertation is submitted for the degree of
Doctor of Philosophy

January 2018

I would like to dedicate this thesis to my loving parents ...

Declaration

I hereby declare that except where specific reference is made to the work of others, the contents of this dissertation are original and have not been submitted in whole or in part for consideration for any other degree or qualification in this, or any other university. This dissertation is my own work, except information derived from the published or unpublished work of which has been acknowledged in the text and a list of references, as well as in Acknowledgements.

I understand that James Cook University will make this thesis available for use within the University Library and, via the Australian Digital Theses network, for use elsewhere.

I understand that, as an unpublished work, a thesis has significant protection under the Copyright Act and;

I do not wish to place any further restriction on access to this work.

I declare that the electronic copy of this provided to the James Cook University Library is an accurate copy of the print thesis submitted, within the limits of the technology available.

Yuan Xiao
January 2018

Acknowledgements

First and foremost, I am grateful to my dedicated supervisor, Professor Wenxian Lin. Without him, this thesis will never become possible. His encouragements for my exploring unknown field, suggestions on my research plan and his profound expertise on theory and numerical simulation support me during the entire period of my PhD candidature. I owe him a debt I will never pay back.

Besides, I would like to thank the rest members of my advisory committee, Prof. Yinghe He and Dr. Situ Rong who cultivate my academic skills and give many constructive advices on my research skills as well as research management. I am grateful to Professor Steven Armfiled and Associate Professor Michael Kirkpatrick from University of Sydney. They offer me a great help on the numerical code development, stability analysis, data analysis, as well as very constructive advice on and improvement of my publications. Their expertise on these research areas have and will always have long-lasting influences on my work.

My sincere appreciation also gives to Associate Professor Shaun Belward and Professor Ian Turner (Queensland University of Technology) for their significant help and suggestions on my code development for QZ algorithm. Moreover, I thank Dr Yongbing Chang for his discussion and help on the fundamental knowledge of stability analysis in both physical and mathematical sense. I thank Dr Mahmud Hasan and Associate Professor Wenfeng Gao (Yunnan Normal University, China) for their helps on my early PhD candidature. In particular, I would like to thank two graduated fourth year undergraduate students, Jessie McCormack and Rhien Philips, for their significant dedications and contributions.

Last but not the least, I would like to thank my parents. Without their support, it is impossible for me to make my life till today. They are the pillows of my research and my life.

Abstract

In nature and engineer, substantial transitional scenarios to turbulent flow commence from a perturbed shear flow without curved streamline, which having been theoretically assumed as a parallel shear flow. In Cartesian coordinates, the parallel shear flow satisfy $V \ll U$, where U and V represent the basic laminar flow velocity component in x and y directions respectively. In addition, the principal direction of the imposed perturbations is also assumed to be aligned with the basic parallel shear flow. However, for flows with a large horizontal extent such as geographical flows, V is possibly comparable to U and therefore the basic laminar flow misaligned with the principal wavenumber direction of the external perturbations. The flow in which $V \sim U$ is called cross shear flow, and the ratio $\xi = V/U$ is called cross shear ratio.

This thesis introduces a cross basic velocity component V into the linearized perturbation equations, namely, the Orr-Somerfield equation for viscous shear flow and the Taylor-Goldstein equations for inviscid shear stratified flow, which takes into account of the influences of V as well as the wavenumber in the y direction. By solving the perturbation equation for cross shear (stratified) flow with the QZ algorithm, the stability features of several cross shear flows, such as cross Poiseuille-Couttee flow, cross linear-hyperbolic flow, and cross shear stratified flow are obtained and compared to the classic linear stability analysis results for different parallel shear (stratified) flows, such as plane Poiseuille flow, plane Couttee flow, and plane mixing layer with same hyperbolic function. It is found based on linear stability analysis that the introduced V will either suppress or prompt the original laminar to turbulence in parallel shear flow, depending on whether V itself is a stable or unstable parallel shear (stratified) flow.

A special but general case, in which a cross shear stratified flow with U and V having the same hyperbolic function profiles, is further examined with direction numerical simulation (DNS) under guidance of linear stability analysis. It is observed that in cross shear stratified (CSS) flow the orthogonal instability modes in the V direction coexist with the forced KH instability in the U direction, during the entire primary instability stage. The cross shear ratio $\xi = V/U$, which is the governing parameter for CSS flow, further distinguish three different initial modes between the forced mode and the orthogonal mode. The coherent structures, energy transfer and mixing are further investigated for these three initial CSS instability

modes at different Reynolds number, Richardson number and cross shear ratio. Correlations between mixing/energy properties and ξ as well as Richardson number are obtained.

The transition to turbulence of the shear convective boundary layer (SCBL) flow, where parallel shear flow coexists with dissipative thermal convection flow, is also preliminarily investigated. The linear stability results on SCBL flow, which is obtained by solving the modified Taylor-Goldstein equations with an unstratified factor defined in this thesis, show the Rayleigh-Benard mode coexists with Kelvin-Helmholtz mode.

List of Associated Publications

1. XIAO, Y., LIN, W., MCCORMARC, J., ARMFIELD, S. W., KIRKPATRICK, M. P. & HE, Y. 2014 Coherent structures in cross sheared flows in weakly stratified environments. in *Proceedings of the 19th Australasian Fluid Mechanics Conference (19AFMC)*, 8-11 December 2014, Melbourne, Australia, Paper ID: 084.

2. XIAO, Y., LIN, W., ARMFIELD, S. W., KIRKPATRICK, M. P. & HE, Y. 2014 Hydrodynamic stability analysis on inviscid cross sheared stratified flows. in *Proceedings of the 19th Australasian Fluid Mechanics Conference (19AFMC)*, 8-11 December 2014, Melbourne, Australia, Paper ID: 082.

3. XIAO, Y., LIN, W., Y. HE, ARMFIELD, S. W. & KIRKPATRICK, M. P. 2015 Hydrodynamic stability analysis of sheared convective boundary layer flows in stratified environments. in *Proceedings of the International Symposium on Turbulence and Shear Flow Phenomena (TSFP-9)*, 30 June - 3 July 2015, Melbourne, Australia, Paper ID: P-51.

4. XIAO, Y., LIN, W., MCCORMARC, J., Y. HE, ARMFIELD, S. W. & KIRKPATRICK, M. P. 2015 Turbulent mixing in cross sheared stratified flow. in *Proceedings of the International Symposium on Turbulence and Shear Flow Phenomena (TSFP-9)*, 30 June - 3 July 2015, Melbourne, Australia, Paper ID: 4C-5.

5. XIAO, Y., LIN, W., MCCORMARC, J., ARMFIELD, S. W., KIRKPATRICK, M. P. & HE, Y. 2017 Instability and coherent structures of primary cross sheared flows in weakly stratified environment. *Journal of Fluid Mechanics*, under review (in re-submission).

6. XIAO, Y., LIN, W., MCCORMARC, J., ARMFIELD, S. W., KIRKPATRICK, M. P. & HE, Y. 2017 Hydrodynamic stability analysis on the inviscid cross sheared stratified flow. To be submitted.

]

List of Symbols

α	horizontal wavenumber
α_κ	thermal diffusivity in thermal boundary convection
β	orthogonal wavenumber of perturbation
κ	thermal viscosity
ν	kinematic viscosity
Φ	general basic flow quantity
ϕ	general perturbation quantity
ρ	density
ρ_0	reference density
ρ_b	density at θ_b
σ	time growth rate of perturbation
$\mathbf{U}$	basic flow velocity vector
$\mathbf{u}$	velocity vector
$\mathbf{x}$	position vector
Θ	basic flow temperature
θ	temperature
θ_b	temperature of thermal boundary
c	perturbation (wave) propagation speed

f	horizontal plane function in temporal normal mode. satisfy the *Helmholtz equation*
P	basic flow pressure
p	pressure
t	time
U	horizontal basic flow velocity
u	horizontal velocity
V	orthogonal basic flow velocity
v	orthogonal velocity
V_c	characteristic velocity
W	vertical basic flow velocity
w	vertical velocity
x	horizontal coordinate
y	orthogonal coordinate
z	vertical coordinate
CSS	cross shear stratified
DNS	direction numerical simulation
KH	Kelvin-Helmholtz
PSS	parallel shear stratified
$\bar{}$	horizontal plane average quantities in flow domain
Δ	normal Laplacian calculator, same to $\nabla \cdot \nabla$
$\hat{}$	amplitude of perturbation quantities in normal mode
∇	divergence calculator
∇_s	Laplacian calculator for spatial normal mode. same to $\nabla_s^2 = D^2 - a^2$
∇_t	Laplacian calculator for temporal normal mode. same to $\nabla_t^2 = D^2 - a^2$

$\prime$	perturbation quantities
$\sum$	summation
$\tilde{}$	Squire transformation quantities in spatial mode
$\vec{i}$	horizontal vector
$\vec{j}$	spanwise vector
$\vec{k}$	vertical vector
D	derivative of perturbation quantities in z direction. same to $\frac{\partial}{\partial z}$
i	imaginary part of complex number
Re	real part of complex number / Reynolds number
$*$	dimensional quantity
1	the divergence in horizontal plane, same to $\frac{\partial}{\partial x} + \frac{\partial}{\partial y}$
$\hat{}$	amplitutde of perturbation quantity.
$\prime$	sign of perturbation quantity
z	derivative of basic flow quantity in z direction, same to $\frac{\partial}{\partial z}$
zz	the second order derivative of basic flow quantity in z direction, same to $\frac{\partial^2}{\partial z^2}$

Table of contents

List of figures

List of tables

Chapter 1

Introduction

1.1 Background

"When I meet God, I am going to ask him two questions: Why relativity? And why turbulence? I really believe he will have an answer for the first."

This is the comment left by German physicist Heisenberg Werner, who dedicated himself to the turbulence study and unfortunately unable to find any satisfied answers. Even nowadays, the turbulence remains a mystic, in spite of its universal presences in nature, at meta length scale such as stellar atmospheres, planetary length scale such as atmosphere and oceanic boundary, at large scale stream flow like river and reservoir flow like lake, at laboratory/industry length scale such as jet and channel flow, and even at small scale flow such as artery blood flow.

Why the turbulence is such a formidable and even frustrating topic for many years? Because turbulence, in general, is an **energetic** and **chaotic** flow state. The energetic essence of turbulence involves a full energy spectrum from large scale dynamics such as vortex stretching to micro scale dynamics such as molecular dissipation. Each level of length scale is signified by different energy and momentum transfer mechanisms, creating an energy waterfall named as the Kolmogorov energy cascade [1].

In spite of the clear delimitation of turbulence length scales, the establishment of length scales discussed above in fact heavily relies on posterior statistics. So far there is barely successful priori deterministic model of energy transfer due to strong non-linear effects. At the energy-containing range, the turbulence flow exhibits itself as coherent structures such as eddies or vortices, whose complex and non-linear interactions inhibit exact predictions of transition to turbulence. At the inertial range, the turbulent flow was assumed as isotropic or homogenous flow in the past decades to simplify the theoretical modelling. However for practical but complicated turbulence such as stratified turbulence and multi-species turbulent

combustion in environmental and engineering flows, turbulent flow is inevitably anisotropic and heterogeneous. At the dissipation range where dominant diffusive effects seems to guarantee local isotropic, such local isotropy is challenged recently due to complicated turbulence as reviewed by Warhaft [2].

The chaotic essence of turbulence mainly refers to the transitional process, which involves many competing instability modes and their iterated bifurcations. When observing a turbulent flow, one can more or less finds certain regular flow patterns or coherent flow structures, such as "cat eye" shape eddy or fluctuating waves in clouds or oceans. These flow patterns or coherent structures stem from certain instability modes of flow dynamic. Turbulence, in terms of the instability concept, can be considered as a multitude of developing or developed instability modes. Figures 1.1 shows a simple but typical bifurcation diagram, which is analogous to how chaotic turbulence states are iterated from a stable laminar flow state. More specifically, Fig. 1.1 is a bifurcation diagram of iteration $x \to rx(1-x)$, much like a baby version of the Navier-Stokes equations that describe the much more complicated flow dynamics, but the diagram shown here is adequate to describe a general transitional routine to chaos. For this iteration, x represents the iteration parameter rather than horizontal coordinate in other chapters, r presents the characteristic constant, similar to the Reynolds number Re in turbulent flow. When r is smaller than 3, there is only a single mode denoted by a single curve, while after about $r = 3$ the primary single mode bifurcates into two secondary modes. As r increases, the bifurcations iterate on the previous two secondary branches and submissive branches, until $r = 3.6$ the bifurcation behaviour immediately transits to chaotic fluctuations where myriad of modes coexisting together, that is, turbulence for fluid motions in fluid mechanics. When it comes to more complicated Navier-Stokes equations, the transient bifurcation process before chaos becomes even more convoluted, but all bifurcation processes will converge into modes of multitudes and randomness, that is, chaos.

Although turbulence remains such a challenging topic in theoretical study, the mixing processes occur in the turbulence flow issues, namely, the turbulent mixing, have more statical significances in industry and engineering applications. Due to its complexity, turbulent mixing can be divided into three levels. The Level 1 turbulent mixing involves passive scalar diffusion that does not couple with turbulence dynamics, such as dye or particle tracker mixing in the turbulence. By contrast, both Level 2 and Level 3 turbulent mixing couple with turbulence dynamics; the differences between two levels are whether the fluid compositions change as result of turbulence dynamics. The Level 2 turbulent mixing usually occurs in stratified flow where the scalar properties such as density and temperature vary with height. In stratified flow turbulence shear stresses keep modifying the background scalar field through turbulence dynamics, creating local density gradient and consequently inducing the

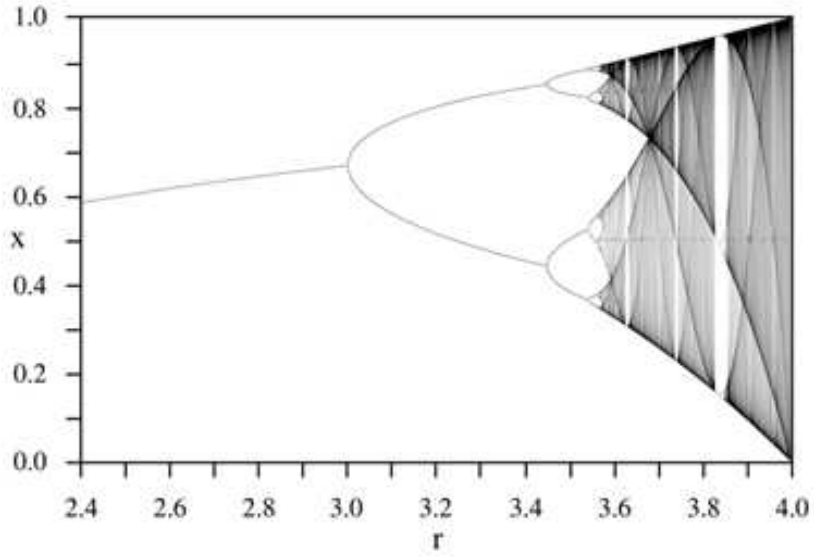

Fig. 1.1 Bifurcation diagram for the logistic map of $x \rightarrow rx(1-x)$, where r play as bifurcation parameter. As r increase, the diagram experience period-doubleing and at last reach chaotic state after $r = 3.6$

background buoyancy forces that reversely stabilize the effect of turbulence dynamics. The competition between turbulence shear stresses and background buoyancy forces represents the coupling between turbulence dynamics and turbulent mixing in Level 2 mixing. The Level 3 turbulent mixing associated with composition changes usually achieves by chemical reactions, which not only introduce much significant buoyancy forces than Level 2 does but also incite further single even chain reactions if both stoichiometric ratio and heat condition for ignition are satisfied.

1.2 Problem addressed

In the past, the most studied theoretical studies on turbulence were built on a parallel flow system. In the Cartesian system, let U and V be the components of the basic velocity in the x and y directions, and let z be the vertical direction aligning with gravitational acceleration. The parallel shear PSS flow is defined as a flow where $V \ll U$ is always satisfied. Based on such a simple and pure "parallel" assumption, the early linear stability analysis on parallel flow system obtained classic solutions that inspired considerable experimental and numerical efforts to discover the mystery of turbulence, that is, the coherent flow structures. On the other hand, further studies on the evolution and dynamics of these "parallel" coherent flow structures will significantly improve the understandings of turbulence, therefore benefiting

effective designs and control of many environmental and engineering systems involving turbulent mixing.

However, the flow is always 'twisted' and misaligned. For instance, in a two-layer flow system as shown in Fig. 1.2, a perfect "parallel" between the top velocity U_t and the bottom velocity U_b is usually assumed in the past theoretical studies, therefore suggesting a two-dimensional basic flow profile as shown in the left-hand side of Fig. 1.2. Nonetheless, as shown in the right-hand side of Fig. 1.2, the top flow velocity might also misalign with the bottom flow velocity in flow systems such as the estuary system where several river streams merge together and the continental shelf system where oblique boundary flows occur perpendicular to the main ocean current due to gravity. The introduced misaligned angle between U_t and U_b induces a cross velocity component $U_{b,y}$ and therefore forms a three-dimensional basic flow state.

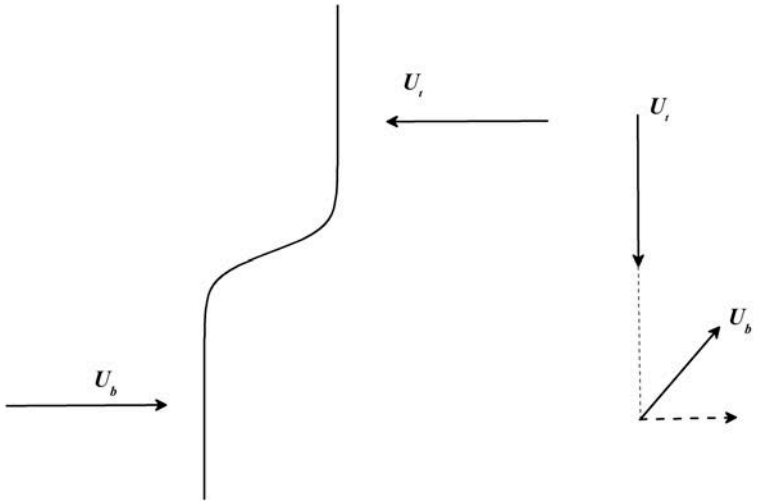

Fig. 1.2 Schematic of misalignment between the top layer velocity U_t and the bottom layer velocity U_b in a two-layer flow system.

Such "twisted" nature of flows encourages this thesis to investigate a different basic flow system, namely a cross shear stratified (CSS) flow, where two components of the basic velocity, that is V and U, are comparable in the Cartesian system. If the spanwise basic velocity component is no longer negligible, the spanwise bulk flow shear induced by V is introduced as the cross shear and the ratio between the spanwise and streamwise bulk flow shears is called cross shear ratio $\xi = V/U$.

So far, only a few studies have involved in such twisted CSS flow systems, nevertheless, their findings are amazing. By introducing a misaligned angle in unstratified two-layer flow system, Lin, Shao & Yu [3] observed through numerical results that a pair of Kelvin-

Helmholtz (KH) "cat eye" eddies appear at both the streamwise and its orthogonal directions. To simulate an oblique boundary flow system, Atsavapranee & Gharib [4] applied a special water tank system which enable the water tank to tilt in both the streamwise and spanwise directions. They also observed the spanwise coherent eddy structures similar to the well-known streamwise KH "cat eye" eddy, when they tilted the water tank to a specific angle in the spanwise (orthogonal) direction.

In spite of a few initiative experimental and numerical attempts, there is no linear stability analysis on basic CSS flow state, which provides necessary condition in the parameter ranges for coherent structures to occur. Furthermore, in spite of successful observations of coherent structures in the CSS flow, the dynamics of three-dimensional primary CSS flow structures, in particular coherent structures, and their dependence on cross shear or cross shear ratio are still unclear, which motivate this thesis and are the problems addressed in this thesis.

1.3 Significance

Current deficiency in understanding the fundamentals of instability, coherent structure, transition to turbulence and turbulent mixing in cross sheared flows in stratified environments seriously undermines our further progress in practical applications. For example, the understanding is important for atmospheric boundary layer modeling, which plays a significant role in global climate models, numerical weather prediction and air quality modeling. It is also crucial for water quality improvement through better modelling of the dynamics and mixing processes in oceans, lakes and rivers where strong stratification and intense current fields interact. The fundamental knowledge of CSS flow is also of significance for and so forth where CSS flow potentially dominate in practical industry flow.

For the first time, this thesis will conduct a systematic linear stability analysis and direct numerical simulation on the CSS flow, from the derivation of linearized perturbation equations, to the analysis of a full set of typical CSS flow configurations, and to the investigations of the role of cross shear ratio in the instability, coherent structures, and turbulent mixing of cross shear flows in stratified environments.

Based on the fundamental results from linear stablity anlaysis results, direct numerical simulations over a wide range of cross shear ratio and stratifications are conducted to serve as the initial numerical investigations on the primary coherent flow structures and turbulence transition routine in the CSS flow. The obtained numerical results will offer a fresh but comprehensive perspective of transition to turbulence in the shear stratified flow, as well as understand the mechanism responsible for the enhanced turbulent mixing due to the introduction of the cross shear, which is not only of fundamental significance for fluid

mechanics, but also benefits the practical application through improved design and control of CSS flow systems with enhanced turbulent mixing.

1.4 Aims and objectives

The main aims of this thesis include developing a linear stability analysis system for general cross shear flow, obtaining preliminary linear stability analysis results of several fundamental cross shear flow configurations and studying the non-linear evolution of cross shear stratified flows. More specifically, the objectives of this thesis are:

1. To derive a set of linearized perturbation equations for the CSS flow systems. Current linearized perturbation equations are based on the PSS flow systems, in which $V \ll U$ is always satisfied. However, for the CSS flow systems, $V \sim U$. A new linearized equation system is thus necessary for the CSS flow systems.

2. To analyse a full set of typical CSS flow configurations and to compare them to the corresponding PSS flow configurations. Only by comparing different shear stratified CSS flows, will this thesis figure out the role of cross shear in the instability of sheared stratified flow. In addition, the linear stability analysis results will sever as important guidance for the selections of parameter ranges in the subsequent direction numerical simulation.

3. To investigate primary flow coherent structures and transition to turbulence in the CSS flow. As linear stability anlaysis will only answer the conditions for turbulence to occur, direct numerical simulation will discover in what exact forms turbulence occurs in the CSS flow.

4. To study the turbulence mixing at different cross shear ratios and stratification conditions. The direct outcome of transition to turbulence is turbulent mixing, which is the key focus of engineering and industry. This thesis will find out how the two critical factors, the cross shear ratio and stratification, change the effectiveness of turbulent mixing.

1.5 Outline

The subsequent body of the thesis is structures as follows:

Chapters 2 presents a comprehensive literature review on the parallel stratified shear flow and the cross shear flow as well as convective sheared flow in stratified environments.

Chapters 3 derives the linear stability analysis equations for cross shear flow, introduce the numerical methods for the linear stability analysis, and examines the stability features of several fundamental cross shear flows with numerical eigenvalue methods.

Chapters 4 investigates numerically the transition to turbulence process of a special cross shear flow configuration, where U and V share the same hyperbolic function but with different magnitudes, using direct numerical simulation. The coherent flow structures and turbulent mixing are investigated at different cross shear intensities in terms of the velocity ratio $\xi = V/U$ but in a weak stratification environment with the initial bulk Richardson number $Ri_0 = 0.01$.

Chapters 5 extends the work of Chapter 4 to focus on the stratification effects on turbulent mixing of CSS flow, through changing the values of the bulk Richardson number Ri which represents the relative intensity of the background stratification with respect to the mainstream velocity shear. The study is conducted again using direct numerical simulation for the CSS flow over the ranges of $\xi = 0 \sim 1$ and $Ri = 0.01 \sim 0.2$.

Chapters 6 extends the work of Chapter 3 to the hydrodynamic stability analysis on sheared convective boundary layer flow, in which both sheared stratified flow and thermally convective flow coexist.

Chapters 7 draws the main conclusions from the outcomes of this thesis and recommend some future works on the topic.

References

[1] POPE, S. B. 2000 *Turbulent Flows*. Cambridge University Press.

[2] WARHAFT, Z. 2000 Passive scalars in turbulent flows. *Annu. Rev. Fluid Mech.* **32**, 203–240.

[3] LIN, J., SHAO, X. & YU, Z. 2000 Numerical research on coherent structures in a mixing layer with cross-shear. *Acta Aeronautica et Astronautica Sinic* **21**(1), 13–20.

[4] ATSAVAPRANEE, P. & GHARIB, M. 1997 Structures in stratified plane mixing layers and the effects of cross-shear. *J. Fluid Mech.* **342**, 53–86.

Chapter 2

Literature review

2.1 General routine of transition to turbulence

The general transitional routine from laminar flow to turbulent flow, usually includes five stages: receptivity, linear growth and nonlinear saturation of the primary instability, and generation of secondary instability and breakdown [1–3].

At the initial receptivity stage, the originally stable laminar flow receives perturbations with different wavenumbers or frequencies from the ambient. Each perturbation agitates a potential growing eigenmode of laminar flow. These different eigenmodes compete with each other; some of them grow much faster than others, while some of them decay earlier. As time proceeds infinity or long enough, one or a group of perturbations will overwhelm others and establish a single dominant eigenmode. The dominance of the one and only (group of) perturbation builds the the first foundation of linear stability analysis.

At the next linear growth stage, the prevailing perturbation (group) keeps growing in exponential rate when the non-linear and non-exponential factors have not yet been developed. Hence, the growth of the dominant perturbation can be predicted by linear stability theory. For receptivity and linear growth stages, the linear stability theory is a very effective deterministic method to predict the critical conditions for primary prevailing eigenmode, or primary mode as conventionally called in turbulence community. As the perturbations are described by exponential waves, such as plane waves, the critical conditions of primary eigenmode refer to wavenumber of perturbations and characteristic number (such as the Reynolds number Re) of the fluid system. The establishment of the most unstable wavenumber or characteristic number from the rigid linear stability analysis will play as a priori guidance to the subsequent investigations of non-linear stage.

Once the initially infinitesimal perturbations grow and reach its amplitude, to the degree that non-linear interactions among the developed perturbations are no longer neglected, the

perturbations will quickly saturate and developinto a group of evident flow structures, which serve as the outcomes of primary mode saturation stage. Similar to the chaotic turbulence stage, generally there is no absolute deterministic model to predict the non-linear saturation of the primary mode, therefore the understandings reply on posteri method such as direct numerical simulation and experimental observations. Nonetheless, if the initial laminar velocity or vorticity profiles of the saturated primary mode are able to be stable and sustained steady or quasi-steady for a sufficient period, linear stability theory still be able to predict the critical wavenumber or characteristic numbers for the subsequent secondary instability. In addition, for a few flow cases, the saturation of the primary mode will directly leap into the turbulence stage without any secondary instabilities as mentioned below, which is called bypass transition.

Once the primary mode is saturated, some new type of subordinate instability modes, called secondary instabilities or secondaries, will emerge to further accelerate the saturation of flow structures in the entire three-dimension physical space. Since the primary mode contains much more kinetic energy than the initial laminar flow, the growth rate of the secondary mode is generally faster.

The last stage is the breakdown of coherent flow structures, following the complete saturation of both primary and secondary modes. The breakdown will occur even faster than the secondary modes, leading to strong nonlinearities and substantially extension of the spectrum of length scales and frequencies in the turbulent flow. Chaotic features with numerous random modes will dominate at this stage. To date, the methods to study the breakdown stage are high resolution direct numerical and laboratory experiments.

Although most of the transition to turbulence process follows the general routine summarized above, the specific transitional process at each stage depends on the initial equilibrium state, namely, the initial laminar flows without any perturbations. Therefore, it is necessary to categorize different basic laminar flow configurations so as to classify different transitional process to turbulence. Fundamentally, basic laminar flows can be divided into three categories: (a) parallel shear flow, (b) flow with curved streamline, and (c) flow with zero mean value [3]. This thesis will not involve (b) and (c) due to the overreaching content, but will focus on the most fundamental types, the parallel shear flow and therefore the derived cross shear flow, which is the major object of this thesis.

2.2 Instability and transition to turbulence in parallel shear flow

In the Cartesian system, let U and V be the components of the basic velocity in x and y direction, and let z be the vertical direction aligning with the gravitational acceleration. The parallel shear flow is defined as a flow where $V \ll U$ is always satisfied. The parallel shear flow can be further divided into two sub-categories: the first is free parallel shear flow without boundaries, such as plane mixing layer flow in large scale atmospheric and oceanic boundary, wake and jet flow in aeronautic applications, large scale water bodies such as lake and reservoir; the second is the bounded parallel shear flow with solid boundaries such as channel flow, pipe flow and any boundary layer flows without curved boundaries.

The study on the instability and transition to turbulence of parallel shear flow has been, and will continue to be, one of the major topic of fluid mechanics due to its vast prevalence in engineering and environmental settings. Since the studies proliferate at the dawn of fluid mechanics, a review to cover all aspects of the parallel shear flow is an impossible task. Therefore, the following review will only summarize those milestones that significantly changed the research perspectives on this area, as well as those critical progresses related to linear stability analysis and subsequent primary/secondary nonlinear flow structures. In addition, a number of academic textbooks on but not limited to instability of parallel shear flow, along with this short review, are recommended for further reading to grasp a general pictures of transition to turbulence, as these textbooks also significantly contribute to the review part of this thesis. These include, among many others, Drazin [4], Drazin & Reid [5] for linear stability analysis, Pope [6] for posteri methods or numerical techniques, Thorpe [7, 8] for stratified turbulence and Peter & Dan [2]; Criminale, Jackson & Joslin [3] for transition to turbulence. In addition, several reviews and papers are also highly recommended to get the latest progresses on parallel shear flow, including Brandt [9] for transition to turbulence for parallel bounded shear flow, Hussain [10] for the coherent structure concept, Fernando [11] and Paul [12] for recent progresses on stratified turbulent mixing.

2.2.1 Bounded parallel shear flow

The main mechanism leading to instability and transition to turbulence in bounded parallel shear flow is the viscosity of fluid, as the basic velocity profile usually involves an inflection point where the second derivative $U'' = 0$. The argument whether viscosity should stabilize the flow or agitate turbulence had lasted for decades. It appears at early experiments that viscosity prevents the flow from transiting into turbulence, for viscosity is always related to

energy dissipation. Nevertheless, thanks to the progress in past decades, viscosity is found to be a more complicated factor in transition to turbulence of bounded shear flow.

At the same time of Reynolds [13], the other cornerstone on inviscid parallel shear flow was founded by a series work of Lord Rayleigh [14–18], who derived the Rayleigh equation to describe the hydrodynamics of inviscid shear flow and accordingly established the Rayleigh inflection point theorem [17]. The Rayleigh theorem proved that $U'' \neq 0$ is a necessary condition for an inviscid flow being unstable. After decades, Fjgrtoft [19] further specified the Rayleigh theorem with the Fjotoft theorem, where not only $U'' \neq 0$ is necessary for inviscid flow, but $U''(U - U_{inf}) < 0$ must also be satisfied at somewhere of the inviscid flow, where subscript inf indicates the inflection point.

At the same period, Orr [20, 21] and Sommerfeld [22] independently derived the Orr-Sommerfield equation that describes the hydrodynamics of viscous parallel shear flow, by their different endeavor to obtain hydrodynamic solutions for plane Couette flow and plane Poiseuille flow, respectively. Tollmien [23] calculated the first neutral curve for plane Poiseuille flow with the function developed by Tietjens [24] and showed that there is indeed a critical Reynolds number as first observed in the Reynolds experiment. For plane Couette flow, on the other hand, no unstable solutions are found by solving the Orr-Sommerfield equation. After numerous attempts in searching linearly unstable solutions for Couette flow, Romanov [25] later gave strict theoretical evidence that plane Couette flow is linearly stable. Schlichting [26–30] extended the theoretical work of Tollmien on plane Poiseuille flow and directly led to the discovery of a general flow structures in parallel bounded shear flow, that is, Tollmien-Schlichting waves, whose corresponding solution only exist when viscosity is included in the hydrodynamics of bounded shear flow.

The linear stability analysis results at the early stage also inspired the significant development of experimental and numerical techniques. The neutral curve of plane Poiseuille flow was verified by experimental work of Schubauer & Skramstad [31], who employed a vibrating ribbon to stimulate a disturbance with desired frequency. The vibrating ribbon method is still nowadays a dominant laboratory method to investigate the instability and transition to turbulence. In addition, the numerical computation, which allows any form of perturbation, emerged as a substitute of theoretical hand calculating tool for the hydrodynamics. The successful control of initial perturbations through either experimental or numerical techniques help to verify the conclusion obtained by early linear stability analysis and to discover some new non-linear flow behaviors in subsequent transition to turbulence.

If the dominant non-exponential perturbation possesses different forms, different secondary instabilities will appear. The main secondary instabilities found in bounded shear flow is reviewed below. Some of them are developed from non-exponential perturbation in

the streamwise direction in alignment with the propagation direction of Tollmien-Schlichting waves, while others independently developed from the non-exponential perturbations in the spanwise direction orthogonal to the propagation direction of Tollmien-Schlichting waves. The latter case is only possible when no other streamwise non-linear instability exists and is called lift-up effects [9].

The first type of secondary instabilities is now known as the K-type instability to memorize Klebanoff [32], the first person reported the experimental observations and theoretical studies in his series of works with his colleagues. Their major discovery is that the upstream two-dimensional Tollmien-Schlichting waves with large wavelength evolve into downstream "Λ" shape vortex structures with small wavelengths, where the peak of one "Λ" vortices align with the adjacent peak of downstream "Λ" vortices. Further in the downstream, the "spike" structures with large amplitudes but short life spans were observed at the peak of "Λ" vortex array. It is found that the K-type instability occupies about five wavelengths at the peak-valley aligned region and one wavelength at the "spike" region of Tollmien-Schlichting waves, therefore the three-dimensional K-type instability grows much faster than its two-dimensional counterpart.

The second type of secondary instability is know as the H-type instability, firstly quantified by Herbert [33] who explained the mechanisms of this type of instability. The first observations of the H-type instability were reported by Kachanov et al. [34, 35], who found that a downstream staggered peak-valley arrangement of "Λ" vortices are also developed from upstream Tollmien-Schlichting waves. Later, Herbert [36] and Orszag & Patera [37, 38] explained that the mechanisms of the peak-valley staggered mode (K-type) and the peak-valley aligned mode (H-type) depends on the finite amplitude of three-dimensional perturbations originated from the developed two-dimensional Tollmien-Schlichting waves. If the finite amplitude of perturbation is small, the sub-harmonic mode (double wavelength of the most unstable linear mode) will prevail and so does the peak-valley aligned mode (H-type) arrangement. If the finite amplitude is large enough so that the nonlinear effects are developed from the most unstable mode, namely, the Tollmien-Schlichting wave, dominates, the peak-valley staggered mode (K-type) arrangement will appear. Similar to the K-type mode, the "spike" structures at the peak of "Λ" vortices are also observed in the H-type mode.

The third type of secondary instability, caused by lift-up effects, is the oblique transition mode, where a secondary instability is originated from a pair of oblique waves with the streamwise wavenumber equals to the spanwise wavenumber. As streamwise and spanwise wavenumber are equal to 1, which is $\alpha = \beta = 1$, the wavenumber vector direction is always 45 degree oblique with the basic flow direction, the "oblique" mode is therefore named. The oblique transition mode will usually incite streak structures after the initial formation

of the streamwise vorticity. Subsequently, the streak structure gradually breaks into an oscillating fashion, with the fundamental secondary instability oscillating in sinuous manner and the subharmonic secondary instability oscillating in various manners. On the other hand, the growth or decay of oblique streak structures are highly sensitive to the streamwise wavenumber number α. The larger α is, the faster oblique mode will decay. If $\alpha = 0$, the oblique mode will sustain. The dependence of α further matches with the lift-up nature of the oblique mode. Note that if the streak structures sustain long enough, their breakdown in the oblique mode will recreate the streak structures in further downstream, forming a regeneration cycle of streaks. This cycle is the fundamental mechanism to create a self-sustained turbulence system [39] and [40].

2.2.2 Free shear flow

Theoretically, parallel free shear flow refers to a two layer flow, where a bulk velocity shear, whether varies smoothly or abruptly, occurs at the middle interface between two different velocity layers. Although its basic velocity profile and free boundary condition are conducive to pure theoretical analysis, such unbounded flow configuration does exist as a paradigm of large scale geographical flows, such as ocean currents and atmospheric flows, where strong shear occurs only within a relatively thin interracial layer. Unlike the bounded parallel shear flow, whose the basic velocity profile is less than two order, the smooth velocity profile of parallel free shear flow always satisfies $U'' \neq 0$ and therefore follows the Rayleigh theorem. As a consequence of $U'' \neq 0$, the inflection point of the basic velocity profile has more influences on flow instability than the viscosity for the parallel free shear flow. Thus, the linear stability analysis on inviscid free shear flow system is very effective even for viscous free shear flow.

As viscosity plays an insignificant role in the free shear flow, early theories on inviscid shear flow, such as the Rayleigh theorem and Fjotoft theorem mentioned above, were quite effective tools. Howard [41] developed the semicircle theorem that describes the necessary relation between the perturbation wave speed and the minimum/maximum basic velocity. At the same time, some analytic solutions on simple inviscid free parallel shear flow such as flow with the piecewise velocity profile, are also obtained based on continuous interface conditions.

In geographical flows, background stratification where density or temperature varies with height, usually accompanies the parallel free shear flow. Based on the interests from geographical flow community, Taylor [42] and Goldstein [43] included the background stratification into the inviscid Rayleigh equation and derived the Taylor-Goldstein (TG) equation, which links the hydrodynamics between velocity shear and buoyancy. By solving

the TG equation, Miles [44] further developed the Howard semicircle theorem in the parallel shear stratified flow and established the classical Miles-Howard theorem, in which the critical condition for linear instability is the gradient Richardson number Ri, as the indicator of relative role of shear and buoyancy, always less than 0.25. Later, this mode with $Ri < 0.25$ was confirmed as the Kelvin-Helmholtz (KH) instability, which was earlier obtained by Lord Kelvin [45] and Helmholtz [46] by solving the Rayleigh equation rather than the TG equation. By further considering the length scale ratio between the shear layer thickness and the background stratified layer, Hazel [47] numerically solved the TG equation and obtained a new mode above $Ri = 0.25$ in consideration of the stratified layer thickness much smaller than the basic shear layer thickness. This high Ri number instability was confirmed later as the Holmboe mode, first observed by Holmboe [48]. Caulfield [49] further extended the range of Ri and found the other instability above the transitional boundary between the KH and Holmboe instability. The third instability is called Taylor-Caulfield instability but has not been widely observed in nature so far.

The primary mode in bounded shear flow appears at large wavenumbers, indicating the length scale of the flow structures such as the Tollmien-Schlichting waves and the subsequent secondary flow structures are relatively small. On the contrary, the primary instability mode of free shear (stratified) flow occurs at relatively smaller wavenumbers, suggesting large length scale of flow structures appears in parallel free shear flow. Indeed, as observed by many laboratory and field experiments, the flow structures in free shear (stratified) flows are indeed at relatively large scales. These large free shear flow structures give the advantage of a coherent structures concept. As these flow structures further develop a group of more sophisticated secondary instabilities or flow structures, together both primary and secondary flow structures will keep growth until their saturation in space. Then all flow structure will collaspe and therefore lead to the eventual turbulent flow state. Based on such transitonal routine of hierarchy, the transition to turbulence in the free shear flow are quite submissive to the original large scale primary flow structures, other than surrounding perturbations. The strong dependence on primary flow structures also gives certain analytical advantages, where the secondary instabilities in free shear flow can be considered as secondary "linear" instabilities developed based on the coherent primary flow structures.

Typical primary coherent structures in parallel free shear flow is the famous Kelvin-Helmholtz (KH) eddy structures, or the Kelvin-Helmholtz mode. In spite of variety of perturbations in substantial studies on KH mode, the primary KH eddy structures always consist of central "cat's eye" shaped eddies (sometimes referred to as rollers or billows), with the axis of the eddies horizontal and orthogonal to the flow direction. If the domain is selected as multiple wavelengths of the KH mode, long "rib" structures appear in the flow

direction and connect adjacent "cat's eye" eddies. Based on somehow established "cat's eye" eddy, some early attempts to apply linear stability analysis on "cat eye" velocity or vorticity profiles are made by Corcos & Lin [1, 50, 51], who successfully predicted a two-dimensional distribution of the spanwise vorticity for the initial rolling-up and following pairing process of the KH eddy structures. The investigations were further extended to three-dimension by numerical simulation by Rogers & Moser [52, 53], and water thank experiments conducted by Thorpe [54, 55], who observed "mushroom" shaped flow structures in the spanwise direction, once a spanwise wavenumber was initialised in the form of forced perturbation in the basic laminar flow field.

In nature, especially for oceanic and atmospheric flow, the background stratification, where density or temperature varies with height, inevitably accompanies with free shear flow. In fact, the parallel free shear flow always connects to stratified layer, together being called the "shear stratified flow". The prominent features of shear stratified flow is the presence of buoyancy, which is created by velocity shear but reversely keeps modifying the shear dynamics. Paul [12] categorized shear stratified flow as level 2 turbulence mixing, where the competition between turbulence shear stress and background buoyancy forces are the major dynamics and mechanism of turbulence mixing.

Once the stratification is included, the Kelvin-Helmholtz instability become more complicated in shear stratified flow compared to parallel free shear flow. Klaassen & Peltier [56, 57] employed the same strategy by assuming a stable "cat's eye" primary profiles to solve secondary instabilities of the KH mode in stratified environments. They found that the pairing processes are inhibited or replaced by a different secondary instability, where some shear-aligned convective rolls were produced at the position of "rib" structures. Caulfield & Peltier [58, 59] further investigated the influences of such secondary instability on turbulence mixing efficiency, which shows as a non-monotonic function of the Richardson number Ri at the late turbulence stage. More recently a series of works from Mashayek & Peltier [60–62] extended the range of Re and Ri and summarized a group of secondary instabilities occurred in shear stratified flow.

As predicted by Hazel [47], once the length scale of stratified layer is smaller than the length scale of shear layer below a certain ratio, the Holmboe mode will appear. Interestingly, the solution of the Holmboe mode from linear stability analysis involves a non-zero wavespeed, indicating the Holmboe mode is the same propagative mode as Tollmien-Schlichting waves in bounded parallel shear flow. The subsequent experimental and numerical studies [63, 64] confirmed the propagative features of the Holmboe mode and revealed more details of Holmboe waves. Different from Tollmien-Schlichting waves, primary Holmboe waves involve a pair of counter-propagating wave groups with the length scale significantly

smaller than the KH "cat's eye". Furthermore, the experimental observation by Schowalter et al. [65] and numerical investigation by Smyth & Winters [66] and Lawrence et al. [64] showed a loop structures along with hairpin-like vortex as secondary instability of the Holmboe mode.

As the actual stratified layer always vary, the actual sheared stratified turbulence in geophysical flows experiences temporal and spatial transitional state between the two modes. Several researchers attempted to find the transitional conditions by linear theory. With one-dimensional linear analysis, Smyth & Peltier [67] investigated the transitional region between the KH mode to the Holmboe mode in terms of the bulk Richardson number Ri_b. They found wave ejection events as Ri_b increases, indicating transition from the KH mode to the Holmboe mode. Meanwhile, the transitional mode with lower growth rate compared to the KH mode was observed, associated special structures in the transitional region. In the subsequent two-dimensional linear analysis associated with numerical simulations, Smyth & Peltier [68] observed more details about transitional structures. In the $Ri_b = 0.25$ case near the margin of the KH mode region, weak appearance of the wave tip loom before the KH eddy pair develops, implying weak Holmboe wave feature. In the $Ri_b = 0.26$ case near the Holmboe mode region, the central isopycnal overturns and KH wave like vortex structure ensues, but the vortexes move with two counter-propagating waves, indicating the Holmboe mode feature still dominate.

A few lab experiments examined the transition from the KH mode to the Holmboe mode. Lawrence et al. [64] and Koop & Browand [69] observed the transition from the KH mode to the Holmboe mode. In the two exchange stratified flow configuration, Hogg & Ivey [70] found that the central isopycnal overturned like the KH eddy but propagated forward regarding to the mean flow, as Ri_b approaches the KH-Holmboe transitional region. Nonetheless the high-vorticity region caused by overturning is not enclosed as the primary vorticity region in the KH mode. In water tank experiments with two layer and linear stratified configurations, Strang & Fernando [71] examined the transition among turbulence modes in various Ri_b values. They found transitional regions in $3.2 < Ri_b < 5$ and $5 < Ri_b < 5.8$. When $Ri_b > 3.2$, the interface layer below the KH primary billow becomes distorted and appears like propagating wave. The distorted part interacts with the primary KH billow in a similar frequency. As Ri_b increases further to $5 < Ri_b < 5.8$, the KH waves emerge less frequently, instead asymmetric waves dominate over the transitional region but break intermittently. As $Ri_b > 5.8$, double side Holmboe waves appear, indicating boundary of transitional region resting on $Ri_b \approx 5.8$.

2.3 Instability and transition to turbulence in cross shear flow

In the parallel shear flow as reviewed above, it is assumed that $V \ll U$ is always satisfied, giving a two-dimensional basic flow. However, the real flows is always three-dimensional, even for the initially stable laminar flow. If $V \ll U$ is no longer satisfied, the instability features of a non-parallel shear flow is expected to be different. Such non-parallel effects were first introduced in the linear stability analysis in the Blasius boundary layer flow by Smith [72], who considered a non-zero V component in basic laminar flow state in order to consider the potential violations of parallel assumption $V \ll U$ in the previous experimental work conducted by Schubauer & Skramstad [31]. In spite of setting non-zero V, the magnitude of V is still very insignificant compared to U in the Smith's model where a small coefficient is also introduced in front of V terms. Even through, Smith found the modified non-parallel model obtained a better correlations with experimental results than the parallel model, suggesting that minor but inevitable non-parallel effects indeed exist in channel flow experiments, where the width of channel is much smaller than the length. Unfortunately, Smith ceased his further theoretical attempt to extend the magnitude of V so that V is comparable to U.

What will a phenomenal non-parallel effects with $V \sim U$ be on shear flow? What will happen to the transition to turbulence? Before answering the questions, let us check a potentially real scenario where $V \sim U$ does exist. Figure 1.2 in Chapter 1 shows the schematic of a two velocity layer flow system, which sometimes occur in an estuary system. If a parallel shear flow is assumed as what most of previous studies did, then top velocity U_t and bottom velocity U_b will be in the same plane, forming a perfect aligned two-dimensional basic flow as shown in the left graphic of Fig. 1.2. Nonetheless, in estuary system the top and bottom stream flows usually misalign with each other while two streams of estuary is merging, as indicated in the right graphic of Fig. 1.2. At this time, there must be an misaligned angel between U_t and U_b. If a parallel plane is consider to be aligned with U_t, then the component of U_b orthogonal to U_t will inevitably induce a cross velocity basic component as denoted by the dash line arrow in the right graphic of Fig. 1.2. The influences of the misaligned angle in unstratified two layer flow system was studied numerically by Lin Shao & Yu [73], who found that there is a pair of KH "cat's eye" eddies appearing at both the streamwise and its orthogonal directions.

The other real circumstances where basic laminar flow with $V \sim U$ exist is also a two layer flow system with an oblique boundary such as continental shelf system, where an oblique boundary shear flow is formed perpendicular to the main streamwise current due to

gravity. Atsavapranee & Gharib [74] created such an oblique boundary flow in laboratory with a special watertank system which enabled water tank tilting in both streamwise and spanwise directions. For the first time, they defined the bulk velocity shear in the spanwise (orthogonal) direction as "cross shear" and considered the relative intensity of the cross shear to the streamwise shear as the major parameter. By tilting a water tank in the spanwise (orthogonal) direction, they produced cross shear stresses as soon as the first streamwise KH billows were captured and found the mixing effects in the "cross shear" flow system improve significantly compared to the parallel shear flow. The similar enhancements of mixing was also reported in the numerical study of Lin Shao & Yu [73]. In addition to the two examples mentioned above, the cross shear due to misalignment in basic flow could also involve reflected flow near coastal topography, two merging ocean currents, and counter flows in estuaries and in multi-port reservoirs. The cross shears, either in large or small length scale, strong or weak, also inherently reside in other physical processes such as convective heat transfer and chemical processes such as dissolution processes.

Besides its potential presence in environments, the cross shear flow implies theoretical significance. As summarized above, the transition to turbulence requires proper initial basic velocity $\vec{U} = Ui + Vj$ profile and perturbations with proper wavenumber. Note that the perturbation is in fact also a vector in terms of wavenumber $\vec{\alpha}$. In linearized perturbation equation of the parallel shear flow, the principal wavenumber $\vec{\alpha} = \alpha\vec{i} + \beta\vec{j}$ is always aligned with basic velocity $\vec{U} = Ui$, as the wavenumber component β and velocity component V deliberately omitted due to the $V \ll U$ assumption, as will be discussed in the next chapter. However, in cross shear flow, as V always exists the wavenumber $\vec{\alpha}$ is able to misalign with basic velocity $\vec{U}$. From this point of view, the cross shear flow can also be defined as the shear flow where basic flow velocity $\vec{U}$ misaligns with the principal perturbation wavenumber $\vec{\alpha}$.

2.4 Turbulence in sheared stratified layers

2.4.1 Turbulence energy transfer and evolution modes

Turbulence mixing in sheared stratified layers is an internal mixing process without any influences from boundary flux, in another word, the mixing in the close system. The dominant energy transfer process varies between the turbulence shear produced by strong velocity difference within the interface layer and internal buoyancy flux generated by disturbed scalar field.

One of the characteristics of sheared stratified turbulence is that most of energy transfer processes are reversible, introducing more complications in theoretical analysis. As shown

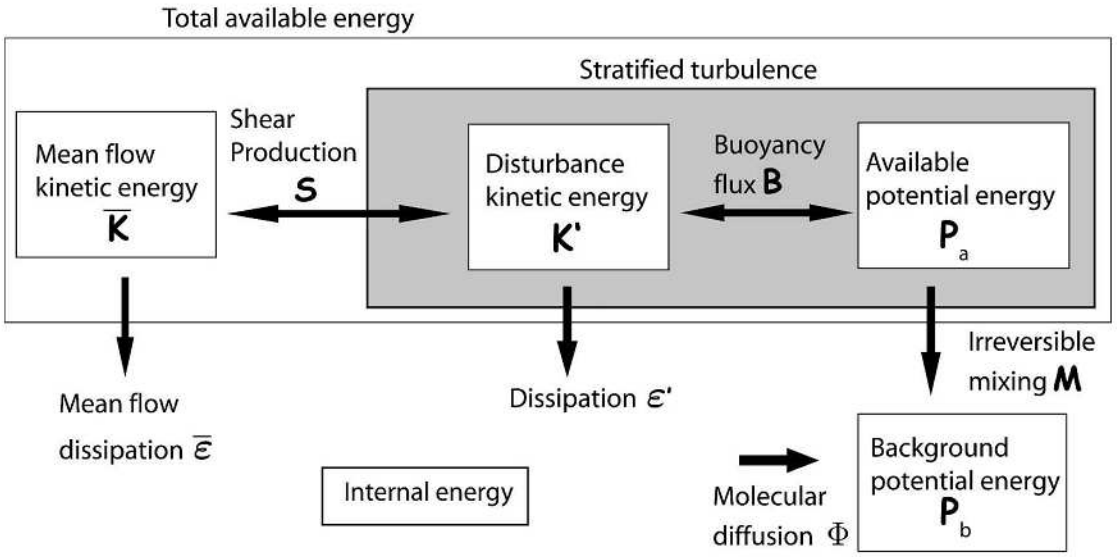

Fig. 2.1 Energy reservoirs and energy transfer process partitions in the sheared stratified turbulence. Arrows show the available energy transfer directions [75, 76].

.

in Fig. 2.1, the turbulence energy reservoir in sheared stratified turbulence are partitioned into: (a) turbulence kinetic energy **K**, (b) potential energy **P** and (c) internal energy. The energy transfer processes among **K**, **P** and internal energy mainly include turbulence shear production (S), internal buoyancy flux (**B**) and dissipation (ε). In fact every energy transfer path between different energy reservoirs is reversible. Despite ε is reversible as well, the energy transfer from ε to **K** called backscatter is negligible compared toε, therefore Fig. 2.1 only draws single arrow from **K** to ε. Winter et al. [75] categorize the reversible potential energy **P** into reversible (available) part $\mathbf{P_a}$ and irreversible (background) part $\mathbf{P_b}$ so that the irreversible (effective) mixing process M occurs from $\mathbf{P_a}$ to $\mathbf{P_b}$. This categorization in **P** employed by Smyth et al. [76–78], Caulfield and Peltier [79, 80] and Carpenter et al. [81] benefits energy transfer analysis and turbulence mixing efficiency. Unfortunately, there is still no effective method that successfully separates reversible and irreversible parts in kinetic energy **K**. With traditional partition in turbulence study, the kinetic energy **K** is separated into mean flow part $\overline{\mathbf{K}}$ and fluctuation part $\mathbf{K}'$ as shown in Fig. 2.1.

The other characteristics of sheared stratified turbulence are different turbulence evolution modes that correspond to distinctive energy transfer processes. The turbulence mixing in sheared stratified layer usually arises from a random perturbation X'. Subsequently, the turbulence shear layer with thickness of δ_v keeps supplying kinetic energy **K** to amplify initial perturbation X', in contrast to X' induced **B** in stratified layer with thickness of δ_ρ that

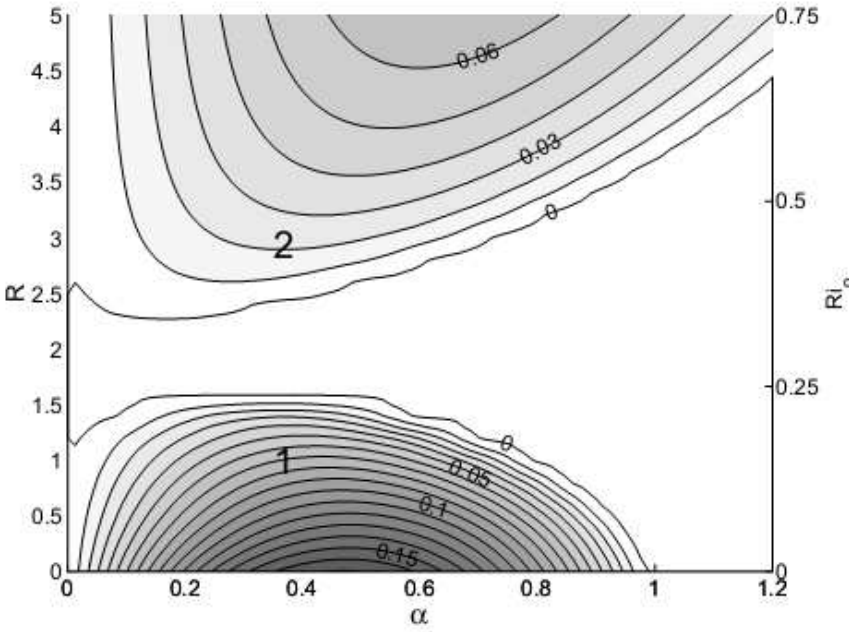

Fig. 2.2 $R = \delta_v/\delta_\rho$ versus the initial perturbation X' growth rate α for linear normal mode. "1" refers to the Kelvin-Helmholtz mode and "2" refers to the Holmboe mode [78].

attempts to stabilize the expanding X'. As a consequence the growth of perturbation X' is determined by competition between **S** and **B**, which leads to a reasonable conjecture that there is a critical condition that separates *S* dominant and **B** dominant turbulence modes. With linear theory where the perturbation X' is assumed to be negligible compared to the mean flow property, Miles [82] and Howard [83] obtained the critical condition with the critical gradient Richardson number of $Ri_{cr} = 0.25$. They concluded that, for all cases with $Ri_g > Ri_{cr}$, the flows are absolutely at stable state due to strong **B** from background stratification. Nevertheless, the strong stratification does not always mean "stable". Holmboe [84] found unstable flow patterns with wave-like features in flow with $Ri_g > Ri_{cr}$. He concluded that the reason for this new instability mode is δ_v is larger than δ_ρ.

Further linear theory analysis by Symth and Peltier [85] and Smyth and Winters [78] considered the effects of ratio of δ_v to δ_ρ, which showed a marginal region between the two different modes as shown in Fig. 2.2, implying the critical condition is not a single value of *Ri*. From Fig. 2.2 there are two fundamental evolution modes in sheared stratified turbulence. The turbulence mode designated by "1" is the "Kelvin-Helmholtz" (KH) mode, in which turbulence is developed from eddy interactions. In the KH mode, the initial small perturbation develops into small eddies, which subsequently coalesce into single or a pair of large overturning eddies (billows). The large overturning eddy keeps stationary with the

mean flow, then saturates in all directions and break down to induce more energetic and chaotic turbulence [86]. The turbulence mode designated by "2" in Fig. 2.2 is the "Holmboe" instability, in which the initial perturbation expands to a cusp-like wave structure, as observed by Thorpe [87], Maxworthy and Browand [88], and Lawrence et al. [89]. The cusp-like waves engulf surrounding fluid wisps to form the adjacent vortex, which moves forward with propagating Holmboe waves rather than being stationary regarding to the mean flows. The entrainment caused by wisps sustains through the entire development of spanwise structure by secondary instability [81]. Due to the wave-like features and wave ejection events, the Holmboe mode spends much longer time to become saturated compared to the KH mode.

2.4.2 Characteristic numbers and length scale

Several characteristic parameters provide effective ways to measure the relative roles of S, B and ε. The relative role between S and B can be denoted in three ways: the bulk Richardson number $Ri_b = N^2/S^2 = g\Delta b/\triangle U^2$ across the interface layer, the gradient Richardson number $Ri_g = (\partial b/\partial z)/(\partial u/\partial z)^2$ at local field, and the flux Richardson number $Ri_f = (\partial \bar{b}/\partial z)/-\overline{uw}(\partial u/\partial z)$ based on statistical average. Ri_f is also a direct measurement of B/S in the energy transfer process and will be compared to other definitions of turbulence mixing efficiency in section 2.6.2. The relative role between S and ε is measured by the shear Reynolds number $Re_s = \bar{\varepsilon}/\nu S^2$. The counterpart between B and ε is the buoyancy Reynolds number $Re_b = \bar{\varepsilon}/\nu B^2$.

In addition, a group of turbulence length scales can not only quantify the relative contributions of individual energy transfer mechanism, but also delineate the turbulence evolution process. The most apparent length scales are the sheared layer thickness δ_v and the stratified layer thickness δ_θ. The quantitative relation between δ_v and δ_θ together with the initial Richardson number Ri_0 determine the turbulence evolution process. If $\delta_v = \delta_\theta = L_z$ where L_z refers to the height of the entire domain, the turbulence grows exponentially at small initial Ri (Ri=0.04) and decays asymptotically at larger initial Ri_0 [90]. If $\delta_v, \delta_\theta \ll L$, δ_v and δ_v expands in a different rate so that different evolution modes develop. If $\delta_v < 2\delta_\theta$ and $Ri_0 < 0.25$, the sheared layer becomes unstable to all wavelengths and the KH instability emerges. If $\delta_v > 2\delta_\theta$, the critical Ri_0 for KH instability dominating in evolution will decrease to 0.07. At this condition the Holmboe mode is able to appear but will be suppressed soon by stronger amplification of the KH mode. On the other hand, at large Ri_0, the KH mode is so suppressed that wave breaking precedes before the KH eddy formation [91], therefore the wave-breaking featured Holmboe mode dominates during the entire turbulence evolution.

The distance d between the central line of the sheared layer and the stratified layer affects the turbulence evolution mode as well. For instance, when $\delta_v > 2\delta_\theta$, $d > 0$ at $Ri_0 < 0.07$,

the turbulence modes bifurcate into the KH and Holmboe branches rather than single KH branches in the $d = 0$ case [92]. Meanwhile the presence of d yields asymmetry in the KH and Holmbe instabilities, as observed by Lawrence et al. [89] from numerical simulations and Strang and Fernando [93] from water tank experiments.

Due to reversibility in energy transfer process as shown in Fig. 2.1, the dissipation term ε that suffers little from wave-like fluctuations is selected as the benchmark to quantify S and B. the Ozmidov scale $L_O = \sqrt{\overline{\varepsilon}/N^2}$ that denotes the smallest scale influenced by buoyancy (or smallest overturning scale) and the Corrsin scale $L_C = \sqrt{\overline{\varepsilon}/S^2}$ that designates the smallest scale influenced by turbulence shear are introduced. In fact Re_b and Re_s can be derived from the combinations among L_O, L_C and the Kolmogorov length scale $L_K = (\nu^3/\varepsilon)^{1/4}$ as $Re_b = (L_O/L_K)^{4/3}$ and $Re_S = (L_C/L_K)^{4/3}$. The new definition of $Re_b = (L_O/L_K)^{4/3}$ brings Re_b a new significance, that is, the extent of the inertial cascade region between the buoyancy-driven overturn scale and the viscosity-driven dissipation scale. When Re_b becomes larger, the inertial cascade region extends longer so that less anisotropy in the large scales is transmitted to the small scales, making the isotropic assumption more valid in the small scales. On the other hand, a small Re_b corresponds to a short inertial cascade that enables significant anisotropy transfer from the large scales to the small scales, therefore debilitating the isotropic turbulence assumption. The influence of Re_b on anisotropy in shear stratified turbulence will be reviewed in section 2.4.4. Similar explanations can be made for Re_S as well. As will be shown in Fig. 2.7, L_O and L_C are also able to describe the turbulence evolution history in the way that indicates the dominant energy transfer mechanism at different stages of turbulence evolution.

Another useful length scale measuring irreversible potential energy is the Thrope scale $L_T = [< \eta >^2]^{1/2}$ obtained by Thrope reordering, which is an arranging method that put the original density field into new sequence where density increases with depth everywhere [94]. η in L_T represents the horizontal shifting distance between the original density profile to the Thrope reordering density profile, therefore serving as a measurement of the fluid parcel displacement. The ratio of L_O and L_T defined as R_{OT} is also suggested by Dillon [95], Wijesekera and Dillon [96] and Smyth and Moum [97] as the turbulence evolution events indicator. The advantage of R_{OT} as the time indicator is to estimate dissipation ε by the scaling relation $\varepsilon = R_{OT}^2 L_T^2 N^3$ without knowing turbulence micro structures [94]. In order to quantify potential energy in the spanwise direction, Smyth and Peltier [98] developed the three-dimensional Thrope scale L_{T3} by averaging the entire domain rather than averaging in vertical columns for $L(\delta_\rho)$.

2.4.3 Temporal evolution and characteristic structure

The turbulence modes determine the turbulence temporal evolution. A typical evolution history for the KH mode consists of four stages as shown in Fig. 2.3. The initial perturbation X' grows into small eddies, which then gradually coalesce into a primary KH overturning eddy at $t = 1414s$. Subsequently at $t = 1979s$ the primary eddy becomes saturated in streamwise and vertical directions and stretches the streaks near the edge of overturning eddies to adjacent eddies core in spanwise direction [80]. This expansion of the primary instability to the spanwise direction is called the secondary instability based on linear theory. After saturating in the spanwise direction, the three-dimensional turbulence structure collapses as the result of inadequate shear supply and strong stabilization from buoyancy and at last enters the decay stage as shown at $t = 3252s$. In the Holmboe mode the turbulence flow experiences four stages as well, as shown in Fig. 2.4, the prominent flow patterns are the counter-propagating wave groups rather than the stationary primary eddy in the KH mode. Although smaller primary vortex that resembles the large primary eddy in the KH mode emerges in the vicinity of the Holmboe wave, these vortexes involve no overturning of the central isopycnal and always move with propagating waves. During the growth stage of the second instability, loop structures along with hairpin-like vortex found by Smyth [78] in from DNS or the cusp-like wave form named by Thorpe [87], Maxworthy and Browand [88], and Lawrence et al. [89] display as distinctive features in the Holmboe mode. Near the edges of loop structure fluid ejections were observed experimentally by Schowalter et al. [99] and confirmed numerically by Smyth and Moum [100] and Carpenter et al. [81, 101]. As can be seen from the time indicators in Figs. 2.3 and 2.4, the saturation of turbulence instability in the Holmboe mode takes much longer time than in the KH mode.

The Richardson number modifies the spanwise structures during the development of the secondary instability. Figure 2.5 shows the contours of turbulence kinetic energy in the spanwise direction for the KH mode. In the unstratified case where $Ri_0 = 0$, the vortex streaks concentrate on the hyperbolic stagnation point in between two primary billow cores. As Ri_0 increases, the vortex streaks progressively approximate to the primary billow core. At $Ri_0 = 0.1$ the vortex streaks wrap through the periphery of billow cores. The strong disturbances in $Ri_0 = 0$ precede the secondary instability translating into turbulence even before the subharmonic merging [79, 80].

Besides its influence on the selections of turbulence modes, the distance d between the central line of the sheared and stratified layer also modifies the streamwise and spanwise structures in the Holmboe instability. Carpenter [81] studied the asymmetric Holmboe mode and found that as $a = 2d/h_0(h_0$ ss the initial value of $\delta_\rho)$ increases, the primary vortex near the Holmboe wave grows larger associated with more pronounced wave ejections. In

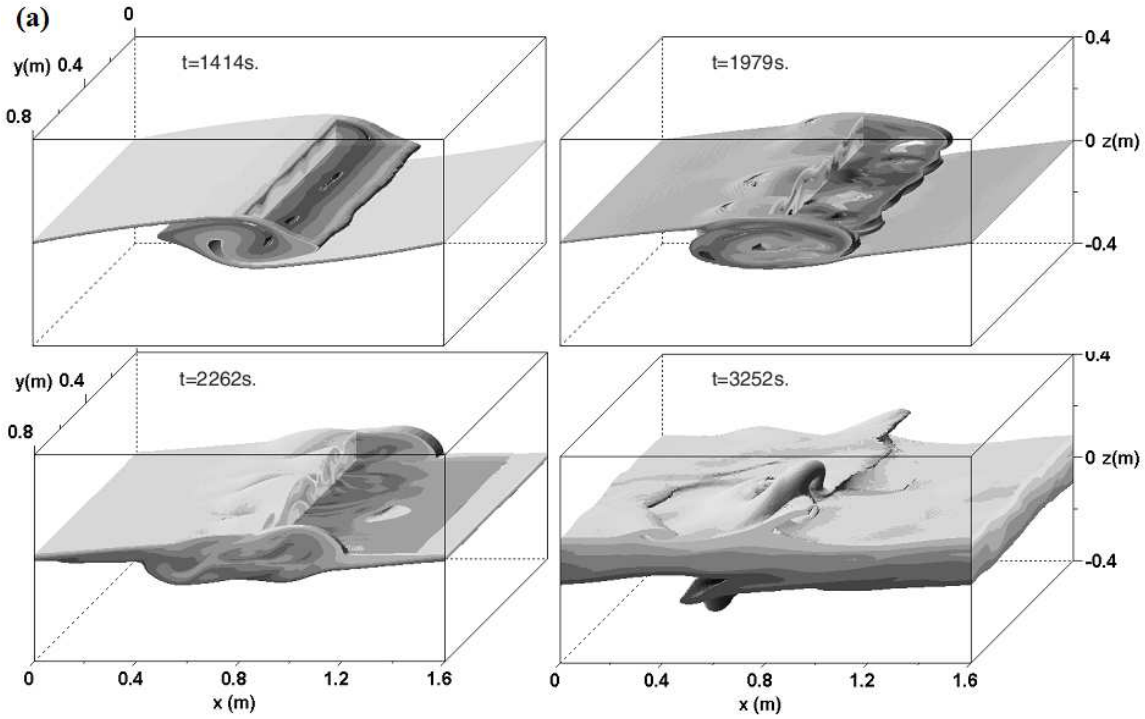

Fig. 2.3 The three-dimensional turbulence evolution of the Kelvin-Helmholtz mode [78].

.

addition, the increased d leads to more complex spanwise structures during the growth of the secondary instability. The density fields of the Holmboe mode with $a = 0.25$ and $a = 0.5$ are shown in Fig. 2.6(a) and (b). The ejections at the upper boundary and entrainment at the lower boundary of the interface layer appear more prominent as d increases from 0.25 to 0.5. As d further increases to unity, the ejections become most prominent as shown by white profiles in Fig. 2.6(c), within which the spanwise turbulence kinetic energy concentrates on the crest of Holmboe wave. The ejection events coincides with the saturation of the secondary instability, indicating that the ejection closely correlates with the secondary instability at large a. If $a > 1$, the Holmboe mode will translate into the Rayleigh instability, in which the pure shear layer lays over (or below) the stratified layer.

From the perspective of energy transfer process, the characteristic length scales are an effective way to construct the turbulence evolution history in which the contributions of each energy transfer mechanism can be easily identified. Figure 2.7(c) shows the evolution history of several length scales in sheared stratified layer with finite thickness. For the purpose of comparison, the length scales evolution in uniform sheared and uniform stratified layer across the entire flow domain are shown in Fig. 2.7(a) and (b) as well. In the uniform stratified

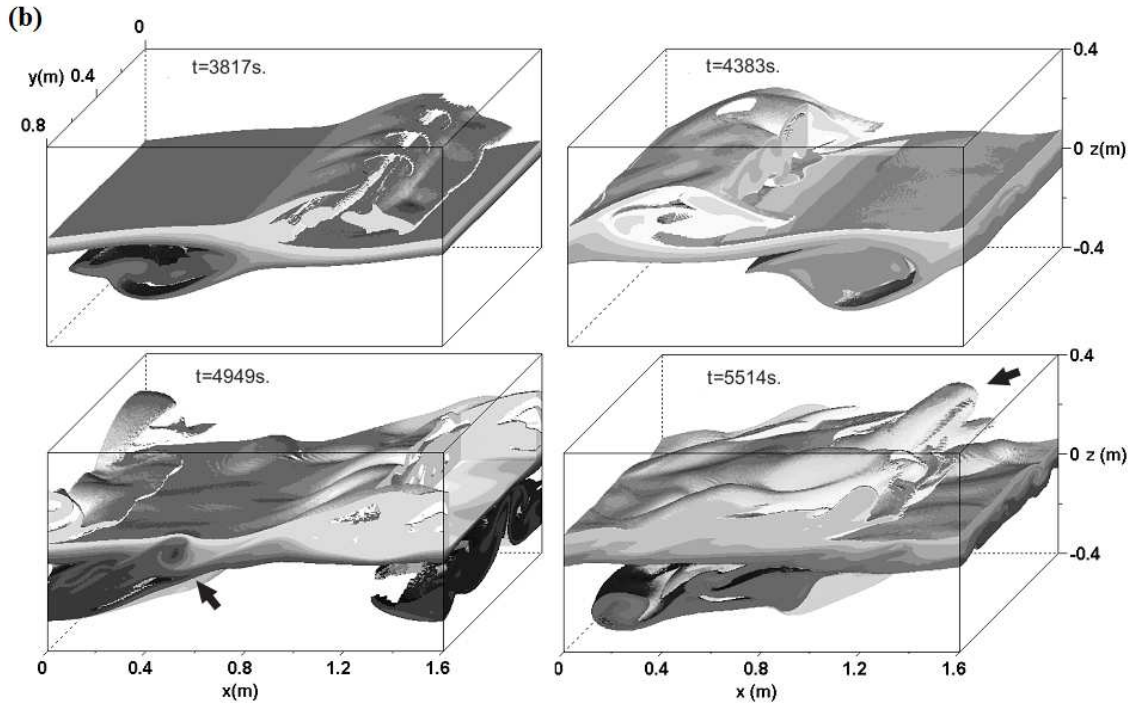

Fig. 2.4 The three-dimensional turbulence evolution of the Holmboe mode [78].

case, the initial perturbation develops into strong turbulence shear but then suffers from even stronger buoyancy from background stratification. The buoyancy effect extends progressively to smaller scales, as indicated by decreasing Ozmidov scale L_O. In the uniform sheared case, the turbulence kinetic energy is supplied incessantly by the sheared layer that spans the entire domain, resulting in unlimited turbulence growth as represented by increasing L_C [90]. The finite sheared stratified turbulence combines the characteristics in both the uniform sheared layer and the uniform stratified layer, producing monotonic tendency of L_C and L_O varying with time in the KH mode as shown in Figure 2.7(a). L_C and L_O evolve simultaneously and overlap during most of time, indicating strong coupling exists between **S** and **B**. At the early time when the primary billow is born, the turbulence kinetic energy is provided by expanding the sheared layer indicated by increasing L_C. As long as the turbulence instability becomes saturated in all directions, B overwhelms S as indicated by $L_O > L_C$ in the mid of turbulence life cycle, followed by the turbulence decay stage. Once the dissipation scale $10L_K$ exceeds L_O, turbulence dissipation replaces buoyancy becoming the dominant energy transfer mechanism, causing even faster turbulence decay.

The Prantle number (Pr) has significant influence on spatial and temporal extension of the inertial energy cascade. The vertical length gap between $L_O(2L_C)$ and $10L_K$ in Fig. 2.7(d)

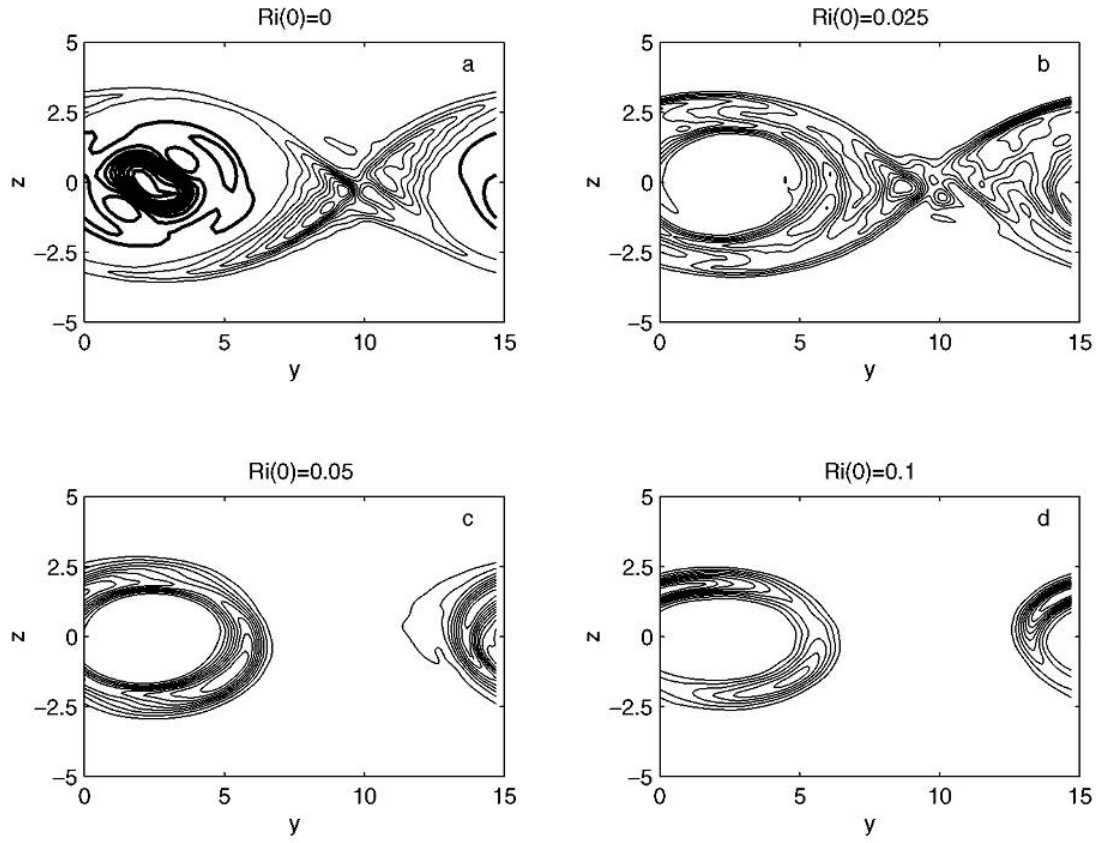

Fig. 2.5 Contours of turbulence kinetic energy in the spanwise direction for the KH mode with the initial Richardson number Ri_0 from 0 to 0.1 [80].

indicates the length scale of the inertial cascade. As Pr increases to 7, the inertial cascade length diminishes approximately from 6×10^{-2} m to 2.5×10^{-2} m. The influences of Pr on the temporal extension of the inertial cascade are observed in turbulence evolution graphic built by Re_b as shown in Fig. 2.8. The horizontal line indicates the critical value $Re_b = 20$, above which does exist the inertial cascade and indicates the buoyancy effects are transmitted to the dissipation scale [97]. Accordingly the horizontal interception for each Re_b data group with $Re_b = 20$ indicates the time duration of the inertial cascade in turbulence evolution. In Fig. 2.8 data groups with different Pr numbers correspond to different horizontal interception, indicating Pr has significant effects on the duration of inertial cascade.

The ratio between L_T and L_O designated by R_{OT} provides the third way to depict turbulence evolution. In Fig. 2.9, the young overturning events before turbulence formation are indicated by the region of $R_{OT} < 0.5$, while the turbulence starts to decay from $R_{OT} = 1$ and continue when $R_{OT} > 1$. Compared to turbulence evolution picture constructed by L_O, L_C and Re_b, the advantage of R_{OT} is to eliminate Pr effects so as to create a universal evolution

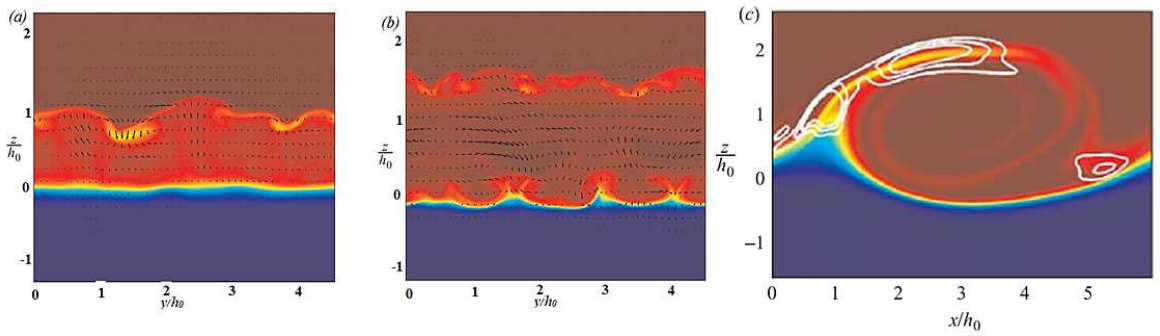

Fig. 2.6 The spanwise density field of the Holmboe instability in (a) $a = 0.25$ and (b) $a = 0.5$. The arrows indicate velocity vectors through which the extend of the primary vortex can be estimated. (c) an ejection event of Holmboe mode with $d = 1$. The color and white profiles indicate density field and the spanwise turbulence kinetic energy "K_{3D}" [81].

tendency in the KH mode. Another advantage of R_{OT} is that it can easily be obtained without knowing the micro-scale information. Therefore R_{OT} can be directly obtained through field and lab experiments, providing a good way to correlate numerical and experimental results so as to test the solidity of the numerical model. As will be reviewed subsequently, R_{OT} provides a good correlation of turbulence mixing efficiency independent of Pr number as well.

2.4.4 Anisotropy in sheared stratified turbulence

As reviewed above, if the spatial extension of the inertial cascade is less than certain value denoted by the critical Re_b, most of the anisotropic information in turbulence kinetic energy and scalar gradients will inherit from large scales to small scales. The presence of anisotropy in small scales challenges one of the most popular numerical method: Large Eddy Simulation (LES), in which the small scales turbulence is artificially modeled instead of being directly solved. The calculations of dissipation ε in LES with prevalent Smargorinsky residual stress model relies on isotropic assumption, while in sheared stratified turbulence with strong anisotropy ε will be seriously overestimated. For instance, with LES with modified Smargorinsky model Pino et al. [102] found that ε stays constant at 5×10^{-4} with time for small flow velocity cases and increases to the order of 10^{-3} for large flow velocity cases, on the contrary with DNS Smyth [76] obtained ε at the order of 10^{-5} in the Holmboe mode and non-monotonic trend of ε with the peak value of 10^{-2} in the KH mode. The overestimation of ε prevents the LES from successfully simulating the secondary instability of sheared stratified turbulence. Consequently, understanding of anisotropic behavior and accordingly

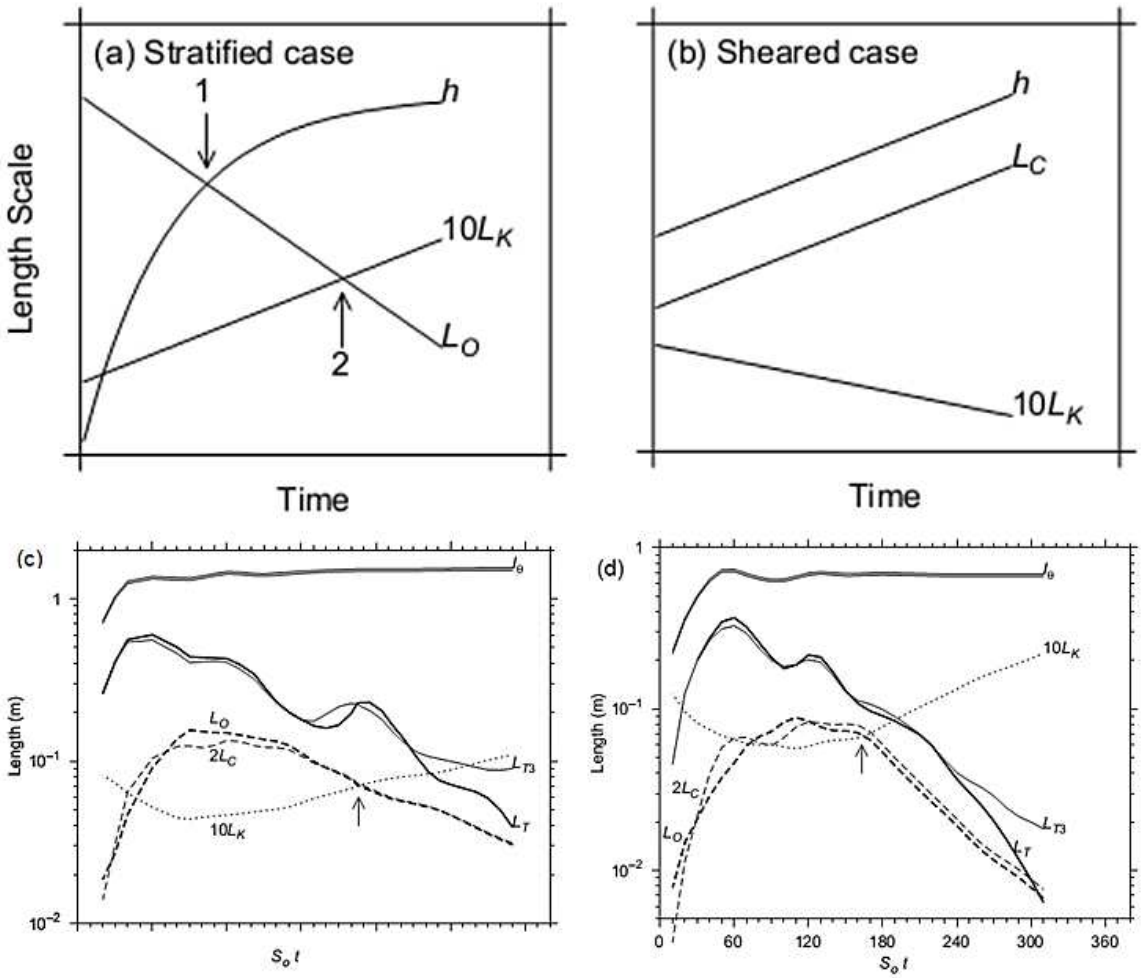

Fig. 2.7 Sheared stratified turbulence evolution characterized by characteristic length scales in (a) sheared case, (b) stratified case, (c) finite sheared stratified case in the KH mode with $Pr = 1$, and (d) with $Pr = 7$ [97].

including anisotropy into residual (unresolved) scales in LES models will largely improve the performance of LES in stratified turbulence.

In uniform sheared stratified layer where the flow is always stable, the anisotropy resides in turbulence shear stress and scalar. Figure 2.10 shows the ratio of horizontal shear strain rate $S_u = \overline{(\partial w/\partial x)^2}$ in the streamwise direction and $S_u = \overline{(\partial u/\partial x)^2}$ in the vertical direction $S_{uw} = S_u/S_w$ in the uniform sheared stratified layer configuration. The isotropic value $S_{wu} = 2$ is also included for the purpose of comparison. As shown in Fig. 2.10, nearly half region lays below $S_{uw} = 2$, indicating strong anisotropy in S_{wu}. Nonetheless, Piccirillo [90] did not give results of S_{vu}, which could increase in the same rate as S_{wu} so that $S_{uw}/S_{vu} \approx 1$ suppresses

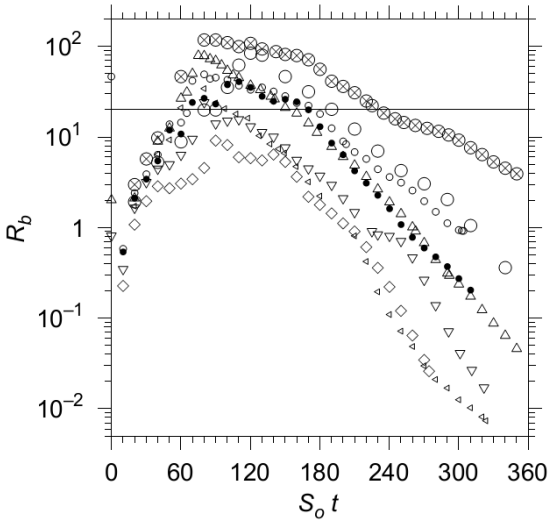

Fig. 2.8 Sheared stratified turbulence evolution described by Re_b in the KH mode. Different symbols denote different Pr number cases. The horizontal line indicates the critical value of $Re_b = 20$ where the buoyancy effect can not be neglected in the dissipation scale [77].

anisotropy. Consequently, Piccirillo [90] gave a conservative conclusion that the anisotropy does exist at least for $Re_b < 2000$.

The critical Re_b for anisotropy in finite sheared stratified layer is suggested at the order of 10^2 by Gargett et al. [103], Yamazaki [104] and Itsweire et al. [105]. Figure 2.11 demonstrates the relative contribution from $S_u = \overline{(\partial w/\partial x)^2}$ and $S_w = \overline{(\partial u/\partial x)^2}$ to turbulence dissipation $\bar{\varepsilon}$ simulated by Smyth and Moum [97] with DNS. Similarly, the horizontal lines indicate the corresponding magnitudes of isotropic turbulence. Both S_u and S_w involve strong but different anisotropy while Re_b is less than the order of 10^2. In fact, Smyth found each component of turbulence shear strain tensor contributes differently to $\bar{\varepsilon}$, likewise each components of the vortice and scalar gradient tensor has different tendency in anisotropy.

Over the entire turbulence evolution process in the KH mode, the anisotropy evolves from streamwise velocity dominating (oblate asymmetry) to spanwise velocity dominating (prolate asymmetry) until the end of turbulence life cycle. Figures 2.12 and 2.12 shows that two invariants $II_b = b_{ij}b_{ji}$ and $III_b = b_{ij}b_{jk}b_{ki}$ in vortices tensor v_{ij} and dissipation tensor d_{ij} evolve with Re_b and buoyancy periods $\tau_N = \int_0^t N(t')dt'/2\pi$, where $b_{ij} = (b_i'b_j'/b_k'b_k') - (\delta_{ij}/3)$ indicates the component of anisotropic tensor, δ_{ij} represents Kronecker calculator and $N(t')$ refers to buoyancy frequency. The second invariant II_b indicates the degree of anisotropy with $II_b = 0$ being the ideal isotropic value. The third invariant $III_b > 0$ indicates streamwise and vertical components dominate over spanwise components, corresponding to

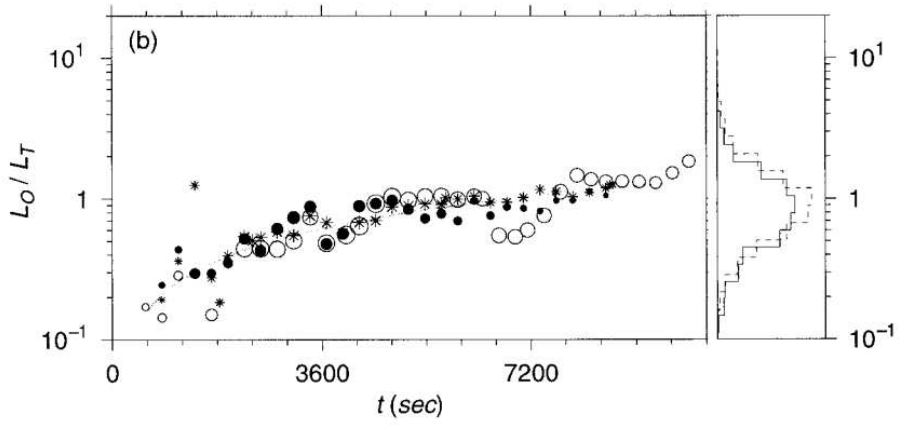

Fig. 2.9 Sheared stratified turbulence evolution described by $R_{OT} = L_O/L_T$ in the KH mode. Different symbols denotes different Pr number cases [77].

primary two dimensional instability. When $III_b < 0$, the spanwise components overwhelms streamwise and vertical components, corresponding to prevalence of secondary instability until turbulence decay stage. In the figures the time when $III_b > 0$ coincides with the early stage before primary and secondary instability saturated and the final stage when the saturated turbulence mode start to collapse. On the other hand, the quasi-isotropy state lasts when both streamwise and spanwise instability saturated, indicating that the saturation of instability in all dimensions leads to isotropic tensor in micro-scale turbulence.

The DNS results above of anisotropy in KH mode imply isotropy turbulence assumption and associated theoretical results still robust as $Re_b > 200$, where most of geophysical flows satisfy [97].However, there is no report of anisotropy analysis in the Holmboe mode. Since the Holmboe mode possesses more wave-like feature and incline to involve emitting of internal gravity that draw energy from unstable turbulence interface layer, the concurrent saturation of primary and secondary instability will be postponed compared to KH mode. Indeed, Smyth et al. [78, 76] and Carpenter et al. [81, 101] observed prolonged period before turbulence complete develop in the Holmboe mode. Consequently, the anisotropic characteristics might sustain for much longer period and much broader range of Re_b for the Holmboe mode.

2.4.5 Transition between two modes

The numerical results on two fundamental mode reviewed above are developed from initial condition where Ri_0, δ_v and δ_θ are specified so as to produce anticipating instability mode. However, the actual sheared stratified turbulence in geophysical flow experiences temporal

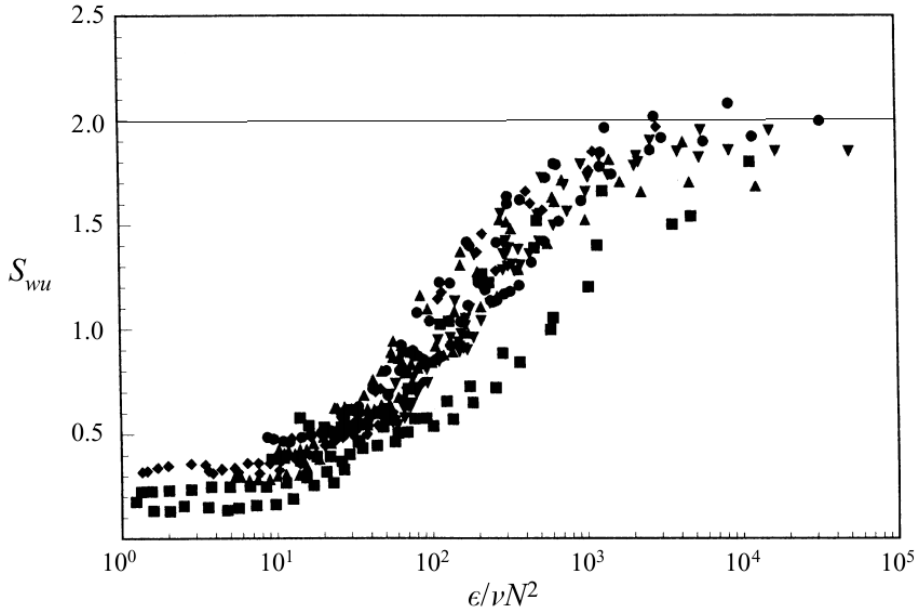

Fig. 2.10 Shear stress component $S_{uw} = \overline{(\partial w/\partial x)^2}/\overline{(\partial u/\partial x)^2}$ for different Ri as function of $Re_b = \varepsilon/\nu N^2$ in uniform sheared stratified layer. The horizontal line indicate the results from isotropic turbulence [90].

and spatial transitional state between the two modes. Several researchers attempt to find the transitional conditions by linear theory. With one dimensional linear analysis, Smyth and Peltier [85] investigated the transitional region between the KH mode to the Holmboe mode in terms of bulk Richardson number Ri_b. They found wave ejection events represented by the deflection and departure of $\overline{p'w'}$ profile as Ri_b increases, indicating transition from KH mode to Holmboe mode. Meanwhile, transitional mode with lower growth rate compared to KH mode was observed, associated special structures in transitional region. In subsequent two-dimensional linear analysis associated with numerical simulations, Smyth and Peliter [98] observed more details about transitional structures. In $Ri_b = 0.25$ case near KH mode region, weak appearance of wave tip loom before the KH eddy pair develops, implying weak Holmboe wave feature. In $Ri_b = 0.26$ close near Holmboe mode region, the central isopycnal overturns and KH wave like vortex structure ensues, but the vortex moves with two counter-propagating waves, indicating that Holmboe mode feature still dominates.

Only a few lab experiment (Koop and Browand [106] and Lawrence et al. [89]) observed the transition from KH mode to Holmboe mode. In two exchange stratified flow configuration, Hogg and Ivey [107] found the central isopycnal overturned like KH eddy but propagated forward regarding to mean flow, as Ri_b approximates the KH-Holmboe transitional region. But the high-vorticity region caused by overturning are not enclosed as primary vorticity

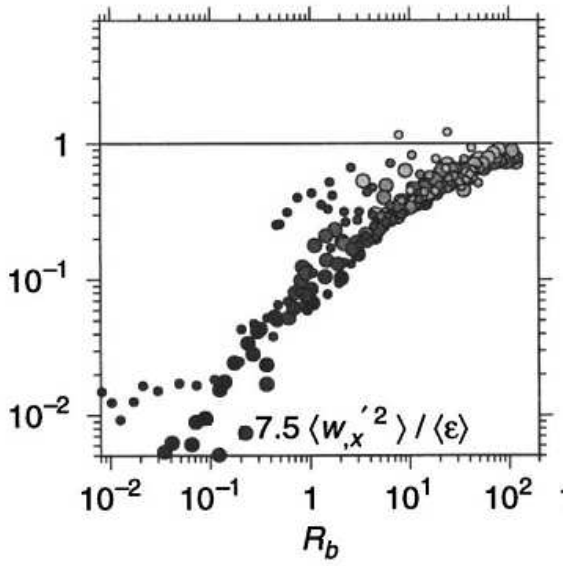

Fig. 2.11 Contribution of (a) $(\partial\bar{w}/\partial x)^2$ and (b)$(\partial\bar{u}/\partial x)^2$ to $\bar{\varepsilon}$ in finite sheared stratified layer. The shade of symbols indicate the time evolution from light to dark. Symbol size indicates the magnitude of Pr [97].

region in KH mode. In water tank experiments with two layer and linear stratified configurations, Strang and Fernando [93] examined the transition among turbulence modes in various bulk Ri_b. They found transitional regions in $3.2 < Ri_b < 5$ and $5 < Ri_b < 5.8$, as shown in Fig. 2.14(a)-(d). As shown in Fig. 2.14(a) when $Ri_b > 3.2$, the interface layer below KH primary billow become distorted and appears as propagating waves. The distorted part interacts with primary KH billow in similar frequency. As Ri_b increases further to $5 < Ri_b < 5.8$, the KH waves emerge less frequently, instead asymmetric waves dominate over the transitional region but break intermittently. As $Ri_b > 5.8$, double side Holmboe waves appear, indicating boundary of transitional region rests on $Ri_b \approx 5.8$.

2.5 Turbulence in convective sheared stratified flows

2.5.1 Introduction

Turbulence mixing is the process in which the surrounding fluid was entrained into turbulence region, dispersed to all turbulence space-time scales by large scale dynamics and diffused by micro scale dynamics [108]. Whether mixing process coupling with turbulence dynamics categorise the turbulence mixing into three levels [109]. The Level 1 turbulence mixing involves passive scalar diffusion that does not couple with turbulence dynamics, such as dye

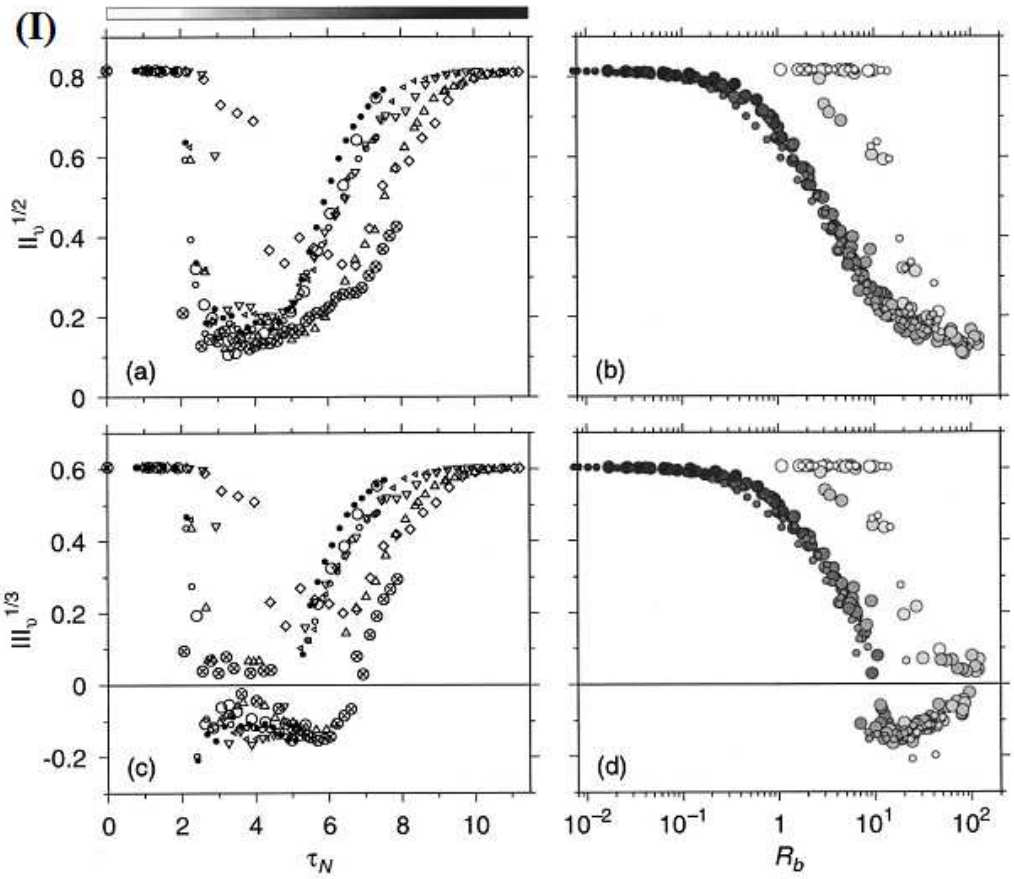

Fig. 2.12 The second invariant ($II_b = b_{ij}b_{ji}$) and third invariant ($III_b = b_{ij}b_{jk}b_{ki}$) of vortices tensor (I) as function of time in buoyancy period and Re_b. The horizontal lines indicate isotropic value for each component.

or particle tracker mixing in the turbulence. By contrast, both Level 2 and Level 3 turbulence mixing couple with turbulence dynamics, the differences between two levels are whether the fluid compositions change as result of turbulence dynamics. The Level 2 turbulence mixing usually occurs in stratified flow where the scalar properties such as density and temperature vary with height. In stratified flow turbulence shear stresses keep modifying the background scalar field through turbulence dynamics, creating local density gradient and consequently inducing the background buoyancy forces that reversely stabilize the effect of turbulence dynamics. The competition between turbulence shear stress and background buoyancy forces represents the coupling between turbulence dynamics and turbulence mixing in Level 2 mixing. The Level 3 turbulence mixing associates with composition changes usually achieved by chemical reactions, which not only introduces much significant buoyancy forces

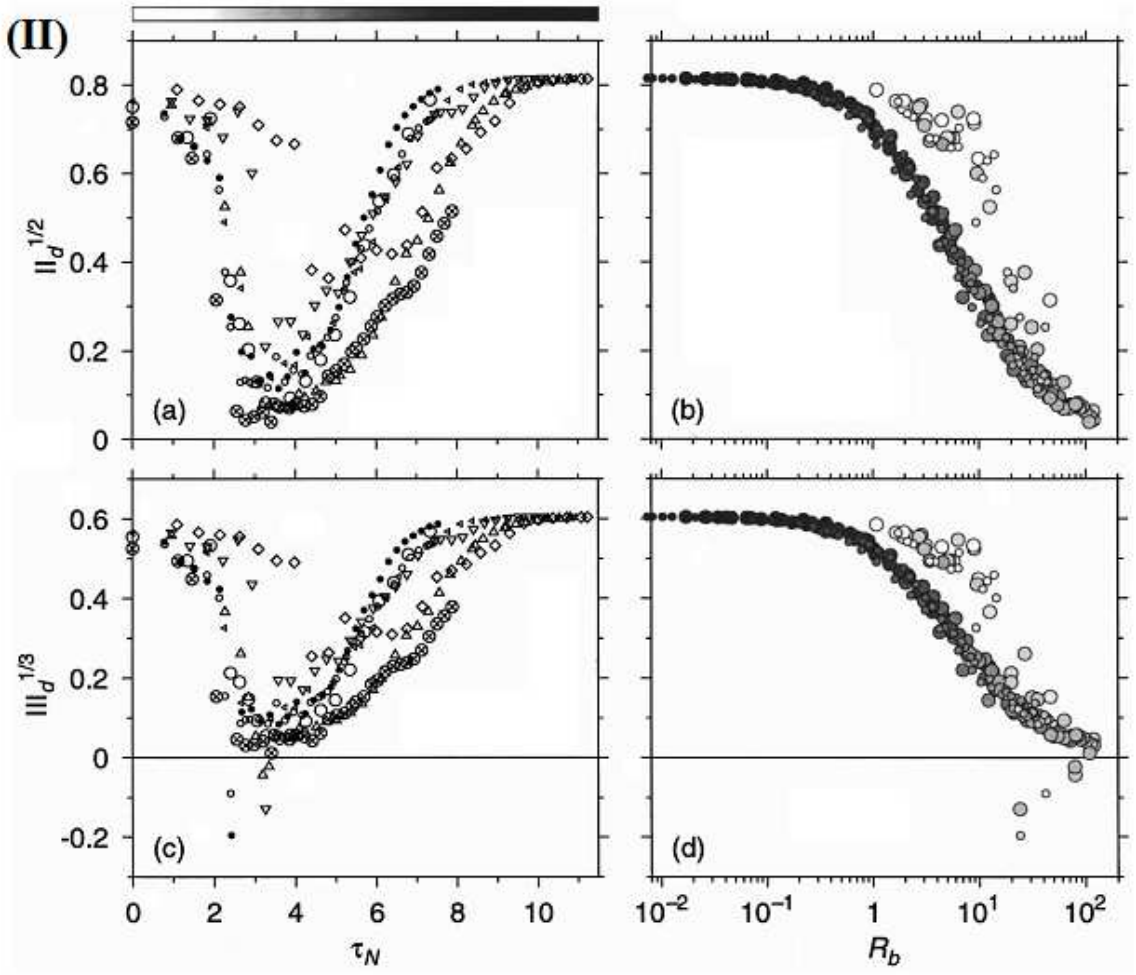

Fig. 2.13 The second invariant ($II_b = b_{ij}b_{ji}$) and third invariants ($III_b = b_{ij}b_{jk}b_{ki}$) of dissipation tensor (II) as function of time in buoyancy period and Re_b. The horizontal lines indicate isotropic value for each component.

than Level 2 does but also incites further single even chain reactions if both stoichiometric ratio and heat condition for ignition are satisfied.

The sheared convective boundary layer (SCBL), usually resides in atmosphere and ocean, both of which are inherently stable stratified as result of heat distributions by the ocean and atmosphere circulation. Thus, the turbulence mixing in the SCBL bears the features of the Level 2 turbulence mixing. In real atmosphere if cloud-topped layer capped over atmospheric boundary layer, lighting and thundering could induce electric-chemical reaction near cumulus, the Level 3 turbulence mixing is involved in the SCBL as well. This review shall prominently concentrate on the Level 2 issue.

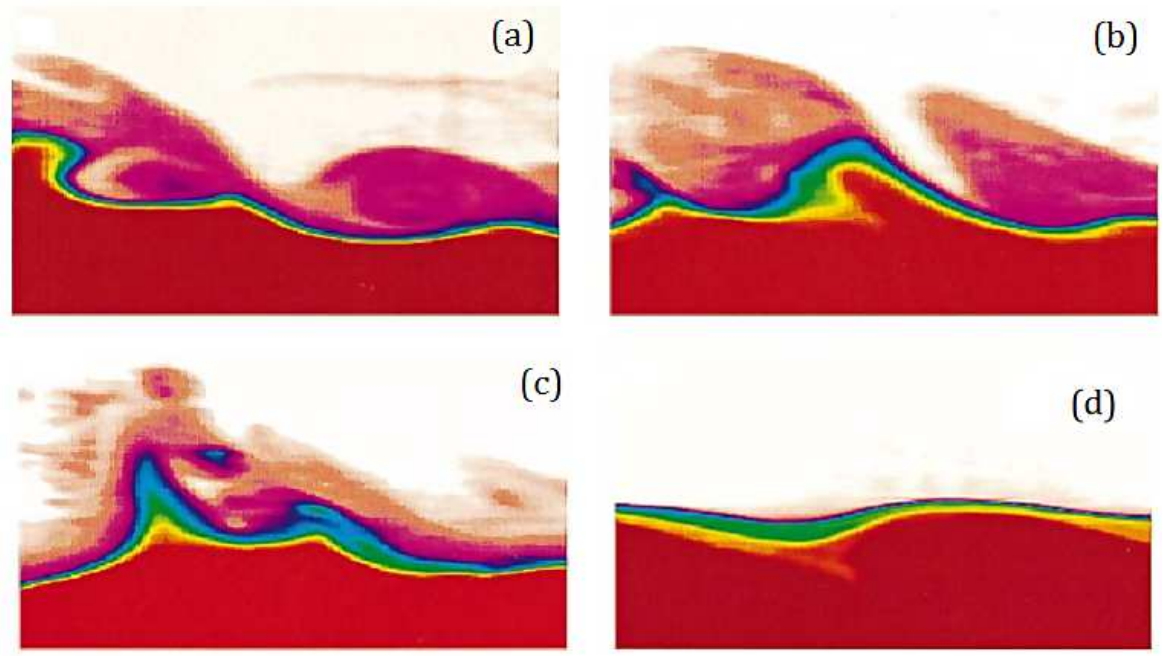

Fig. 2.14 Experimental false color photographs of concentration (density) field in various Ri_b and $\overline{Ri}_g$. (a) $Ri_b = 4.5$, $\overline{Ri}_g = 0.83$; (b) $Ri_b = 5.5$, $\overline{Ri}_g = 1.21$; (c) $Ri_b = 5.8$, $\overline{Ri}_g = 1.78$; (d) $Ri_b = 9.2$, $\overline{Ri}_g = 2.82$.

2.5.2 Sheared convective boundary layer

The sheared convective boundary layer is the boundary layer where turbulent flows arise, develop and decay under the interactions among three shear sources, turbulence shear stress, background stratification and convective turbulence flow. Figure 2.15 shows a typical configuration of the SCBL, where there are two main regions separated by the interface layer. Below the interface layer is the mixed boundary layer, along with wind flow with mean velocity of U_1 and bottom heated surface with constant heat flux B_s. The convective flows induced by B_s fully develop after passing through the free convection zone, then either evolve into coherent plume structures or dissipate by convective turbulence shear. Meanwhile the turbulence shear from wind modifies the temporal evolution and spatial structure of convective turbulence. Over the interface is a stable stratified layer called inversion layer in atmospheric community, where wind flows with mean velocity of U_2 prevail. Within the interface layer does exist strong velocity difference and density difference, which will amplify a random fluctuation X' to the unstable flow pattern and at last to chaotic turbulence.

Since the convective turbulence flow in the mixed boundary layer are much chaotic and energetic, the fluid in the stable inversion layer will be engulfed by or entrain into the mixed

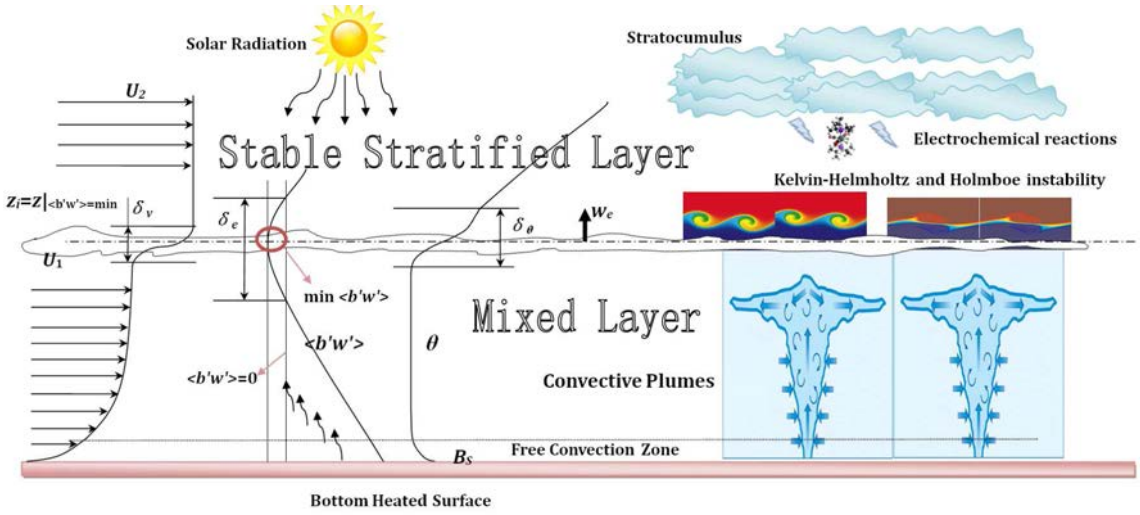

Fig. 2.15 Schematic of sheared convective boundary layer in atmosphere. B_S and $\overline{b'w'}$ represent the surface buoyancy flux and the convective turbulence buoyancy flux. z_i represents height of the interface layer defined by minimum $\overline{b'w'}$. U_1 and U_2 represent horizontal wind velocity in mixed layer and stable stratified layer. $w_e = dz_i/dt$ represents the grow rate of the mixed layer. δ_v, δ_θ and δ_e represent the thickness of the shear interface layer, temperature interface.

layer, forming the interface layer within which the velocity and scalar vary intensely. The ongoing entrainment appears as if the mixed layer keep "pushing" the inversion layer upward. Accordingly the interface layer elevates all the time. During the elevation, the interface layer occasionally radiate part of enlarged waves that carry mass, momentum and energy away to the upper inversion layer.

The SCBL configuration prevails in various environmental and engineering circumstances. For example, the less dense pollutions rise through convective flow and mix in the atmospheric boundary, deteriorating the air quality and causing sour rains. The water vapour from surface of ocean, estuary lake and other reservoirs shares the same transfer and mixing mechanism as well, determining the precipitation of nearby regions. Moreover, the SCBL inherently exists in the upper ocean layer, where the heat and mass mixing is one of the main impetus for cyclone formation. In lakes and reservoirs, entrainment and mixing process in the SCBL flows directly determine the ramification of water layer and the distributions of nutrients and pollutants. Besides its significance in environmental science, the SCBL widely dwells in numerous engineering circumstances, including air-condition and ventilation in buildings, industry heat-exchangers, storage site, heat dissipation for electrical components, smoke transportation in fire scenario and so forth.

2.5.3 Coupling between convective turbulence and sheared turbulence

Mathematically if the reference coordinates are fixed at the interface layer, the upper stratified layer and bottom heated surface can be viewed as the Neumann boundary condition (constant gradient) and the Dirichlet boundary condition (constant flux). Therefore, it is reasonable to consider the turbulence mixing in the SCBL as the coupling solution between convective stratified turbulence and sheared stratified turbulence. On the other hand, pure convective boundary condition and sheared boundary condition for the stratified turbulence can be considered as two extreme solutions in the SCBL as well.

Indeed the convective stratified turbulence and sheared stratified turbulence are distinctively different. In convective stratified turbulence the pressure gradient nearly aligns with background density gradient, while in sheared stratified turbulence the pressure gradient deviates from background density gradient. In atmospheric study, the former case is called barotropy and the latter case is called barocliny. The geometric alignment between velocity/pressure gradients and density gradients results in distinctive turbulence structures and turbulence modes in two configurations. In convective stratified layer, the turbulence structure exhibits the cellular pattern like plumes or thermals. In contrast, the sheared stratified turbulence involves baroclinc vortex and wave-like fluctuations.

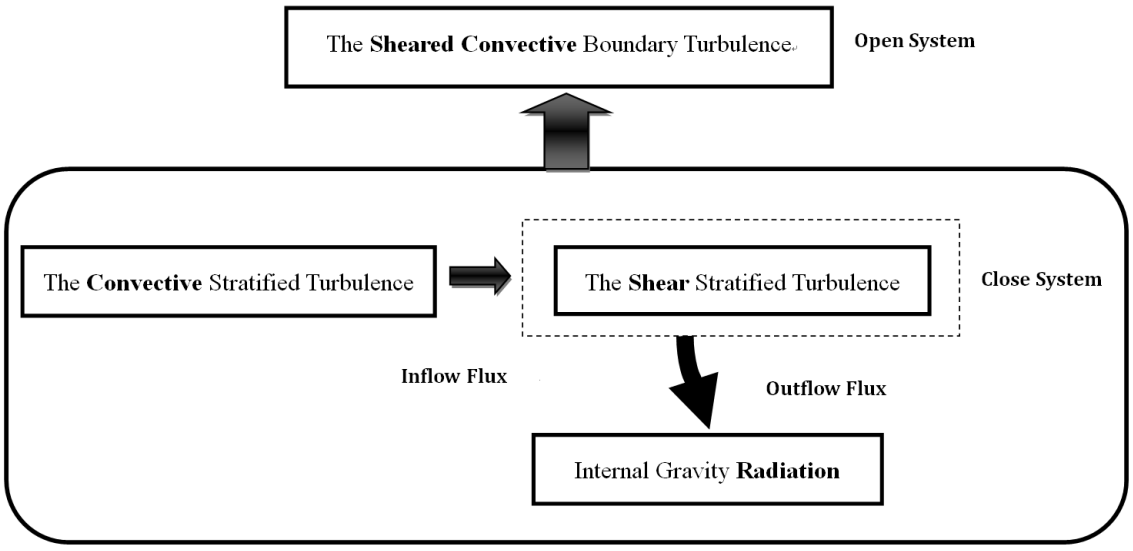

Fig. 2.16 Anatomy of the turbulence mixing in the SCBL.

2.5.4 Scaling parameterization: bulk models

The real atmospheric and oceanic systems comprise considerable internal interactions and external influences, therefore turbulence field experiments inevitably suffer from convoluted mass, momentum and energy transfer mechanisms and variable external boundary conditions. For instance, stratocumulus cloud-topped inversion layer involves complex physical and chemical process such as radiation and multiphase heat and mass transfer and electric-chemical process, not to mention the complicated interactions between physical groups and chemical groups. As for the bottom mixed layer, turbulence shear near complex topography such as region of mountains and valleys contains overreflections of internal gravity wave. As for the wind shear condition, monsoon and other periodical geographical winds entangle the contribution of turbulence shear. Rather than constant B_S shown in Fig. 2.15, the surface buoyancy flux changes with diurnal circle, therefore producing intermittent and patchy convective boundary layer. Similar negative effects from variable conditions prevent oceanic field experimental studies.

As a result, the field experimental results inevitably embrace largely scattered data pool (see, *e.g.* [111–113]). To obtain a converged turbulence statistical data from real but convoluted dynamic field requires substantially temporal and spatial measurements, which extend the technical difficulties and expense to an unaffordable degree. Even if massive information had been successfully collected, only small part will be conserved since the abandoned information is too irregular to analyse. Meanwhile, the resolution of available experimental instruments prevents the field studies from providing adequate information for turbulence prediction and theoretical study. All limitations mentioned above create "fact gap" between field experiments and theoretical needs as described by Bradshaw [115].

In order to solve the "fact gap", the scaling parameterizations campaign has proceeded for several decades. The aims of scaling parameterizations is to develop bulk models, in which some interesting but unavailable bulk properties are related by averaging properties from limited data collected by field experiments. The first bulk properties is the mixed boundary layer growth rate Dz_i/Dt or equivalently entrainment rate w_e. Sometimes the ratio between w_e and characteristic convective velocity $w_* = (B_S z_i)^{1/3}$ [116] will replace the w_e in the bulk model. The second bulk property is the entrainment flux ratio $\beta = \overline{b'w'}|_i/B_s$ where $\overline{b'w'}$ indicates the minimum convective buoyancy flux within the interface layer. w_e and β together with the velocity and scalar flux extracted from field experiments play as input of high level models such as global climate model for weather prediction [117].

Several bulk models in the CBL were developed by simplifying the complex interface layer into simple mathematical forms. According to applied mathematical forms, the bulk models are divided into (a) zero order model (ZOM) [118], where the interface layer is

assumed to be the infinitesimal layer with discontinuous jump of both velocity and scalar, (b) the first order model (FOM) [119] where the velocity and scalar vary linearly across the interface layer, and (c) the general structure model [120] where the variation of velocity and scalar follow polynomial representations. Figure 2.17 displays the buoyancy profile and the horizontal mean velocity profile in the ZOM and the FOM, meanwhile the numerical results calculated by Conziums and Fedorovich [121] are also shown for comparisons. After specific expressions of the interface layer is established, an integration of Turbulence Kinetic Energy (TKE) budget will be operated through the entire domain. Usually, the TKE budget assumes homogeneous turbulence in horizontal direction [122]. After organizing the integration results, the simple mathematical equations associated with the bulk properties w_e and β can be obtained. Conzenmius and Fedorovich [123] listed detailed information of ZOM and FOM bulk models developed so far, except for the FOM developed by Kim [124] and Conzenmius and Fedorovich [121].

Bulk models in the CBL have been proved to reproduce the scaling laws $w_e/w_* = Ri_*^{-n}$ obtained by Deardorff et al. [125] in their water tank experiment and $\beta = 0.2$ [125–127] that has been widely observed by atmospheric field experiments [128] and numerical simulations [129–131, 127, 123, 124, 133]. Nonetheless, the bulk model require pre-input of velocity and buoyancy flux from either field experiments or numerical simulation, whose results still need further justifications. As reviewed above, the field experiments produce largely scattered results, in which numerous unexpected internal and external sources can hardly be eliminated. Recent inter comparisons [134, 135] among a wide range of LES codes showed inconsistent results, in which most of LES codes overestimate turbulence dissipation up to 50%.

Moreover, despite that the bulk models are able to reduplicate the scaling law of entrainment ratio $\beta = 0.2$, such correlation strongly depends on how to select $\overline{b'w'}$ on the numerator. As shown in Fig. 2.18, Fedorovich and Conzenmius [127] found that $\beta = 0.2$ was satisfied only when β was calculated from the buoyancy difference Δb across the interface layer as $\beta = \Delta b(dz_i/dt)/B_S$. If the local buoyancy flux at z_i was selected to calculate β strictly follow the $\beta = \overline{b'w'}|_i/B_s$, the β was found to vary with buoyancy frequency $N = db/dt$. In fact, Schmidt and Schumann [136] and Sullivan et al. [137] found the similar dependence of β on N, as will be shown in next section.

2.5.5 Stratified turbulence structures in the convective boundary layer(CBL)

In spite of the uniform and constant profile in the mixed layer as in Fig. 2.15, the convective flows in fact comprise vivid and rich cellular structures consisted of two fundamental cellular structure: plumes and thermals. The plumes refer to the updraghts extending from heated

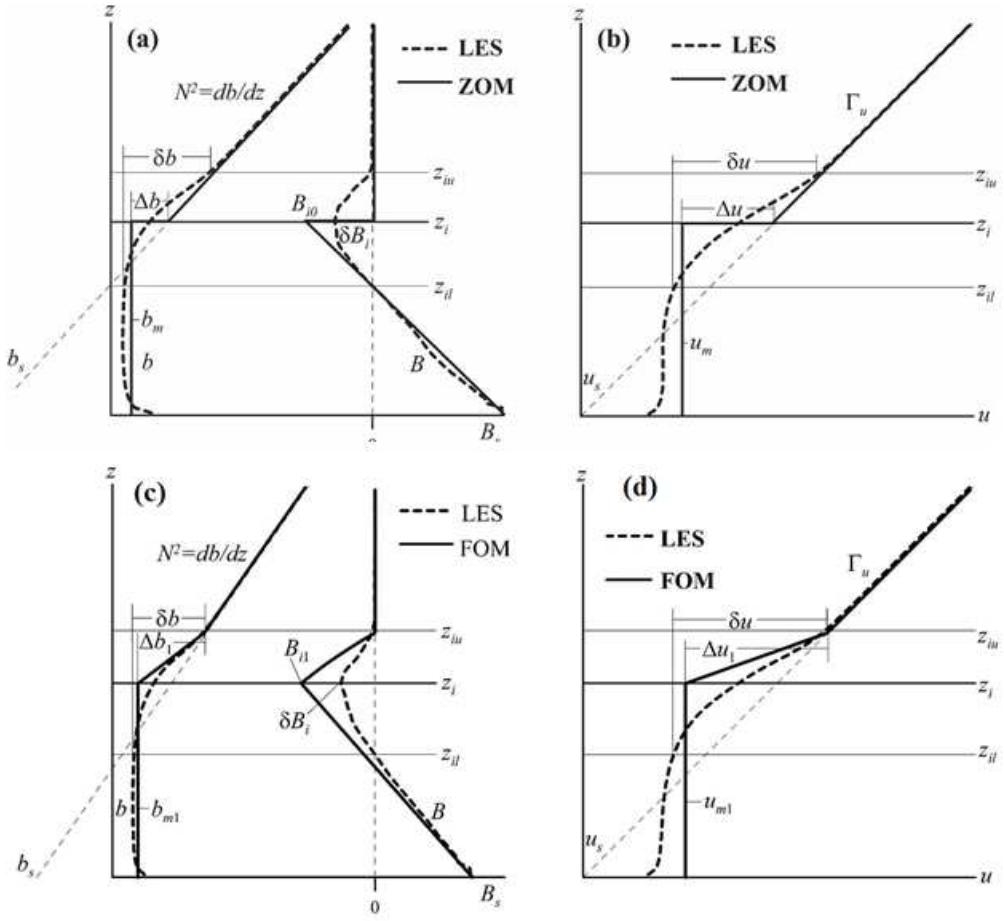

Fig. 2.17 Schematic of the zero order jump model (ZOM) in (a) buoyancy profile and (b) horizontal mean velocity profile compared with numerical results. Schematic of the first order model (FOM) are shown in (c) buoyancy profile and (d) horizontal mean velocity [121].

surface to the inversion layer. The thermals refer to those rising fluid parcels detached from heated surface [138]. Two fundamental elements were observed in water tank experiments by Willis and Deardorff [132, 139], Deardorff and Willis [140] and Adrian, Ferreira and Boberg [141] and field observation by Kaimal et al. [142], Lenschow and Stephens [143], Wilczak and Tillman [144], Greenhut and Khalsa [145, 146], Grossman [147, 148], Crum, Stull and Eloranta[149], among others.

The convective structures below the convective interface layer were investigated in details by Schmidt and Schumann [136] with LES. The numerical results showed that the small and weak thermals are unable to enter the interface layer, instead they merge into large themals or directly decay to disapperence during their rising. On the contrary the large thermals evolve into coherent plume structures. As shown in Fig. 2.18, several plumes along with their

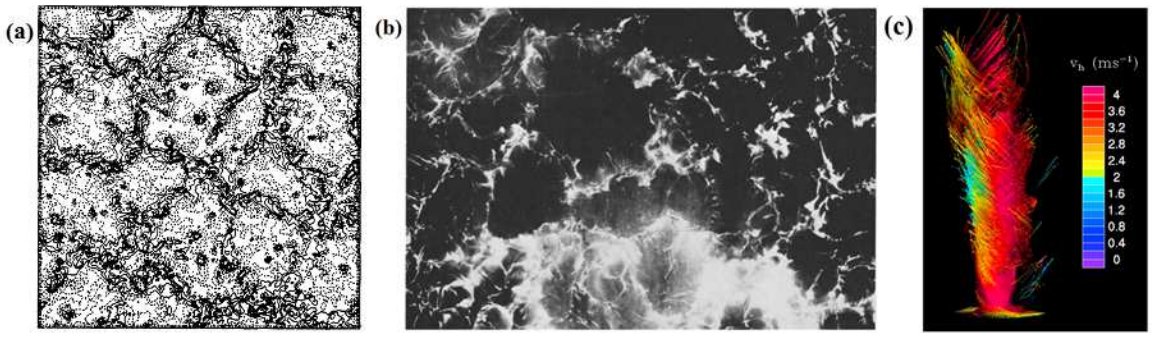

Fig. 2.18 Convective spoke pattern near the lower heated surface (a) simulated by Schmidt [136] with LES and (b) observed by Willis and Deardorff [139] in water tank experiments. (c) Flow visualizations of the dust devils structures. Results from Raasch [151] with LES with high resolution of 2094^3 grids.

bases form the "polygon spoke pattern" [139, 136], which is quite similar to the hexagon structure predicted by linear theory for convection. In water tank experiments by Willis and Deardorff [139] observed analogous patterns as in Fig. 2.18(b). Schmidt and Schumann concluded that the spokes patterns were attributed to the competition between narrow but strong updraughts and large but weak downdraughts. Recently, with high resolution LES, Raasch and Franke [151] and Sullivan and Patton [152] studied smaller micro-structures called "dust devils" near the spoke lines as shown in Fig. 2.18(c). The dust devil vortex appears near the joints between spoke lines and center hubs in spoke structures and survive from a few minutes to several hours based on their length scales [151]. The tails of the dust devil vortex develop into updraughts, which rise and merge with other updraughts into plumes. During the expansion process, Raasch conjectured that the initial vortices generated by dust devils vortex evolve into strong vortices that were observed by Willis and Deardorff [139] near the interface layer surface.

Unlike the coherent plume structure, the interface layer displays strong undulating appearance because the fluid from stable stratified layer entrains into the interface layer. Meanwhile, the fluids within the interface layer are ejected out to the stratified layer. Deardorff [125] observed in water tank experiments that the "wisp" like fluid parcels occasionally ejected out from the small protruding of the interface as shown by the arrows in Fig. 2.19, he called such ejection events as detrainment. Yet, Deardorff observed that the detainment agitated extra entrainment which pulled the detained fluids back to the interface layer. As a result, an overall dynamic equilibrium state between entrainment and detainment was established. Schmidt and Schumann [136] found more complex structures of the fluctuating interface layer. In their LES simulations the intense and narrow updraughts penetrate into upper

stable layer where large regions of warm downdroughts surround. The rising updraughts pull plentiful warm downdraughts downwards and form "tongue" shape structure. The upward "wisp" structures and downward "tongue" structures together compose of a "ring" shape fluctuating structures that embrace the head of plumes on the interface surface. Sometimes double ring layers were observed, as if round wave radiate from the center of plume head.

Furthermore, dependence of interface layer appearance on Richardson number was found in LES by Sullivan et al. [137]. At lower Richardson number (Ri=13.6), the interface layer exhibited "folding" structure similar to detrainment and pull back phenomena in Deardorff's water tank experiment [125]. At stronger Richardson number (Ri=34.5) the upper strong stratification suppresses the rising plume from protruding and turns upward momentum to horizontal direction, then pull the warm air entrain back into the interface layer at the height less than inversion height z_i.

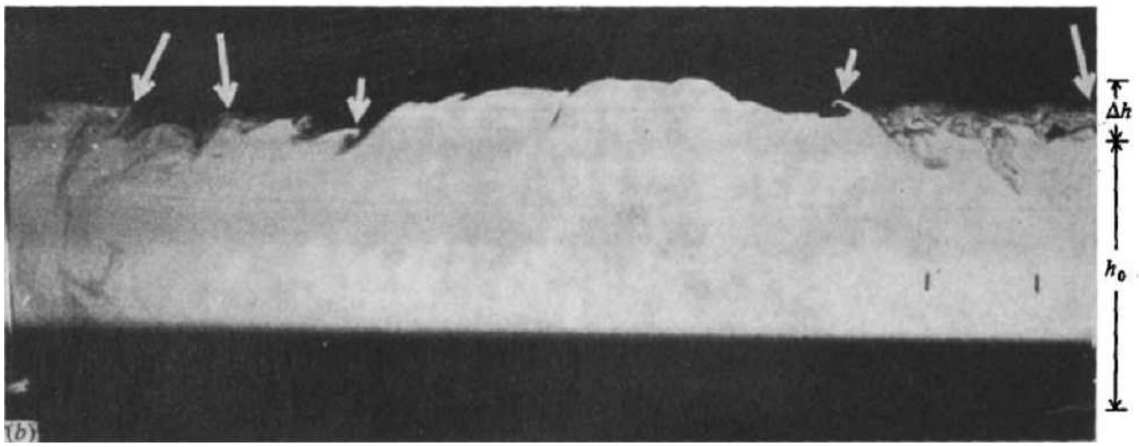

Fig. 2.19 Side view of the interface layer in the CBL observed in water tank experiment [125].

2.5.6 Extrapolation of bulk models to turbulence mixing in the SCBL

The studies on turbulence mixing in the SCBL are mostly from atmospheric community. The methodology of these studies is to inherit and improve the bulk models concept from CBL. In the early time when the CBL bulk model were developed, Stull [126, 153, 154], Zeman and Tennekes [155], Tennekes and Driedonks [156], Driedonks [157], Boers et al. [158], Batchvarova and Gryning [159, 160], Fedorovich [161], and Pino et al. [129] included the wind shear in the ZOM in different ways, because the CBL can not completely spare from the horizontal shear in actual atmosphere. Recently Conzenmius and Fedorovich [122, 123, 121] inherited the horizontal homogeneity assumption in the CBL, therefore excluding turbulence

shear near the interface layer into the scaling and parameterization. On the other hand, Pino et al. [129, 128, 102] and Kim et al. [124] simplified the turbulence shear as surface friction velocity u_* and include u_*or corresponding sheared terms into the TKE budget integration. However, there is no agreement on whether should the shear be included, let alone how to model shear in bulk models.

The controversy was attempted to be resolved by whether modified bulk models correlate well with field experimental results and numerical results, unfortunately none of them give satisfactory answers. The field experiment inevitably involves convoluted physical process, because of highly irregular and scattered experimental results there is no strong correlations between bulk models and field experimental results, as in most recent field experimental study by Canut et al. [114] . These field experimental results incite more uncertainties in creating and evaluating bulk models. Another challenge comes from the the numerical models. Usually, the bulk model need necessary inputs extracted from numerical model, then the derived bulk model results are directly compared with corresponding numerical results. The correlation between two data groups evaluates the quality of the bulk model. Such evaluation procedure requires strong robustness of the numerical model, usually the Large Eddy Simulation mode. Nevertheless, several recent inter comparisons among a large group of LES codes [134, 135] challenge the LES itself as benchmark for bulk models. The LES with Smargorinsky residual stress model intrinsically excludes anisotropic information of stratified turbulence, therefore capture inadequate information of the secondary instability and transitional structures in spanwise direction. For instance, with LES-Smargorinsky model Kim [162] only found some ambiguous features of KH instability compared to clear visualization from lab experiments and Direct Numerical Simulations (DNS). Whether or not capturing these secondary instability in spanwsie direction is crucial to successful simulations of sheared stratified turbulence evolution.

2.5.7 Comments

In the pure convective stratified turbulence, the buoyancy flows/fluxes dominate in the vertical direction, leaving much less kinetic energy in the horizontal direction, therefore at this time horizontal homogeneity are acceptable. On the other hand, the neutralization between entrainment and detainment of the fluid parcels near the interface layer provides equilibrium state in vertical direction. The horizontal homogeneity and vertical equilibrium state produce a statistically stable state where the variations of bulk properties within the interface layer can be assumed into simple mathematical expressions, that is, the bulk models. Indeed in the pure CBL, even the simplest ZOM can correctly capture the profiles of bulk properties across the interface layer.

However, as turbulence shears are introduced by horizontal flows into the CBL, the sheared turbulence instabilities invalidate both horizontally homogeneous turbulence assumptions and vertical equilibrium state. Unlike the vertical equilibrium state in the CBL, a random and small perturbation in the sheared stratified layer will not be counteracted by another negative perturbation, instead it will be amplified by non-linear process to different sheared stratified turbulence instability based on *Ri*. Recently, considerable evidences of sheared instability in the SCBL configuration were found . The shear sheltering phenomena where the presence of shear prevents the convective flux entraining into the interface layer were observed by Conzenmius and Fedorovich [122] in their LES results, indicating the surface shear can neither be neglected nor be simplified as constant friction velocity u_*. Meanwhile, some transitional structures in the SCBL similar to Kelvin-Helmholtz eddy are found numerically by Kim [162] and Conzenmius and Fedorovich[122]. Khanna and Brasseur [163] found that shear streaks at the interface surface concentrate warm air into vertical buoyant sheets, which are quite similar to 'wisps' ejection in Holmboe instability or internal gravity wave radiation found in Kelvin-Helmholtz instability. In addition to numerical simulations, recent experiment in the SCBL induced by strong fire source and exhaustive fan observed potential combined flow structures between Kelvin-Helmholtz eddies and Holmboe waves.

All evidences above indicate the inclusion of horizontal turbulence shear completely changes the statistical equilibrium state of the CBL, leading to unstable mixing process and more turbulence flow patterns. Therefore, the same strategy that simplifies the interface layer will hardly represent the characteristic of sheared stratified turbulence. The SCBL is the coupling boundary layer between convective turbulence and sheared turbulence in stratified layer, therefore it is necessary to understand the characteristics of sheared stratified turbulence as the other extreme case in the SCBL turbulence besides the convective stratified turbulence.

2.6 Discussion

2.6.1 Implication of interactions between shear and buoyancy in stratified layer

The coherent plume structures sustains the connections between the bottom heat flux boundary and the upper rising interface layer by absorbing the evanescent thermals, therefore providing horizontal homogeneity and vertical equilibrium state that enable statistical stable energy transfer in the CBL. When turbulence shear is introduced in the CBL, the formation of plume

will be threatened by shear stress dissipation, leading to more thermals to be dissipated instead of being absorbed by plume. Meanwhile, the shear instability at the surface of the interface layer could also destroy the vortex centers, as implied by the numerical results in Fig. 2.20 from Raasch and Franke [151], who found the cellular pattern transferred into band-shape patterns that resemble the flow pattern in sheared stratified turbulence modes.

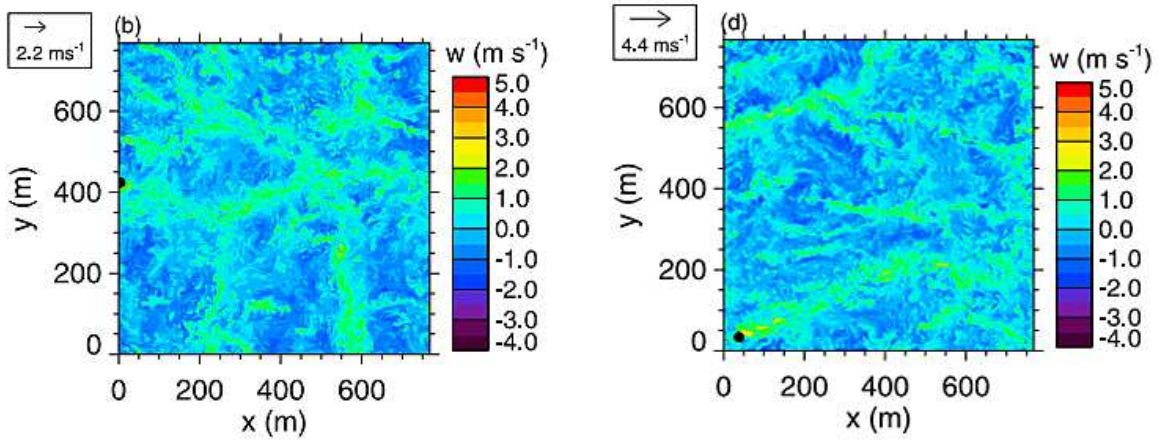

Fig. 2.20 Horizontal cross section of velocity field in high resolution simulation by Raasch and Franke [151] with flow velocity of (a) 2.2 m/s and (b) 4.4 m/s.

Which mechanism will dominate in the SCBL, convective stratified turbulence or sheared stratified turbulence? Recently, an interesting experimental study on fire-induced buoyancy flow by Yang et al. [169] may give some implications. The experimental configuration is shown in Fig. 2.21(a) and the photographs of flow pattern are shown in Fig. 2.21(b). The convective flow was induced by propane gas burner. Usually the temperature of gaseous flame is 1500K~2000K [170], which is ten times larger than heated surface with temperature of 300~330 K in convective boundary. Since the flame induced buoyancy flow is much stronger, one would expect that the flow pattern follows the convective plume structure and fluctuating interface. Interestingly, Yang et al. [169] found Holmboe wave and KH billow at the downstream of fire spot with different flow velocity, indicating that sheared stratified mode dominates over convective flow pattern.

Nevertheless, in the fire-induced buoyancy experiment the photographic in Fig. 2.21 was collected far from the only convective source. In contrast the entire bottom surface with constant heat flux is able to induce a group of convective sources which produce more enduring plume network. Numerical results obtained by Conziumius and Ferdorovich [122] support this conjecture. Figure 2.22 showed the evolution of the interface height z_i in various bottom heat flux Q and background stratification $d\theta/dz$, Fig.2.23 showed the counterparts

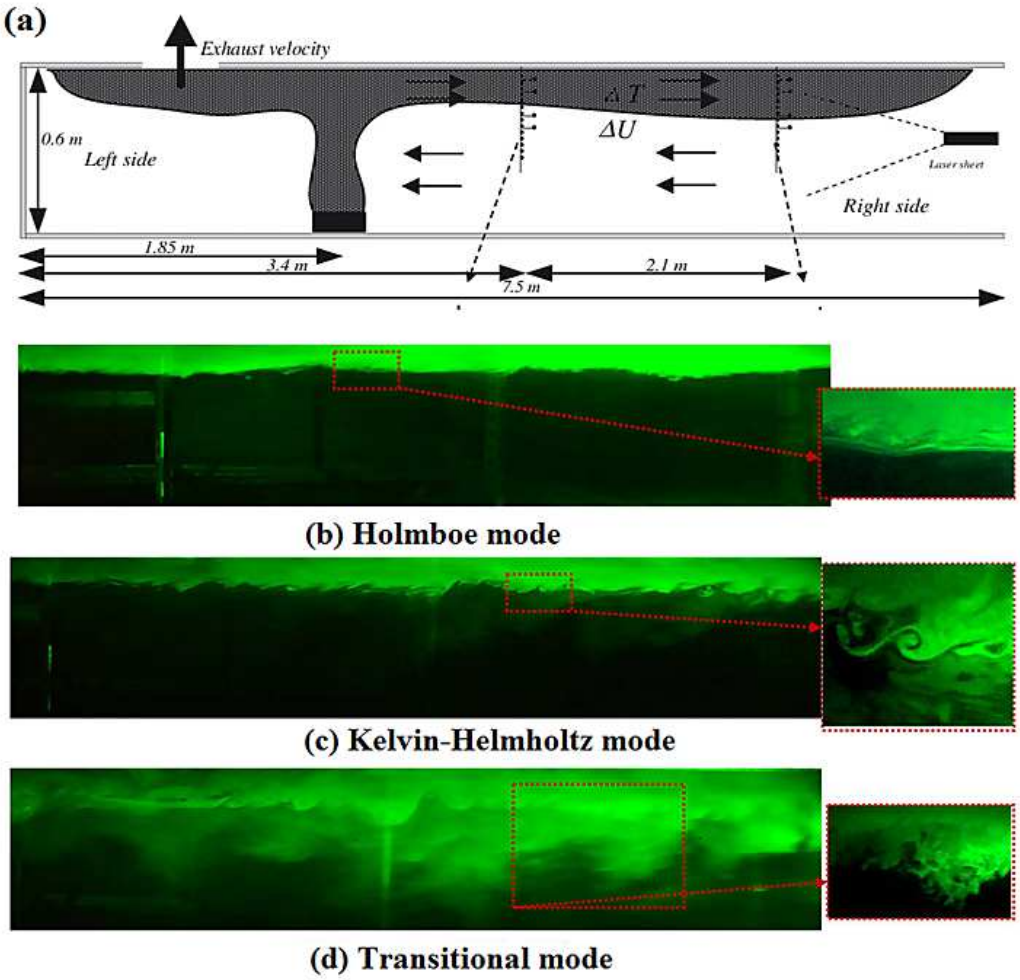

Fig. 2.21 (a) Schematic of fire experiments configuration by Yang et al. [169]. (b)-(d) Photographs of three flow patterns observed in the experiments.

in entrainment ratio β. The meaning of NS, GS and GC refer to caption of Fig. 2.22. In Fig. 2.22(c), (f), (h) and (i), the z_i in sheared convective cases and in pure convective cases nearly overlap, meanwhile the entrainment ratio stay relative constant as shown in Fig. 2.23(c), (f), (h) and (i). The variation of z_i and β suggests that the convective plume remain intact. On the other hand, in Fig. 2.22(d) and (g) z_i, in the GS and GC cases increase with faster rate than the NS case, indicating strong mixing event caused by sheared stratified instability. The corresponding z_i decrease in β in Fig. 2.23(b), (d). The fluctuation of β in Fig. 2.23(e) and (g) and the decreasing of β in Fig. 2.23(b) and (d) imply the dominance of sheared stratified instability, since the decreasing β called "shear sheltering" might indicate the destroying of convective plume.

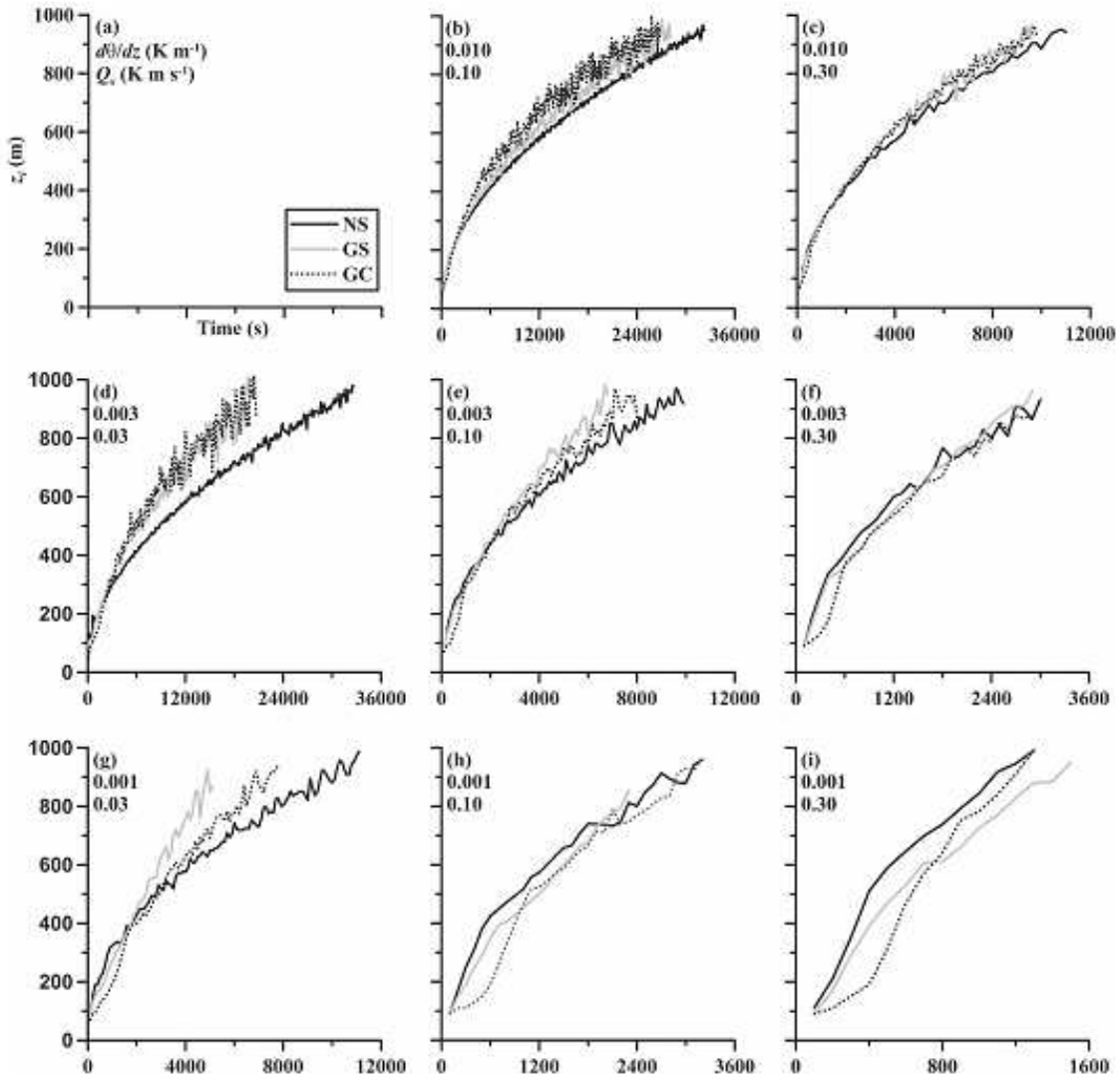

Fig. 2.22 The LES results from Conziumius and Ferdorvich [122] of the height of the inversion layer z_i vary with time. NS, GS, GC indicate no shear case, geographical wind of 20 m/s near the interface and constant geographical wind of 20 m/s throughout flow domain. $d\theta/dz$ and Q represent background temperature gradients and constant buoyancy flux from bottom surface.

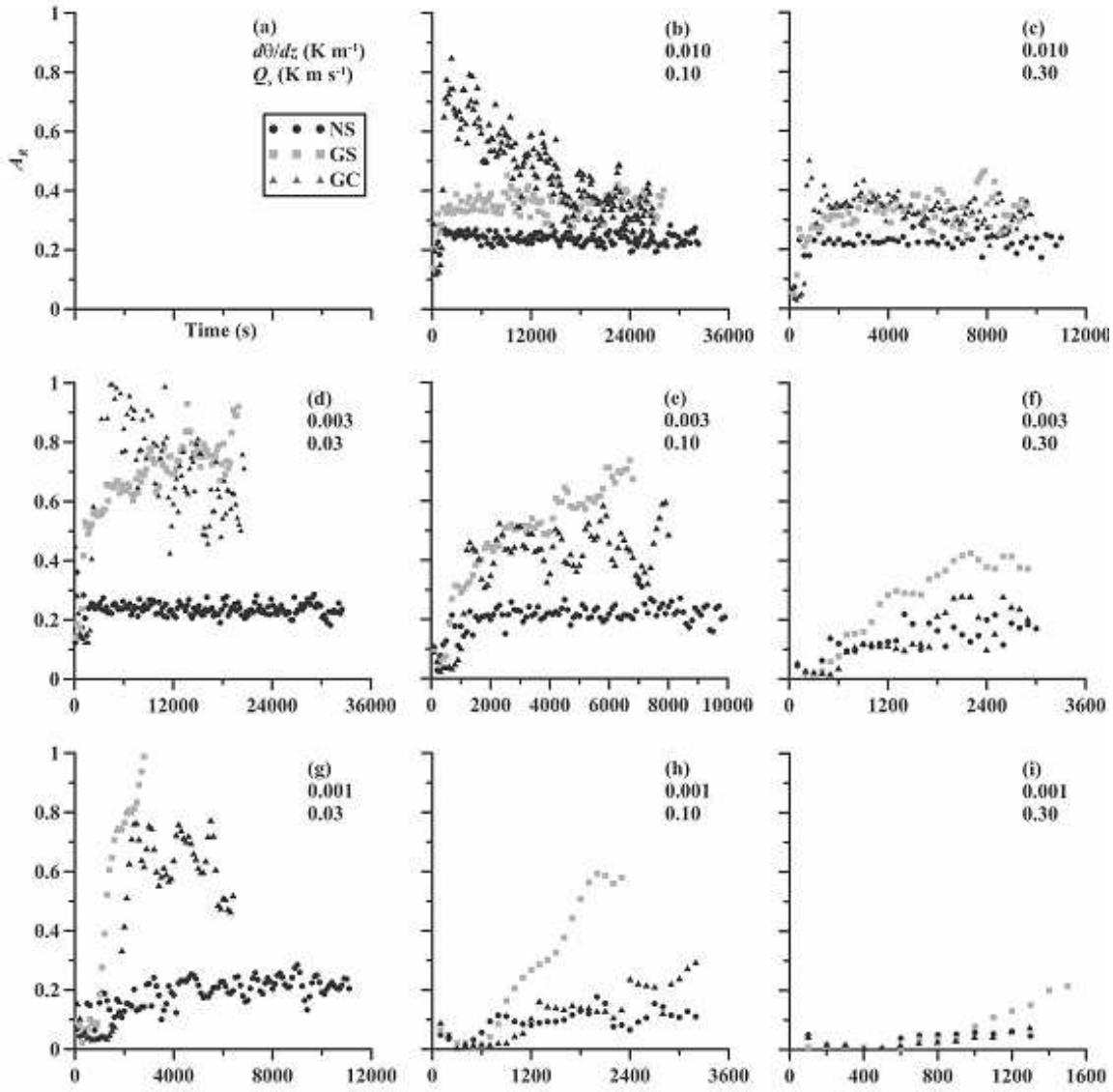

Fig. 2.23 The LES results from Conzium and Ferdorvich [122] of the entrainment ratio A_R (β) vary with time. NS, GS, GC indicate no shear case, geostropic wind of 20 m/s near the interface and constant geostropic wind of 20 m/s throughout flow domain. $d\theta/dz$ and Q represent background temperature gradients and constant buoyancy flux from bottom surface.

It is conjectured that there are two fundamental modes: S dominant mode and B_S convection dominant mode in the SCBL. When turbulence shear dominates in the SCBL, most of the coherent plume structures will be undermined and destroyed. As a result the residual convective plume cannot defend the equilibrium state near and within the interface layer, which will be conducive to sheared stratified instability. Despite that Fig. 2.21 implicates the flow patterns in S dominant mode, in practical SCBL the interface layer keeps elevating and engulfing the fluids from upper stable stratified layer rather than being blocked by walls as in fire-induced buoyant flow experiments. The rising of the interface has what kind of influences on sheared stratified turbulence? The answer still blank, but one thing that can be sure is that effect of B_S cannot be neglected, even though B_S plays the second role in the sheared convective turbulence.

When B_S dominates in the SCBL, more plumes associated with spoke pattern at their base will be established and survive from attack of turbulence shear. At this time, the equilibrium state at the interface layer will be well preserved to the degree that the entrainment ratio β stay relatively constant as shown in Fig. 2.22(c), (e) and (f) but might be large than $\beta = 0.2$ as shown in Fig. 2.23(e) and (f), because the weak turbulence shear provides more turbulence kinetic energy to the interface layer.

If S dominant mode and B_S convection dominant mode do exist, there will be a critical condition or transitional regions that separate two modes. The classic Ri number can only provide a relative measurement between S and internal buoyancy B in the turbulence interface, rather than external buoyancy stems from B_S. It is conjectured that new characteristic numbers that can measure the ratio among S, B, B_S in the mixed layer and S , B , $b'w'$ within the interface layer could be the key to describe the critical conditions or transitional regions.

2.6.2 Mixing efficiency Γ and entrainment ratio β

Turbulence mixing efficiency Γ is of great interests among engineers and scientists, who want to know how many turbulence kinetic energy is able to convert into potential energy and the density and temperature profiles after mixing. Traditionally, turbulence mixing efficiency Γ could estimate the turbulence diffusivity $K_\rho = \Gamma\varepsilon/N^2$. In oceanic community, Γ is considered as a constant value of 0.2 based on laboratory observations by Ivey and Imberger [164]. Yet several observations [165–167] suggest variable Γ during the mixing. In recent DNS studies by Smyth et al. [97, 100, 79, 80], Γ was found to vary in non-monotonic tendency: Γ increases during pre-turbulence stage, then reaches the summit when the saturated structures start to collapse, subsequently decreases exponentially as turbulence decay and finally approximate to constant value. The evolution history indicates inaccurate assumption of $\Gamma = 0.2$.

There are several ways to define turbulence efficiency in sheared stratified layer. The first definition is analogous to the definition in engine, where the "efficiency" is defined as the ratio of achieved work to energy input. Therefore the ratio of $\mathscr{B}$ and $\mathscr{S}$ equivalently the flux Richardson number Ri_f becomes a candidate of mixing efficiency. Nevertheless, because both $\mathscr{B}$ and $\mathscr{S}$ are reversible, the turbulence mixing resembles an electric vehicle that recycle part of energy input back to recharge itself more than an ideal engine that convert all energy input in irreversible way [76]. Therefore using Ri_f sometimes produce negative values and is not adequate to provide convincing measurement of mixing efficiency.

To avoid negative value, a substitute of Ri_f introduced by McEwan [168] is defined as:

$$\Gamma_f = \frac{e_i}{1-e_i}[1+\frac{1}{\varepsilon'}\frac{d}{dt}(\mathscr{K}'+\mathscr{P}_\mathrm{a}]$$

in which $e_i = \mathscr{M}/\mathscr{S}$ indicate the ratio of work done to dissipation. But as dissipation ε' become small, the Γ_i will become large therefore unable to predict the practical mixing efficiency either.

Inspired by Winter [75] who separate irreversible potential energy $\mathscr{P}_b$ from total potential energy $\mathscr{P}_t$, Smyth and Peltier [98] suggested the turbulence mixing efficiency Γ should be the ratio of irreversible mixing rate $\mathscr{M}$ and energy dissipation ε:

$$\Gamma_i = \frac{\mathscr{M}}{\bar{\varepsilon}+\varepsilon'}$$

which avoids the difficulties to separate $\mathscr{S}$ into reversible parts and irreversible parts. The virtue of using ε as denominator is that energy dissipation happened in small scale where wave-like structure has less influence.

A more advanced definition is E_i defined by Caulfield and Peltier [79, 80]:

$$E_i = \frac{\mathscr{M}}{\mathscr{M}+\bar{\varepsilon}+\varepsilon'}$$

in which E_i reduces the error caused by small ε and shows the best results in DNS simulation with relatively small Re [76, 80]. However, since ε strongly depends on Re, whether E_i is validated in high Re cases requires further justifications.

Moreover, as shown in Fig. 2.24 Γ_i in different Pr could be correlated by modified $\hat{R}_{OT} = L_O/L_{En}^{3/4}L_T^{1/4}$, in which $L_{En} = w_{rms}^3/\varepsilon_z$ indirectly indicates the isotropic kinetic energy carried by primary large eddies [77]. Smyth also found after pre-turbulence stage L_E evolve proportionally with L_T, therefore L_{En} is qualified to measure energy containing scale during

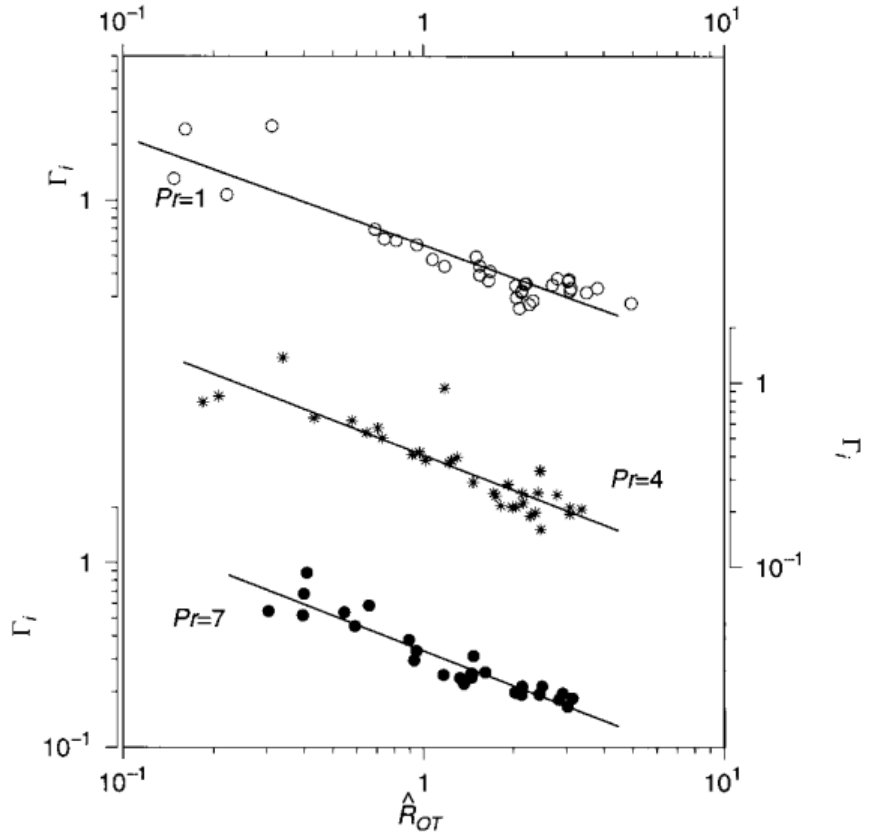

Fig. 2.24 Γ_i as a function of $\hat{R}_{OT}$ in $Pr = 1, 4, 7$ calculated by Smyth et al. [76] with DNS.

saturation of turbulence instability. Smyth obtained a correlation:

$$\Gamma_i \approx 0.33 \hat{R}_{OT}^{-0.63}$$

which imply a potential estimation of Γ_i by $\hat{R}_{OT}$ in KH mode.

Since the buoyancy flux from the bottom heated surface play as the dominant energy supply source in the CBL, the statistic equilibrium state of the interface layer observed by Deardorff et al. [125] indicate statistically stable energy transfer between upper stratified layer and the convective interface, resulting in the scaling laws $w_e/w_* = Ri^{-n}$ and $\beta \approx 0.2$. However, in the SCBL the turbulence shear play as the other energy source, introducing reversible energy transfer within the interface layer and more importantly stratified turbulence modes. Turbulence instability modes as well as more complex energy transfer among turbulence shear S, internal buoyancy B , the external buoyancy flux $\overline{b'w'}$ developed from B_S and dissipation ε will not allowβ and w_e/w_*in the SCBL being in equilibrium state anymore. Similarly, the mixing efficiency Γ within the interface layer will also become more

complicated, because after the external flux boundary join in, the close system in Fig. 2.1 translates into open system in which the energy transfer processes involving S, B, ε and $\overline{b'w'}$.

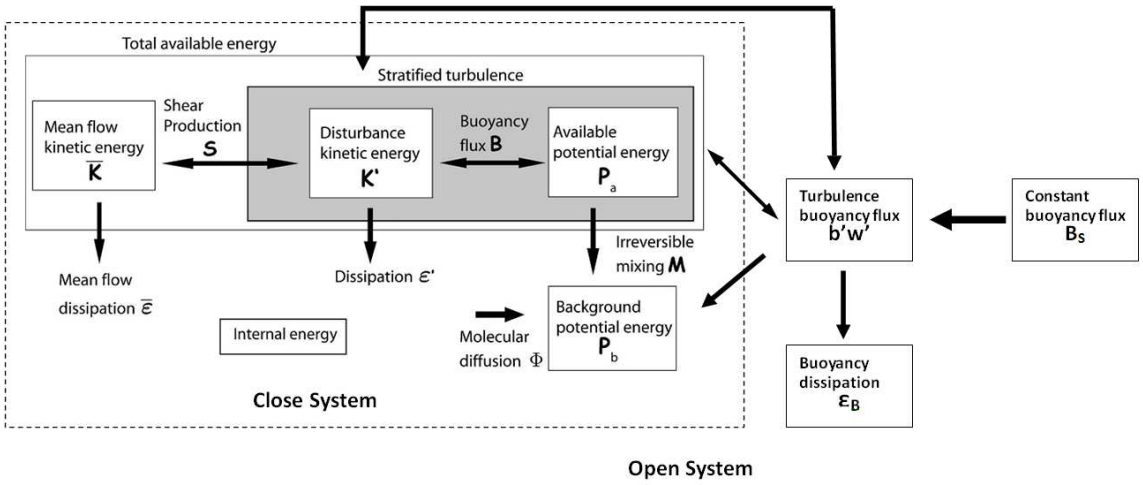

Fig. 2.25 Energy partition and transfer for convective sheared stratified turbulence. Arrows show the capable energy transfer directions.

Determined by energy transfer process in the same open sytem, The β and Γ must have certain correlation . Here this review give some conjectures on how theβ and Γ interact with each other. Figure 2.25 showed the potential energy transfer among energy reservoirs in open system with external flux boundary condition B_S. Inspired by Winter [75], the contribution of $b'w'$to potential energy was divided in reversible and irreversible part. Therefore, the background potential energy P_b consist of one part $P_{b,S}$ within the interface layer and the other part $P_{b,B}$ from $b'w'$, in a word, $P_b = P_{b,S} + P_{b,B}$. Following the $\Gamma_i = [(dP_b/dt) - \Phi]/(\bar{\varepsilon} + \varepsilon')$ from Smyth and Moum [97] and the $\beta = \overline{b'w'}|_{min}/B_S$, it is expected to obtain certain correlation between Γ_i and β by new characteristic numbers or length scales that include $P_{b,B}$ and dissipation ε within the interface layer.

2.7 Summary of Literature Review

Since the early linear stability analysis on the parallel shear stratified flow were established, where $V \ll U$ in the Cartesian system is always satisfied, substantial numerical and experimental investigations had confirmed the existences of instability modes and unveiled the beauty of coherent flow structures. With the further knowledge of coherent flow structures, significant progress were also made in field experiments, which further improve the modelling at atmospheric and global scale level. In addition, the understanding of coherent flow

structures and how they transit to turbulent flow state, significantly contribute to the industry design related to turbulence mixing.

However, as suggested in Chapter 1, as long as flow is twisted V is always comparable to U. The existence of cross shear from V will add extra basic velocity terms in classic linearized equation group of parallel shear flow. As will be shown in the following chapters, the additional cross shear not only modify the features of known coherent flow structures, but also introduce potentially new coherent flow structures and different transitional routine to turbulence.

References

[1] Corcos, G. M. & Sherman, F. S. 1984. The mixing layer: deterministic models of a turbulent flow. Part 1. Introduction and the two-dimensional flow. *J. Fluid. Mech,*. 139: 29-65.

[2] Peter, J. S. & Dan, S. H. 2003. Stability and Transition in Shear Flows: Chapter 9 Transition to Turbulence. *Springer*.

[3] Criminale, W. O., Jackson, T. L. & Joslin R. D. 2003. Theory and Computation of Hydrodynamics Stability. *Cambridge University Press,* New York.

[4] Drazin, P. G. 2002. Introduction to Hydrodynamic. *Cambridge University Press.*

[5] Drazin, P. G. & Reid, W. H. 2004. Hydrodynamic Stability (second edition). *Cambridge University Press.*

[6] Pope, S. B. 2000. Turbulent flows. *Cambridge University Press,* New York.

[7] Thorpe, S. A. 2005. The Turbulent Ocean. *Cambridge University Press.*

[8] Thorpe, S. A. 2007. An introduction to ocean turbulence. *Cambridge University Press.*

[9] Brandt, L. 2014. The lift-up effect: the linear mechanism behind transition and turbulence in shear flows. *European Journal of Mechanics B: Fluids.* 47: 80-96

[10] Hussain, A. K. M. 1986. Coherent structures and turbulence. *J. Fluid. Mech,*. 173: 303-356.

[11] Fernando, H. J. S. 1991. Turbulent mixing in stratified fluids. *Annual Review of Fluid Mechanics.* 23: 455-493.

[12] Paul, E. D. 2015. Turbulence mixing. *Annual Review of Fluid Mechanics.* 37: 329-56.

[13] Reynolds, O. 1883. An experimental investigation of the circumstances which determine whether the motion of water shall be direct or sinuous, and of the law of resistance in parallel channels. *Scientific papers*, 2: 51-105.

[14] Rayleigh, Lord (Strutt, J. W). 1899. On the stability or instability of certain fluid motions. *Scientific Papers,* 1: 474-487

[15] Rayleigh, Lord (Strutt, J. W). 1900. On the stability or instability of certain fluid motions: Part II. *Scientific Papers,* 2: 200-207

[16] Rayleigh, Lord (Strutt, J. W). 1902. On the question of the stability of the flow of fluids. *Scientific Papers,* 3: 575-584

[17] Rayleigh, Lord (Strutt, J. W). 1913. On the stability of the laminar motion of an inviscid fluid. *Scientific Papers,* 6: 197-204

[18] Rayleigh, Lord (Strutt, J. W). 1920. Further remarks on the stability of viscous fluid motion. *Scientific Papers,* 6: 266-275

[19] Fjgrtoft, R. 1950. Application of integral theorems in deriving criteria of stability of laminar flow and for the baroclinc circular vortex. *Geofysiske Publikasjoner,* 17: 1-52.

[20] Orr, W. M. 1907. Lord Kelvin's investigations, especially the case of stream which is shearing uniformly. *Proceedings Royal Irish Academy.* A27: 80-138.

[21] Orr, W. M. 1907. The stability or instability of the stready motions of a perfect liquid and of a viscous liquid. *Proceedings Royal Irish Academy.* A27: 9-138.

[22] Sommerfeld, A. 1908. Ein Beitraz zur hydrodynamischen erklaerung der turbulenten fluessigkeitsbewegungen. *Proc. Fourth Inter. Congr.* Mathematicians, Rome, 116-124.

[23] Tollmien, W. 1929. The production of turbulence. *NACA TM-609,* 1931.

[24] Tietjens, O. 1925. Beitrage zur entschung der turbulenz, textbfZeitschrift fuer Angewandte Mathematik und Mechanik, 5: 200-217.

[25] Romanov, V. A. 1973. Stability of plane-parallel Couette flow. *Functional Analysis & its Applications, 7,* 137-146.

[26] Schlichting, H. 1932. Uber die stabilitata deer Couettestromung. *Ann. Physik(Leipzig),* 14: 905-936. (in Germany)

[27] Schlichting, H. 1932. Uber die enstchung der turbulenz bei der Plattenstromung. Gessellschaft der Wissenschaften. *Gottingen. Mathematisch-Naturwissenschaftliche Klasse,* 160-198. (in Germany)

[28] Schlichting, H. 1933. Zur entstchung der turbulenz bei der Plattenstromung, Gessellschaft der Wissenschaften. *Gottingen. Mathematisch-Naturwissenschaftliche Klasse,* 181-208. (in Germany)

[29] Schlichting, H. 1933. Laminar spread of a jet. *Zeitschrift fuer Angewandte Mathematik und Mechanik,* 13(4): 260-263. (in Germany)

[30] Schlichting, H. 1935. Amplitudenvertcilung und Energiebilanz der kleinen Storungen bei der Plattengrenzschicht. Gesellschaft der Wissenschatten. *Gottingen. Mathematisch-Naturwissenschattliche Klasse,* 1: 47- 78. (in Germany)

[31] Schubauer, G. B. & Skramstad, H. K. 1947. Laminar boundary layer oscillations and stability of laminar flow. *Journal of the Aeronautical Sciences. 14(2),* 69-78.

[32] Klebanoff, P. S., Tidstrom, K. D. & Sargent, L. M. 1962. The three-dimensional nature of boundary layer instability. *J. Fluid. Mech,.* 12: 1-34

[33] Herbert, T., Bertolotti, F. P. & Santos, G. R. 1985. Floquet analysis of secondary instability in shear flows. In *Stability of Time Dependent and Spatially Varying Flows,* August 19-23, 1985, 43-57.

[34] Kachanov, Y. S, Kozlov, V. V & Levchenko, V. Y. 1979. Experiments on non-linear interaction of waves in boundary layers. In *Laminar-Turbulent Transition. IUTAM Symposium.* Stuttgart. Germany. 135-152

[35] Kachanov, Y.S. & Levchenko, V. Y. 1984. The resonant interaction of disturbances at laminar-turbulent transition in a boundary layer. *J. Fluid. Mech,.* 138: 209-247.

[36] Herbert, T. 1988. Secondary instability of boundary layers. *Annu. Rev. Fluid Mech.,* 20, 487-526.

[37] Orszag, S. A. & Patera, A. T. 1980. Subcritical transition to turbulence in plane channel flows. *Phy. Rev. Letter.,* 45: 989-993.

[38] Orszag, S. A. & Patera, A. T. 1981. Subcritical transition to turbulence in plane shear flows. In *Transition and Turbulence.* 127-146.

[39] Waleffe, F. 1997. On a self-sustaining process in shear flows. *Phys. Fluids.,* 9: 883-900.

[40] Hamilton, J.M., Kim, J. & Waleffe, F. 1995. Regeneration mechanisms of near-wall turbulence structures. *J. Fluid. Mech,*. 287: 317-348.

[41] Howard, L.N. 1961. Note on a paper of John W. Miles. *J. Fluid. Mech.*, 10: 509-512.

[42] Taylor, G. I. 1931. Effect of variation in density on the stability of superposed streams of fluid. *Proceedings of the Royal Society of London. Series A.* 132: 499-523.

[43] Goldstein, S. 1931. On the stability of superposed streams of fluids of different densities. *Proceedings of the Royal Society of London. Series A.* 132: 524-548.

[44] Miles, J. W. 1961. On the stability of heterogeneous shear flows. *J. Fluid. Mech,.* 10(4): 496-508.

[45] Lord Kelvin (Thomson, W.). 1871. Hydrokinetic solutions and observations. Philosophical Magazine 42: 362-377.

[46] Helmholtz H. V. 1868. On the discontinuous movements of fluids. *Monthly Reports of the Royal Prussian Academy of Philosophy in Berlin.* 23: 215-228.

[47] Hazel, P. 1972. Numerical studies of the stability of inviscid stratified shear flows. *J. Fluid. Mech,.* 51: 39-61.

[48] Holmboe, J. 1962. On the behavior of symmetric waves in stratified shear layers. *Geophysical Publication.* 24: 67-113.

[49] Caulfield, C. P. 1994. Multiple linear instability of layered stratified shear flow, *J. Fluid. Mech,.* 258: 255-285.

[50] Corcos, G. M. & Lin, S. J. 1984. The mixing layer: deterministic models of a turbulent flow. Part 2. The origin of the three-dimensional motion. *J. Fluid. Mech,.* 139: 67-95.

[51] Lin, S. J. & Corcos, G. M. 1984. The mixing layer: deterministic models of a turbulent flow. Part 3. The effect of plane strain on the dynamics of streamwise vortices. *J. Fluid. Mech,.* 141: 139-178.

[52] Rogers, M. M. & Moser, R. D. 1992. The three-dimensional evolution of a plane mixing layer: the Kelvin-Helmholtz rollup. *J. Fluid. Mech,.* 243: 183-226.

[53] Moser, R. D. & Rogers, M. M. 1992. The three-dimensional evolution of a plane mixing layer: pairing and transition to turbulence. *J. Fluid. Mech,.* 247: 275-320.

[54] Thorpe, S. A. 1973. Turbulence in stably stratified fluids: a review of laboratory experiments. *Boundary-Layer Meteorology.* 5: 95-119.

[55] Thorpe, S. A. 1985. Laboratory observations of secondary structures in Kelvin-Helmholtz billows and consequences for ocean mixing. *Geophysical & Astrophysical Fluid Dynamics.* 34: 175-199.

[56] Klaassen, G. P. & Peltier, W. R. 1985. The evolution of turbulence in finite amplitude Kelvin-Helmholtz billows. *J. Fluid. Mech,.* 155:1-35.

[57] Klaassen, G. P. & Peltier, W. R. 1989. The role of transverse secondary instabilities in the evolution of free shear layers. *J. Fluid. Mech,.* 202: 367-402.

[58] Caulfield, C. P. & Peltier, W. R. 2000. The anatomy of the mixing transition in homogeneous and stratified free shear layers. Journal of Fluid Mechanics. 413: 1-47.

[59] Peltier, W. R. & Caulfield, C. P. 2003. Mixing efficiency in stratified shear flows. *Annu. Rev. of Fluid Mech.,* 35: 135-167.

[60] Mashayek, A. & Peltier, W. R. 2012. The "zoo" of secondary instabilities precursory to stratified shear flow transition. Part 1. Shear aligned convection, pairing, and braid instabilities. *J. Fluid. Mech,.* 708: 5-44.

[61] Mashayek, A. & Peltier, W. R. 2012. The "zoo" of secondary instabilities precursory to stratified shear flow transition. Part 2. The influence of stratification. *J. Fluid. Mech,.* 708: 45-70.

[62] Mashayek, A. & Peltier, W. R. 2013. Time-dependent, non-monotonic mixing in stratified turbulent shear flows: implications for oceanographic estimates of buoyancy flux. *J. Fluid. Mech,.* 736: 570-593.

[63] Maxworthy, T. & Browand, F. K. 1975. Experiments in rotating and stratified flows: oceanographic application. *Annu. Rev. of Fluid Mech.,* 7: 273-305.

[64] Lawrence, G. A., Browand, F. K. & Redekopp, L. G. 1991. The stability of a sheared density interface. *Phys. Fluids.,* 3: 2360-2370.

[65] Schowalter, D. G., Van Atta, C. W. and Lasheras, J. C. 1994. A study of streamwise vortex structure in a stratified shear layer. *J. Fluid. Mech,.* 281: 247-291.

[66] Smyth W. D. & Winters, K. 2003. Turbulence and mixing in Holmboe waves. *J. Phys.l Ocean.,* 33: 694-711.

[67] Smyth, W. D. & Peltier, W. R. 1989. The transition between Kelvin-Helmholtz and Holmboe instability: an inverstigation of the overreflection hypothesis. *J. Atmo. Sci.,* 46: 3698-3720.

[68] Smyth, W. D. & Peltier, W. R. 1991. Instability and transition in finite amplitude Kelvin-Helmholtz and Holmboe waves. *J. Fluid. Mech,.* 228: 387-415.

[69] Koop, C. G. & Browand, F. K. 1978. Instability and turbulence in a stratified fluid with shear. *J. Fluid. Mech,.* 93: 135-159.

[70] Hogg, A. M. & Ivey, G. 2003. The Kelvin-Helmholtz to Holmboe instability transition in stratified exchange flows. *J. Fluid. Mech,.* 477: 339-362.

[71] Strang, E. J. & Fernando, H. J. S. 2001. Entrainment and mixing in a stratified shear flows. *J. Fluid. Mech,.* 428: 349-386.

[72] Smith, F. T. 1979. On the non-parallel flow stability of the Blasius boundary layer. *Proceedings of the Royal Society of London. Series A.* 366: 91-109.

[73] Lin, J., Shao, X. & Yu, Z. 2000. Numerical research on coherent structures in a mixing layer with cross-shear. *Acta Aeronautica et Astronautica Sinic.* 21(1), 13-20. (In Chinese)

[74] Atsavapranee, P. & Gharib, M. 1997. Structures in stratified plane mixing layers and the effects of cross-shear. *J. Fluid Mech. 342*, 53-86.

[75] Winter, K., Lombard, P., Riley, J. and D'Asaro, E. A. 1995. Available potential energy and mixing in density-stratified fluids. *J. Fluid. Mech.*, 289: 115–128.

[76] Smyth, W.D., Carpenter, J.R. and Lawrence, G.A. 2007. Mixing in Symmetric Holmboe Waves. *J. Phys. Oceanogr.*, 37: 1566-1583.

[77] Smyth, W.D., Moum, J. and Caldwell, D. 2001. The efficiency of mixing in turbulent patches: Inferences from direct simulations and microstructure observations. *J. Phys. Oceanogr.*, 31: 1969–1992.

[78] Smyth, W.D. and Winters, K. 2003. Turbulence and mixing in Holmboe waves. *J. Phys. Oceanogr.*, 33: 694–711.

[79] Caulfield, C.P. and Peltier, W.R. 2000. Anatomy of the mixing transition in homogeneous and stratified free shear layers. *J. Fluid. Mech.*, 413: 1–47.

[80] Peltier, W.R. and Caulfield, C.P. 2003. Mixing efficiency in stratified shear flows. *Annu. Rev. Fluid Mech.*, 35: 135-167.

[81] Carpenter, J.R., Lawrence, G.A. and Smyth, W.D. 2007. Evolution and mixing of asymmetric holmboe instabilities. *J. Fluid. Mech.*, 582: 103-132.

[82] Miles, J.W. 1961. On the stability of heterogeneous shear flows. *J. Fluid. Mech.*, 10: 496-508.

[83] Howard, L.N. 1961. Note on a paper of John W. Miles. *J. Fluid. Mech.*, 10: 509-512.

[84] Holmboe, J. 1962. On the behavior of symmetric waves in stratied shear layers. *Geophys. Publ.*, 24: 67-72.

[85] Smyth, W.D. and Peltier, W.R. 1989. The transition between Kelvin-Helmholtz and Holmboe instability: an inverstigation of the overreflection hypothesis. *J. Atmos. Sci.*, 46: 3698-3720.

[86] Fernando, H.J.S. 1991. Turbulent mixing in stratified fluids. *Annu. Rev. Fluid Mech.*, 23: 455-493.

[87] Thorpe, S.A. 1968. A method of producing a shear flow in a stratified fluid. *J. Fluid. Mech.*, 32: 693–704.

[88] Maxworthy, T. and Browand, F.K. 1975. Experiments in rotating and stratified flows: oceanographic application. *Annu. Rev. Fluid Mech.*, 7: 273–305.

[89] Lawrence, G.A., Browand, F.K. and Redekopp, L.G. 1991. The stability of a sheared density interface. *Phys. Fluids.*, 3: 2360–2370.

[90] Picirillo, P. and Van Atta, C. 1997. The evolution of a uni-formly sheared thermally stratified turbulent flow. *J. Fluid. Mech.*, 334: 61-86.

[91] Narimousa, S. and Fernando, H.J.S. 1987. On the sheared density interface of an entraining stratified fluid.*J. Fluid. Mech.*, 174: 1-22.

[92] Lawrence, G.A., Lasheras, J.C. and Browand, F.K. 1990. The stability of a sheared den sity interface. *Phys. Fluids.*, 3: 2360-2370.

[93] Strang, E.J. and Fernando, H.J.S. 2001. Entrainment and mixing in a stratified shear flows. *J. Fluid. Mech.*, 428: 349–386.

[94] Thrope, S.A. 2005. The Turbulent Ocean. Cambridge Press.

[95] Dillon, T. 1982. Vertical overturns: a comparison of Thorpe and Ozmidov scales. *J. Geophys. Res.*, 87: 9601-9613.

[96] Wijesekera, H. and Dillon, T. 1997. Shannon entropy as an indicator of age for turbulent overturns in the oceanic thermocline. *J. Geophys. Res.*, 102: 3279-3291.

[97] Smyth, W.D. and Moum, J. 2000. Length scales of turbulence in stably stratified mixing layers. *Phys. Fluids.*, 12: 1327-1342.

[98] Smyth, W.D. and Peltier, W.R. 1991. Instability and transition in finiteamplitude Kelvin–Helmholtz and Holmboe waves. *J. Fluid. Mech.*, 228: 387-415.

[99] Schowalter, D.G., Van Atta, C.W. and Lasheras, J.C. 1994. A study of streamwise vortex structure in a stratified shear layer. *J. Fluid. Mech.*, 281: 247–291.

[100] Smyth, W.D. and Moum, J. 2000. Anisotropy of turbulence in stably stratified mixing layers. *Phys. Fluids.*, 12: 1343-1362.

[101] Carpenter, J.R., Tedford, E.W., Rahmani, M. and Lawrence, G.A. 2010. Holmboe wave fields in simulation and experiment. *J. Fluid. Mech.*, 648: 205-223.

[102] Pino, D. and Vilà–Guerau de Arellano J. 2008. Effects of shear in the convective boundary layer: analysis of the turbulent kinetic energy budget. *Acta Geophysica.*, 56: 167-193.

[103] Gargett, A., Osborn, T. and Nasmyth, P. 1984. Local isotropy and the decay of turbulence in a stratified fluid.*J. Fluid. Mech.*, 144: 231-280.

[104] Yamazaki, H. 1990. Stratified turbulence near a critical dissipation rate. *J. Phys. Oceanogr.* 20: 1583-1598.

[105] Itsweire, E., Koseff, J., Briggs, D., and Ferziger, J. 1993. Turbulence in stratified shear flows: Implications for interpreting shear-induced mixing in the ocean.*J. Phys. Oceanogr.*, 23: 1508-.1522.

[106] Koop, C.G. and Browand, F.K. 1978. Instability and turbulence in a stratified fluid with shear. *J. Fluid. Mech.*, 93: 135-159.

[107] Hogg, A.M. and Ivey, G. 2003. The Kelvin-Helmholtz to Holmboe instability transition in stratified exchange flows. *J. Fluid. Mech.*, 477: 339-362.

[108] ECKART, C. 1948 An analysis of the stirring and mixing processes in incompressible fluids. *J. Mar. Res. 7*, 265-275.

[109] Paul, E.D. 2005. Turbulenvce mixing. *Annu. Rev. Fluid Mech.*, 37: 329-56.

[110] Barr, A.G. 1996. First international satellite land surface climatology field experiment 1987 sonde budget revisited.*J. Geophys. Res.*, 101: 23285- 23288.

[111] Davis, K.J., Lenschow, D.H., Oncley, S.P., et al. 1997. The role of entrainment in surface-atmosphere interactions over the boreal forest. *J. Geophys. Res.*, 102: 29219-29230

[112] Angevine, W.M., 1999. Entrainment results including advection and case studies from the Flatland boundary layer experiments. *J. Geophys. Res.*, 104: 30947-30963.

[113] Margulis, S.A. and Entekhabi, D. 2004. Boundary-layer entrainment estimation through assimilation of radiosonde and micrometeorological data into a mixed-layer model. *Bound. Layer Meteor.*, 110: 405–433.

[114] Canut, G., Couvreux, F., Lothon, M., Pino, D. and Said, F. 2012. Observations and large eddy simulations of entrainment in the sheared sahelian boundary layer. *Bound. Layer Meteor.*, 142: 79-101.

[115] Bradshaw, P. 1972. The Understanding and Prediction of Turbulent Flow, *Aero. J.*, 76: 403–418.

[116] Deardorff, J.W. 1970. Preliminary results from numerical integrations of the unstable planetary boundary layer. *J. Atmos. Sci.*, 27: 1209-1211.

[117] Ayotte, K.W., Sullivan, P.P., Andren, A., et al. 1996. An evaluation of neutral and convective planetary boundary-layer parameterizations relative to large eddy simulations. *Bound. Layer Meteor.*, 79: 131-175.

[118] Lily, D.K. 1968. Models of cloud-topped mixed layer under a strong inversion. *Quart. J. Roy. Meteor. Soc.*, 94: 292-309.

[119] Betts, A.K. 1974. Reply to comment on the paper "Non-precipitating cumulus convection and its parameterization.". *J. Atmos. Sci.*, 37: 131-147.

[120] Deardorff, J.W. 1979. Prediction of convective mixed-layer entrainment for realistic capping inversion structure. *J. Atmos. Sci.*, 36: 424-436.

[121] Conzenmius, R. and Fedorovich, E. 2007. Bulk models of the sheared convective boundary layer: evaluation through large eddy simulations. *J. Atmos. Sci.*, 64: 786-807.

[122] Conzenmius, R. and Fedorovich, E. 2006. Dynamics of sheared convective boundary layer entrainment. part I: methodological background and large-eddy simulations. *J. Atmos. Sci*., 63: 1151-1178.

[123] Conzenmius, R. and Fedorovich, E. 2006. Dynamics of sheared convective boundary layer entrainment. part II: evaluation of bulk model predictions of entrainment flux. *J. Atmos. Sci*., 63: 1179-1199.

[124] Kim, S.W., Park, S.U., Pino, D. and Vilà-Gueraude Arellano, J. 2006. Parameterization of entrainment in a sheared convective boundary layer using a first-order jump model. *Bound. Layer Meteor.*, 120: 445–475.

[125] Deardorff, J.W., Willis, G.E. and Stockton, B.H. 1980. Laboratory studies of the entrainment zone of a convectively mixed layer. *J. Fluid. Mech.*, 100: 41-64.

[126] Stull, R.B. 1976. The energetics of entrainment across a density interface. *J. Atmos. Sci*., 33: 1260-1267.

[127] Fedorovich, E. and Conzenmius, R. 2004. Convective entrainment into a shear-free, linearly stratified atmosphere: bulk models reevaluated through large eddy simulations. *Bound. Layer Meteor.*, 61: 281-295.

[128] Pino, D., Vilà–Guerau de Arellano J. and Kim S.W. 2006. Representing sheared convective boundary layer by zeroth- and first-order-jump mixed layer models: Large-eddy simulation verification. *J. Appl. Meteor. Clim.*, 45: 1224-1243.

[129] Pino, D., Vilà-Guerau de Arellano, J. and Duynkerke, P.G. 2003. The contribution of shear to the evolution of a convective boundary layer. *J. Atmos. Sci*., 60: 1913–1926.

[130] Sorbjan, Z. 2004. Large-eddy simulations of the baroclinic mixed layer. *Bound. Layer Meteor.*, 112: 57-80.

[131] Sorbjan, Z. 2006. Statistics of scalar fields in the atmospheric boundary layer based on large eddy simulations. Part II: forced convection. *Bound. Layer Meteor.*, 119: 57-79.

[132] Willis, G.E. and Deardorff, J.W. 1974. A laboratory model of the unstable planetary boundary layer. *J. Atmos. Sci*., 31:1297-1307.

[133] Sun, J. and Yuan, W. 2008. Effect of the entrainment flux ratio on the relationship between entrainment rate and convective Richardson number. *Bound. Layer Meteor.*, 126: 237–247

[134] Bretherton, C.S., et al. 1999. An intercomparison of radiatively- driven entrainment and turbulence in a smoke cloud, as simulated by different numerical models. *Quart. J. Roy. Meteor. Soc*., 125: 391-423.

[135] Stevens, B. et al. 2005. Evaluation of large-eddy simulations via observations of nocturnal marine stratocumulus. *Mon.Wea.Rev.*, 133: 1443–1462.

[136] Schmidt, H., and U. Schumann. 1989. Coherent structure of the convective boundary layer derived from large eddy simulations. *J. Fluid. Mech.*, 200: 511–562

[137] Sullivan, P.P., Moeng, C.H., Stevens, B., Lenschow, D.H. and Mayor, S.D. 1998: Structure of the entrainment zone capping the convective atmospheric boundary layer. *J. Atmos. Sci*., 55: 3042–3064.

[138] Turner, J.S. 1986. Turbulent entrainment: the development of the entrainment assumption, and its application to geophysical flows.*J. Fluid. Mech.*, 173:431–71

[139] Willis, G.E. and Deardorff, J.W. 1979. Laboratory observations of turbulent penetrative-convection planforms. *J. Geo. Res.*, 84:295- 302.

[140] Deardorff, J.W. and Willis, G.E. 1985. Further results from a laboratory model of the convective planetary boundary layer. *Bound. Layer Meteor.*, 32: 205-236.

[141] Adrian R. J., Ferreira R. T. D. S. and Boberg T. 1986. Turbulent thermal convection in wide horizontal fluid layers. *Exps. Fluids*., 4: 121-141.

[142] Kaimal, J.C., Wynoaard J.C., Hauoen D.A. et al. 1976. Turbulence structure in the convective boundary layer. *J. Atmos. Sci*., 33: 2152-2169.

[143] Lenschow, D.H. and Stephens, P.L. 1980. The role of thermals in the convective boundary layer. *Bound. Layer Meteor.*, 19: 509-532.

[144] Wilczak, J.M. and Tillman, J.E. 1980. The three-dimensional structure of convection in the atmospheric surface layer. *J. Atmos. Sci*., 37: 2424-2443.

[145] Greenhut, G.K. and Khalsa, S.G.S. 1982. Updraft and downdraft events in the atmospheric boundary layer over the equatorial Pacific Ocean. *J. Atmos. Sci*., 39: 1803-1818.

[146] Greenhut, G.K. and Khalsa, S.G.S. 1987. Convective elements in the marine atmospheric boundary layer. Part I : Conditional sampling statistics. *J. Clim. Appl. Met.*, 26: 813-822.

[147] Grossman, R.J. 1982. An analysis of vertical velocity spectra obtained in the BOMEX fair- weather, trade-wind boundary layer. *Bound. Layer Meteor.*, 23: 323-357.

[148] Grossman, R.J. 1984. Bivariate conditional sampling of moisture flux over a tropical ocean. *J. Atmos. Sci.*, 41: 3238-3253.

[149] Crum, T.D., Stull, R.B. and Eloranta, E.W. 1987. Coincident lidar and aircraft observations of entrainment into thermals and mixed layers. *J. Clim. Appl. Met.*, 26:774-788.

[150] Turner, J.S. 1979. Buoyancy Effects in Fluids. Cambridge University Press.

[151] Raasch, S. and Franke, T. 2011. Structure and formation of dust devil-like vortices in the atmospheric boundary layer: A high-resolution numerical study. *J.Geo.Phy.Re.*, 116: D16120, doi:10.1029/2011JD016010.

[152] Sullivan, P.P and Patton E.G. 2011. The effect of mesh resolution on convective boundary layer statistics and structures generated by large-eddy simulation. *J. Atmos. Sci.*, 68: 2395-2415.

[153] Stull, R.B. 1976. Internal gravity waves generated by penetrative con-vection. *J. Atmos. Sci.*, 33: 1279–1286.

[154] Stull, R.B. 1976. Mixed-layer depth model based on turbulent ener-getics. *J. Atmos. Sci.*, 33: 1268–1278.

[155] Zeman, O. and Tennekes, H. 1977. Parameterization of the turbulent energy budget at the top of the daytime atmospheric boundary layer.*J. Atmos. Sci.*, 34: 111–123.

[156] Tennekes, H. and Driedonks, A.G.M. 1981. Basic entrainment equations for the atmospheric boundary layer. *Bound. Layer Meteor.*, 20: 515–531.

[157] Driedonks, A.G.M. 1982. Models and observations of the growth of the atmospheric boundary layer. *Bound. Layer Meteor.*, 23: 283–306.

[158] Boers, R., Eloranta, E.W. and Coulter, R.L. 1984. Lidar observations of mixed layer dynamics: tests of parameterized entrainment models of mixed layer growth rate. *J. Climate Appl. Meteor.*, 23: 247–266.

[159] Batchvarova, E. and Gryning, S.E. 1991. Applied model for the growth of the daytime mixed layer. *Bound. Layer Meteor.*, 56, 261–274.

[160] Batchvarova, E. and Gryning, S.E. 1994. An applied model for the height of the daytime mixed layer and the entrainment zone. *Bound. Layer Meteor.*, 71: 311–323.

[161] Fedorovich, E. 1995. Modeling the atmospheric convective boundary layer within a zero-order jump approach: An extended theoretical framework. *J. Appl. Meteor.*, 34: 1916– 1928.

[162] Kim, S.W., Park, S.U., Moeng, C.H. 2003. Entrainment processes in atmospheric boundary layer structure driven by wind shear and surface Heat Flux. *Bound. Layer Meteor.*, 108: 221–245

[163] Khanna, S. and Brasseur, J.G. 1998. Three-Dimensional Buoyancy- and Shear-Induced Local Structure of the Atmospheric Boundary Layer. *J. Atmos. Sci.*, 55: 710-743.

[164] Ivey, G. and Imberger, J. 1991. On the nature of turbulence in a stratified fluid. Part I: The energetics of mixing.*J. Phys. Oceanogr.*, 21: 650–658.

[165] Gargett, A.E. and Moum, J. 1995. Mixing efficiencies in turbulent tidal fronts: Results from direct and indirect measurements of density flux. *J. Phys. Oceanogr.*, 25: 2583–2608.

[166] Moum, J. N. 1996a. Efficiency of mixing in the main thermocline. *J. Geophys. Res.*, 101: 12057–12069.

[167] Ruddick, B., Walsh, D. and Oakey, N. 1997. Variations in apparent mixing efficiency in the North Atlantic Central Water. *J. Phys. Oceanogr.*, 27: 2589–2605.

[168] McEwan, A. 1983. Internal mixing in stratified fluids. *J. Fluid. Mech.*, 128: 59–80.

[169] Yang, D., Hu, L.H., Hou, R., et al. 2010. Experimental study on buoyant flow stratification induced by a fire in a horizontal channel. *App. Therm. Eng.*, 2010: 872-878.

[170] Law, C.K. 2006. Combusiton Physics. Cambridge Press.

Chapter 3

Hydrodynamic stability analysis on inviscid CSS flow

The results of this chapter are presented in the following publications:

1. XIAO, Y., LIN, W., ARMFIELD, S. W., KIRKPATRICK, M. P. & HE, Y. 2014 Hydrodynamic stability analysis on inviscid cross sheared stratified flows. in *Proceedings of the 19th Australasian Fluid Mechanics Conference (19AFMC)*, 8-11 December 2014, Melbourne, Australia, Paper ID: 082.

2. XIAO, Y., LIN, W., MCCORMARC, J., ARMFIELD, S. W., KIRKPATRICK, M. P. & HE, Y. 2017 Hydrodynamic stability analysis on the inviscid cross sheared stratified flow. To be submitted.

3.1 Introduction

Hydrodynamics analysis, which studies the critical conditions and the effective domain for flow instability, plays a fundamental role in the study of shear stratified flows. So far, the majority of the hydrodynamic analysis on shear stratified flows has been largely prompted by the earlier linear stability analysis on parallel sheared stratified (PSS) flows, whose basic flow velocity components satisfy $V \ll U$, where U and V are the streamwise and spanwise components of the basic flow in the x and y directions, respectively.

The linear stability analysis in PSS flows was initiated by [1] and [2], who derived the Taylor-Goldstein (TG) equation which describes the hydrodynamics between velocity shear and buoyancy flux. By solving the TG equation, [3] and [4] further established the classical Miles-Howard theorem in which $Ri_g \leq 0.25$ becomes the absolute critical condition

for a stationary instability mode under infinitesimal perturbations, where Ri_g is the local Richardson number. Such an instability mode corresponds to the Kelvin-Helmholtz (KH) instability. By considering the length scale ratio between the shear layer and the stratified layer, [5] solved the TG equation numerically and obtained a propagative instability mode in the $Ri > Ri_g$ region, which corresponds to the Holmboe instability mode first observed by [6]. The transition from the stationary KH mode to the propagative Holmboe mode was investigated by [7] in linear stability analysis with the numerical shooting method. [8] argued that the wave interaction is the fundamental factor to decide whether KH or Holmboe mode will appear in a PSS flow; they suggested that the stationary mode appears due to the shear effects, which reduce the wave speed of a pair of counter-propagating waves to a relatively stationary degree.

However, shear stratified flows are inherently three dimensional flows in nature and in engineering applications. In three dimensional flows where the length scale in the spanwise direction can no longer be ignored, the velocity shear from the spanwise direction, which is cross shear, will be inevitably produced by either bulk flow motions or local shear sources. The examples where cross shear occurs from bulk flows include two interacting ocean currents, estuaries where two or more river branchs merge, and multi-port reservoirs and reflected water currents due to topology. The example sources to create local cross shear include internal waves and convective flux in stably stratified environment, and local heat transfer processes led by radiation and chemical processes. These bulk and local sources of cross shear will inevitably modify the actual flow behavior which will be different from that in PSS flow.

To distinguish from a PSS flow which is with $V \ll U$, a shear stratified flow with comparable V and U can be appropriately named a 'cross' sheared stratified (CSS) flow, as velocity shears occur in both U and V. The past studies on CSS flows, although very scarce, revealed distinctive and more complicated flow instabilities than PSS flows. For example, [9] observed experimentally smaller spanwise eddy structures developed from the 'braid' region of the main streamwise KH eddy, whereas [10] examined numerically the effects of the cross shear stresses on a two-layer stratified flow. A common and noteworthy conclusion from these two studies is that the mixing effect of CSS flows is significantly enhanced compared to PSS flows at the same conditions. Although CSS flows seem to be a promising basic flow configuration in terms of mixing effect, to our best knowledge, the relevant stability analysis has not been reported, which motivates this study.

In a CSS flow system, the intensity of cross velocity shear $\partial V/\partial z$ can be created by introducing a velocity differences ΔV across the cross shear layer or by modifying the length scale of the existing cross shear layer δ_{cs}, leading to two governing parameters that quantify

the intensity of cross shear to be introduced in this study. If the cross shear is purely created by the spanwise velocity difference ΔV, a cross shear ratio, which is defined as

$$\xi = \Delta V / \Delta U, \tag{3.1}$$

where ΔU is the initial streamwise velocity changes across the sheared layer, can be introduced to quantify the relative intensity of the cross shear with respect to the mainstream shear. If the cross shear change is due to the modified length scale of the cross shear layer δ_{cs}, a cross shear thickness ratio, which is defined as

$$R_s = \delta_{cs} / \delta_s, \tag{3.2}$$

where δ_s and δ_{ss} are the initial thicknesses of the streamwise and spanwise shear layerss, can be introduced to describe the relative length scale of the cross shear layer. If $R_s \to 0$, the cross shear will occur in an infinitesimal layer. If $R_s \to \infty$, the cross shear will occur everywhere. Apparently, R_s is only valid when there is a spanwise velocity difference or cross shear ratio ξ is not zero.

By considering the cross shear from the basic spanwise velocity V, this study derives the three-dimensional linearized perturbation equations for CSS flow based on the original two-dimensional Taylor-Goldstein equation system. The introduction of V brings ξ into the perturbation equations and therefore extends the two-dimensional TG equation into the three-dimensional perturbation equations, implying that PSS flow becomes a special case of a CSS flow with $\xi = 0$. Using the derived perturbation equations for CSS flow, this study then examines the influences of ξ and R_s on the linear stability features of different CSS flow configurations, with some involving the same type of hyperbolic velocity profiles and stratification profiles as used in [5].

This chapter is organized as follows. The linear perturbation equations for CSS flow are derived in § 3.2, followed by the brief description of the numerical methodology in § 3.3. The stability analysis results for several CSS flow configurations are presented in § 3.4, which focuses on the influences of ξ and R_s on the stability boundary and temporal growth rate $\tilde{\alpha}$ of infinitesimal perturbations, for the CSS flow configurations where the length scale of the stratified layer is no less than the length scale of the shear layer, and in § 3.5, which mainly investigates the influence of ξ and R_s on the transition from stationary instability modes to propagative instability modes, for CSS flow configurations where the length scale of the stratified layer is less than that of the shear layer. Finally, a discussion is conducted and the major conclusions are drawn in § 4.4.

3.2 Linearized perturbation equations

The linear stability analysis of this study aims to estimate the stability boundary of CSS flow in the parameter space made of the major governing parameters. Within the unstable region enclosed by the stability boundary, a proper wavenumber will be selected to excite the primary instability, which is the focus of this study. The viscosity will therefore be excluded in the linear perturbation equations. With the Boussinesq approximation, the governing equations for an inviscid, incompressible, and stratified flow are:

$$\nabla_* \cdot \mathbf{u}_* = \mathbf{0}, \tag{3.3}$$

$$\frac{\partial \mathbf{u}_*}{\partial t_*} + (\mathbf{u}_* \cdot \nabla_* \mathbf{u}_*) = -\frac{1}{\bar{\rho}_*}\nabla_* p_* - g\frac{(\rho_* - \bar{\rho}_*)}{\bar{\rho}_*}\vec{k}, \tag{3.4}$$

$$\frac{\partial \rho_*}{\partial t_*} + \mathbf{u}_* \cdot \nabla_* \rho_* = 0, \tag{3.5}$$

where the subscript '*' denotes the dimensional quantities, $\mathbf{u}_*$ is the velocity vector with the components (u_*, v_*, w_*) in the Cartesian coordinates (x_*, y_*, z_*), p_* is pressure, ρ_* is density, $\bar{\rho}_*$ is the reference density, t_* is time, g is the acceleration due to gravity, and the differential operator ∇_* is

$$\nabla_* = \frac{\partial}{\partial x_*}\vec{i} + \frac{\partial}{\partial y_*}\vec{j} + \frac{\partial}{\partial z_*}\vec{k},$$

in which $\vec{i}$, $\vec{j}$ and $\vec{k}$ represent the unit vector in x_*, y_* and z_* directions.

The equations (5.3)-(3.5) can be made dimensionless as follows,

$$\nabla \cdot \mathbf{u} = 0, \tag{3.6}$$

$$\frac{\partial \mathbf{u}}{\partial t} + (\mathbf{u} \cdot \nabla \mathbf{u}) = -\frac{1}{\bar{\rho}}\nabla p - \frac{1}{Fr^2}\frac{(\rho - \bar{\rho})}{\bar{\rho}}\vec{k}, \tag{3.7}$$

$$\frac{\partial \rho}{\partial t} + \mathbf{u} \cdot \nabla \rho = 0, \tag{3.8}$$

where the dimensional quantities are made dimensionless using their respective characteristic scales, *i.e.* ,

$$\mathbf{x} = \frac{\mathbf{x}_*}{L}, \quad t = \frac{t_* V_c}{L}, \quad \mathbf{u} = \frac{\mathbf{u}_*}{V_c}, \quad p = \frac{p_*}{\Delta\rho_* V_c^2}, \quad \rho = \frac{\rho_*}{\Delta\rho_*}, \quad \bar{\rho} = \frac{\bar{\rho}_*}{\Delta\rho_*},$$

in which $\mathbf{x}$ is the dimensionless coordinate vector $(x\vec{i} + y\vec{j} + z\vec{k})$, L is the characteristic length scale which is one half of the effective sheared layer based on the streamwise velocity profile of the basic flow, V_c is the characteristic velocity scale which is the effective velocity changes

across the sheared layer based on the streamwise velocity profile of the basic flow, and $\Delta\rho_*$ is the characteristic density scale which is the effective density changes across the stratified layer based on the basic density profile. Fr in (3.7) is the *Froude* number which is defined by,

$$Fr = \frac{V_c}{\sqrt{gL}}.$$

It is assumed that the flow quantities consist of the basic flow and infinitesimal perturbations:

$$\mathbf{u}(\mathbf{x},t) = \mathbf{U}(z) + \mathbf{u}'(\mathbf{x},t), \tag{3.9}$$

$$\rho(\mathbf{x},t) = \rho_b(z) + \rho'(\mathbf{x},t), \tag{3.10}$$

$$p(\mathbf{x},t) = P(z) + p'(\mathbf{x},t) = p_0 - \frac{1}{Fr^2}\int_0^z \rho_b(z)dz + p'(\mathbf{x},t), \tag{3.11}$$

where $\mathbf{U}$ is the dimensionless basic flow velocity vector whose components in x, y and z directions are U, V and W, ρ_b is the dimensionless basic density profile, p_0 is the dimensionless reference pressure corresponding to the dimensionless reference density $\bar{\rho}$. The superscript symbol '$'$' represents the perturbation part of the corresponding physical property.

For the CSS flows considered in this study, all the basic flow properties are assumed to vary with the vertical coordinate z only, and the basic flow velocities are as follows,

$$\mathbf{U}(z) = U(z)\vec{i} + V(z)\vec{j}. \tag{3.12}$$

Both the basic flow and the total flow (basic flow + infinitesimal perturbations) are governed by the equations (5.5)-(5.6), *i.e.* ,

$$\nabla\cdot\mathbf{U} = 0, \tag{3.13}$$

$$\frac{\partial\mathbf{U}}{\partial t} + \mathbf{U}\cdot\nabla\mathbf{U} = -\frac{1}{\bar{\rho}}\nabla P(z) - \frac{1}{Fr^2}\frac{[\rho_b(z)-\bar{\rho}]}{\bar{\rho}}\vec{k}, \tag{3.14}$$

$$\frac{\partial\rho_b(z)}{\partial t} + \mathbf{U}\cdot\nabla\rho_b(z) = 0, \tag{3.15}$$

and

$$\nabla\cdot(\mathbf{U}+\mathbf{u}') = 0, \tag{3.16}$$

$$\frac{\partial(\mathbf{U}+\mathbf{u}')}{\partial t} + (\mathbf{U}+\mathbf{u}')\cdot\nabla(\mathbf{U}+\mathbf{u}') = -\frac{1}{\bar{\rho}}\nabla[P(z)+p'] - \frac{1}{Fr^2}\frac{[\rho_b(z)+\rho'-\bar{\rho}]}{\bar{\rho}}\vec{k}, \tag{3.17}$$

$$\frac{\partial[\rho_b(z)+\rho']}{\partial t} + (\mathbf{U}+\mathbf{u}')\cdot\nabla[\rho_b(z)+\rho'] = 0. \tag{3.18}$$

Therefore, by subtracting the equations for the basic flow, *i.e.* , (3.13)-(3.15), from the equations for the total flow, *i.e.* , (3.16)-(3.18), and assuming the product of an infinitesimal quantity and its gradient is negligible [11], *i.e.* , $\mathbf{u}' \cdot \nabla \mathbf{u}' \approx 0$ and $\mathbf{u}' \cdot \nabla \rho' \approx 0$, the following perturbation equations are deduced,

$$\nabla \cdot \mathbf{u}' = 0, \tag{3.19}$$

$$\frac{\partial \mathbf{u}'}{\partial t} + (\mathbf{U} \cdot \nabla \mathbf{u}' + \mathbf{u}' \cdot \nabla \mathbf{U}) = -\frac{1}{\bar{\rho}} \nabla p' - \frac{1}{Fr^2} \frac{\rho'}{\bar{\rho}} \vec{k}, \tag{3.20}$$

$$\frac{\partial \rho'}{\partial t} + \mathbf{U} \cdot \nabla \rho' + \mathbf{u}' \cdot \nabla \rho_b(z) = 0. \tag{3.21}$$

For the CSS flows, the basic flow velocities are,

$$\mathbf{U}(z) = U(z)\vec{i} + V(z)\vec{j}.$$

Therefore, the dot product terms in (3.20) and (3.21) become,

$$\mathbf{U} \cdot \nabla \mathbf{u}' = (U\frac{\partial u'}{\partial x} + V\frac{\partial u'}{\partial y})\vec{i} + (U\frac{\partial v'}{\partial x} + V\frac{\partial v'}{\partial y})\vec{j} + (U\frac{\partial w'}{\partial x} + V\frac{\partial w'}{\partial y})\vec{k},$$

$$\mathbf{u}' \cdot \nabla \mathbf{U} = w' \left(\frac{\partial U}{\partial z}\vec{i} + \frac{\partial V}{\partial z}\vec{j} \right), \quad \mathbf{U} \cdot \nabla \rho' = U\frac{\partial \rho'}{\partial x} + V\frac{\partial \rho'}{\partial y}, \quad \mathbf{u}' \cdot \nabla \rho_b(z) = w' \frac{\partial \rho_b(z)}{\partial z}.$$

The following perturbation equations are thus deduced,

$$\nabla \cdot \mathbf{u}' = 0, \tag{3.22}$$

$$\frac{\partial \mathbf{u}'}{\partial t} + (\mathbf{U} \cdot \nabla \mathbf{u}' + \mathbf{u}' \cdot \nabla \mathbf{U}) = -\frac{1}{\bar{\rho}} \nabla p' - \frac{1}{Fr^2} \frac{\rho'}{\bar{\rho}} \vec{k}, \tag{3.23}$$

$$\frac{\partial \rho'}{\partial t} + \mathbf{U} \cdot \nabla \rho' + \mathbf{u}' \cdot \nabla \rho_b(z) = 0, \tag{3.24}$$

where

$$\mathbf{U} \cdot \nabla \mathbf{u}' = (U\frac{\partial u'}{\partial x} + V\frac{\partial u'}{\partial y})\vec{i} + (U\frac{\partial v'}{\partial x} + V\frac{\partial v'}{\partial y})\vec{j} + (U\frac{\partial w'}{\partial x} + V\frac{\partial w'}{\partial y})\vec{k},$$

$$\mathbf{u}' \cdot \nabla \mathbf{U} = w' \left(\frac{\partial U}{\partial z}\vec{i} + \frac{\partial V}{\partial z}\vec{j} \right), \quad \mathbf{U} \cdot \nabla \rho' = U\frac{\partial \rho'}{\partial x} + V\frac{\partial \rho'}{\partial y}, \quad \mathbf{u}' \cdot \nabla \rho_b(z) = w' \frac{\partial \rho_b(z)}{\partial z}.$$

The following normal mode is used in the subsequent linear stability analysis,

$$\phi'(\mathbf{x}, t) = \hat{\phi}(z) e^{i(\alpha x + \beta y) - i\alpha c t} = \hat{\phi}(z) e^{i(\alpha x + \beta y) - \sigma t}, \tag{3.25}$$

where i is the imaginary unit of a complex number, α and β are the streamwise and spanwise wavenumbers respectively, and the perturbation quantity ϕ' represents velocity, density, temperature, buoyancy flux, and other physical quantities. The hat symbol denotes the peak amplitude of the corresponding perturbation. $\omega = \alpha c$ is the angular frequency for the perturbation, where c is the wave (phase) speed, giving $\sigma = i\alpha c$ as the temporal growth rate of the perturbation.

Substituting the above normal modes into (3.22)-(3.24) leads to the following,

$$i\alpha\hat{u} + i\beta\hat{v} + D\hat{w} = 0, \tag{3.26}$$

$$(i\alpha U + i\beta V + \sigma)\hat{u} + U_z\hat{w} = -\frac{i\alpha\hat{p}}{\bar{\rho}}, \tag{3.27}$$

$$(i\alpha U + i\beta V + \sigma)\hat{v} + V_z\hat{w} = -\frac{i\beta\hat{p}}{\bar{\rho}}, \tag{3.28}$$

$$(i\alpha U + i\beta V + \sigma)\hat{w} = -\frac{1}{\bar{\rho}}D\hat{p} - \frac{1}{Fr^2}\frac{\hat{\rho}}{\bar{\rho}}, \tag{3.29}$$

$$(i\alpha U + i\beta V + \sigma)\hat{\rho} + \rho_{b,z}\hat{w} = 0, \tag{3.30}$$

where $D = \partial/\partial z$ is the differential operator for the perturbation properties, $\rho_{b,z} = \partial\rho_b(z)/\partial z$, and the subscript '$z$' denotes the first order differentiation with respect to z.

The Squire transformations can reduce the three-dimensional perturbation equations (3.26)-(3.30) to the equivalent two-dimensional perturbation equations, as shown below.

If the following relations are defined,

$$\tilde{\alpha} = (\alpha^2 + \beta^2)^{1/2}, \quad \tilde{p} = \frac{\tilde{\alpha}}{\alpha}\hat{p}, \quad \tilde{u} = \frac{\alpha\hat{u} + \beta\hat{v}}{\tilde{\alpha}}, \quad \tilde{\rho} = \frac{\tilde{\alpha}}{\alpha}\hat{\rho}, \tag{3.31}$$

where the tidle symbol denotes the Squire transformation properties [11, 12], then the operation of $[\alpha \times (3.27) + \beta \times (3.28)]/\alpha$ will lead to,

$$\tilde{\alpha}(iU + i\frac{\beta}{\alpha}V + \frac{\sigma}{\alpha})\tilde{u} + (U_z + \frac{\beta}{\alpha}V_z)\hat{w} = -i\tilde{\alpha}\frac{\tilde{p}}{\bar{\rho}} \tag{3.32}$$

The differentiation with respect to z of the above equation results in,

$$\begin{aligned} i\tilde{\alpha}U_z\tilde{u} + i\tilde{\alpha}UD\tilde{u} + \frac{\tilde{\alpha}\sigma}{\alpha}D\tilde{u} + i\frac{\tilde{\alpha}\beta}{\alpha}(V_z + VD)\tilde{u} + (U_{zz} + U_zD)\hat{w} \\ + \frac{\beta}{\alpha}(V_{zz} + V_zD)\hat{w} = -i\frac{\tilde{\alpha}}{\bar{\rho}}D\tilde{p}, \end{aligned} \tag{3.33}$$

where the subscript 'zz' denotes the second order differentiation with respect to z.

Putting the above relation $\tilde{u} = (\alpha\hat{u} + \beta\hat{v})/\tilde{\alpha}$ into the continuity equation (3.26) gives the following equation,

$$i\tilde{\alpha}\tilde{u} = -D\hat{w}, \tag{3.34}$$

and a further differentiation with respect to z of this equation leads to,

$$D\tilde{u} = -\frac{D^2\hat{w}}{i\tilde{\alpha}}. \tag{3.35}$$

With (3.34) and (3.35), (3.33) changes to,

$$i\frac{\sigma}{\alpha}D^2\hat{w} - UD^2\hat{w} - \frac{\beta}{\alpha}VD^2\hat{w} + U_{zz}\hat{w} + \frac{\beta}{\alpha}V_{zz}\hat{w} = -i\frac{\tilde{\alpha}}{\bar{\rho}}D\tilde{p}. \tag{3.36}$$

The product of $(\tilde{\alpha}/\alpha)$ and (3.29) is then,

$$\tilde{\alpha}(iU + i\frac{\beta}{\alpha}V + \frac{\sigma}{\alpha})\hat{w} = -\frac{1}{\bar{\rho}}D\tilde{p} - \frac{\tilde{\rho}}{\bar{\rho}Fr^2}, \tag{3.37}$$

and the product of $i\tilde{\alpha}$ and the above equation is,

$$-\tilde{\alpha}^2(U - i\frac{\sigma}{\alpha})\hat{w} - \frac{\tilde{\alpha}^2\beta}{\alpha}V\tilde{w} = -i\frac{\tilde{\alpha}}{\bar{\rho}}D\tilde{p} - i\frac{\tilde{\alpha}\tilde{\rho}}{\bar{\rho}Fr^2}. \tag{3.38}$$

Substracting (3.36) from (3.38) and then multiplying by $(-i)$ give

$$\frac{\sigma}{\alpha}(D^2 - \tilde{\alpha}^2)\hat{w} + iU(D^2 - \tilde{\alpha}^2)\hat{w} + i\frac{\beta}{\alpha}[V(D^2 - \tilde{\alpha}^2) - V_{zz}]\hat{w} - iU_{zz}\hat{w} = \frac{\tilde{\alpha}\tilde{\rho}}{\bar{\rho}Fr^2}. \tag{3.39}$$

The product of $\tilde{\alpha}/\alpha^2$ and (3.30) is

$$\frac{\sigma}{\alpha}\tilde{\rho} = -\frac{\tilde{\alpha}}{\alpha^2}\rho_{b,z}\hat{w} - (iU + i\frac{\beta}{\alpha}V)\tilde{\rho}. \tag{3.40}$$

Multiplying (3.39) and (3.40) by $\tilde{\alpha}$ and then writing them in matrix form gives,

$$\tilde{\sigma}\begin{bmatrix} \nabla_s^2 & \\ & I \end{bmatrix}\begin{bmatrix} \hat{w} \\ \tilde{\rho} \end{bmatrix} = \begin{bmatrix} -i\tilde{\alpha}(U\nabla_s^2 - U_{zz}) - i\frac{\tilde{\alpha}\beta}{\alpha}(V\nabla_s^2 - V_{zz}) & \frac{\tilde{\alpha}^2}{\bar{\rho}Fr^2} \\ -\tilde{\rho}_{b,z} & -i\tilde{\alpha}(U + \frac{\beta}{\alpha}V) \end{bmatrix}\begin{bmatrix} \hat{w} \\ \tilde{\rho} \end{bmatrix}, \tag{3.41}$$

where $\tilde{\sigma}$ is the Squire temporal growth rate of the perturbations properties and $\tilde{\rho}_{b,z}$ is the Squire density gradient. The Squire Laplacian operator ∇_s^2 is defined as $\nabla_s^2 = D^2 - \tilde{\alpha}^2$.

Notice that the terms $i\tilde{\alpha}\dfrac{\beta}{\alpha}(\nabla_s^2 V - V_{zz})$ of V on the RHS has same differential operators as the terms $i\tilde{\alpha}(U\nabla_s^2 - U_{zz})$ of U, only their coefficient are different.

if $V = 0$ and $V_{zz} = 0$ or $\beta = 0$, the perturbation equations for CSS flows (3.41) would reduce to the Taylor-Goldstein equations in matrix form, with $\alpha = \tilde{\alpha}$ inherently. Consequently, a PSS flow with $\xi = V/U = 0$ becomes a special case of a CSS flow, where ξ is the cross shear ratio which is defined by (3.1). The above equations are the equivalent two-dimensional perturbation equations written in matrix form. Note that it is the product of cross shear ratio ξ and wavenumber ratio β/α play as the amplitude of velocity shear term $-i\tilde{\alpha}(U\nabla_s^2 - U_{zz})$. To focus on the influences of cross shear, this linear stability analysis will assume $\beta/\alpha = 1$, so that the hydrodynamic of CSS flow will rely on ξ only. Nevertheless, if the same amplitudes of product $\xi(\beta/\alpha)$ are achieved either by fixing ξ and changing β/α or vice verse, the same results are obtained based on mathematical form of 3.41.

If the Squire buoyancy $\tilde{b} = \tilde{\rho}/\bar{\rho}$ is used instead of the Squire density $\tilde{\rho}$, the perturbation equations for CSS flows (3.41) will become,

$$\tilde{\sigma}\begin{bmatrix} \nabla_s^2 & \\ & I \end{bmatrix}\begin{bmatrix} \hat{w} \\ \tilde{b} \end{bmatrix} = \begin{bmatrix} -i\tilde{\alpha}(U\nabla_s^2 - U_{zz}) - i\dfrac{\tilde{\alpha}\beta}{\alpha}(V\nabla_s^2 - V_{zz}) & \dfrac{\tilde{\alpha}^2}{Fr^2} \\ \tilde{N}^2 & -i\tilde{\alpha}(U + \dfrac{\beta}{\alpha}V) \end{bmatrix}\begin{bmatrix} \hat{w} \\ \tilde{b} \end{bmatrix}, \tag{3.42}$$

where $\tilde{N}^2 = -\tilde{\rho}_{b,z}/\bar{\rho}$ is the local Squire buoyancy Brunt-Väisälä frequency.

For inviscid sheared stratified flow, the velocity shear and the buoyancy form a single governing parameter, the local Richardson number $Ri_g(z_*)$, which is defined as,

$$Ri_g(z_*) = \frac{-(\partial b_*/\partial z_*)}{(\partial u_*/\partial z_*)^2} = \frac{N_*^2}{(\partial u_*/\partial z_*)^2} \tag{3.43}$$

where, again, the subscript '*' denotes the dimensional quantities, $b_* = g\rho_*/\bar{\rho}_*$ is the dimensional buoyancy, $N_*^2 = -g(\partial\rho_*/\partial z_*)/\bar{\rho}_*$ is the dimensional local Brunt-Väisälä frequency, and $\bar{\rho}_*$ is the dimensional reference density, respectively.

[5] suggested that when the dimensionless basic velocity and background stratification are of typical hyperbolic profiles, and if

$$\left.\frac{\partial u}{\partial z}\right|_{z=0} = 1, \qquad \left.\frac{\partial \rho}{\partial z}\right|_{z=0} = 1, \tag{3.44}$$

where $z = 0$ is the central line of the sheared/stratified layer, then Ri_g at the interface $z = 0$, which corresponds to $z_* = 0$, become,

$$\begin{aligned} Ri_g|_{z=0} &= \frac{(N_*|_{z=0})^2}{[(\partial u_*/\partial z_*)|_{z=0}]^2} = \frac{-(\partial b_*/\partial z_*)|_{z=0}}{[(\partial u_*/\partial z_*)|_{z=0}]^2} \\ &= \frac{-g(\partial \rho_*/\partial z_*)|_{z=0}}{\bar{\rho}_*[(\partial u_*/\partial z_*)|_{z=0}]^2} = -\frac{gL}{\bar{\rho}V_c^2}\frac{(\partial \rho/\partial z)|_{z=0}}{[(\partial u/\partial z)|_{z=0}]^2} = J\frac{-(\partial \rho/\partial z)|_{z=0}}{[(\partial u/\partial z)|_{z=0}]^2}, \end{aligned}$$

in which $J = gL/(\bar{\rho}V_c^2) = 1/(\bar{\rho}Fr^2)$ is a dimensionless stratification factor. J is introduced and used by [5] for PSS flows and has the same form of the bulk Richardson number usually applied in sheared stratified flow. The hyperbolic velocity/density profiles are usually in the form of $\Delta u_0 f(z)$ and $\Delta \rho_0 f(z)$, where Δu_0 and $\Delta \rho_0$ are the velocity and density changes across the interficial layer and $f(z)$ is the hyperbolic function. If Δu_0 and $\Delta \rho_0$ are selected as the characteristic velocity and density scales, respectively, and if the conditions of (5.2) suggested by [5] are met, $Ri_g(z)$ for the hyperbolic profiles can be simplified as,

$$Ri_g(z) = \frac{N_*^2(z)}{(\partial u_*/\partial z_*)^2} = J\frac{-(\partial \rho/\partial z)}{(\partial u/\partial z)^2}. \tag{3.45}$$

As a result, stratification factor J will replace Ri_g to become the dominant parameter for the CSS flows.

3.3 Numerical methodology

The temporal mode of (3.42), where α is a real number and c is a complex number, is solved in this study. It should be noted that the real part of the temporal growth rate, $\sigma = i\alpha c$, of the perturbation is only determined by the imaginary part of the complex wave speed c, for the wavenumber α is fixed as a real number. As c is uniform in space and only varies with time as assumed by the normal mode [11], the temporal growth rate is the function of time only.

The matrix methods are used to solve the eigenvalue problems formed by discretising the perturbation equations (3.42) with uniform grid and using the second-order central difference scheme. The QZ algorithm developed by [13], which is integrated in the LAPACK routine CGGEV, is used as the complex eigenvalue solver. The robustness of the QZ algorithm in hydrodynamic stability analysis has been demonstrated in some recent studies (*e.g.* [14–16]).

For cross shear flow configurations, the boundary conditions $u = w = v = b = 0$ are applied at both the top and the bottom boundaries. The dimensionless vertical coordinate z varies between -5 and 5, giving the computational domain a size ten times that of L, where the characteristic length L is selected as one half of the sheared layer thickness. Other

domain sizes of 20, 40, 50 are also tested, with less than 1% variations observed. As the computational domain size increases, the grid number should be increased to keep the same resolution. To avoid prohibitive computational costs at very large grid numbers, the length scale of $10L$ is selected as the total length scale, which is sufficiently large to capture the asymptotic hydrodynamic behaviors obtained in other settings with the total domain length scale being more than $10L$.

3.4 Expansion of untable regions in several CSS flows

3.4.1 Two-stratified-layer CSS flow

Influence of ξ

The following hyperbolic functions, which have been frequently used in the stability analysis on two-stratified-layer PSS flow, are used as the free shear velocity and buoyancy frequency profiles for two-stratified-layer CSS flow,

$$U = tanh(z), \quad V = \xi\, tanh(z), \quad N^2 = J\, sech^2(z), \tag{3.46}$$

where U, V, and N are all dimensionless properties as defined in § 3.2. The cross shear ratio for the basic flow states described by (3.46) is $\xi = V/U$.

The stability analysis results obtained by solving (3.42) for the two-stratified-layer CSS flow defined by (3.46) are presented in figure 3.1 where the contours of the real part of $\tilde{\sigma}$ are plotted in the $J - \tilde{\alpha}$ plane for the CSS flow with $\xi = 0$, 0.5 and 1.0, respectively. As the solutions of (3.42) fluctuate slightly around a specific $\tilde{\sigma}$ value, each $\tilde{\sigma}$ contour curve is in fact an approximation to the value represented by that specific $\tilde{\sigma}$ value. For example, the $\tilde{\sigma} = 0.02$ contour curve may be slightly above or below the real value corresponding to $\tilde{\sigma} = 0.02$. Nevertheless, the errors are in the range from $\pm 1\%$ for large growth rates (*i.e.* $\tilde{\sigma} > 0.08$) to $\pm 5\%$ for small growth rates (*i.e.* $\tilde{\sigma} < 0.08$), which will not have noticeable influences on the contours. To determine the exact stability boundary for $\tilde{\sigma} = 0$, the matrix methods used in this study will require an extremely large grid number to distinguish the true solutions from the noises. In fact, to get the exact contour curve for $\tilde{\sigma} = 0$, a gird number of more than 4×10^7 will be required with the matrix methods, which imposes a prohibitive restriction on the computation resources. The PSS flow with $\xi = 0$ was also tested in this study with the matrix methods, and it was found that the contour curves for $\tilde{\sigma} \leq 0.01$ are almost the same. Thus, the $\tilde{\sigma} = 0.01$ contour curve can be adequately approximated as the stability boundary for the unstable mode region for linear stability analysis. In the

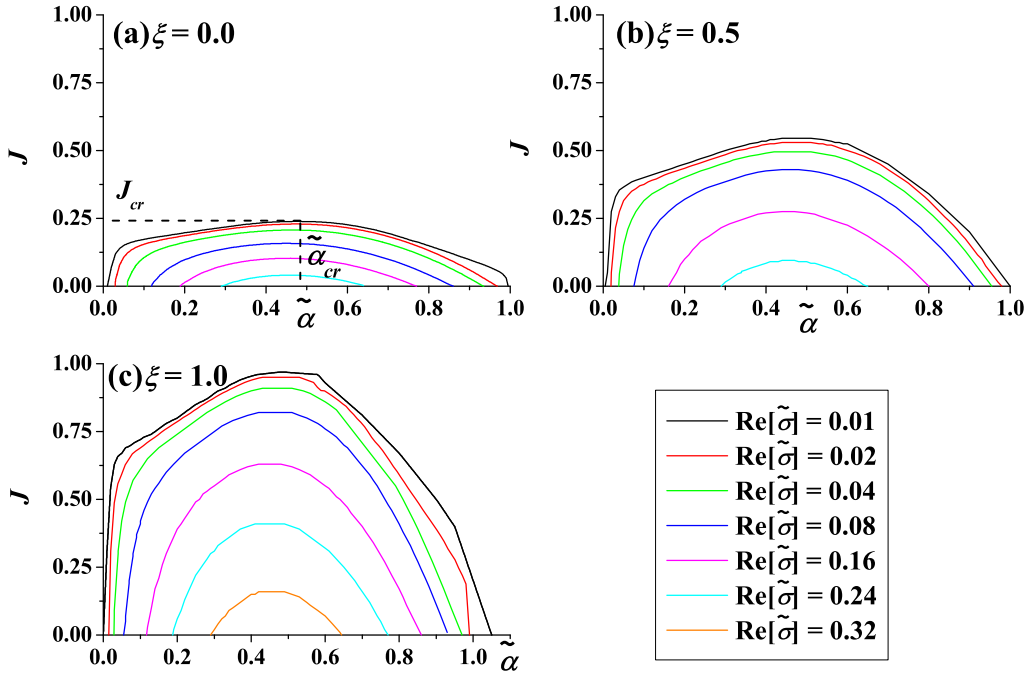

Fig. 3.1 Contours of the real part of $\tilde{\sigma}$ in the $J-\tilde{\alpha}$ plane for the two-stratified-layer CSS basic flow difined by (3.46) with (*a*) $\xi = 0$, (*b*) $\xi = 0.5$, and (*c*) $\xi = 1.0$, respectively.

subsequent sections, the stability boundaries are then determined approximately with the $\tilde{\sigma} = 0.01$ contour.

For the pure PSS flow with $\xi = 0.0$, as shown in figure 3.1(*a*), the contour curve of the stability boundary (*i.e.* , the $\tilde{\sigma} = 0.01$ contour curve) is very close to the semi-circle shape obtained by [5] with the shooting methods. The critical stratification factor J_{cr}, which corresponds to the location for the maximum J in the $J-\tilde{\alpha}$ plot, is close to, but slightly less than 0.25, the classic Miles-Howard theorem value obtained by [3] and [4], as clearly exhibited in figure 3.1(*a*) indicated by the horizontal dash line. The critical wavenumber $\tilde{\alpha}_{cr}$ corresponding to J_{cr} occurs at $\tilde{\alpha} \approx 0.5$ as marked by the vertical dash line in figure 3.1(*a*). It is noted that all the solutions for $\tilde{\sigma}$ are real numbers, indicating that the instability mode corresponds to the stationary wave mode where the instability in the form of a propagative wave will not leave the basic flow with wave speed relative to the basic mean velocity. For PSS flow, such a stationary instability corresponds to the Kelvin-Helmholtz instability.

From figure 3.1(*b*) and 3.1(*c*), it is observed that, similar to the PSS flow, only stationary solutions are obtained for the CSS flows considered. As the cross shear in terms of ξ

is imposed, the entire unstable region expands towards the positive J direction based in comparison to the original unstable region of the PSS flow, as if the entire contour curves are stretched upwards. It is apparent that the extent of such a 'stretch' depends on ξ, as the contour curves with $\xi = 1.0$ cover a much larger region than those with $\xi = 0.5$, as clearly shown in figure 3.1(b) and 3.1(c). Similar expansion of the entire unstable region is also found for other ξ values in the range $0 \leq \xi \leq 1$. In addition, inside the unstable region, the increase of ξ also leads to the increase of the maximum $\tilde{\sigma}$, *e.g.* , when ξ is increased from 0 to 0.5 and then to 1.0, $\tilde{\sigma}$ at the center increases from about 0.24 to 0.28 and then to 0.32, respectively.

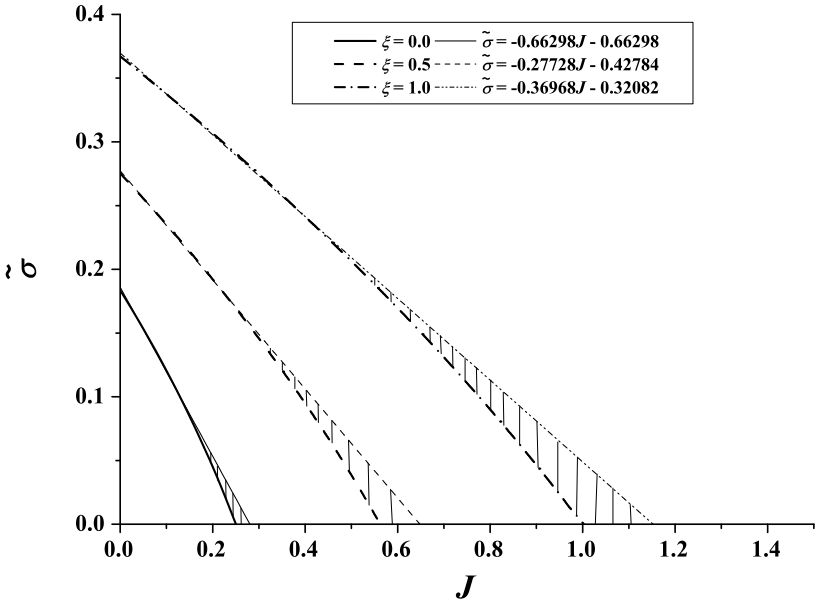

Fig. 3.2 Numerically obtained real temporal growth rate $\tilde{\sigma}$ versus the stratification factor J at $\tilde{\alpha} = 0.5$ for ξ=0.0 (solid line), 0.5 (dash line) and 1.0 (dash dot line) for the two-stratified-layer CSS flow. For each ξ value, the numerical solutions are represented by thick lines and the linear fitting curves are represented by thin lines. The gap between the numerically obtained line and the linear fitting line is highlighted by section lines for each ξ value.

To examine how $\tilde{\sigma}$ changes inside the unstable region for the two-stratified-layer CSS flow represented by (3.46), the values of $\tilde{\sigma}$ are obtained numerically by solving (3.42) with different values of the stratification factor J at $\tilde{\alpha} = 0.5$, which is the critical wavenumber where the maximum growth rate occurs as shown in figure 3.1. The results are presented in figure 3.2, which can be considered as a vertical slice plot of figure 3.1 across $\tilde{\alpha} = 0.5$. Three ξ values are included in line with figure 3.1. For each ξ value, it is seen from figure 3.2 that $\tilde{\sigma}$ decreases monotonically when J increases. The maximum $\tilde{\sigma}$ value for each ξ value,

occurring on the $\tilde{\sigma}$ axis, represents the growth rate under the unstratified condition ($J = 0$) as well as the most unstable mode. The $\tilde{\sigma} = 0$ points on the J axis is very close to the critical J_{cr} as shown in figure 3.1, as $\tilde{\alpha} = 0.5$ is very close to $\tilde{\alpha}_{cr}$. For each ξ value, between the maximum $\tilde{\sigma}$ value and $\tilde{\sigma} = 0$, $\tilde{\sigma}$ initially decreases with J in a linear fashion where the linear fitting curve essentially coincides with the numerical results, and then gradually deviates from the linear trend, as clearly shown in figure 3.2. The linear fitting lines presented in figure 3.2 are found to be represented by

$$\tilde{\sigma} = \begin{cases} -0.66298J - 0.66298 & \text{for } \xi = 0.0, \\ -0.27728J - 0.42784 & \text{for } \xi = 0.5, \\ -0.36968J - 0.32082 & \text{for } \xi = 1.0. \end{cases} \tag{3.47}$$

In comparison to the PSS flow, it is found that the increase of ξ pushes the $\tilde{\sigma} \sim J$ curve towards the positive $\tilde{\sigma}$ and J directions, therefore substantially increasing $\tilde{\sigma}$ for the most unstable mode at the unstratified condition and expanding J_{cr} on the boundary of the unstable region. The gradient of the linear fitting line decreases with increasing ξ, as seen from (3.47), suggesting that $\tilde{\sigma}$ decays in a slower rate in a stronger stratification when the cross shear increases. The deviation of the numerically obtained $\tilde{\sigma} - J$ curve from the corresponding linear fitting line enlarges with increasing ξ, implying that a larger cross shear ratio will lead to a faster decay rate at non-linear stage close to J_{cr}, which is opposite to its influences at linear stage where J is far from J_{cr}. Similar results at $\tilde{\alpha} = 0.5$ shown in figure 3.2 are also found at other $\tilde{\alpha}$ within 0-1 when ξ increases.

Figure 3.3 presents the read part of the growth rate $\tilde{\sigma}$ plotted against the wavenumber $\tilde{\alpha}$ at different values of the stratification factor J for the two-stratified-layer CSS flow. Each sub-plot in this figure can be considered as a horizontal slice plot of figure 3.1 at the designated J value. Four typical J values are selected, with $J = 0.0$ representing the unstratified case, $J = 0.15$ representing a intermediately stratified case, $J = 0.25$, which is equal to the Miles-Howard theorem value, representing the critical stratification case, $J = 0.5$ representing a strongly stratified case. For each case, the results for three values of ξ, *i.e.* , $\xi = 0.0$, 0.5 and 1.0, respectively, are obtained and plotted in the figure.

For the PSS flow, the dispersion relations at unstratified case where $J = 0$ in figure 3.3(a) shows a non-monotonic behavior, with its maximum value close to $\tilde{\alpha}_{cr} = 0.5$. As cross shear ξ is included, the dispersion curves for two CSS flow cases expand based on the original dispersion curve for PSS flow in positive J direction, as if a chord is stretched from its middle maximum point. Note that the gaps among dispersion curves at different ξ, which indicates the amplifications of $\tilde{\sigma}$ with increasing ξ, are not uniformly distributed in $\tilde{\alpha}$ space,

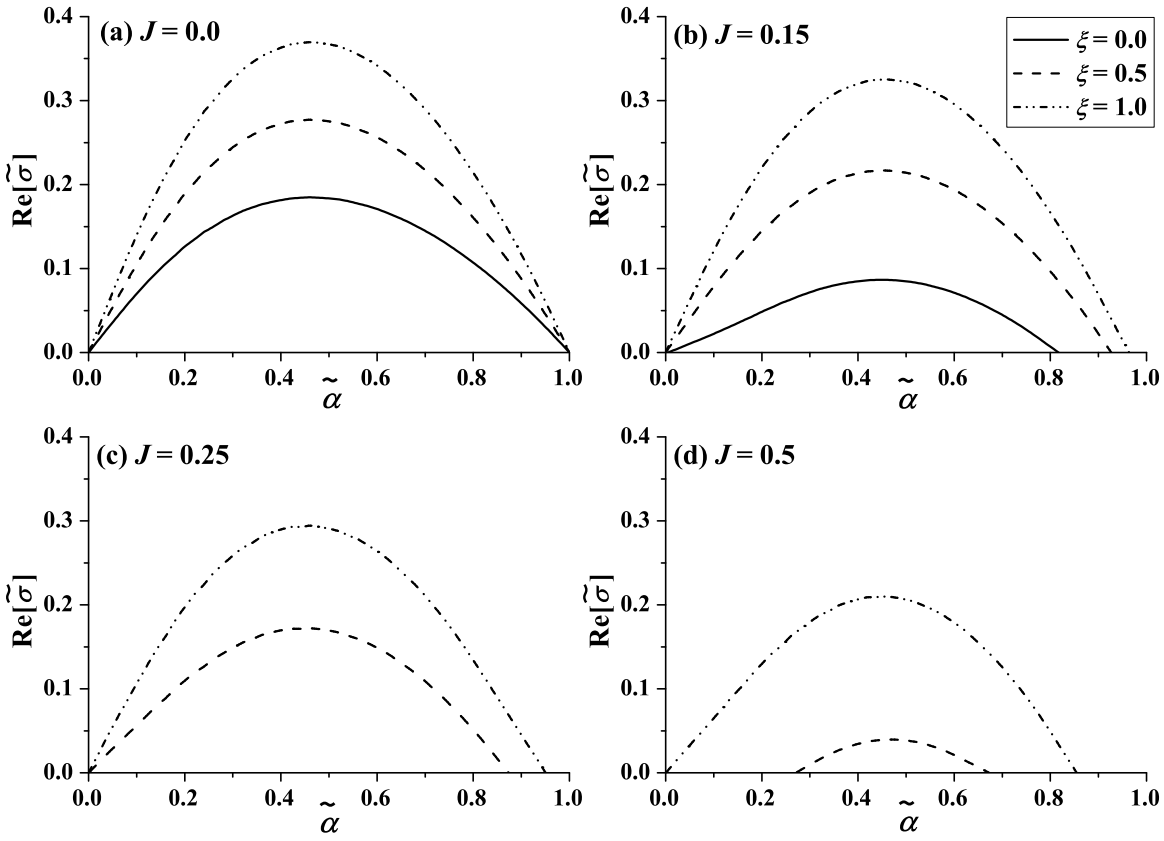

Fig. 3.3 Calculated temporal growth rate $\tilde{\sigma}$ versus wavenumber $\tilde{\alpha}$ at (*a*) $J = 0.0$, (*b*) $J = 0.1$, (*c*) $J = 0.25$, and (*d*) $J = 0.5$ for the two-stratified-layer CSS flow.

therefore implying that there will be different gradient $\partial\tilde{\sigma}/\partial\xi$ at different wavenumber. As J increase to 0.15 as shown in figure 3.3(b), the dispersion curves shows similar non-monotonic behavior to those obtained in $J = 0.0$ case, except for the PSS flow case whose magnitudes of $\tilde{\sigma}$ decrease significantly compared to figure 3.3(a). As J increase to the critical Miles-Howard theorem value, the dispersion curve for PSS flow reduce to $\tilde{\sigma} = 0.0$. Meanwhile, the dispersion curve for $\xi = 0.5$ case also start to decay, as its extension on $\tilde{\alpha}$ axis further decrease at $\tilde{\alpha} = 0.8$.

When J increase to 0.5, the dispersion curve for $\xi = 0.5$ case decay in a remarkable way, with the maximum $\tilde{\sigma}$ falling from 0.17 in figure 3.3(c) to 0.04 figure 3.3(d) and the horizontal extension on $\tilde{\alpha}$ axis converging towards its center. On the contrary, the dispersion curve for $\xi = 1.0$ case keep a relatively weak and stable decay fashion. The different behaviors between dispersion curves of $\xi = 0.5$ and $\xi = 1.0$ as J increase could be attributed to the features of figure 3.2, where at $J = 0.25 \sim 0.5$ growth rate $\tilde{\sigma}$ for $\xi = 0.5$ case decrease in a faster non-linear fashion and for $\xi = 1.0$ decrease in a slower linear fashion.

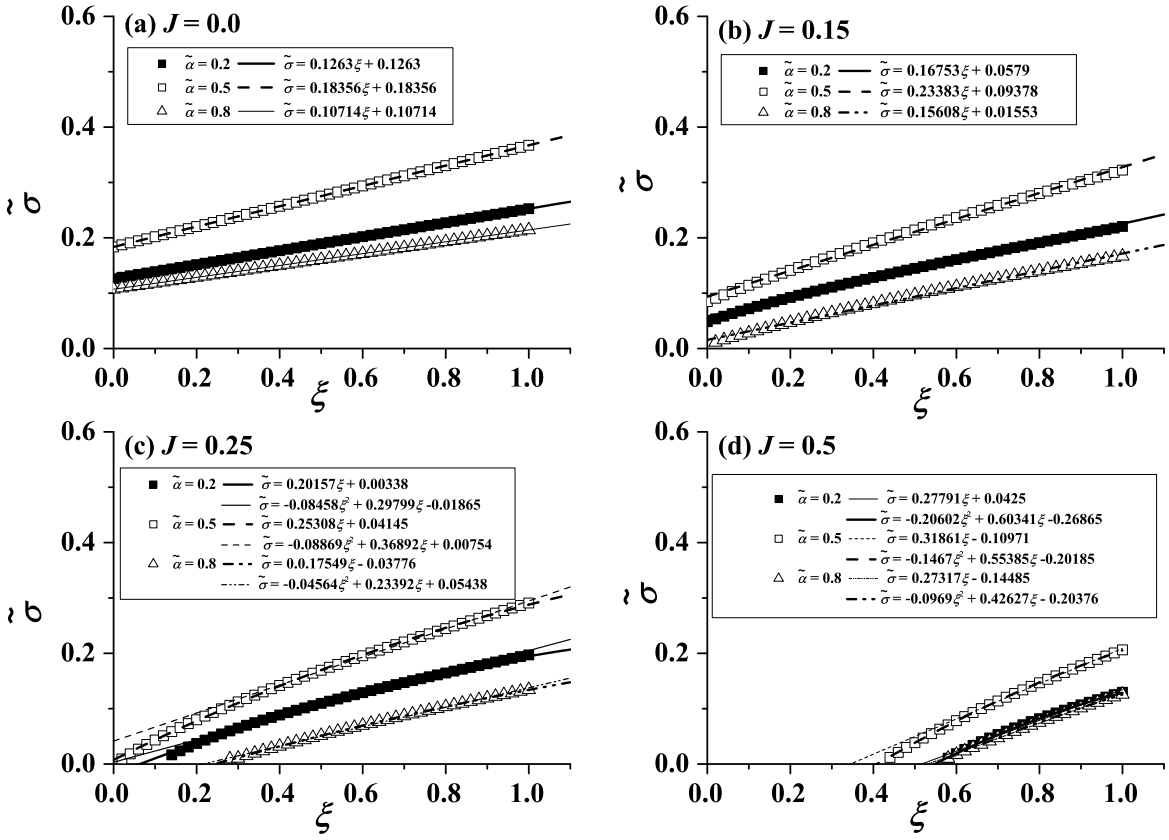

Fig. 3.4 Calculated temporal growth rate plotted against ξ at J=(a)0.0, (b)0.1, (c)0.25 and (d)0.5 for CSS flows Eq.[3.46]. For each J case, three $\tilde{\alpha}$ are chosen as 0.2, 0.5 and 0.8 as well as their linear/parabolic fitting functions indicated by thick/thin solid lines, dash lines and dash dot dot lines.

The results above give qualitative descriptions of how cross shear ratio ξ expand $\tilde{\sigma}$ at the stability boundary and insider the instability regions in $\tilde{\alpha} \sim J$ space. However, to quantify the influences of ξ on the stability features of CSS flow, it is necessary to consider ξ as a continuous parameter and its relation to J and $\tilde{\alpha}$. Figure 3.4 plot $\tilde{\sigma}$ against ξ at a wavenumber set with $\tilde{\alpha}$=0.2, 0.5 and 0.8. Corresponding to figure 3.3, each wavenumber set is further plotted at $J = 0.0$, 0.1, 0.25 and 0.5, as shown in figure 3.4(a)-(d). At $J = 0.0$ and 0.15 as shown in figure 3.4(a) and (b), the linear function (line) between $\tilde{\sigma}$ and ξ almost coincide with numerical results (scattered points). As J further increase to $J \geq 0.25$, slight deviations between linear correlations and numerical results appear at the incipient stage of $\tilde{\sigma} \sim \xi$ plot for $J = 0.25$ and $J = 0.5$ cases as shown in figure 3.4(c) and (d), where the parabolic correlations obtain better results. Although not shown here, the discrepancies between the $J < 0.25$ region where $\tilde{\sigma}$ vary linearly with ξ and the $J \geq 0.25$ region where $\tilde{\sigma}$

vary as parabolic function of ξ are also found in entire $J = 0 \sim 1$ range. In addition, when J is increasing from 0 to $J = 0.25$ and further exceeding beyond, the initial points of $\tilde{\alpha} \sim \xi$ plot results first local on $\tilde{\sigma}$ axis as shown in figure 3.4(a), then move downwards to origin of $\tilde{\alpha} - \xi$ coordinate as shown in figure 3.4(c) and at last move onto the ξ axis as shown in figure 3.4(d)) . Thus, the Miles-Howard theorem value $J = 0.25$ remains a critical value that distinguish different behaviors of $\tilde{\alpha} \sim \xi$ variation.

In spite of better results from parabolic correlations for $J \geq 0.25$ cases, the linear correlations are found to be able to sufficiently describe the gradient of $\partial\tilde{\sigma}/\partial\xi$ in range of $J \geq 0.25$, as shown in figure 3.4(c) and (d). Based on the extremely well fitting results in $J < 0.25$ and adequately well fitting results in $J \geq 0.25$, linear correlation is a qualified candidate to generally describe the gradient $\partial\tilde{\sigma}/\partial\xi$. As demonstrated by figure 3.4, each $[\tilde{\alpha}, J]$ pair corresponds to a single and constant gradient $\partial\tilde{\sigma}/\partial\xi$. In other words, $\partial\tilde{\sigma}/\partial\xi$ would be treated as a two dimensional function of $\tilde{\alpha}$ and J, which is the same as growth rate itself $\tilde{\sigma}$.

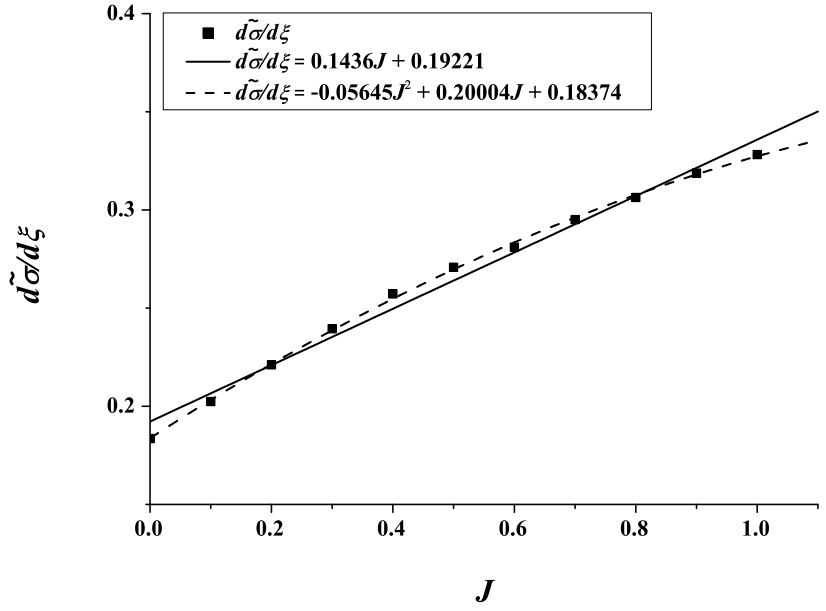

Fig. 3.5 $\partial\tilde{\sigma}/\partial\xi$ plotted against J at $\tilde{\alpha}$=0.5 for CSS flows Eq.[3.46]. Solid and dash line represent linear and parabolic fitting functions based on numerical results represented by solid square points.

Figure 3.5 shows the gradient of temporal growth rate $\partial\tilde{\sigma}/\partial\xi$ versus J at wavenumber $\tilde{\alpha} = 0.5$, which is near the critical wavenumber $\tilde{\alpha}_{cr}$. The magnitudes of $\partial\tilde{\sigma}/\partial\xi$ are obtained by the same linear correlation techniques used in figure 3.4. When $J > 0.5$, the maximum ξ are extended to 2.0 so that the linear fashion between $\tilde{\sigma}$ and ξ endure sufficiently along ξ axis. For $\tilde{\alpha} = 0.5$ case shown in figure 3.5, gradient $\partial\tilde{\sigma}/\partial\xi$ increase monotonically

with increasing J, indicating that $\tilde{\sigma}$ even increases in a faster rate with increasing ξ at strong stratified environment than at the weak stratified environment. Linear and parabolic correlation are both applied as shown in figure 3.5, where parabolic correlation shows a better results. In addition to wavenumber $\tilde{\alpha} = 0.5$ shown here, at other wavenumber in $\tilde{\alpha} = 0 \sim 1$ the parabolic fashion are found between $\partial\tilde{\sigma}/\partial\xi$ and J as well.

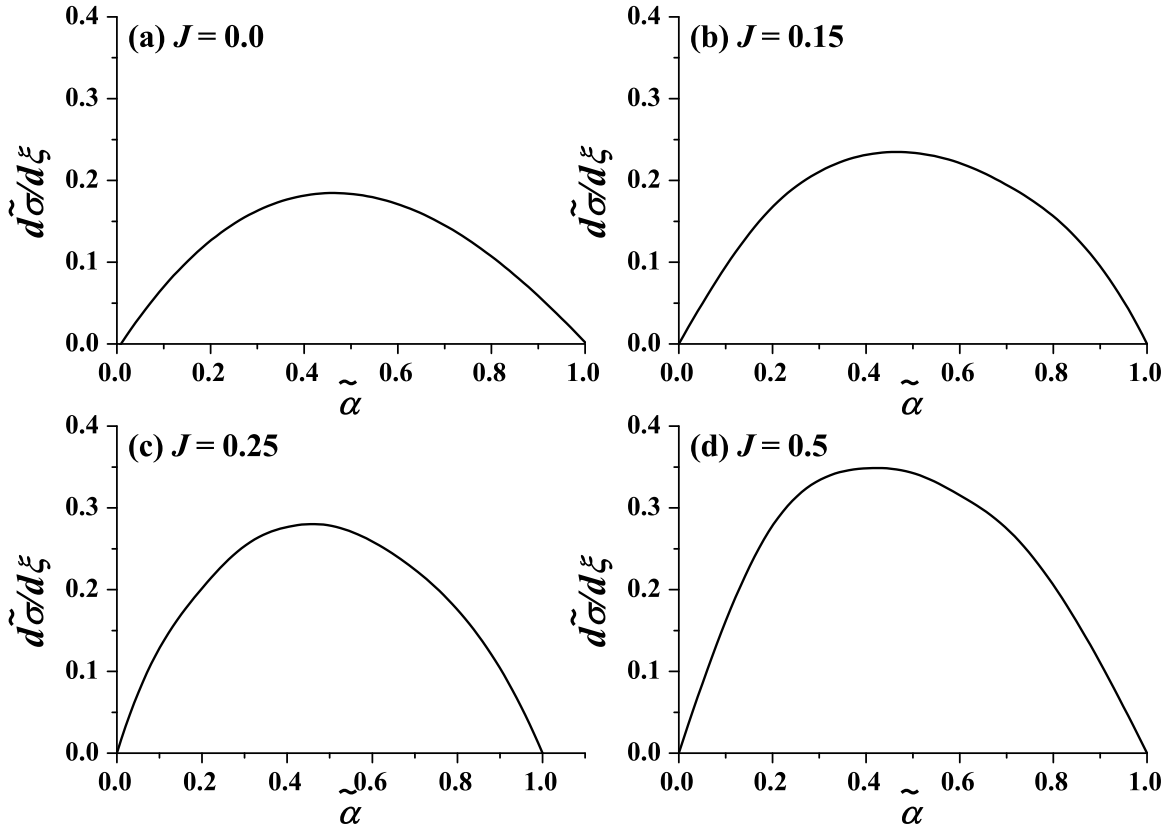

Fig. 3.6 $\partial\tilde{\sigma}/\partial\xi$ plotted against $\tilde{\alpha}$ at J=(a)0.0, (b)0.15, (c)0.25 and (d)0.5 for CSS flows Eq.[3.46].

Figure 3.6 shows the gradient of temporal growth rate $\partial\tilde{\sigma}/\partial\xi$ distribute along wavenumber $\tilde{\alpha} = 0 \sim 1$ at four stratification factors J=0.0, 0.15, 0.25 and 0.5. Similar to traditional dispersion describing a spectrum of how growth rate $\tilde{\sigma}$ distribute in wavenumber $\tilde{\alpha}$ space, figure 3.6 can be considered as a spectrum of the acceleration $\partial\tilde{\sigma}/\partial\xi$ distributed in $\tilde{\alpha}$ space. Similar to dispersion curve shown in figure 3.3, four $\partial\tilde{\sigma}/\partial\xi$ versus $\tilde{\alpha}$ dispersion curves display the similar non-monotonic shapes to the dispersion curves shown in figure 3.3, therefore leading to the way how ξ stretch the unstable regions shown in figure 3.1 and dispersion curves in figure 3.3. Note that the maximum points of non-monotonic $\partial\tilde{\sigma}/\partial\xi$ dispersion curves occur at $\tilde{\alpha} \approx 0.5$ in figure 3.6(a), which is the same position of the maxi-

mum point of $\tilde{\sigma} \sim \tilde{\alpha}$ dispersion curve shown in figure 3.3(a). Therefore, the coincidence of maximum points between gradient $\partial\tilde{\sigma}/\partial\xi$ dispersion curves and growth rate $\tilde{\sigma}$ dispersion curves indicates that the most unstable mode is also the fastest expansions mode with increasing ξ. In addition, comparing four subfigures with different J values, it is found that J stretch the $\partial\tilde{\sigma}/\partial\xi \sim \tilde{\alpha}$ dispersion curves towards positive J direction, so that at every wavenumber $\partial\tilde{\sigma}/\partial\xi$ increases as J increases. Such stretch effects by stratification factor J on $\partial\tilde{\sigma}/\partial\xi \sim \tilde{\alpha}$ dispersion curves closely relate to the increasing parabolic fitting functions obtained in figure 3.5.

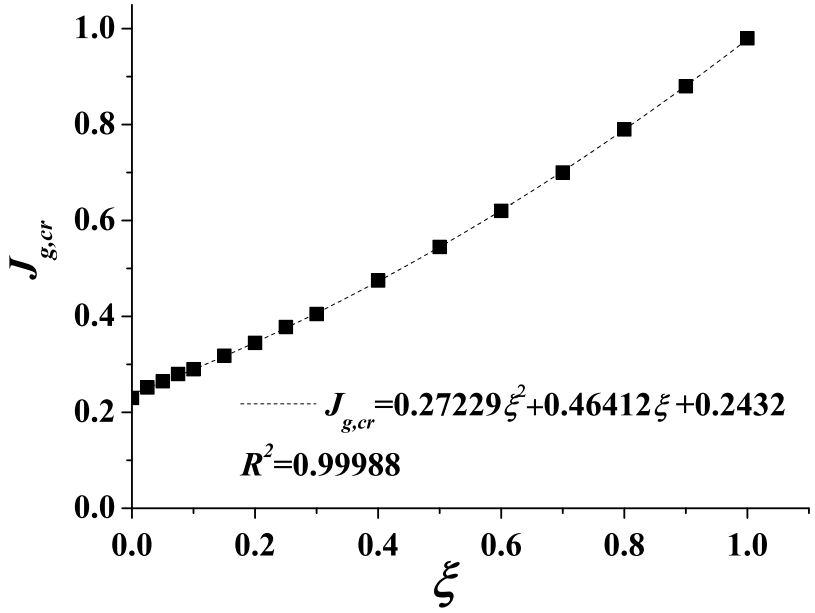

Fig. 3.7 Critical stratification factor J_{cr} plot against cross shear ratio ξ for CSS flows Eq.[3.46]. Dash line represent the parabolic fitting function based on numerical results.

At last, the influences of ξ on the critical stratification factor J_{cr}, which represent the absolute boundary stable and unstable region, are presented in figure 3.7. It is found that the critical wavenumber $\tilde{\alpha}_{cr}$ where J_{cr} occurs is found to be independent of ξ, therefore all J_{cr} are actually obtained at the same critical wavenumber $\tilde{\alpha}_{cr} = 0.5$. For the CSS flow with $\xi = 0 - 1$, parabolic correlations are found extremely well between J_{cr} and ξ. The exact formula is:

$$J_{g,cr} = 0.27229\xi^2 + 0.46412\xi + 0.2432 \tag{3.48}$$

Note that the interception for Eq.[3.48] is 0.2432, which is very close to the Miles-Howard theorem value. As $\xi < 0.1 \sim 0.2$, all J_{cr} are in fact less than the Miles-Howard theorem

value, suggesting that a weak cross shear will not modify the boundary of unstable region. Due to the parabolic formula, J_{cr} will increase in a faster rate as ξ further increase, which corresponds to the parabolic fashion between gradient $\partial\tilde{\sigma}/\partial\xi$ and J as shown in figure 3.6.

Influences of R_s

In sections above, the thickness of streamwise and spanwise sheared layer are the same, as U and V has exact the same hyperbolic function. However, the length scale of sheared layer might be different in streamwise and spanwise direction in large scale flow field. Based on basic flow states Eq.3.46, the thickness ratio R_s between streamwise and spanwise sheared layer is introduced in the basic flow state as:

$$U = tanh(z), \quad V = \xi\, tanh(R_s z), \quad N^2 = J\, sech^2(z), \tag{3.49}$$

in which the dimensionless thickness of spanwise sheared layer now become $1/R_s$. R_s will increase the cross shear by decreasing the length scale of spanwise velocity shear. As R_s has physical meaning only if $\xi \neq 0$, in the following sections ξ will be fixed at 0.5 as a typical setting. When ξ is fixed at other values within $\xi = 0 - 1$, the typical stability features introduced by R_s in this subsection also exist.

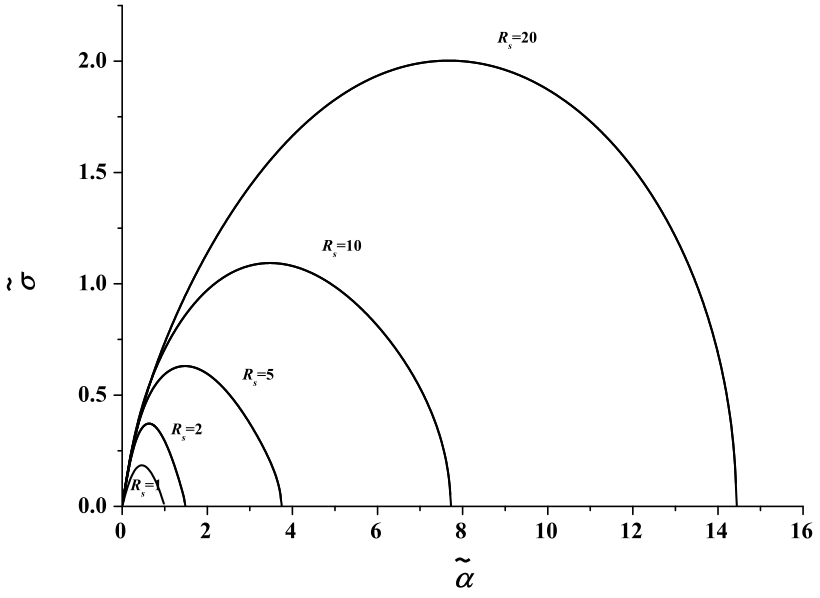

Fig. 3.8 Calculated growth rate $\tilde{\sigma}$ plot against wavenumber $\tilde{\alpha}$ at unstratified case where $J = 0.0$, $\xi = 0.5$ and R_s =1, 2, 5, 10, 20 for CSS flows Eq.[3.49].

Figure 3.8 shows the dispersion relation between temporal growth rate $\tilde{\sigma}$ and wavenumber $\tilde{\alpha}$ at different R_s for unstratified case with $J = 0$ and cross shear ratio $\xi = 0.5$. Compare to figure 3.3 where dispersion curve simply stretch towards positive $\tilde{\sigma}$ direction with increasing ξ, the dispersion curves in figure 3.8 shows different expansion behaviors at their left and right branches separated by the mid maximum points. The left branches behave as an envelop of the family of R_s curves, below which the unstable region for all different R_s cases are contained. On the contrary, the right branch of the dispersion curve expand significantly in both positive $\tilde{\sigma}$ and $\tilde{\alpha}$ direction as R_s increases. As a result of dual expansion in $\tilde{\sigma}$ and $\tilde{\alpha}$ axis, introducing R_s will not only expand the unstable regions by increasing $\tilde{\sigma}$, but also incite unstable mode at large wavenumber range $\tilde{\alpha} > 1.0$. This is physically reasonable, because R_s would relatively decrease length scale of shear layer, so that the perturbation with comparable wavelength to the thickness of shear layer could also incite unstable mode.

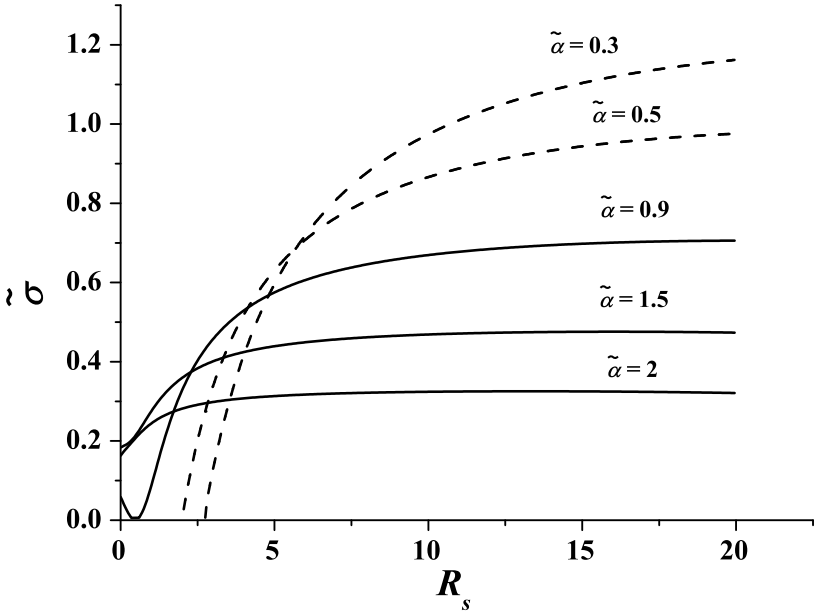

Fig. 3.9 Calculated growth rate $\tilde{\sigma}$ plot against thickness ratio of cross shear thickness ratio R_s at unstratified condition where $J = 0.0$ for CSS flows Eq.[3.49]. The magnitudes of wavenumber $\tilde{\alpha}$ are marked near corresponding plotting curves. The solid and dash lines are used to distinguish the cases where $\tilde{\alpha} \geq 0.9$ and $\tilde{\alpha} < 0.9$

To further quantify how $\tilde{\sigma}$ responds to continuous R_s, figure 3.9 shows $\tilde{\sigma}$ as functions of R_s at unstratified case with $J = 0.0$ and $R = 1$. Figure 3.9 can be considered as vertical slice plot of figure 3.8 at specific wavenumber with continuously varying R_s. At all selected wavenumber shown in figure 3.9, the asymptotic behaviors are found between $\tilde{\sigma}$ and R_s. For other $\tilde{\alpha}$ not shown here, similar asymptotic behaviors are also observed. Such asymptotic

behaviors that generally exist in $\tilde{\sigma} \sim R_s$ relation represent the mathematical features of envelops on the left branch of R_s curves in figure 3.8. Despite of same asymptotic behaviors, the initial and terminal $\tilde{\sigma}$ values of each asymptotic curves are different as shown in figure 3.9. For $\tilde{\alpha} < 0.9$ cases as denoted by dash lines, the initial points located on R_s axis. As $\tilde{\alpha}$ approach 0.9, the initial points of asymptotic curves gradually move towards the origin point of $R_s \sim \tilde{\sigma}$ coordinate and once $\tilde{\alpha} > 0.9$, the initial points of asymptotic curves move onto $\tilde{\sigma}$ axis. For those $\tilde{\alpha} > 0.9$ cases whose initial points locate on $\tilde{\sigma}$ axis, the basic flow could be unstable under infinitesimal perturbations because $\tilde{\sigma} \neq 0$ even at $R_s = 0$ condition corresponding to is infinitely large length scale of cross shear layer. On the other hand, the terminal values of asymptotic $\tilde{\sigma} \sim R_s$ curves are found to simply increase with increasing R_s, following the gradient of the envelop curve shown in figure 3.8.

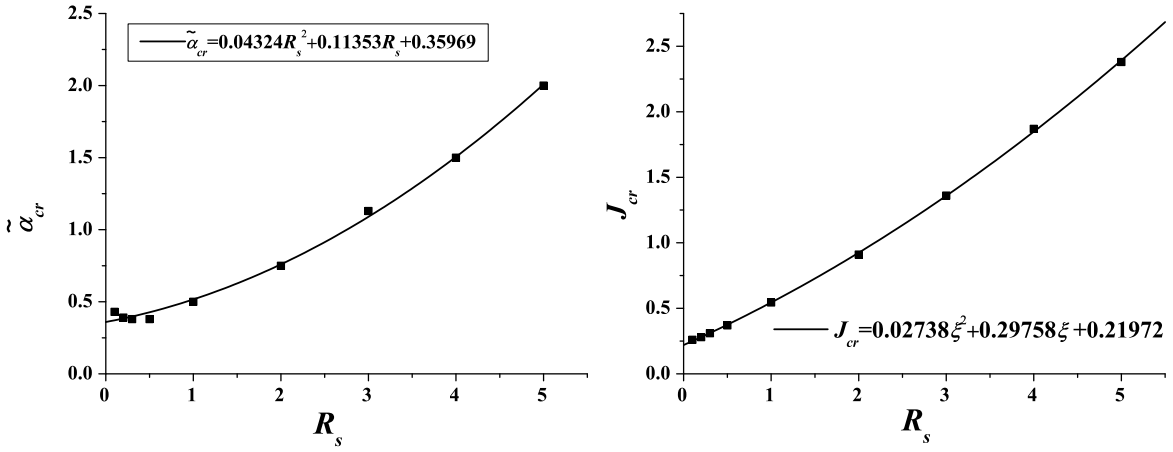

Fig. 3.10 (a)Critical wavenumber $\tilde{\alpha}_{cr}$ and (b) stratification factor J_{cr} plot against R_s. Solid line represent the parabolic correlation based on numerical results.

Figure 3.10 shows the critical stratification J_{cr} and corresponding critical wavenumber $\tilde{\alpha}_{cr}$ as a function of R_s. The extremely well correlations between J_{cr} and $\tilde{\alpha}_{cr}$ with R_s are established by parabolic functions:

$$\begin{aligned} \tilde{\alpha}_{cr} &= 0.04324R_s^2 + 0.11353R_s + 0.35969 \\ J_{g,cr} &= 0.02738R_s^2 + 0.29758R_s + 0.21972 \end{aligned} \tag{3.50}$$

Similar to figure 3.7 where J_{cr} increase with increasing ξ, parabolic relation are found between J_{cr} and R_s. Nevertheless, $\tilde{\alpha}_{cr}$ are also found to vary with R_s, in contrast to the constant critical wavenumber $\tilde{\alpha}_{cr} \approx 0.5$ found in 3.4.1. The larger critical wavenumber with increasing R_s relate to the expansion behaviors caused by R_s shown in figure 3.10 and also

suggest that the most unstable mode is inclined to perturbations with large wavenumber(small wavelength) as R_s increases.

3.4.2 Cross free shear flow in linear stratified configuration

In large flow field such as ocean and atmosphere, the stratified layer usually vary with height continuously. Therefore, in this subsection, typical linear stratified layer will be considered so that the basic flow states become:

$$U = tanh(z), \quad V = \xi\, tanh(R_s z), \quad N^2 = J, \tag{3.51}$$

Theoretically, the linear stratified profile in Eq.[3.59] indicates that the thickness of stratified layer is absolutely infinite. For finite thickness of stratified layer, please refer to subsequent 3.5.

Figure 3.11 shows the stability boundary, which is the contour of $Re[\tilde{\sigma}] = 0.0$, for basic flow state Eq.[3.51] at cross shear ratio ξ=0.0, 0.5 and 1.0. As a result of linear stratified profile Eq.[3.51] , the critical wavenumber $\tilde{\alpha}_{cr}$ as well as the peak sections shown in figure 3.11 tends to move to large wavenumber sections compared to those with hyperbolic stratification profiles in figure 3.1. Nevertheless, the way cross shear ratio ξ that stretch the stability boundary in figure 3.11 is very similar to the stretch fashion found in figure 3.1, in that the contour curves of $Re[\tilde{\sigma}] = 0.0$ at $\xi = 0.5$ and 1.0 show stretched non-monotonic shapes from the middle peak sections of the original $Re[\tilde{\sigma}] = 0.0$ contour curves at $\xi = 0.0$.

To further quantify if ξ varies $\tilde{\sigma}$ in the same linear fashion in linear stratified environment, figure 3.12 shows $Re[\tilde{\sigma}]$ plot against continuous ξ for linear stratified profile Eq.[3.51] at wavenumber set $\tilde{\alpha}$ =0.3, 0.5 and 0.8, where the linear correlations are also included. Similar to figure 3.4, the linear correlations (lines) coincide with numerical results (scatter points) in the majority of ξ range, except for a short span where $\xi < 0.2$ at $\tilde{\alpha} = 0.3$ where $Re[\tilde{\sigma}]$ grow in a non-linear pattern slower than linear correlation. In addition to three wavenumber and specific $J = 0.15$ shown in figure 3.12, $\tilde{\sigma} \sim \xi$ relations are widely examined at other wavenumber within $\tilde{\alpha} = 0 - 1$ and stratification factor. As same as the results found in section 3.4.1, the linear correlations are found to adequately describe the gradient $\partial\tilde{\sigma}/\partial\xi$ in majority of ξ range. Therefore, for the linear stratified profile Eq.[3.51], $\partial\tilde{\sigma}/\partial\xi$ could also be considered as a two-dimensional function of $\tilde{\alpha}$ and J.

Figure 3.13 shows the dispersion curves between gradient $\partial\tilde{\sigma}/\partial\xi$ and wavenumber $\tilde{\alpha}$. The results of figure 3.4(b) where hyperbolic stratified profile Eq.[3.46] at the same J is also included for comparison. Compare to the results from hyperbolic stratified profile, the

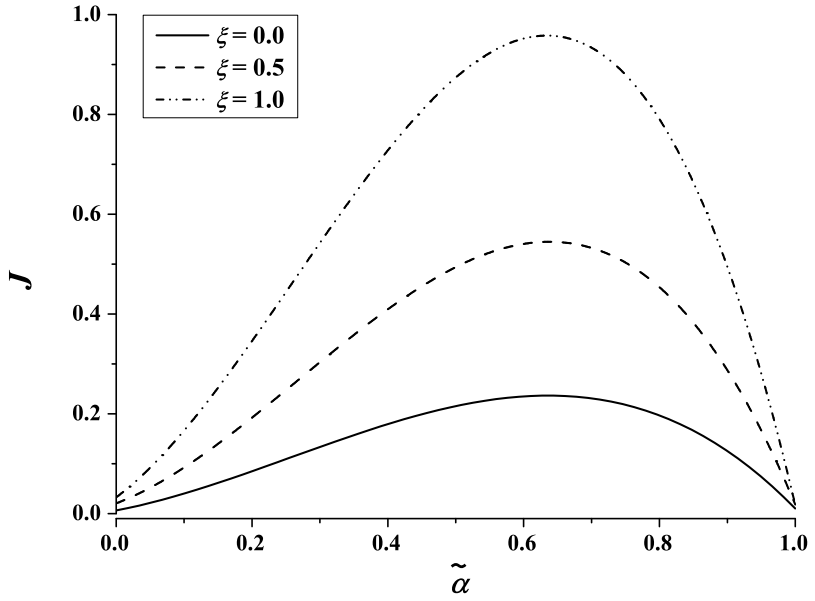

Fig. 3.11 Calculated contour of $Re[\tilde{\sigma}] = 0$ in $J \sim \tilde{\alpha}$ plane for the CSS flows Eq.[3.51] with ξ =0.0, 0.5 and 1.0, respectively

dispersion curve of $\partial\tilde{\sigma}/\partial\xi \sim \tilde{\alpha}$ remain non-monotonic tendency but its peak move from $\tilde{\alpha} \approx 0.5$ to $\tilde{\alpha} \approx 0.4$, as indicated by dash lines.

Figure 3.14 shows J_{cr} plot against ξ for linear stratified profile Eq.[3.51]. Similar to figure 3.7, J_{cr} and ξ correlate extremely well with parabolic function:

$$J_{g,cr} = 0.24359\xi^2 + 0.46641\xi + 0.24245 \tag{3.52}$$

Compare to correlation results Eq.[3.48] for hyperbolic stratification profiles Eq.[3.46], the major difference is the coefficient of the quadratic term, which is 0.27229 in Eq.[3.48] and 0.24359 in current Eq.[3.52], indicating that the different stratified profiles have minor influence on $J_{cr} \sim \xi$ curve.

Figure 3.15 shows the dispersion relations between $\tilde{\sigma}$ and $\tilde{\alpha}$ for linear stratification profiles Eq.[3.51] at $J = 0.15$ and different R_s. The dispersion curve for hyperbolic stratification profile Eq.[3.46] at same $J = 0.15$ are also plotted in dash curves. Apparently, the differences between dispersion curves at two stratification profile are insignificantly, as the dash lines and the solid lines almost overlap. The features found at unstratified case shown in figure 3.8 reproduce in figure 3.15, where the left branches of $\tilde{\sigma} \sim \tilde{\alpha}$ curves behave as the envelop of R_s curve family and the right branches are the main contributor to the expansions of unstable regions.

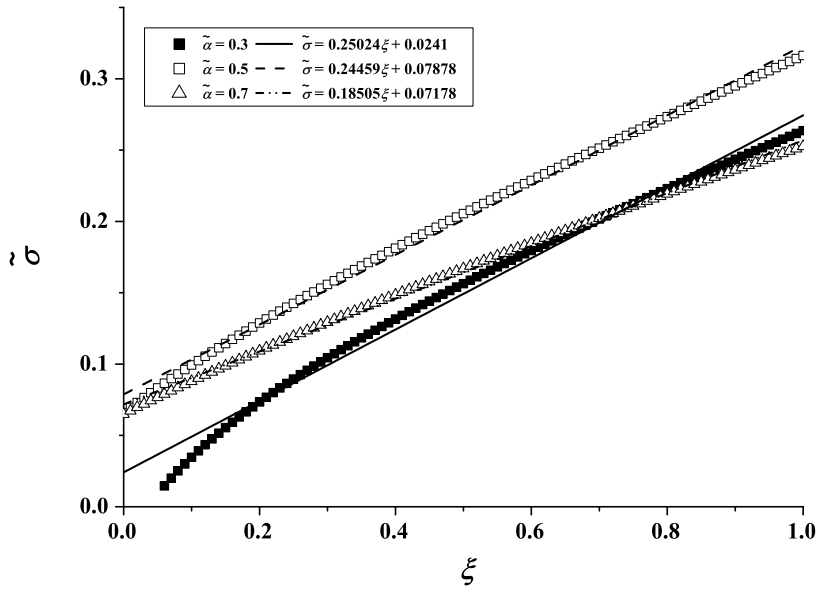

Fig. 3.12 Calculated temporal growth rate $\tilde{\sigma}$ plotted against ξ at J=0.15 for CSS flows Eq.[3.51]. Numerical results for three $\tilde{\alpha}$=0.3 (solid square points), 0.5 (void square points) and 0.7 (triangle points) as well as their linear fitting functions (solid line for $\tilde{\alpha} = 0.3$, dash line for $\tilde{\alpha} = 0.5$ and dash dot dot line for $\tilde{\alpha} = 0.7$) are plotted.

Figure 3.16 shows the critical wavenumber $\tilde{\alpha}_{cr}$ and stratification factor J_{cr} plot against cross shear thickness ratio R_s, where parabolic correlations are included. Similar to figure 3.10, extremely well correlations by parabolic functions:

$$\begin{aligned} \tilde{\alpha}_{cr} &= 0.3718R_s^2 + 0.17306R_s + 0.47155 \\ J_{g,cr} &= 0.04208R_s^2 + 0.27398R_s + 0.21894 \end{aligned} \tag{3.53}$$

are found for both $\tilde{\alpha}_{cr}$ versus R_s and J_{cr} versus R_s. The similar parabolic correlations found in hyperbolic and linear stratification profile suggest parabolic function might be a general way how cross shear expand the stationary unstable region, regardless of any background stratifications.

3.4.3 Cross bounded shear flow in linear stratified environment

Based on the hyperbolic cross free shear profile 3.46, the cross bounded shear flows have the following profiles:

$$U = sin(z), \quad V = \xi\, sin(z), \quad N^2 = J, \tag{3.54}$$

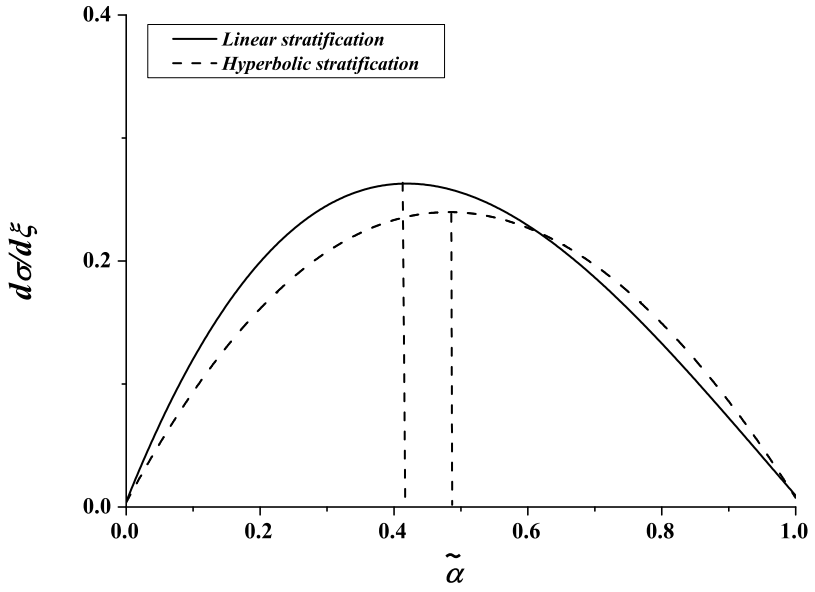

Fig. 3.13 $\partial\tilde{\sigma}/\partial\xi$ plotted against $\tilde{\alpha}$ at $J = 0.15$ for CSS flows Eq.[3.51]. The results from figure 3.4(b) are also plotted in dash curve. Two vertical dash lines indicate the wavenumber $\tilde{\alpha}$ where maximum $\partial\tilde{\sigma}/\partial\xi$ occur.

in which *sin* function are adapted to simulate the velocity profile changes near the solid boundary. The same triangular functions and stratification profiles for bounded PSS flow are used in [5]. Different from previous sections where $Im[\tilde{\sigma}] = 0$, non-zero $Im[\tilde{\sigma}] = 0$ are always obtained for the cross bounded shear flows, but the variations of $Im[\tilde{\sigma}]$ are very slight in the entire $J \sim \tilde{\alpha}$ space. Therefore, this subsection will only concentrate on $Re[\tilde{\sigma}]$.

Figure 3.17 shows the contour of $Re[\tilde{\sigma}]$ in $J \sim \tilde{\alpha}$ plane for CSS flow Eq.[3.54]. Compare to figure 3.1 and figure 3.11, the critical wavenumber $\tilde{\alpha}$ further move to larger $\tilde{\alpha}$ at about 0.8, then $Re[\tilde{\sigma}]$ steeply fall down to zero within a very short span on $\tilde{\alpha}$ axis. This agrees with the results obtained by [5]. As ξ increase, the similar stretch fashion to figure 3.1 and figure 3.11 are also observed in figure 3.17.

Figure 3.18 shows the critical stratification factor J_{cr} plot against ξ, where once again parabolic relations between J_{cr} and ξ are found in cross bounded shear flow. The parabolic function for cross bounded flow are:

$$J_{g,cr} = 0.27077\xi^2 + 0.39673\xi + 0.20821 \tag{3.55}$$

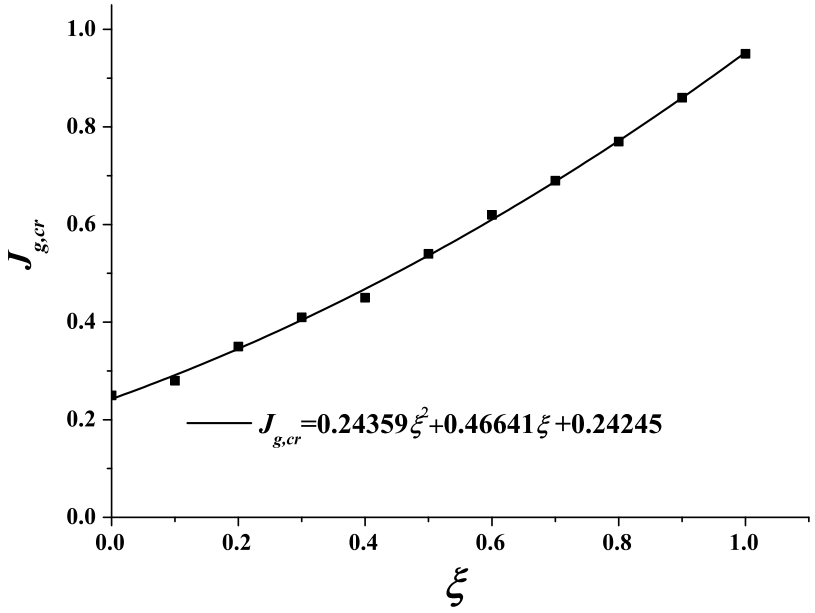

Fig. 3.14 Critical stratification factor J_{cr} plot against cross shear ratio ξ for CSS flows Eq.[3.51]. Dash line represent the parabolic correlation based on numerical results

3.4.4 Cross jet flow in linear stratified environment

Following [5], the basic flow states for cross jet flow are:

$$U = sech(z), \quad V = \xi\, sech(z), \quad N^2 = J, \tag{3.56}$$

Based on [5], there are two instabilty mode for jet flow. This study only examines the peak corresponding to 'varicose mode' within $\tilde{\alpha} = 0 - 1$ which is the same range used in previous sections.

Figure 3.19 shows the contour of $Re[\tilde{\sigma}]$ in $J \sim \tilde{\alpha}$ plane. Similar to the contour plot shown in previous sections, the expansion of stability boundary due to increasing ξ are observed in the 'varicose mode'.

Figure 3.20 shows the critical stratification factor J_{cr} plot against ξ for cross jet flow, where parabolic relations between J_{cr} and ξ are found for the 'varicose mode' as:

$$J_{g,cr} = 0.09889\xi^2 + 0.20824\xi + 0.08322 \tag{3.57}$$

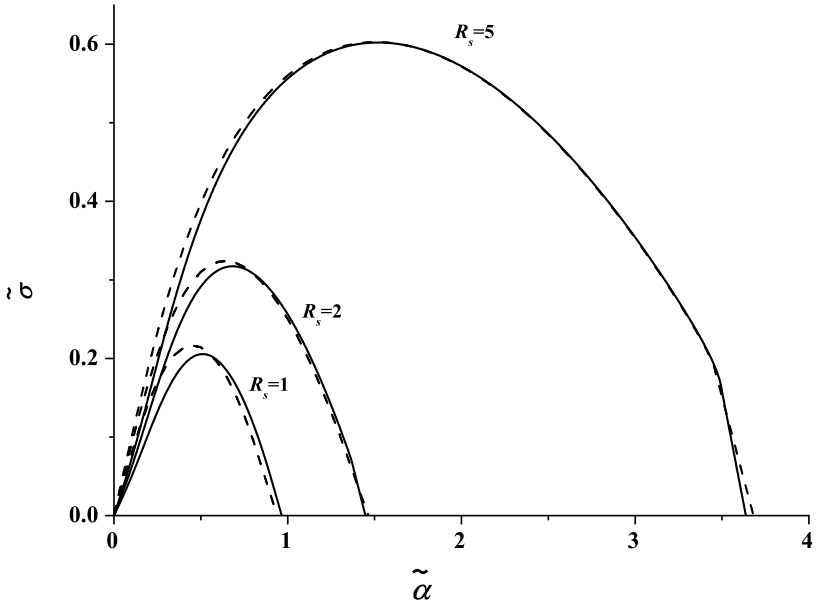

Fig. 3.15 Calculated $Re[\tilde{\sigma}]$ plot against in $\tilde{\alpha}$ at $J = 0.15$ for CSS flows Eq.[3.51] with R_s =1.0, 2.0 and 5.0. Results for CSS flows Eq.[3.46] at same $J = 0.15$ and R_s values are also plotted in dash curves

3.5 Transition from stationary mode to propagative mode in cross shear flows

3.5.1 influences of ξ

In nature, the length scales of shear layer and stratified layer are usually different, due to different kinetic viscosity ν and thermal diffusivity κ, that is, Prandlt number $Pr = \nu/\kappa \neq 1$. Therefore, the thickness of stratified layer are usually different from the thickness of sheared layer. To describe the differences between shear and stratified layer, [5] first introduce a ratio of thickness of shear/stratified layer R in the basic flow state, so that Eq.3.46 become:

$$U = tanh(z), \quad V = \xi\, tanh(z), \quad N^2 = J\, sech^2(Rz), \tag{3.58}$$

in which the dimensionless thickness of stratified layer become $1/R$.

When the length scale of stratified layer decrease and become smaller than the shear layer, the propagative instability modes will appear at large stratification factor J. Figure 3.21(a) shows the real and imaginary parts of growth rate $\tilde{\sigma}$ distribute along stratification factor J axis, for PSS flow with $\xi = 0.0$ at $\tilde{\alpha} = 0.3$ and $R = 8$. The results with same parameter settings are obtained by [7] with shooting method. Compare to figure 3.2 where Im[$[\sigma]$]=0,

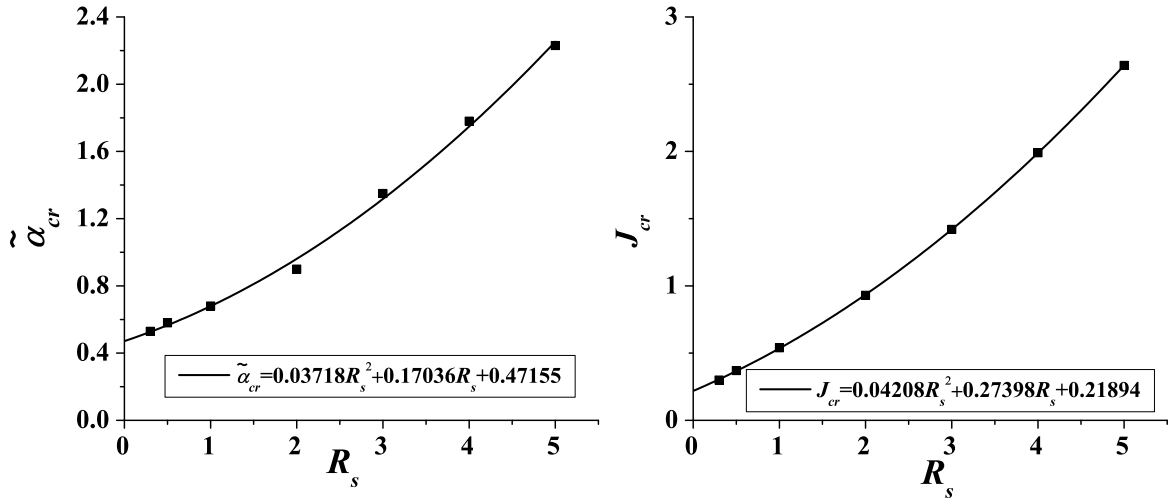

Fig. 3.16 (a)Critical wavenumber $\tilde{\alpha}$ and (b) stratification factor J_{cr} plot against R_s for CSS flows Eq.[3.51]. Solid line represent the parabolic correlations for the numerical results

figure 3.21(a) include a pair of non-zero imaginary part of growth rate $Im[\sigma]$ at every single stratification factor J after about $J = 0.46$. As $Im[\tilde{\sigma}] = i\tilde{\alpha}c_r$ indicate the propagation speed of unstable mode where c_r is the real part of wave speed, non-zero $Im[\tilde{\sigma}]$ suggest the unstable mode would move in a speed of c_r regarding to basic flow. In addition, a conjugate pair of non-zero $Im[\tilde{\sigma}]$ means a pair of counter-propagate waves. For PSS flow, the propagative mode corresponds to Holmboe instability.

Based on whether the imaginary part of growth rate $Im[\tilde{\sigma}]$ are zero or non-zero, figure 3.21(a) can be divided into two part by the transitional point whose stratification factor is defined here as J_t. The $Im[\tilde{\sigma}] = 0$ section corresponding to Kelvin-Helmholtz mode include two branches of $Re[\tilde{\sigma}]$, which later merge together at about $J_t = 0.46$. After the merging point $J_t = 0.46$, a conjugate pair of $Im[\tilde{\sigma}]$ corresponding to Holmboe mode appear at every single J point, meanwhile its $Re[\tilde{\sigma}]$ counterpart become a single merged branch and gradually decrease with increasing J.

As cross shear in terms of ξ is introduced, J_t are pushed towards positive J as shown in figure 3.21(b)-(d) compare to figure 3.21(a). An important outcome from the postponed J_t is that the unstable region once belonged to propagative mode in $\xi = 0$ case translate into stationary mode, e.g. at $J = 0.5$ a conjugate pair of Im[$\tilde{\sigma}$] in $\xi = 0.0$ in figure 3.21(a) becomes Im[$\tilde{\sigma}$]=0 with Re[$\tilde{\sigma}$]$\neq 0$ at in $\xi = 0.5$ cases in figure 3.21(b). In addition, ξ also gradually increase the magnitude of $\tilde{\sigma}$ at J_t. For the propagative mode after J_t, the gradients where $Re[\tilde{\sigma}]$ decrease with J gradually weaken with increasing ξ, leading to nearly constant $Re[\tilde{\sigma}]$ at large ξ, e.g. figure 3.21(d) $Re[\tilde{\sigma}]$.

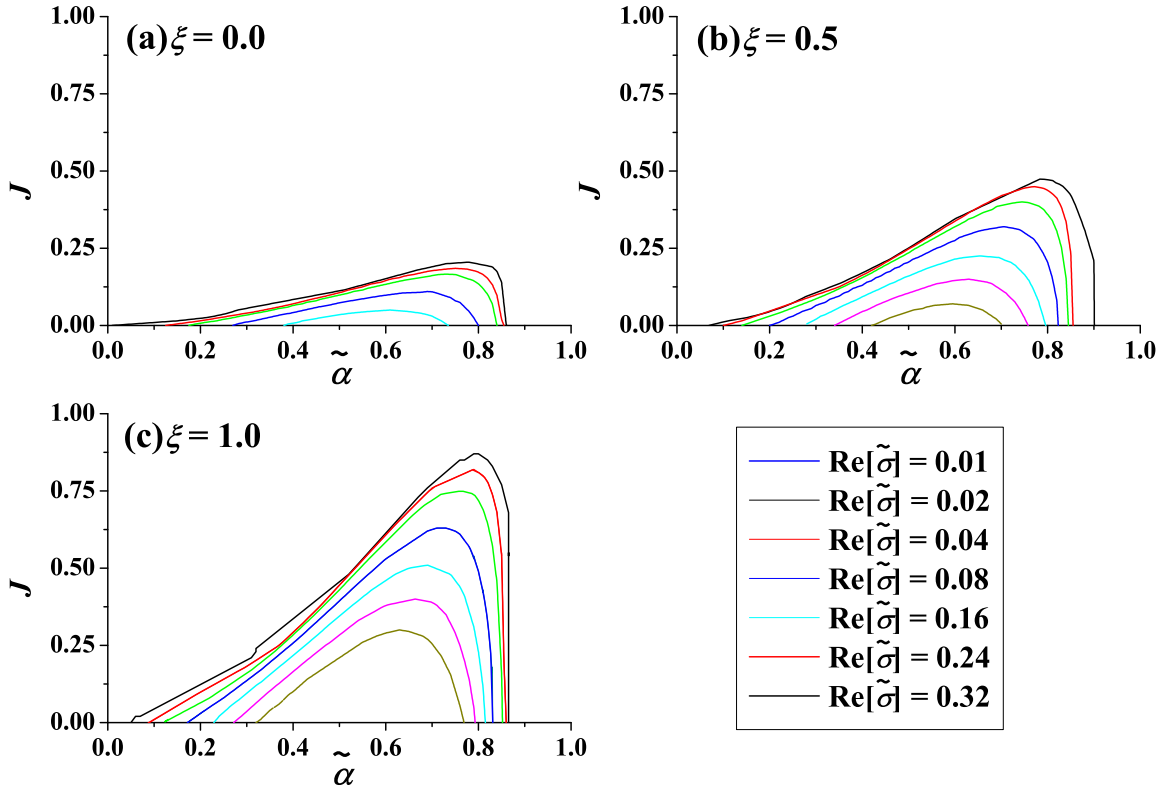

Fig. 3.17 Contours of real part of $\tilde{\sigma}$ in the $J-\tilde{\alpha}$ plane for CSS flows Eq.[3.54] with (a) $\xi = 0$; (b) $\xi = 0.5$; and (c) $\xi = 1.0$, respectively.

The transition from stationary mode to propagative mode also occur as $\tilde{\sigma}$ vary in wavenumber $\tilde{\alpha}$ space, giving the transitional wavenumber α_t. Figure 3.22 shows the dispersion relations between growth rate $\tilde{\sigma}$ and wavenumber $\tilde{\alpha}$ at $J = 0.25$ and $R = 8$ for different ξ. Similar to figure 3.21, transitional behaviors from stationary mode with only non-zero $Re[\tilde{\sigma}]$ to propagative mode with conjugate $Im[\tilde{\sigma}]$ are found in all sub-figures of figure 3.22.

Similar to figure 3.21 where transitional point move towards large stratification factor J, in figure 3.22 α_t move towards large $\tilde{\alpha}$ as ξ increases. Nonetheless, in figure 3.22 the magnitude of $Re[\tilde{\sigma}]$ change differently with increasing ξ compared to those in figure 3.21. For the top branch of stationary mode $Re[\tilde{\sigma}]$ increase significantly with increasing ξ, while for the low branch increase in slower rate. As a result, the increasing ξ enlarge the gap between two $Re[\tilde{\sigma}]$ branches. For the propagative mode after α_t, as α_t grow with increasing ξ, the span of the propagative mode on the wavenumber axis become smaller and smaller with increasing ξ, suggest that the wavenumber regions dominant by propagative mode are suppressed by cross shear in terms of ξ.

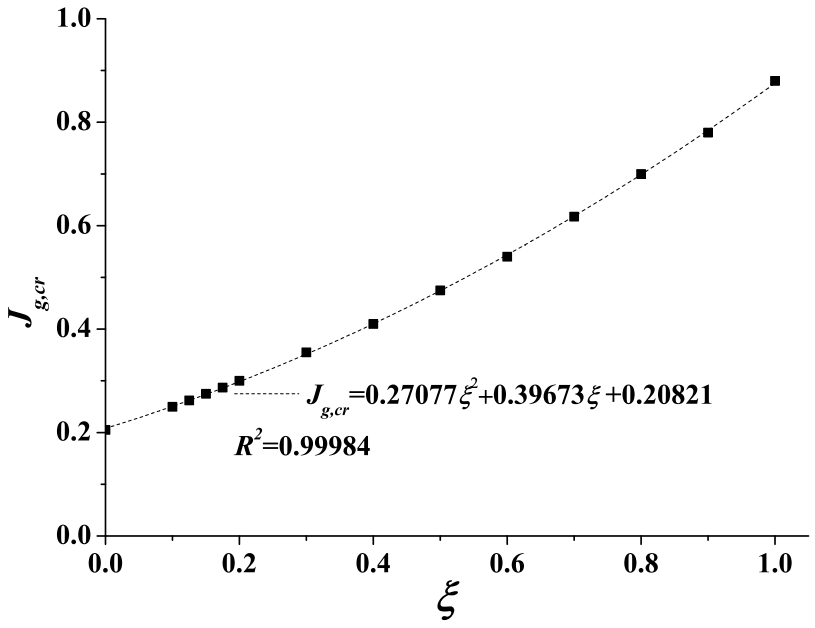

Fig. 3.18 Critical stratification factor J_{cr} plot against cross shear ratio ξ for CSS flows Eq.[3.54]. Dash line represent the parabolic correlation based on numerical results.

The similar transitional behaviors from stationary mode to propagative mode at $R = 8$, as shown in figure 3.21 and figure 3.22, are found in the entire $J \sim \tilde{\alpha}$ space. It is found that every single transitional point corresponds to a pair of critical stratification factor J_t and wavenumber $\tilde{\alpha}_t$, that means every J_t found in $\tilde{\sigma} \sim J$ space corresponds to the only α_{cr} in $\tilde{\sigma} \sim \tilde{\alpha}$ space. Figure 3.23 shows J_t versus $\tilde{\alpha}_t$ at $R = 8$, where three ξ cases with ξ =0.0, 0.5 and 1.0 are represented. As $\tilde{\alpha} < 0.1$, no transitional behaviors are solved, therefore the J_t versus $\tilde{\alpha}_t$ curves in figure 3.23 start from $\tilde{\alpha}_t = 0.1$. $J_t \sim \tilde{\alpha}_t$ curve represent transitional boundary between stationary mode and propagative mode, for the PSS flow it is the transitional boundary between Kelvin-Helmholtz mode and Holmboe mode. As ξ increases, the area covered by $J_t \sim \tilde{\alpha}_t$ curves gradually increases, indicating the unstable regions dominated by stationary mode are extending with increasing ξ. Such expansion of stationary mode concentrate on the small wavenumbers $\tilde{\alpha}_t < 0.7$, where the remarkable gaps among $J_t \sim \tilde{\alpha}_t$ curves at different ξ are observed. At large wavenumbers $\tilde{\alpha}_t > 0.7$, the expansions effects caused by cross shear weaken as the gaps among $J_t \sim \tilde{\alpha}_t$ curves decrease and become even insignificant.

To quantify the expansions of transitional boundary with increasing ξ, figure 3.24 shows J_t vary with continuous ξ at three wavenumber $\tilde{\alpha}$=0.3, 0.5, 0.7, where the continuous expansion trend of $J_t \sim \tilde{\alpha}_t$ curves towards J_t are shown. Notably, parabolic functions between J_t and ξ correlate extremely well with numerical results at three wavenumber. Although

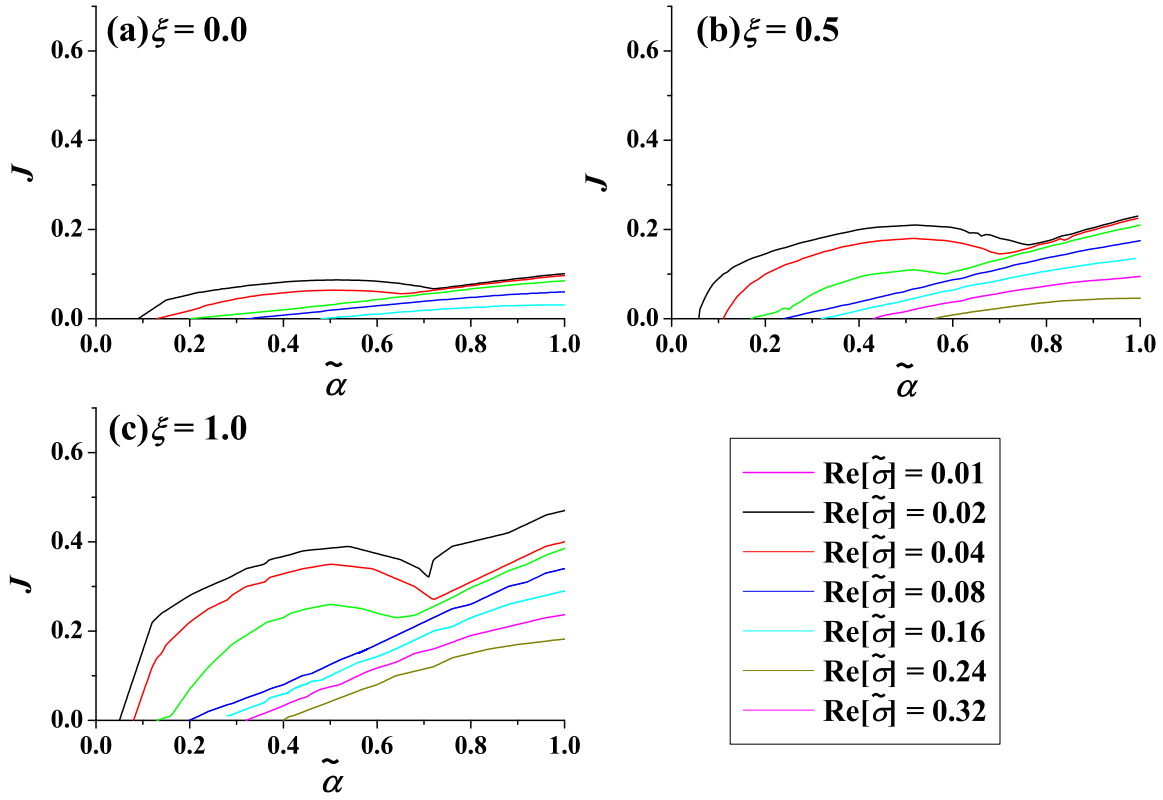

Fig. 3.19 Contours of real part of $\tilde{\sigma}$ in the $J-\tilde{\alpha}$ plane for for CSS flows Eq.[3.56] with (a) $\xi = 0$; (b) $\xi = 0.5$; and (c) $\xi = 1.0$, respectively.

not shown here, same parabolic function also correlate perfectly with numerical results at other wavenumber in the range of $\tilde{\alpha} = 0 \sim 1$. Thus, the entire transitional boundary shown in figure 3.23 above expand in a general parabolic fashion towards positive J_t direction as ξ increases.

Recall that same parabolic fashion governed by cross shear ratio ξ are also found in $J_{cr} \sim \xi$ relation in previous section, where thickness ratio $R = 1$. As both J_{cr} and J_t represent the (transitional) boundary of unstable regions, it is conjectured that ξ might expand the stability boundary of other sheared stratified flow in a parabolic fashion.

3.5.2 Influences of R_s

In this subsection, the influences of R_s will be also considered together with R, so that the different length scale among mainstream shear, cross shear and stratified layer will coexist.

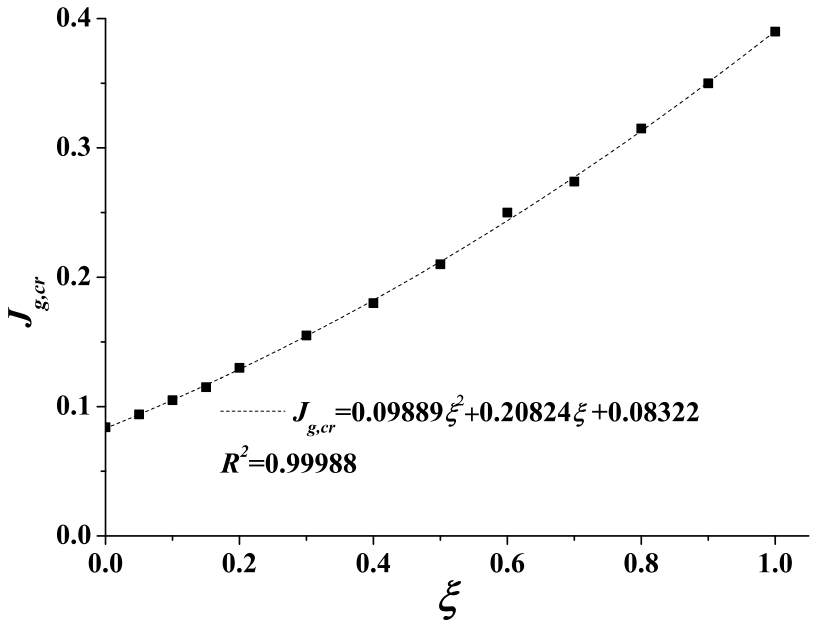

Fig. 3.20 Critical stratification factor J_{cr} plot against cross shear ratio ξ for CSS flows Eq.[3.56]. Dash line represent the parabolic correlation based on numerical results.

The basic flow state including R_s and R becomes:

$$U = tanh(z), \quad V = \xi\, tanh(R_s z), \quad N^2 = J\, sech^2(Rz), \tag{3.59}$$

Similar to 3.4.1, $\xi = 0.5$ will be fixed at 0.5 as a typical value. In $\xi = 0-1$, the features of transitional behaviors found in this subsection are also found.

Figure 3.25 shows the real and imaginary parts of growth rate $\tilde{\sigma}$ plot against stratification factor J axis at different R_s at $\tilde{\alpha} = 0.3$ with $R = 8$. Compare to figure 3.21 whose major controlling parameter is ξ, the transitional stratification factor J_t also move towards positive J direction as R_s increases. However, Re[$\tilde{\sigma}$] at J_t decrease with increasing R_s, in contrast to Re[$\tilde{\sigma}$] at J_t in figure 3.21 where Re[$\tilde{\sigma}$] at J_t increase with increasing ξ. As R_s approach 8, the same value as specific R, the propagative mode nearly vanish as shown in figure 3.25(d), due to the decreasing Re[$\tilde{\sigma}$] with increasing R_s. Such typical transitional behaviors found from figure 3.25(a)-(d), where Re[$\tilde{\sigma}$] at transitional point keep decreasing and even reduce to zero as long as R_s approach specified R, are also observed at wavenumber range $\tilde{\alpha} = 0-1$ and other R values not shown here.

To investigate how the spectrum of J_t on wavenumber space as shown in figure 3.23 changes as R_s approach specified R, figure 3.26 shows J_t plot against $\tilde{\alpha}$ at different R_s. For $R_s < 3$, J_t monotonically decrease with increasing $\tilde{\alpha}$, indicating weak stationary modes at

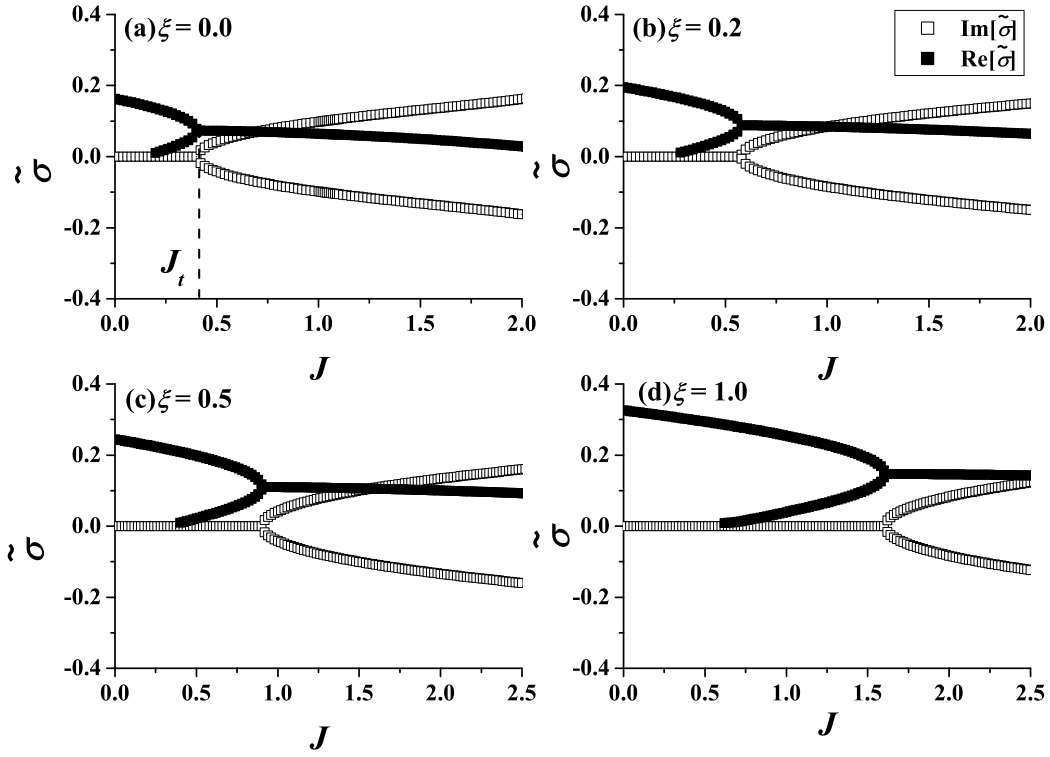

Fig. 3.21 Calculated growth rate $\tilde{\sigma}$ plot against stratification factor J at $\tilde{\alpha} = 0.3$ and $R = 8$ for (a)ξ=0.0, (b)0.2, (c)0.5 and (d)1.0. The solid and void data points represent real and imaginary part of $\tilde{\sigma}$.

large wavenumber. As R_s increase to 4, J_t start to vary with $\tilde{\alpha}$ in a non-monotonic fashion, with its maximum being at $\tilde{\alpha} \approx 0.5$. When R_s increase, J_t at large wavenumber further rise and start monotonically to increase with $\tilde{\alpha}$ at $R_s = 8$, the same value as R fixed here. For the $R_s > 8$ curves though not shown here, the same monotonic increasing trend are found to the $R_s = 8$ curve plotted here. As a result of transitional behavior when R_s increase from 0.2 to 8, significant expansions of transitional boundary denoted by $J_t \sim \tilde{\alpha}_t$ curves are found at large wavenumber range when $\tilde{\alpha} > 0.5$ compared to the expansions at small wavenumber range when $\tilde{\alpha} < 0.4$. Therefore, the expansions of transitional boundary brought by increasing R_s is different from and more complicated than the expansion brought by increasing ξ, where transitional boundary monotonically expand at small wavenumber range $\tilde{\alpha} > 0.7$ as shown in figure 3.23. Although not shown here, the same transitional behaviors from monotonic decreasing to non-monotonic and at last to monotonic increasing observed in figure 3.26 are also found as R_s gradually approach R.

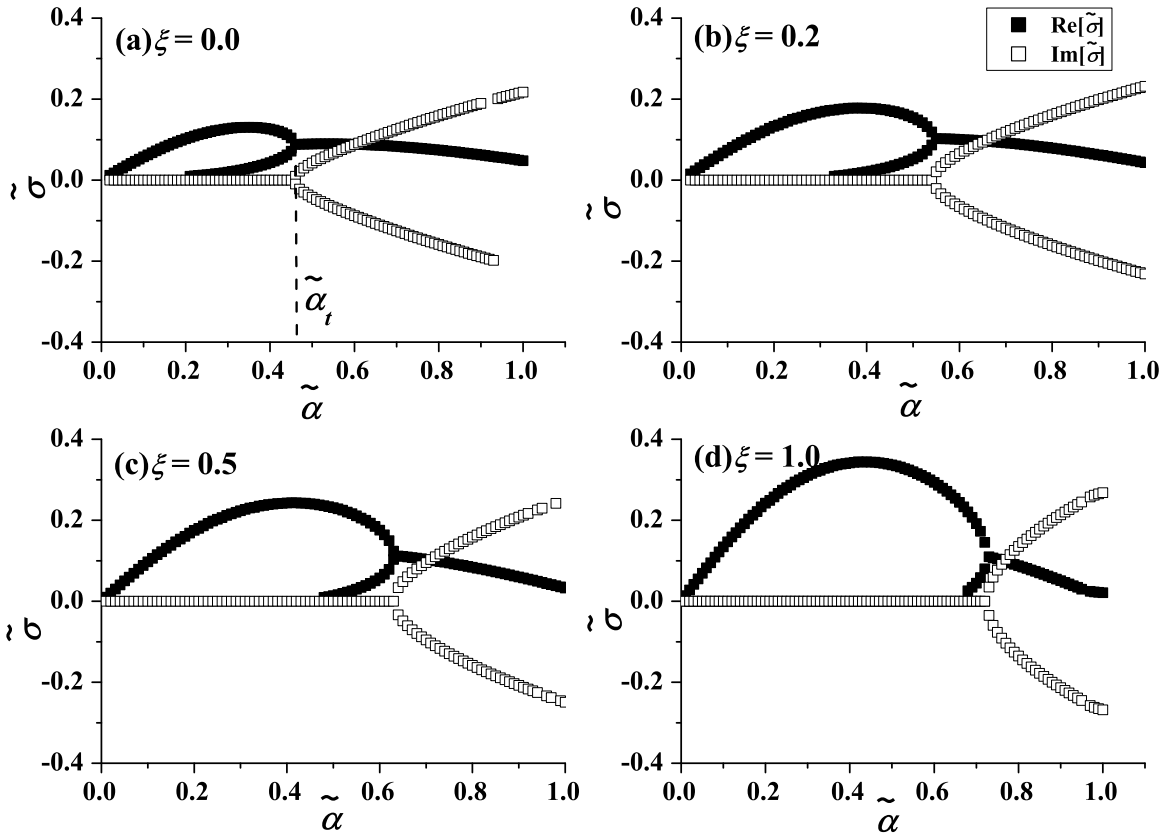

Fig. 3.22 Calculated growth rate $\tilde{\sigma}$ plot against wavenumber $\tilde{\alpha}$ at $J = 0.25$ and $R = 8$ for (a)ξ=0.0, (b)0.2, (c)0.5 and (d)1.0. The solid and void data points represent real and imaginary part of $\tilde{\sigma}$.

To quantify how J_t vary with R_s at different wavenumber $\tilde{\alpha}$ in figure 3.26, figure 3.27 shows J_t plot against continuous R_s at $\tilde{\alpha}$ =0.3, 0.5 and 0.8 with $R = 8$. Generally, non-monotonic variations between J_t and R_s are found at three wavenumber cases. At small R_s range before which three curves start to intersect at $R_s \approx 5$ (marked by 'I'), the magnitudes of J_t at larger $\tilde{\alpha}$ e.g. $\tilde{\alpha} = 0.8$ case are found to be smaller than those at smaller $\tilde{\alpha}$ e.g. $\tilde{\alpha} = 0.3$ case. Such decreasing J_t with increasing $\tilde{\alpha}$ before $R_s \approx 5$ relate to monotonic decreasing $J_t \sim R_s$ curve shown in figure 3.26. After intersection point, the magnitudes of J_t follow the same sequence as their corresponding wavenumber $\tilde{\alpha}$. The transitions before and after intersection point correspond to the transitional behaviors as R_s approach R shown in figure 3.26. In addition, the turning points for three wavenumber curves approximately occur around $R_s = 8$, which is the same value of specific $R = 8$.

After turning points, a flat peak sections (marked by 'II') where J_t vary slightly with R_s are observed. Compare to initial magnitude of J_t at $R_s = 1$, the J_t during these long peak

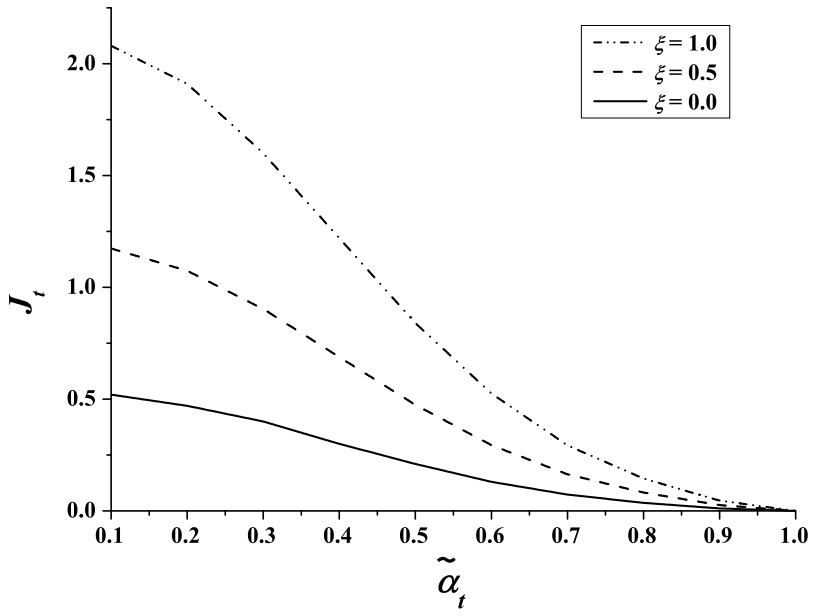

Fig. 3.23 Transitional stratification factor J_t plot against wavenumber $\tilde{\alpha}$ at $R = 8$. The solid line, dash line and dash dot dot line represent the results from $\xi = 0.0$, 0.5 and 1.0 separately.

sections grow significantly, e.g. for $\tilde{\alpha} = 0.3$ the J_t increase from $0.6 \sim 0.7$ at $R_s = 1$ up to $3.2 \sim 3.3$ at $R_s \approx 10$. The maximum growth of J_t seems to occur at $R_s \approx 15 - 20$ which is two to three times of specific $R = 8$. As R_s further increases, J_t monotonically decrease with increasing R_s and further reduce back to the magnitude at $R_s = 1$, indicating that the reducing length scale of cross shear will not unlimitedly expand the unstable regions dominant by stationary mode like what cross shear ratio ξ enhance J_t in 3.5.1.

To further examine if the non-monotonic variations found in figure 3.27 universally exist at other R values, especially if the turning points and maximum points are directly relate to the specific magnitude of R, figure 3.28 shows J_t plot against R_s at three R values and the same wavenumber $\tilde{\alpha} = 0.3$ as plot in figure 3.27. Similar to figure 3.27, non-monotonic fashion are found for three $J_t \sim R_s$ at $R = 5$ and $R = 10$ cases. It is found that as R increases, the position of the turning point for three $J_t \sim R_s$ curves also move towards positive R_s direction. The advancing turning point with increasing R further support that R will determine the turning points of $J_t \sim R_s$ curves. In addition, the gaps among three $J_t \sim R_s$ curves increase significantly after turning points, indicating that increasing R or decreasing length scale of stratified layer will further expand the unstable regions dominated by stationary mode based on available expansion effects by R_s

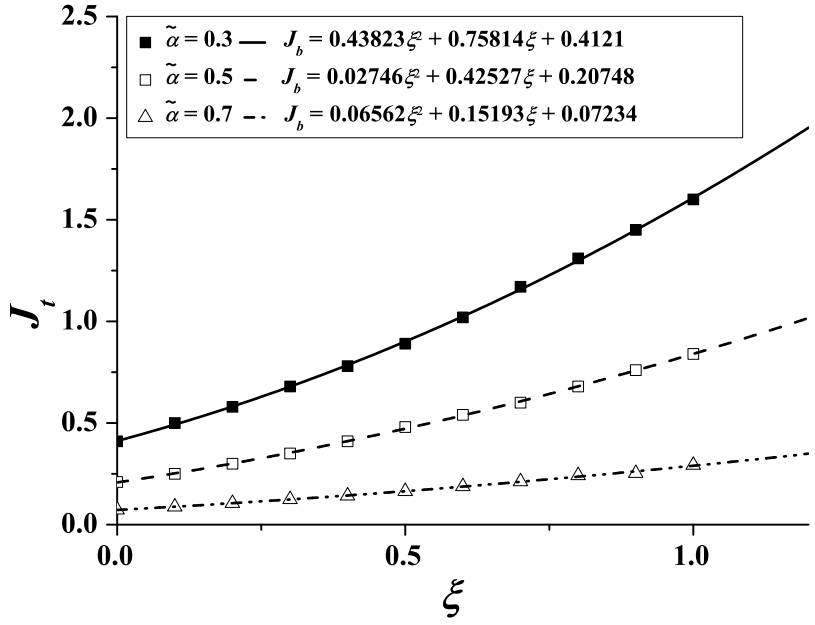

Fig. 3.24 Transitional stratification factor J_t plot against ξ at $\tilde{\alpha}$= 0.3 (solid point), 0.5(void point) and 0.7(triangle point), with relevant parabolic correlation represented by solid line, dash line and dash dot dot line.

3.6 Discussion and conclusions

This study derived a linear perturbation equations 3.42 for the CSS flow. As assumed in this paper, if streamwise basic velocity component U and spanwise component V share the same hyperbolic profile, V can be denoted by ξU, so that 3.42 becomes:

$$\tilde{\sigma}\begin{bmatrix} \nabla_s^2 & \\ & I \end{bmatrix}\begin{bmatrix} \hat{w} \\ \tilde{b} \end{bmatrix} = \begin{bmatrix} -i\tilde{\alpha}(1+\xi\frac{\beta}{\alpha})(U\nabla_s^2 - U_{zz}) & \frac{\tilde{\alpha}^2}{Fr^2} \\ \tilde{N}^2 & -i\tilde{\alpha}(1+\xi\frac{\beta}{\alpha})U \end{bmatrix}\begin{bmatrix} \hat{w} \\ \tilde{b} \end{bmatrix}, \quad (3.60)$$

where if either ξ or wavenumber ratio β/α is zero, the 3.60 will reduce to the Taylor-Goldstein equation. Based on 3.60, the cross shear ratio ξ (same as wavenumber ratio β/α) will play as linear amplifier for the diagonal elements, which determine the magnitude of $Re[\tilde{\sigma}]$. The coefficient $1+\xi(\beta/\alpha)$ is the source of all the stability features involving ξ in this study. Rather than ξ which directly indicate the amplifications of shear effect, the other new parameter R_s indicate the length scale where 3.60 are valid, as cross shear will not exist beyond the cross shear layer with thickness of R_s. Therefore, ξ and R_s are two governing parameters that directly relate to the perturbation equations regardless of any specific basic flow states.

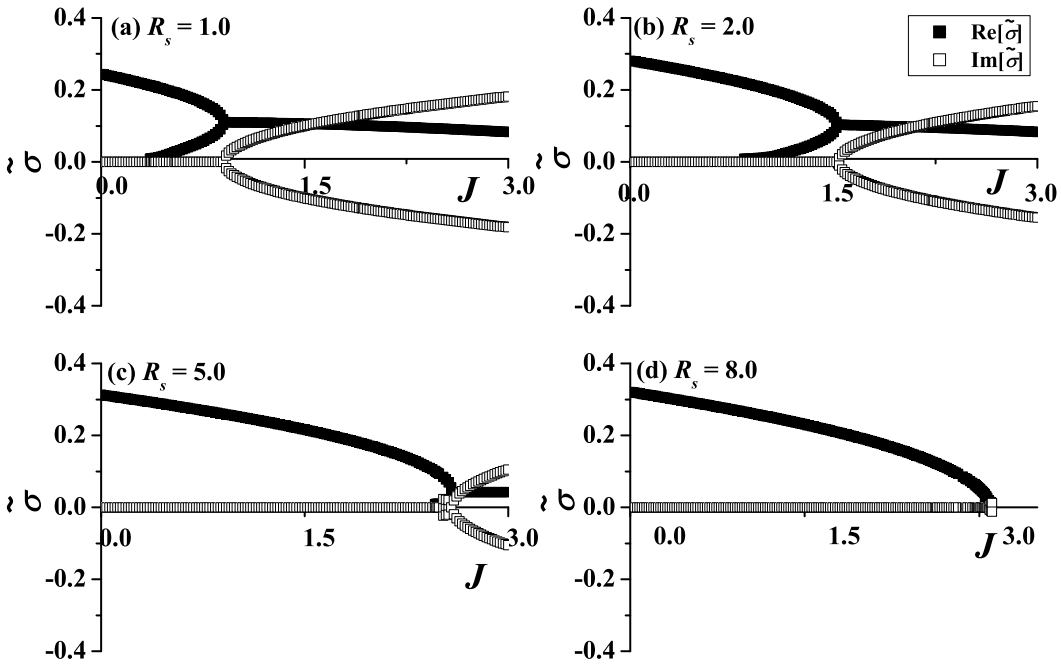

Fig. 3.25 Calculated growth rate $\tilde{\sigma}$ plot against stratification factor J at $\tilde{\alpha} = 0.3$ and $R = 8$ for (a)R_s=1.0, (b)2.0, (c)5.0 and (d)8.0. The solid and void data points represent real and imaginary part of $\tilde{\sigma}$.

The common linear stability features corresponding to the influences of ξ and R_s, are found among different CSS flow configurations. The common features for ξ effects are represented by significant boundary expansion of unstable regions and remarkable increase of the growth rate Re[$\tilde{\sigma}$] with increasing ξ. The boundary expansions and increase of Re[$\tilde{\sigma}$] inside are further quantified by parabolic function between critical stratification factor J_{cr} and ξ, and the linear functions between $\tilde{\sigma}$ and ξ. As the growth gradient $\partial\tilde{\sigma}/\partial\xi$, which corresponds to the coefficients of linear correlations, are distributed along wavenumber $\tilde{\alpha}$ axis, a new dispersion relation between gradient $\partial\tilde{\sigma}/\partial\xi$ and $\tilde{\alpha}$ are established to describe how ξ would expand Re[$\tilde{\sigma}$] in wavenumber space for CSS flows. In this new dispersion relation, the general non-monotonic shape are found such as those shown in figure 3.6, whose profiles seem the extensions of the $\tilde{\sigma} \sim \tilde{\alpha}$ dispersion curve.

On the other hand, the common features of R_s effects on different CSS flows are well illustrated by two branches observed in $J \sim \tilde{\alpha}$ space, e.g. in figure 3.9. The left branch at

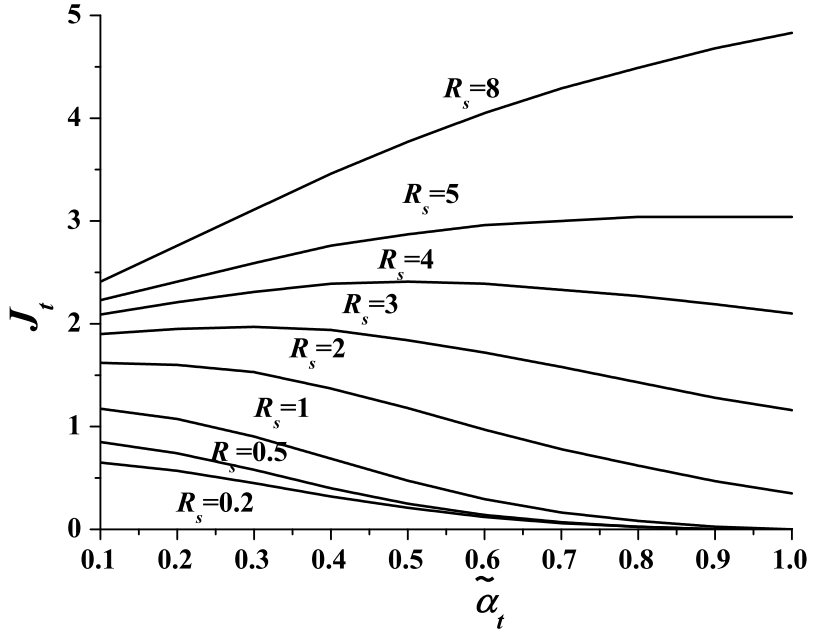

Fig. 3.26 Transitional stratification factor J_t plot against $\tilde{\alpha}$ at $R = 8$. The R_s values are marked for corresponding curves.

small wavenumber behave as the envelop of R_s dispersion curve family which restrict the growth of $\tilde{\sigma}$ with increasing R_s. The restrictions from the left envelop branch are represented by widely observed asymptotic behaviors in $\tilde{\sigma} \sim R_s$ plot shown in figure 3.9. Moreover, the right branch at large wavenumber behave as major expanding front with increasing R_s for the unstable regions, which develop its domain in both J and $\tilde{\alpha}$ axis. Such stronger dual expansions lead to parabolic functions between the critical wavenumber $\tilde{\sigma}_{cr}$ as well as critical stratification factor J_{cr} and varying R_s.

The influences of ξ and R_s on transitions from stationary mode to propagative mode, when the length scale of stratified layer are smaller than the length scale of shear layer once $R > 1$, are also investigated in hyperbolic stratified environment. It is found that the transitional boundary denoted by $J_t - \tilde{\alpha}_t$ curve significantly expand at small wavenumber range $\tilde{\alpha} < 0.7$ but grow slowly at large wavenumber range $\tilde{\alpha} > 0.7$. The expansion of transitional boundary with increasing ξ are further quantified by parabolic functions between J_t and ξ. For influences of R_s, it is observed that the transition stratification factor J_t also increase with increasing R_s, but the unstable regions for propagative mode reduce significantly as R_s increases.

It is further found that when the magnitudes of R_s gradually approach and exceed specified R, the transitional boundary denoted by $J_t - \tilde{\alpha}_t$ curve transit from monotonically

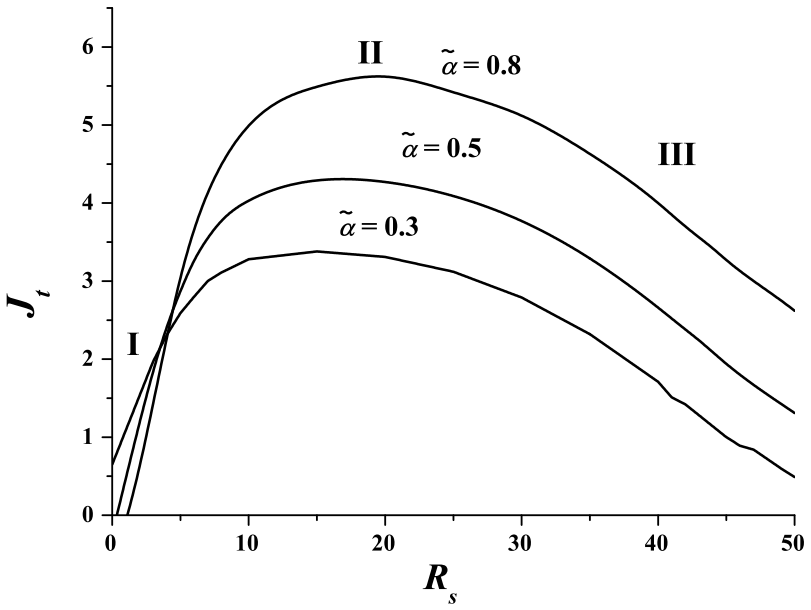

Fig. 3.27 Transitional stratification factor J_t plot against R_s at $R = 8$ and $\tilde{\alpha}$ =0.3, 0.5 and 0.8. The magnitude of $\tilde{\alpha}$ are marked for corresponding curves.'I', 'II' and 'III' represent different growth stage of non-monotonic $J_t \sim R_s$ curves.

decreasing function to monotonically increasing function. As a result of such transitional behaviors, significant expansions of transitional boundary are found at large wavenumber range $\tilde{\alpha} > 0.5$. The transitional behaviors when R_s approach specified R also lead to non-monotonic variations between J_t and R_s at different $\tilde{\alpha}$. The turning points of such non-monotonic $J_t \sim R_s$ functions relate to specified R. At other R cases, the same non-monotonic $J_t \sim R_s$ variations are observed and the dependence of turning point position on R values are observed as well.

There are several interesting implications from stability analysis results in this study. Firstly, ξ and R_s substantially increase the growth rate $\tilde{\sigma}$ at both unstratified cases ($J = 0$) and stratified cases $J \neq 0$, therefore the cross shear is expected to accelerate the transition to turbulence. This has been partly confirmed by experimental study from [9], who found the faster transition to turbulence when cross shear is introduced by tilting the water tank towards spanwise direction. Secondly, ξ and R_s will significantly extend the Miles-Howard theorem values, so that even at large stratification conditions the CSS flows will be very sensitive to unstable mode, which is a very interesting point that will be studied in the future. In some experimental and numerical study, the stationary instability modes are observed when $Ri > 0.25$, it is possible that this deviations of $Ri_{cr} = 0.25$ might be caused by inevitably local or weak cross shear in actual three-dimensional flows. Thirdly, as the transitional boundary

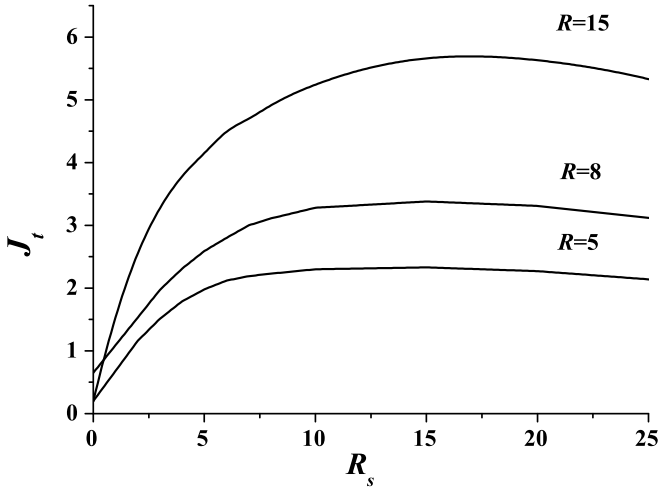

Fig. 3.28 Transitional stratification factor J_t plot against R_s at $\tilde{\alpha} = 0.3$ and R =5, 8 and 15. The magnitude of R are marked near corresponding curves.

in terms of $J_t \sim \tilde{\alpha}_t$ expand by increasing ξ and R_s, it is possible that the condition where propagative mode such as Holmboe instability occur in PSS flow, will be transferred into condition where stationary mode dominate once the cross shear are introduced. Such reverse transitions from propagative mode to stationary mode induced by cross shear are suggested to be further studied by numerical simulations.

References

[1] TAYLOR, G. I. 1931 Effect of variation in density on the stability of superposed streams of fluid. *Proc. Roy. Soc. London Ser. A.* **132**, 499–523.

[2] GOLDSTEIN, S. 1931 On the stability of superposed streams of fluids of different densities. *Proc. Roy. Soc. London Ser. A.* **132**, 524–548.

[3] MILES, J. W. 1961 On the stability of heterogeneous shear flows. *J. Fluid Mech.* **10**(4), 496–508.

[4] HOWARD, L. N. 1961 Note on a paper of John W. Miles. *J. Fluid Mech.* **10**(4), 509–512.

[5] HAZEL, P. 1972 Numerical studies of the stability of inviscid stratified shear flows. *J. Fluid Mech.* **51**, 39–61.

[6] HOLMBOE, J. 1962 On the behavior of symmetric waves in stratified shear layers. *Geophys. Publ.* **24**, 67–113.

[7] SMYTH, W. D. & PELTIER W. R. 1989 The transition between Kelvin-Helmholtz and Holmboe instability: an investigation of the overreflection hypothesis *J. Atmo. Sci.* **46**, 3698–3720.

[8] BAINES, P. G. & MITSUDERA, H. 1994 On the mechanism of shear flow instabilities. *J. Fluid Mech.* **276**, 327–342.

[9] ATSAVAPRANEE, P. & GHARIB, M. 1997 Structures in stratified plane mixing layers and the effects of cross-shear. *J. Fluid Mech.* **342**, 53–86.

[10] LIN, J., SHAO, X. & YU, Z. 2000 Numerical research on coherent structures in a mixing layer with cross-shear. *Acta Aeronautica et Astronautica Sinic* **21**(1), 13–20.

[11] DRAZIN, P. G. & REID, W. H. 2004 *Hydrodynamic Stability* (second edition). Cambridge University Press.

[12] SQUIRE, H. B. 1933 On the stability of three-dimensional disturbances of viscous flow between parallel walls. *Proc. Roy. Soc. London Ser. A.* **142**, 621–628.

[13] MOLER, C. B. & STEWART, G. W. 1973 An algorithm for generalzied matrix eigenvalue problems. *SIAM J. Numer. Anal.* **10**, 241–256.

[14] SMYTH, W. D., MOUM, D. J. & NASH, J. D. 2011 Narrowband, high-frequency oscillations at the equator. Part II: Properties of shear instabilities. *J. Phys. Oceanogr.* **41**, 412–428.

[15] LIU, Z., THORPE, S. A. & SMYTH, W. D. 2012 Instability and hydraulics of turbulent stratified shear flows. *J. Fluid Mech.* **695**, 235–256.

[16] THORPE, S. A., SMYTH, W. D. & LI, L. 2013 The effect of small viscosity and diffusivity on the marginal stability of stably stratified shear flows. *J. Fluid Mech.* **731**, 461–476.

Chapter 4

Instability and coherent structures in weakly CSS flows

The results of this chapter are presented in the following publications:

1. XIAO, Y., LIN, W., MCCORMARC, J., ARMFIELD, S. W., KIRKPATRICK, M. P. & HE, Y. 2014 Coherent structures in cross sheared flows in weakly stratified environments. in *Proceedings of the 19th Australasian Fluid Mechanics Conference (19AFMC)*, 8-11 December 2014, Melbourne, Australia, Paper ID: 084.

2. XIAO, Y., LIN, W., MCCORMARC, J., ARMFIELD, S. W., KIRKPATRICK, M. P. & HE, Y. 2017 Instability and coherent structures of primary cross sheared flows in weakly stratified environment. *Journal of Fluid Mechanics*, under review (in re-submission).

4.1 Introduction

For many flows, transitions from laminar basic flows to turbulence can be divided in to five stages: receptivity, linear growth, nonlinear saturation (primary instability), secondary instability and breakdown [1]. Therefore, knowledge of these primary instabilities associated with dependent secondary instabilities will provide a good understandings of turbulence transitions [1]. The understandings of primary and secondary flow coherent structures also enables effective design and control of many environmental and engineering systems involving turbulent mixing [2].

A sheared stratified flow is a fundamental flow configuration in which the fluid motion with a mean velocity shear develops in a stably stratified environment. As a representative of

geophysical flows that occur inherently in stratified environments, sheared stratified flows prevail in meso-scale geophysical flows (*e.g.* the planetary or oceanic boundary layers), large-scale stream flows (*e.g.* rivers and estuaries), large water bodies (*e.g.* reservoirs and lakes), and engineering applications (*e.g.* mixing control in solar ponds and methane gas mixing in mine shafts) [3]. The mixing processes in sheared stratified flows have profound significance in air quality, water quality, biological and ecological systems, etc., as they modify the heat/mass transfer processes that determine the mixing processes in atmospheres, oceans, rivers and other ecological and engineering systems [4].

So far, the majority of the studies on sheared stratified flow have been largely inspired by the early linear stability analysis on the parallel sheared stratified (PSS) flow, a two-dimensional basic laminar flow states whose velocity components in the Cartesian coordinates satisfy $V \ll U$, where U and V are the streamwise and spanwise components of the horizontal basic flow velocity in the x and y directions. The linear stability analysis on PSS flows was initiated by [5] and [6], who derived the Taylor-Goldstein (TG) equation, which describes the hydrodynamics linking the velocity shear and convective flux. By solving the TG equation, [7] and [8] further established the classical Miles-Howard theorem, in which the gradient Richardson number less than 0.25 becomes the critical condition for a stationary instability mode under infinitesimal perturbations. Such an instability mode corresponds to the Kelvin-Helmholtz (KH) instability. By considering the ratio between the sheared layer thickness and the stratified layer thickness, [9] used a numerical method to solve the TG equation and obtained the other instability mode, the Holmboe instability, firstly observed by [10].

On the basis of the early linear stability analysis results, considerable experimental and numerical efforts have been made which are able to provide more structural details and non-linear dynamics than linear stability analysis is. With specific perturbations being imposed, typical coherent structures, especially the KH eddy structures, have been produced in laboratory experiments and numerical simulations. The typical coherent KH instability structures consist of central 'cat eye' (or roller or billow in some literature) shaped streamwise eddies and peripheral long 'braid' (or rib in some literature) structures that connect two adjacent 'cat eye' eddies. The early study on three-dimensionalization of KH instability commence from stability analysis based on developed primary two-dimensional KH 'cat eye' eddy, *e.g.* [11–13]. Subsequently, three-dimensional numerical studies are conducted by [14] and [15], who investigated more structure details of three-dimensional 'braid' structures and pairing process. The experimental works such as [16] and [17] further observed more complicated three-dimensional dynamics of the KH instability. Recently, the study of the KH coherent structures has been further elaborated by consideration of, *e.g.* secondary instabilities of KH mode in stratified environment [18–20] and in high Reynold number

[21–25], mixing efficiency at moderately stratified environment [26, 27, 20, 28, 29, 25], micro-scale anisotropy and characteristic length scales [30], and other important issues that further extend and enrich the understanding of the dynamics of the KH instability and its ensuing transition to turbulence.

However, in geophysical, environmental and engineering scenarios, the shear stratified flow sometimes inevitably develops from a three-dimensional basic laminar flow state, where the spanwise basic velocity V and associated bulk spanwise shear are comparable to the streamwise counterparts U. Such three-dimensional basic flow might occur, for instance, when misalignments of velocity shear in two layer flow system or in oblique boundary layer flow system with a significant horizontal extend. In two layer flow system, a perfect alignment between top velocity U_t and U_b is usually assumed in previous theoretical and numerical studies, therefore suggesting a two-dimensional basic flow profile as shown in the left graphic of figure 4.1. Nonetheless, as shown in the right graphic of figure 4.1, the top flow velocity might also misalign with the bottom flow velocity in the example of estuary system where several river stream merge together. The introduced misaligned angle between U_t and U_b induce a cross velocity component $U_{b,y}$ and therefore form a three-dimensional basic flow state. The influences of misaligned angle in unstratified two layer flow system was studied numerically by [31] (abbreviated to LSY00 hereafter). The other circumstance where three dimensional basic flows exist is the two layer flow system with oblique boundary such as continental shelf system, where an oblique boundary shear flow are formed perpendicular to the main streamwise current due to gravity. [32] (abbreviated to AG97 hereafter) create such oblique boundary flow in laboratory with a special water tank system which enable water tank tilt in both streamwise and spanwise direction. They defined the spanwise bulk shear as 'cross shear' and considered the relative intensity of cross shear to streamwise shear as major parameter. By tilting a water tank in the spanwise direction, they produced cross shear stresses as soon as the first streamwise KH billows were captured. In addition, the cross shear due to misalignment in basic flow could also involve reflected flow near coastal topography, two merging ocean currents, and counter flows in estuaries and in multi-port reservoirs. The cross shears, either in large or small length scale, strong or weak, also inherently reside in other physical processes such as convective heat transfer and chemical processes such as dissolution processes.

Interestingly, in spite of different mechanisms applied to create a three dimensional basic flow states, LSY00 and AG97 observed common incidences of spanwise coherent eddy structures similar to well-known streamwise KH 'cat eye' eddy. In addition, both studies found the new born spanwise flow structures remarkably prompt turbulent mixing. By increasing the misaligned angle in LSY00 and elevating the tilting angle in AG97, it is

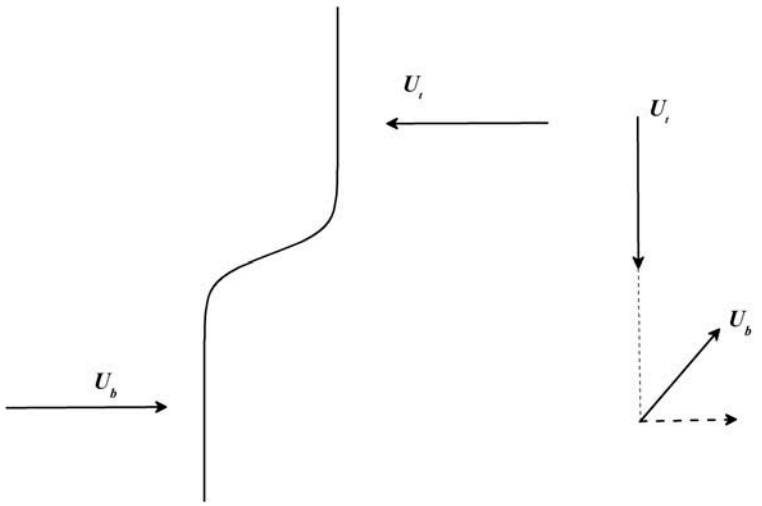

Fig. 4.1 Schematic of misalignment between top layer velocity U_t and bottom layer velocity U_b in two layer flow system.

further found that turbulent mixing even become stronger. The fascinating phenomena and mixing features found in LSY00 and AG97 motivate this study to back to the theoretical origin, that is, the basic shear stratified flow state, which has been usually considered as two-dimensional flow in nearly all previous hydrodynamics, numerical and experimental studies. As a deviation from substantial studies focusing on PSS flow where only streamwise basic velocity component U exists, this study will officially consider a three-dimensional shear stratified basic flow states with comparable basic streamwise velocity component U and spanwise velocity components V in Cartesian system, namely, cross shear stratified (CSS) flow. This definition enables theoretical convenience especially a hydrodynamic stability analysis on CSS flow, as different types of U and V profiles can be adapted in theoretical analysis. Accordingly, the spanwise bulk flow shear induced by V is called the cross shear and the ratio between spanwise and streamwise bulk flow shear is called cross shear ratio, defined by ξ in this paper.

As CSS flow is a three-dimensional basic flow configuration, the initial perturbations will develop based on not only streamwise basic flow but also spanwise basic flow, therefore forming three-dimensional primary structures. This conjecture is supported by AG97 and LSY00, both of which observed spanwise coherent eddies coexisting with streamwise KH 'cat eye' eddies at the onset of evolution of flow structures. However, the knowledge of three-dimensional primary CSS flow structures and their dependence on ξ are still in blank, even for the flow structures in a simplest single wavelength domain as setup in numerical study of LSY00. Firstly, the critical conditions in terms of ξ for the occurrence of spanwise eddy

structures in CSS flows and the mechanisms involved in the interaction between the spanwise and streamwise structures are still unknown. Furthermore, a comprehensive perspective of coherent structures is still unclear, as the information presented in AV97 and LSY00 are rather fragmentary and preferable to condition where the ratio of the spanwise velocity and the streamwise velocity is much less than 1. Current study will not only reproduce the spanwise eddies of LSY00 using direct numerical simulation (DNS) results, but also provide a comprehensive view of the three-dimensional primary coherent structures in CSS flows, by significantly extending the ratio ξ of the spanwise velocity and the streamwise velocity (to 1) and by investigating the influences of ξ on these flow structures.

Before the detailed investigations on primary coherent structures in CSS flow, however, an issue of great importance should be clarified first is the increasing number of potential primary instabilities and the massive number of dependent secondary instabilities in CSS flow, if the parameter space is unrestricted at all in the study. Due to extended parameter space by the new introduced parameter ξ in the shear stratified flow system, the number of potential primary instabilities in CSS flow is expected to be extended. As will be shown later, for CSS flow there are three types of primary flow structures being found in terms of not only the intensity of ξ but also the features of coherent structures. The existences of three CSS flow primary instabilities suggest the secondary instabilities dynamic features will much more complicated if the other parameter ranges are further expand in the same way as previous PSS flow studies summarized in [24] and [25], in which a number of secondary instabilities of KH mode and their critical conditions rely on different domain size (single or multiple wavelength of the most unstable mode), Reynold number, Pradtle number and Richardson number. Based on rich content of secondary instabilities derived from the only two-dimensional primary KH mode, it is formidable for this study to adapt the parameter range at the same level as what have been included in PSS flow studies for past decades, to the three-dimensional primary CSS modes. To avoid entangling into vast sea of potential secondary instabilities in CSS flow, this study will intentionally limit the parameter space and set up a 'clean' numerical environment to eliminate any potential secondary instabilities based on previous experience of PSS flow studies, so as to only focus on the primary instabilities which exclusively rely on ξ in the CSS flow. Such an initial step will help our further understanding of how the secondary instabilities of CSS flow are developed based on the primary CSS modes found here, as well as understanding of the roles of other parameter in addition to ξ.

To achieve this purpose, this study will limit the domain in a single wavelength of one of the most unstable modes (See 3 for more information) and reduce the influences of background stratification by setting initial bulk Richardson number at $Ri = 0.01$. The choice of single wavelength aims to suppress the pairing process in shear dominant environment,

as pairing inevitably involve secondary instabilities which require the preliminary understandings of primary instabilities in single wavelength domain. The limitations of single wavelength domain were also applied by early three-dimensional numerical study on PSS flow such as [14]. On the other hand, the choice of weakly stratified environment aims to emphasize the cross shear dynamics without involving many dynamics from buoyancy. Meanwhile such weakly stratified environment will also allow the potential correlations between current numerical studies and the only experiment studies reported by AG97, which also conducted their CSS flow experiments in small *Ri* number environment. Thirdly, the weakly stratified environment also suppress some potential secondary instabilities induced by stronger buoyancy, which might be similar to the secondary shear convective secondary instability developed from primary KH instability in moderate stratified environment. We believe that the fundamental and primary dynamic features induced by ξ found in this study will significantly help the future study considering pairing and stronger stratified environment.

The remainder of this chapter is organized as follows. The methodology for the DNS study of CSS flows is described in § 4.2, together with the description of the perturbations imposed on the initial conditions and the PUFFIN code used for DNS. A detailed description of the DNS results, including the observed coherent structures in three different CSS flow instability modes, in terms of the density concentration and the spanwise and streamwise vorticities, is presented in § 4.3. Various kinetic and potential energies and their budget, as well as the mixing effect in CSS flows, are also presented in this section. Finally, the main conclusions from this chapter are drawn and discussed in § 4.4. 4.5 will show the kinetic energy budget test results to support the solidity of our DNS results.

4.2 Numerical methodology

The governing equations for DNS are the continuity, Navier-Stokes, and density equations for incompressible viscous flows with the Boussinesq approximation, which are written in the Cartesian coordinates (x_*, y_*, z_*) as follows,

$$\nabla_* \cdot \mathbf{u}_* = 0, \tag{4.1}$$

$$\frac{\partial \mathbf{u}_*}{\partial t_*} + \mathbf{u}_* \cdot \nabla_* \mathbf{u}_* = -\frac{1}{\bar{\rho}_*} \nabla_* p_* - \frac{g(\rho_* - \bar{\rho}_*)}{\bar{\rho}_*} \vec{k} + \nu \nabla_*^2 \mathbf{u}_*, \tag{4.2}$$

$$\frac{\partial \rho_*}{\partial t_*} + \mathbf{u}_* \cdot \nabla_* \rho_* = \kappa \nabla_*^2 \rho_*, \tag{4.3}$$

where the subscript '*' denotes the dimensional quantities, $\mathbf{u}_*$ is the velocity vector with the components (u_*, v_*, w_*) in the Cartesian coordinates (x_*, y_*, z_*), p_* is pressure, ρ_* is density, $\bar{\rho}_*$ is the reference density, t_* is time, g is the acceleration due to gravity which is in the negative z_* direction, ν and κ are the kinematic molecular viscosity and the thermal diffusivity of fluid, and the operators ∇_* and ∇_*^2 are

$$\nabla_* = \frac{\partial}{\partial x_*}\vec{i} + \frac{\partial}{\partial y_*}\vec{j} + \frac{\partial}{\partial z_*}\vec{k}, \quad \nabla_*^2 = \frac{\partial^2}{\partial x_*^2} + \frac{\partial^2}{\partial y_*^2} + \frac{\partial^2}{\partial z_*^2},$$

in which $\vec{i}$, $\vec{j}$ and $\vec{k}$ represent the unit vector in x_*, y_* and z_* directions.

The above governing equations (4.1)-(4.3) can be dimensionalized as follows,

$$\nabla \cdot \mathbf{u} = 0, \tag{4.4}$$

$$\frac{\partial \mathbf{u}}{\partial t} + \mathbf{u} \cdot \nabla \mathbf{u} = -\frac{1}{\bar{\rho}}\nabla p - (c - 0.5) Ri_0 \vec{k} + \frac{1}{Re_0}\nabla^2 \mathbf{u}, \tag{4.5}$$

$$\frac{\partial \rho}{\partial t} + \mathbf{u} \cdot \nabla \rho = \frac{1}{PrRe_0}\nabla^2 \rho, \tag{4.6}$$

where the dimensional quantities are made dimensionless using their respective characteristic scales, *i.e.* ,

$$\mathbf{x} = \frac{\mathbf{x}_*}{\delta_s}, \quad t = \frac{t_* \Delta u_0}{\delta_s}, \quad \mathbf{u} = \frac{\mathbf{u}_*}{\Delta u_0}, \quad p = \frac{p_*}{\Delta \rho_0 (\Delta u_0)^2}, \quad \rho = \frac{\rho_*}{\Delta \rho_0}, \quad \bar{\rho} = \frac{\bar{\rho}_*}{\Delta \rho_0}, \tag{4.7}$$

in which δ_s, Δu_0 and $\Delta \rho_0$ are the characteristic length, velocity and density scales, respectively, which are the dimensional thickness of the effective sheared layer based on the streamwise velocity profile of the basic flow, and the dimensional initial velocity and density changes across δ_s, as will be detailed later, $\mathbf{x}$ is the dimensionless coordinate vector $(x\vec{i} + y\vec{j} + z\vec{k})$, $\mathbf{u}$ is the dimensionless velocity vector $(u\vec{i} + v\vec{j} + w\vec{k})$, t is the dimensionless time, p is the dimensionless pressure, ρ is the dimensionless density, $\bar{\rho}$ is the dimensionless reference density, and the dimensionless operators ∇ and ∇^2 are

$$\nabla = \frac{\partial}{\partial x}\vec{i} + \frac{\partial}{\partial y}\vec{j} + \frac{\partial}{\partial z}\vec{k}, \quad \nabla^2 = \frac{\partial^2}{\partial x^2} + \frac{\partial^2}{\partial y^2} + \frac{\partial^2}{\partial z^2}.$$

Re_0 is the initial bulk Reynolds number, which represents the relative importance of inertial forces to viscous forces in the flow, Ri_0 is the initial bulk Richardson number, which quantifies the relative importance of shear effects to stratification effects, and Pr is the Prandtl number, which denotes the relative importance of momentum diffusivity to thermal diffusivity. These

three dimensionless numbers dictate the stability of the flow, and are defined as follows:

$$Re_0 = \frac{\Delta u_0 \delta_s}{\nu}, \quad Ri_0 = \frac{g\Delta\rho_0\delta_s}{\bar{\rho}(\Delta u_0)^2}, \quad Pr = \frac{\nu}{\kappa}. \tag{4.8}$$

c in (4.5) is the dimensionless density concentration, which is used to describe the density field and is defined as follows,

$$c = \frac{\rho_* - \rho_1}{\rho_2 - \rho_1}, \tag{4.9}$$

where $\rho_1 = \bar{\rho}_* - 0.5\Delta\rho_0$ and $\rho_2 = \bar{\rho}_* + 0.5\Delta\rho_0$.

The following typical dimensionless velocity and density profiles for free shear flows are used for the DNS runs of CSS flows,

$$u_0 = tanh\left[2(z - \frac{1}{2}L_z)\right], \tag{4.10}$$

$$v_0 = \xi tanh\left[2(z - \frac{1}{2}L_z)\right], \tag{4.11}$$

$$\rho_0 = tanh\left[2(z - \frac{1}{2}L_z)\right], \tag{4.12}$$

in which the subscript '0' denotes the initial magnitude of the parameter, L_z is the size of the computational domain in the vertical direction (z direction) which is made dimensionless by δ_s, and ξ, called the cross shear ratio, is the ratio of the dimensional spanwise velocity change to the dimensional streamwise velocity change, both across the initial sheared/stratified layer. u_0, v_0, and ρ_0 are made dimensionless by Δu_0 and $\Delta\rho_0$, respectively.

To initiate the formation of coherent structures, the following perturbations used by [33] are imposed on the initial conditions, aiming to excite the primary and secondary instabilities,

$$u_{pri} = -0.02cos\left(\frac{2\pi x}{L_x}\right) sech\left[2(z - \frac{1}{2}L_z)\right] tanh\left[2(z - \frac{1}{2}L_z)\right], \tag{4.13}$$

$$v_{pri} = -0.02cos\left(\frac{2\pi x}{L_x}\right) sech\left[2(z - \frac{1}{2}L_z)\right] tanh\left[2(z - \frac{1}{2}L_z)\right], \tag{4.14}$$

$$u_{ran} = 0.1\left\{1 - \left|tanh\left[2(z - \frac{1}{2}L_z)\right]\right|\right\} r_u(x, y, z), \tag{4.15}$$

$$v_{ran} = 0.1\left\{1 - \left|tanh\left[2(z - \frac{1}{2}L_z)\right]\right|\right\} r_v(x, y, z), \tag{4.16}$$

$$\rho_{ran} = \frac{\Delta\rho_0}{2}\left\{1 - \left|tanh\left[2(z - \frac{1}{2}L_z)\right]\right|\right\} r_\rho(x, y, z), \tag{4.17}$$

where the subscript '*pri*' and '*ran*' denote the perturbations for exciting primary instability and following non-linear saturation process, respectively, r_u, r_v and r_ρ are random numbers between -1 and 1 for perturbations in the u, v and ρ fields, and L_x is the length of the computation domain in the streamwise direction (x direction) which is made dimensionless by δ_s. u_{pri}, v_{pri}, u_{ran} and v_{ran} are made dimensionless by Δu_0, and ρ_{ran} is made dimensionless by $\Delta\rho_0$. As predicted in Chapter 3, the primary instability mode in CSS flows is the stationary mode usually corresponding to vortex structures, and the velocity shear will therefore be the predominant source to excite the primary instability. As background stratification considered in this study is very weak, '*pri*' perturbations are only imposed on the two basic velocity components u and v, not on ρ.Just in case, this study has tested if '*pri*' on ρ have any influences and find adding the primary perturbation on density field has no influences on the DNS results. Thus,the initial field of a quantity will be the sum of the background profile, the primary perturbation, plus the secondary perturbation if applicable. The amplitudes of 'pri' perturbations are selected as 0.02, which give the kinetic energy of initial flow field are sufficiently small compared to those of primary flow structures, so that adequate approximations between DNS experiments and linear stability analysis will be obtained. The amplitude of 'ran' are selected as 0.1 in order to incite non-linear saturation after the development of primary flow structures. Since the amplitude for 'pri' perturbations are quite small, the dependence of the precise form of perturbations are minimized.

Periodic boundary conditions are set in the horizontal directions, *i.e.* ,

$$F(x+L_x, y, z) = F(x, y+L_y, z) = F(x, y, z), \tag{4.18}$$

where F is the solution field of any property, and L_y is the length of the computation domain in the spanwise direction (y direction) which is made dimensionless by δ_s. For the top and bottom boundaries, an impermeable condition is set for w, *i.e.* ,

$$w|_{z=0} = 0, \quad w|_{z=L_z} = 0, \tag{4.19}$$

the following zero flux boundary condition is set for u and v,

$$\left.\frac{\partial u}{\partial z}\right|_{z=0} = \left.\frac{\partial u}{\partial z}\right|_{z=L_z} = \left.\frac{\partial v}{\partial z}\right|_{z=0} = \left.\frac{\partial v}{\partial z}\right|_{z=L_z} = 0, \tag{4.20}$$

and for density the following boundary condition is set,

$$\rho|_{z=0} = \frac{\bar{\rho}}{\Delta\rho_0} + \frac{1}{2}, \quad \rho|_{z=L_z} = \frac{\bar{\rho}}{\Delta\rho_0} - \frac{1}{2}. \tag{4.21}$$

A summary of parameter settings of all DNS runs can be found in table 4.1, which are divided into four groups. The major group 'ξ' takes ξ as main variable and fix other paramter at constant value. 'Re', 'mesh size' and 'δ_s' group are designed to test the influences of Re, mesh resolution, initial shear/stratified layer thickness and influences of initial wavenumber. As discussed in § 4.1, this study aims to only investigate the 'clean' primary coherent structures of CSS flows without inciting any types of potential secondary instabilities, three major parameters Re_0, Pr and Ri_0 as well as single wavelength domain size are intentionally selected to serve this purpose. Re_0 is selected in the range of 600-2000 for laboratory flows and fixed at 1200 for our major cases, which will not trigger the potential secondary pairing instabilities occur at high Re_0 number based on experiences from KH instability studies such as [13, 29, 24] and so on. Pr are set as 1 for all DNS runs, as large Pr number might precede the secondary pairing instabilities of the KH instability occur at high Re number to low Re number conditions. To minimize the influences of convective buoyancy and emphasize the dynamic features only involving ξ, Ri_0 is selected as 0.01 to achieve a sufficiently weakly stratified flow where the streamwise and spanwise cross shear will completely dominate over convective buoyancy. Meanwhile, a weakly stratified environment where Ri_0 allow this study to build correlations between DNS results and the water tank experimental results reported in AG97, where the experiments for CSS flow were conducted in weakly stratified environment as well.

The streamwise domain size L_x is chosen as $L_x = (2\pi/\alpha)$, which is made dimensionless by δ_s and is one wavelength of the instability mode. The initial shear layer thickness δ_s is set as 0.1795 m, which refers to the same setting used in [33]. $\alpha = 1/3 \approx 0.333333$ is selected for the major DNS runs, which is the wavenumber close to the most unstable mode based on the linear stability analysis results in 3. Other wavenumber $\alpha = 1/6$, 2/3 and 1/2 are also selected by varying the initial shear layer thickness δ_s for the three typical CSS flow cases with ξ =0.2, 0.5 and 0.8 as well. The variances of α and δ_s are found to have no influences of conclusions drawn from typical $\alpha = 1/3$ and $\delta_s = 0.1795$m. L_y is set to be equal to L_x, as the spanwise basic flow will be equally important for a CSS flow, especially at a large ξ. L_z is also set to be equal to L_x, which is different from that ($L_z = 0.5L_x$) used in the numerical studies on the PSS flow such as [33]. The reason for the doubling in L_z here is to prevent the boundary intervention when coherent structures in the CSS flow become more expansive at $\xi > 0.5$. According to our observations not shown in table 4.1, $L_z \geq L_x$ is sufficiently large enough to prevent any interferences from boundary, while $L_z = 0.5L_x$ can not prevent the boundary interferences in the CSS flow cases.

A reliable numerical code, PUFFIN, is used to perform the DNS [34]. The governing equations (5.8)-(4.6) are discretized in space using a finite volume formulation on a uniform,

Table 4.1 Details of DNS experiments (all at $Ri_0 = 0.01$, $Pr = 1$, $L_x = L_y = L_z = 1.691747$).

Case	Re	ξ	δ_s	α	N_x	N_y	N_z
ξ	1200	0	0.1795	1/3	256	256	128
	1200	0.1	0.1795	1/3	256	256	128
	1200	0.2	0.1795	1/3	256	256	128
	1200	0.3	0.1795	1/3	256	256	128
	1200	0.4	0.1795	1/3	256	256	128
	1200	0.5	0.1795	1/3	256	256	128
	1200	0.6	0.1795	1/3	256	256	128
	1200	0.7	0.1795	1/3	256	256	128
	1200	0.8	0.1795	1/3	256	256	128
	1200	0.9	0.1795	1/3	256	256	128
	1200	1.0	0.1795	1/3	256	256	128
Re	600	0.5	0.1795	1/3	256	256	128
	2000	0.5	0.1795	1/3	256	256	128
Mesh size	1200	0.5	0.1795	1/3	256	256	256
	1200	0.5	0.1795	1/3	256	128	128
	1200	0.5	0.1795	1/3	128	128	128
δ_s	1200	0.2, 0.5, 0.8	0.359	2/3	256	256	128
	1200	0.2, 0.5, 0.8	0.08975	1/6	256	256	128
	1200	0.2, 0.5, 0.8	0.26925	0.5	256	256	128

staggered, Cartesian grid. The advection terms in both the momentum and scalar transport equations used a 4th-order central difference scheme, while all other spatial derivates are discretised using a second-order central difference scheme. The spatial derivatives are discretised by the 4th-order central finite difference scheme for both the momentum and scalar equations. The ULTRA-flux limiter is applied to the scalar advective terms. The pressure correction approach is used to correct the pressure and velocity fields. The 2nd-order Adams-Bashforth and Crank-Nicolson schemes are used for the time advancement. The CFL number criterion is used to make sure the simulation is stable, with the minimum and maximum limits of 0.3 and 0.4, respectively. The discretised momentum and scalar equations are solved by the Gauss-Seidel method. The pressure correction equation is solved by the BiCGSTAB (BiConjugate Gradient STABilized method) solver with a modified strongly implicit preconditioner [35, 36]. The code is parallelized using Message Passing Interface (MPI). The PUFFIN code has been successfully used for a wide range of flows (see, e.g., [37–40]).

Due to the influence of the extra spanwise velocity component in the basic flow, the flow dynamics in a CSS flow may be quite different from that in a PSS flow. To ensure that the

DNS runs produce accurate results, a mesh-independence test was conducted in terms of two key representative parameters of the flow dynamics, *i.e.* , the streamwise perturbation kinetic energy K'_u and the mixedness thickness δ_θ, which are defined by (4.26) and (5.10), respectively. K'_u is a statistical parameter for the flow dynamics and δ_θ is a parameter quantifying the mixing effects in the flow, as will be discussed in § 4.3.3 and § 4.3.5, respectively. Five different meshes were chosen for this test, including $128 \times 128 \times 128$, $128 \times 128 \times 256$, $128 \times 128 \times 512$, $256 \times 256 \times 128$, and $256 \times 256 \times 256$. The time series of these two parameters, obtained by DNS, are presented in figure 4.2 for these five meshes for the case of $\xi = 0.5$. From figure 4.2(a), it is seen that the time series of K'_u for all five meshes are very similar. Noticeable differences occur mainly at the very early stage and the $128 \times 128 \times 128$ mesh produces the largest differences from the remaining meshes. However, during the period from $t \approx 15$ to $t \approx 30$, which corresponds to the primary instability stage for $\xi = 0.5$ with the dynamics predicted by the linear stability analysis, the time series of K'_u are essentially the same for all five meshes. After $t \approx 30$, there are only slight differences in the time series of K'_u among the meshes other than the $128 \times 128 \times 128$ mesh. Though it is not shown in figure 4.2, the magnitude of the minimum dimensional K'_u for the $256 \times 256 \times 128$ and $256 \times 256 \times 256$ meshes are of the order 10^{-9} J/kg, which is at the same order as found by the numerical study of [33], indicating that these two meshes are able to reproduce, with satisfactory accuracy, the flow dynamics of the CSS flows under investigation in terms of K'_u. The differences among the meshes in terms of δ_θ are much smaller, except, again, the $128 \times 128 \times 128$ mesh, as clearly shown in figure 4.2(b). Nevertheless, the $256 \times 256 \times 256$ mesh produces slightly lower values of δ_θ at the later flow development stage. In view of the results presented in both figures 4.2(a) and 4.2(b), it is believed that the $256 \times 256 \times 128$ mesh is an appropriate mesh for the DNS for the CSS flows considered in this study which provides a good compromise of computational requirement and accuracy. Furthermore, as the horizontal directions are more sensitive to the numbers of cells, the doubling of the cells in the horizontal directions (x and y, *i.e.* , 256×256) is also justifiable. Hence all subsequent DNS runs in this study are carried out using the $256 \times 256 \times 128$ mesh. In addition, the resolution of mesh size Δ_x, Δ_y, Δ_z in x, y and z direction are tested by Kolmogorov scale $L_k = (\nu^3/\varepsilon)^1/4$, where the kinetic dissipation ε for L_k is selected as the maximum dissipation during the entire transition to turbulence for each DNS cases. It is found Δ_x, Δ_y are within $2L_k$ and Δ_z is within $4 - 5L_k$, therefore the resolution settings of mesh in all directions are sufficient for convincing DNS runs. The total and turbulence kinetic energy budget tests are also conducted as shown in Appendix 4.5, where the conserved kinetic energy budget though every evolution stages are justified.

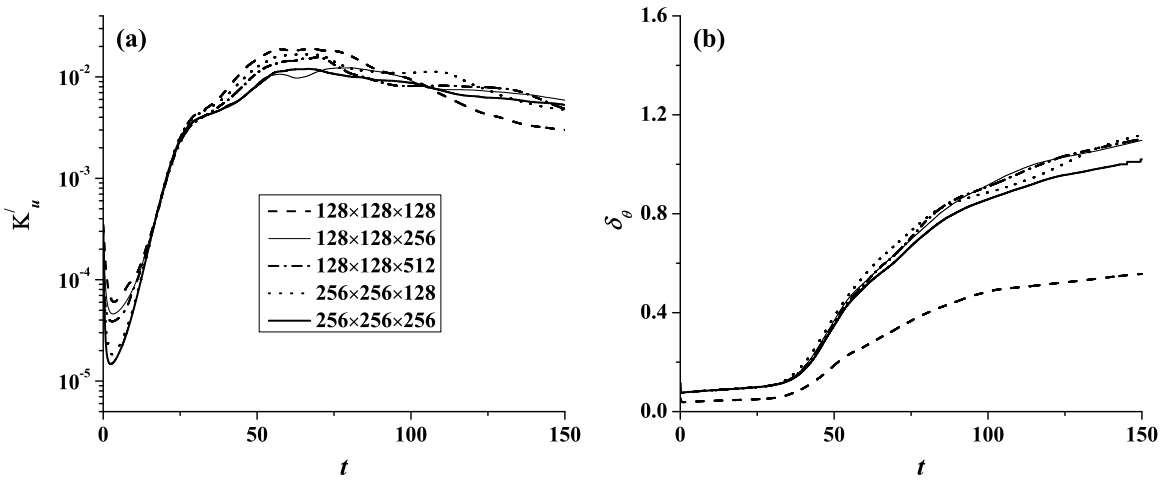

Fig. 4.2 Comparison of the time series of (*a*) the perturbation kinetic energy K_u' and (*b*) the mixedness thickness δ_θ obtained by DNS with five different meshes for the case of $\xi = 0.5$.

4.3 Results

4.3.1 Evolution of coherent structures

The evolution of primary coherent structures at four typical ξ values ξ=0, 0.2, 0.5, 0.8, with parameter settings following major DNS runs listed in table 4.1, will be demonstrated by the dimensionless concentration c defined in (4.9). The selections of these four specific ξ cases here are mainly based on the distinctive flow structure appearances and dynamic features that will be shown in 4.3.2.

As a special case of the CSS flow with $\xi = 0$, the evolution of the coherent structures in the KH instability mode is shown in terms of c in figure 4.3, where the DNS results at the representative moments of four development stages of the coherent structures are presented. The embryo of the primary KH eddy forms at around $t = 30$ and keeps growing until $t \approx 50$, when a clear center region and an adjacent braid region of a developed 'cat eye' eddy is clearly seen as shown in figure 4.3(*a*). Such a braid region is explicitly labeled in the vorticity contours of figures 4.9 and 4.10 which will be presented later in § 4.3.2. As the two-dimensional primary KH eddy is fully developed in the x direction, the streamwise KH eddy starts to extend in spanwise direction to achieve its three-dimensionalization. At this stage, the alignment of the the coherent structure in the y direction is completely destroyed, as shown in figure 4.3(*b*), forming inside a ''hatched cup' eddy core structures as will be shown in figure 4.7. The whole coherent structure keeps expanding until the entire flow structures are also saturated, at about $t = 101$, as demonstrated in figure 4.3(*c*). After that,

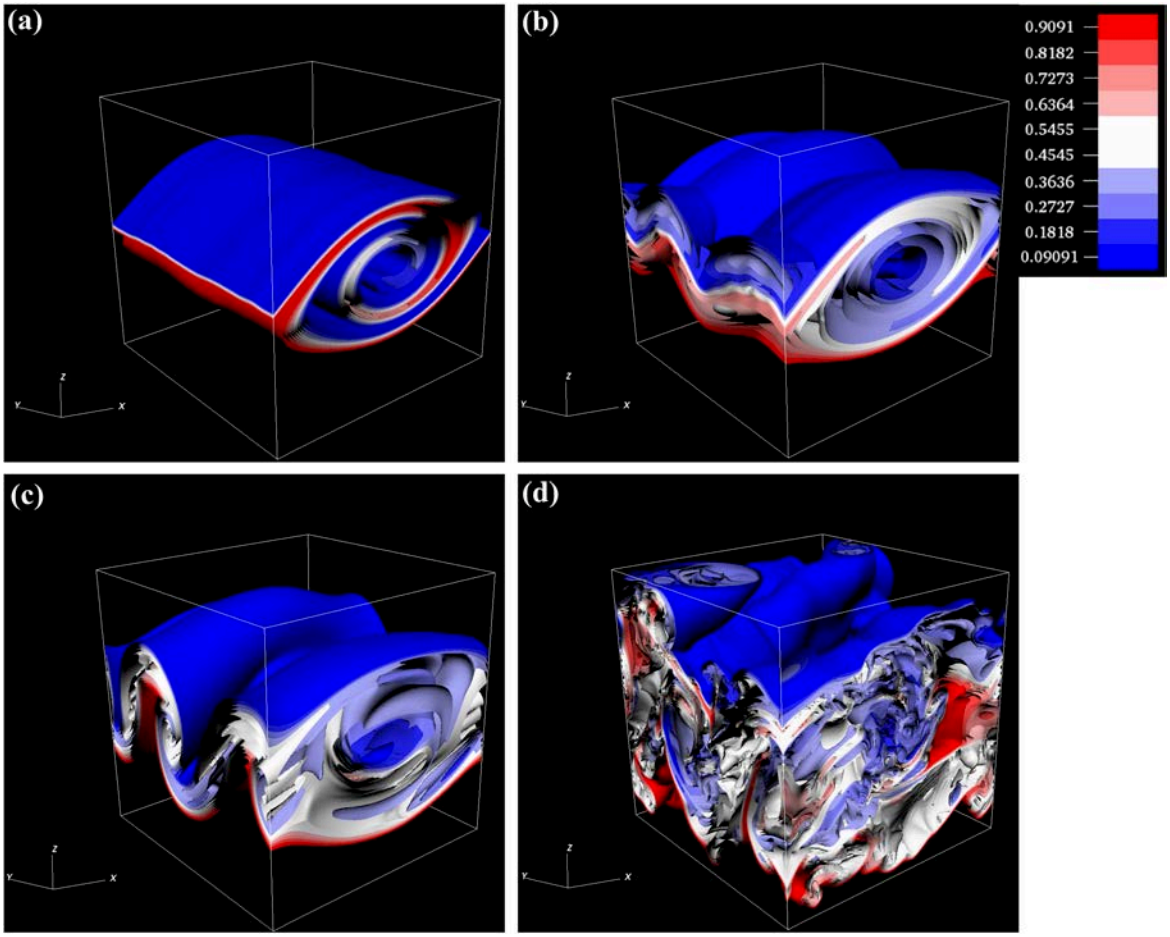

Fig. 4.3 Three-dimensional contours of concentration c for the KH instability in the $\xi = 0$ case: (a) the primary KH eddy at $t = 50$; (b) the secondary instability in the y direction at $t = 85$; (c) the saturation of coherent structures at $t = 101$; and (d) the collapse and decay into turbulence at $t = 120$.

the three-dimensional structures start to collapse and decay into a turbulent flow state as shown in figure 4.3(d).

When a weak spanwise basic velocity with $0.1 \leq \xi \leq 0.3$ is introduced, the spanwise eddies begin to emerge, but are not strong enough to survive under the spanwise expansion of the streamwise KH 'cat eye' eddy. Such a 'streamwise-dominant' CSS flow instability mode is shown, as an example, in figure 4.4 for the $\xi = 0.2$ case, where the DNS results of the three-dimensional contours of concentration c at four representative times are presented. At the early stage as shown in figure 4.4(a), the weak spanwise velocity creates several visible but small spanwise vortex 'spots', which deflect the initially spanwise aligned interfacial layer much earlier than that for the $\xi = 0$ case. However, these spanwise vortex 'spots' grow

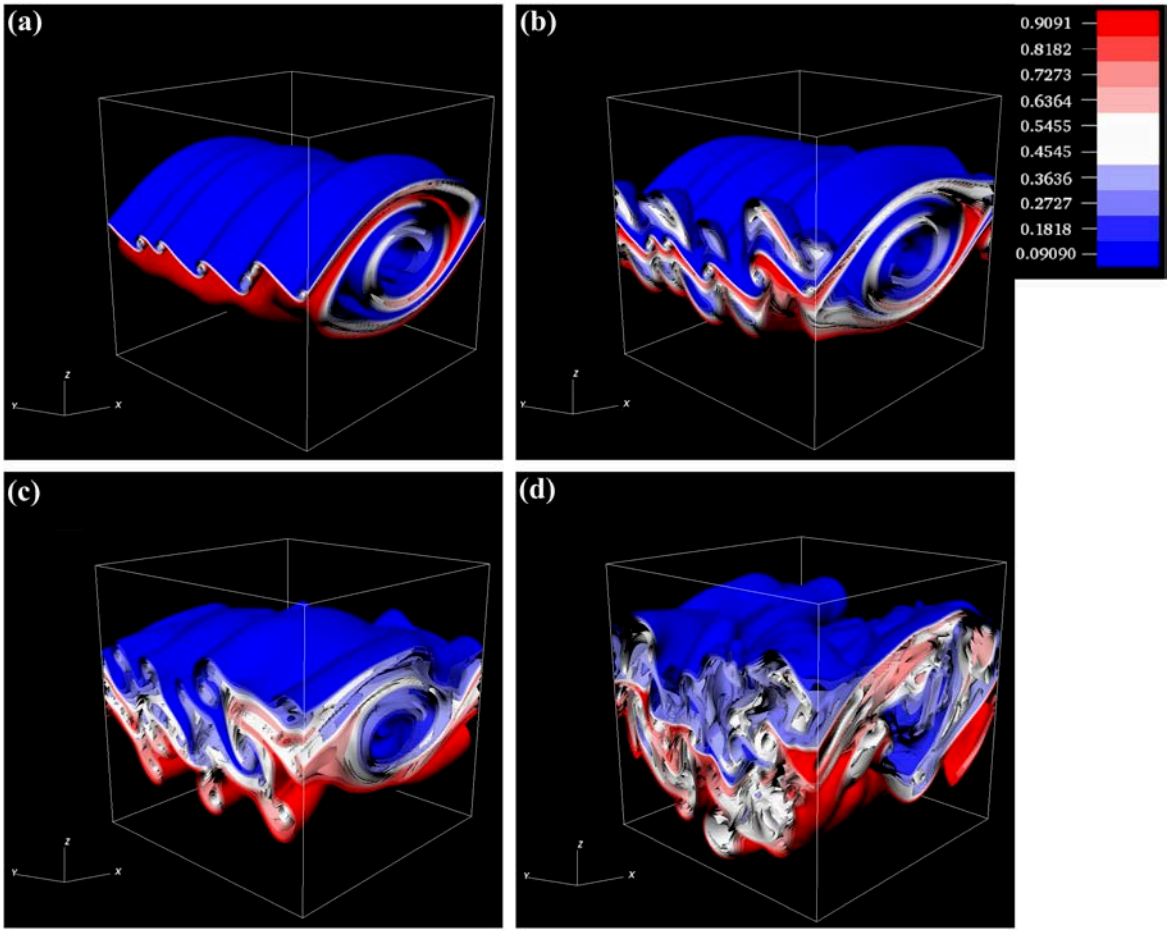

Fig. 4.4 Three-dimensional contours of concentration c for the CSS flow instability in the $\xi = 0.2$ case: (a) the weak spanwise eddy born at $t = 50$; (b) the spanwise eddy overwhelmed by the streamwise expansion of the 'cat eye' eddy at $t = 55$; (c) the multiple spanwise roll-ups forming at $t = 68$; and (d) the decay into turbulence at $t = 89$.

at a much slower rate than the streamwise 'cat eye' eddy, which becomes more developed and starts to further expand in the x direction as shown in figure 4.4(b). As a result, the spanwise vortex 'spots' are overwhelmed by the expanding 'cat eye' eddy before their further development. Nevertheless, these weak spanwise vortex spots also change the appearances of coherent structures during the three-dimensionlization of the streamwise 'cat eye' eddy. When compared to the $\xi = 0$ case shown in figure 4.3(b) where the spanwise fluid interface is distorted, smaller but multiple spanwise roll-ups are observed in the $\xi = 0.2$ case as shown in figure 4.4(c). Therefore, the interfacial layer looks more deformed in the $\xi = 0.2$ case, suggesting that a stronger mixing is happening. Eventually, the streamwise 'cat eye' eddy collapses at about $t = 89$, as shown in figure 4.4(d), which is significantly earlier than the

$\xi = 0$ case and the entire coherent structures completely collapse at about $t = 120$. The collapse time observed in c plots are further supported by time series of kinetic energy as shown later in § 4.3.3. Similar coherent structures and the 'streamwise-dominant' CSS flow instability mode are also found for the other cases over the range $0.1 \leq \xi \leq 0.3$, with the emergences of weak spanwise vortex flow structures.

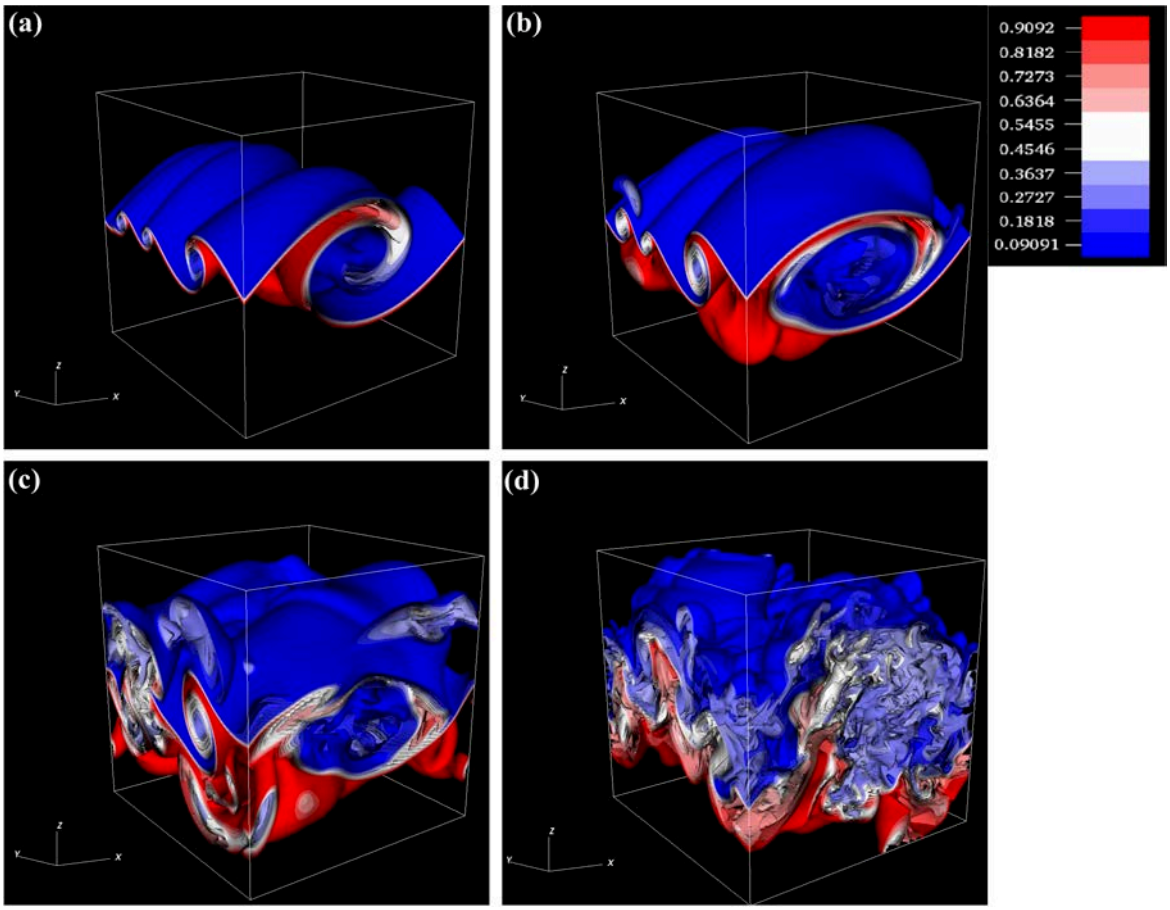

Fig. 4.5 Three-dimensional contours of concentration c for the CSS flow instability in the $\xi = 0.5$ case: (a) the primary eddy wrap structure at $t = 37$; (b) the collapse of the streamwise eddy and the growth of the spanwise eddy at $t = 48$; (c) the collapse of the streamwise eddies and the entire coherent structure at $t = 55$; and (d) the decay into turbulence at $t = 74$.

As ξ is further increased to $0.4 \leq \xi \leq 0.6$, the spanwise eddy becomes comparable to the streamwise eddy, which is the feature of a 'balanced' CSS flow instability mode. Figure 4.5 presents the three-dimensional contours of concentration c at four representative times obtained by DNS for the $\xi = 0.5$ case, as an example to demonstrate the features of the 'balanced' CSS flow instability mode. As shown in figure 4.5(a), three spanwises eddies, especially the one close to the streamwise eddy, are more visible in terms of enlarging

size compared to figure 4.4(a). Furthermore, it seems that the body of the largest spanwise eddies not only extends across the periodic domain in the x direction, but also wraps over the developing streamwise eddy. Such spanwise 'spiral eddy wrap' structures are more obvious in the vorticity plot as will be presented and detailed in § 4.3.2. At the next stage, as shown in figure 4.5(b), the spanwise eddies become more developed as their sizes further increase. On the other hand, the streamwise eddy is less developed in terms of size when compared to the 'cat eye' eddy in figure 4.4(b), meanwhile a sign of ambiguous streamwise core structures is found in the center region instead of clear 'cat eye' shape shown in figure 4.4(b). Nevertheless, the size of the streamwise eddy in the $\xi = 0.5$ case is still close to that in the $\xi = 0.2$ case, suggesting that the streamwise eddy is still an important part in the entire coherent structures. As time proceeds to $t = 55$, as shown in figures 4.5(c), the expanding spanwise eddies still keep a part of their eddy core structures as seen from the left, while the collapsing streamwise eddy completely collapse. Finally, the three-dimensional coherent structures in the $\xi = 0.5$ case start to decay at about $t = 74$, which is considerably earlier than that in the $\xi = 0.2$ case, indicating a faster transition to turbulence as ξ increases. The events observed in current c plots for $\xi = 0.5$ case will be reporduced again in terms of the time series of kinetic energy in § 4.3.3 The comparable spanwise and streamwise coherent structures in such a 'balanced' mode are also found in the other cases over the range $0.4 \leq \xi \leq 0.6$, with the size of the spanwise eddy becoming slightly smaller when ξ is near 0.4 or larger when ξ is near 0.6.

For $\xi \gtrsim 0.7$, the streamwise 'cat eye' eddy is found to be significantly suppressed by the spanwise 'eddy wrap' structures, introducing a distinctively different collapsing mechanism from the $\xi \lesssim 0.7$ cases. Such a 'spanwise-dominant' CSS flow instability mode is demonstrated in figure 4.6, as an example, by the three-dimensional contours of concentration c at four representative moments for the $\xi = 0.8$ case, again obtained by the DNS. At the early stage as shown in figure 4.6(a), the spanwise eddies in the $\xi = 0.8$ case become stronger than those in the $\xi = 0.5$ case, as similar 'cat eye' shape is observed in the spanwise eddy cores which is of a comparable size to the streamwise eddy. Meanwhile, the streamwise 'cat eye' is less obvious as the primary flow structures only start to turn upwards, without fully rolling into the 'cat eye' structures. At the second stage as shown in figure 4.6(b), the spanwise 'spiral eddy wrap' structures expand in both the spanwise and vertical directions, with more developed eddy cores where more visible streamlines make 'cat eye' shape even more clear in spanwise eddy core regions. In contrast, the size of the streamwise eddy only increases to a limited extent compared to that in figure 4.6(a), with its undeveloped core even starting to collapse. At the next stage, the earlier collapse of the streamwise 'cat eye' eddy is more evident in the $\xi = 0.8$ case, as shown in figure 4.6(c),

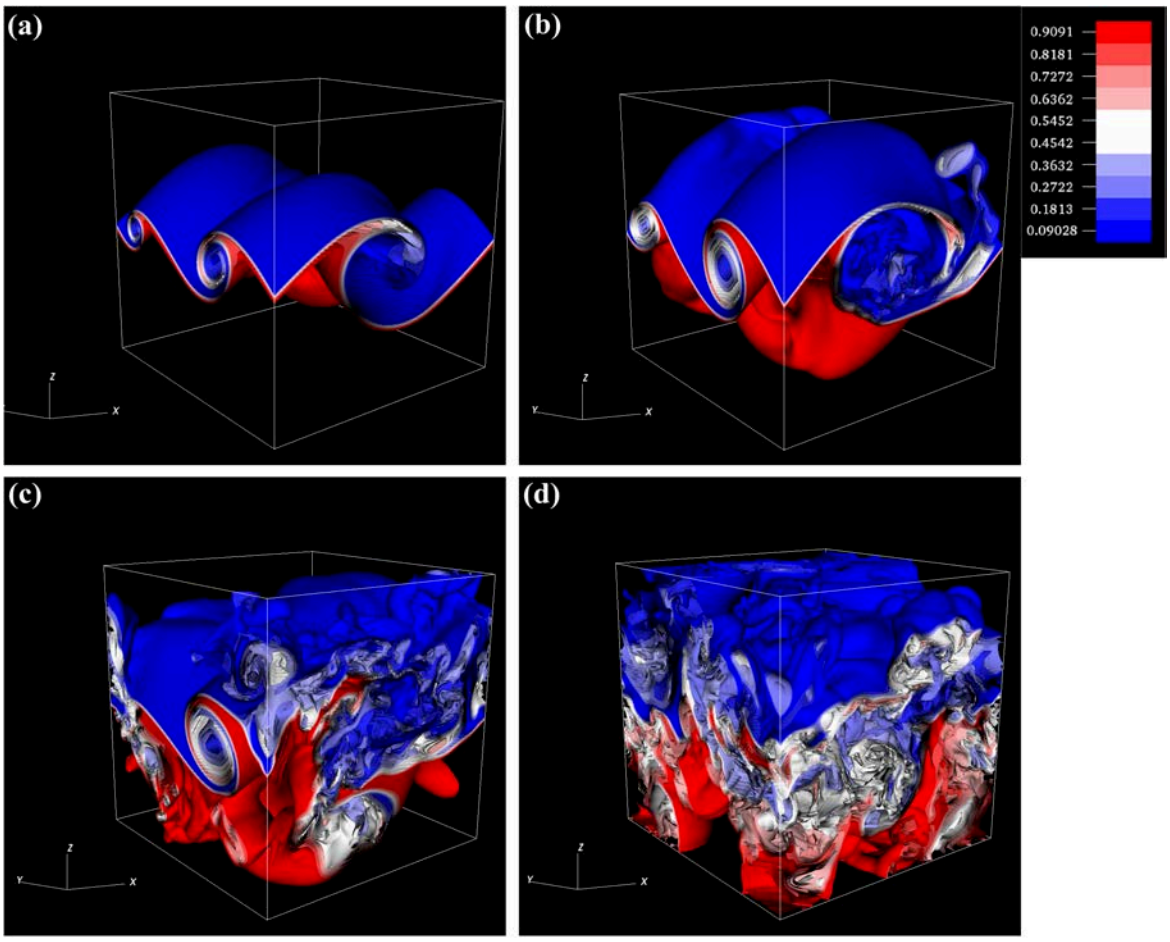

Fig. 4.6 Three-dimensional contours of concentration c for the CSS flow instability in the $\xi = 0.8$ case: (a) the primary eddy wrap structure at $t = 33$; (b) the 'internal collapse' of the streamwise eddy and the growth of the spanwise eddy at $t = 44$; (c) the complete collapse of the spanwise eddies at $t = 52$; and (d) the decay into turbulence at $t = 63$.

where the spanwise 'eddy wrap' structures still keep their coherence. The complete collapse of the whole flow structure occurs at $t = 63$, as exhibited in figure 4.6(d), which is earlier than that in the $\xi = 0.5$ case. This remarkably early collapse of the streamwise 'cat eye' eddy is also observed in the other cases over the range $0.7 \leq \xi \leq 1.0$, giving the 'spanwise-dominant' CSS flow instability mode an 'internal-collapse' feature. This 'internal-collapse' will be illustrated in 4.3.2 more clearly.

4.3.2 Vorticity structures

The three-dimensional coherent structures observed above in the concentration contours further verify the dominance of the stationary mode as predicted by our linear stability

analysis in Chapter 3 and [41]. The dominant eddy-featured structures imply that it is quite possible that the coherent structures are developed from the small vortex spots, which are formed by the initial perturbations following the dynamics governed by the perturbation equations for CSS flows [41]. Therefore it is insightful to examine how the coherent structures observed in the previous section develop from the initial weak vortex structures and helpful to precisely define the spanwise flow structures. This can be done by using the streamwise vorticity ω_x and the spanwise vorticity ω_y, both made dimensionless by $\Delta u_0/\delta_s$, which are defined as follows,

$$\omega_x = \frac{\partial w}{\partial y} - \frac{\partial v}{\partial z}, \quad \omega_y = \frac{\partial u}{\partial z} - \frac{\partial w}{\partial x}. \tag{4.22}$$

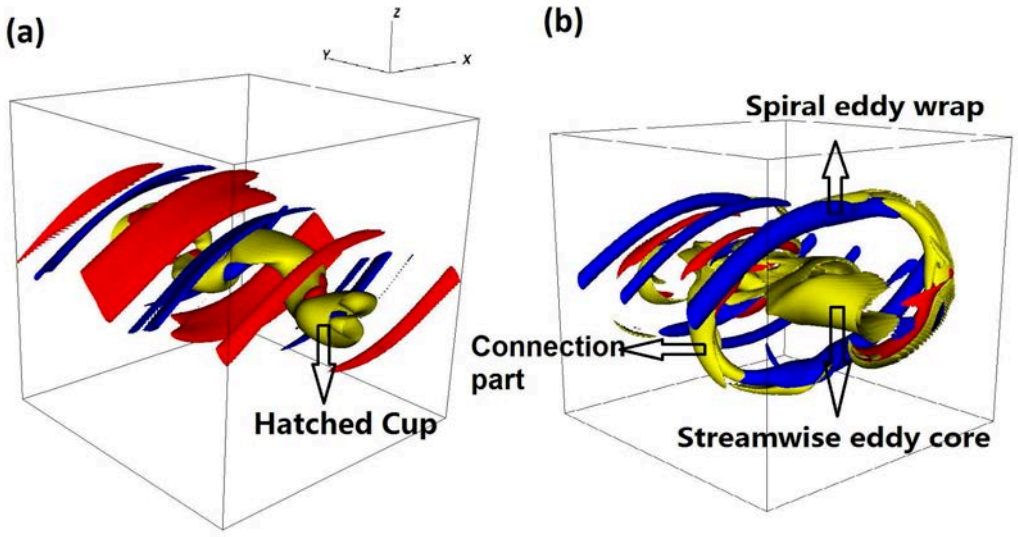

Fig. 4.7 Three dimensional contours of positive $\omega_x = 0.2699$ (red), negative $\omega_x = -0.2699$ (blue) and $\omega_y = 0.8097$ (yellow) for (a) the KH instability in the $\xi = 0$ case at $t = 84$ and (b) $\omega_x = 1.6194$ (red), $\omega_x = -1.6194$ (blue) and $\omega_y = 1.0796$ the CSS 'balanced mode' instability at $t = 45$. The 'hatched cup' streamwise KH eddy core in $\xi = 0$ case and spanwise 'Spiral eddy wrap' eddy structures are marked in each subfigure respectively.

Figure 4.7 shows a three-dimensional contour plot of combined ω_x and ω_y for KH instability at $\xi = 0$ and CSS primary 'balanced mode' at $\xi = 0.5$. For KH instability as shown in figure 4.7(a), the 'hatched cup' shape of streamwise KH eddy core structure (as marked by 'hatched cup' in figure 4.7), which is represented by yellow spanwise vorticity ω_y contour and named by [14], was gradually developed after the formation of two-dimensional streamwise 'cat eye eddy'. As the 'hatched cup' structures is a typical PSS flow structures in a unstratified or weakly stratified environment where buoyancy play insignificant role, reproducing such structures satisfy our purpose to minimize the influences of buoyancy and

to concentrate on streamwise and spanwise shear-dynamics only. Surrounding the 'hatched cup' core structures are strips of spanwise vortex structures.As emphasized in introduction section, the vorticity plots above only involve single wavelength flow structures. Of course, as the domain extend to multiple wavelength, the pairing process associated with secondary pairing instability at braid regions of streamwise 'cat eye' eddy will appear. However, the pairing process are beyond the scope of current study. In the near future, more results about pairing of CSS primary modes will be reported.

Distinctively different primary flow structures are observed in CSS flow as shown in figure 4.7(b). A typical spanwise 'spiral eddy wrap' structures, as marked in figure 4.7(b), includes three pairs of spiral-shaped eddy tubes (denoted by blue ω_x) at the top and bottom of the central streamwise eddy core structures (as marked by 'streamwise eddy core' in figure 4.7(b)). The connecting structures between spanwise 'spiral eddy wrap' and streamwise eddy core are also spiral-shaped yellow ω_y contours as marked by 'connection part' in figure 4.7(b). These three components defined here with figure 4.7(b) constitute of the typical three-dimensional primary flow structures in CSS flow, as they directly develop from the initial perturbed flow field rather than any types of primary coherent flow structures. Generally, for three primary CSS flow instabilities, similar spanwise 'spiral eddy wrap' structures along with 'connection part' are also observed, in spite of their increasing size of with increasing ξ. Note that the 'spiral' shape of spanwise eddy structures are also observed in AG97, which reported that the spanwise eddy structures originate from the braid regions of streamwise 'cat eye' eddy, suggesting the 'spiral eddy wrap' and 'connection part' structures shown in figure 4.7(b) could exisit in real laboratory environment.

As ξ increases, the size of spanwise 'spiral eddy wrap' structures increases significantly, so that the streamwise 'cat eye' eddy structures are suppressed and forced to collapse before its spanwise saturation. To illustrate this 'internal collapse' mechanism, figure 4.8 (a) and (b) shows the three-dimensional vorticity plots combined with ω_x and ω_y contour for 'spanwise dominant' mode at $\xi = 0.8$. It is found that the size of streamwise eddy core structures is remarkably smaller than those in 'balanced mode' shown figure 4.7(b). At $t =$ as shown in figure 4.8 (b), the spanwise 'spiral eddy wrap' is still enlarging its size, whereas the streamwise eddy core structures have already collapsed. Such 'internal collapse' mechanism of streamwise 'cat eye' eddy structures is quite different from the classic collapse due to saturation and breakdown of KH 'cat eye' eddy structures [11]. In fact, as $\xi > 0.5$, the streamwise 'cat eye' eddy cores are found to be unable to form a clear 'hatched cup' shape as found in $\xi = 0$ cases. Therefore, the existences of spanwise 'spiral eddy wrap' structures not only coexist with streamwise 'cat eye' eddy, but also compete with and therefore suppress the further development process of 'cat eye' eddy.

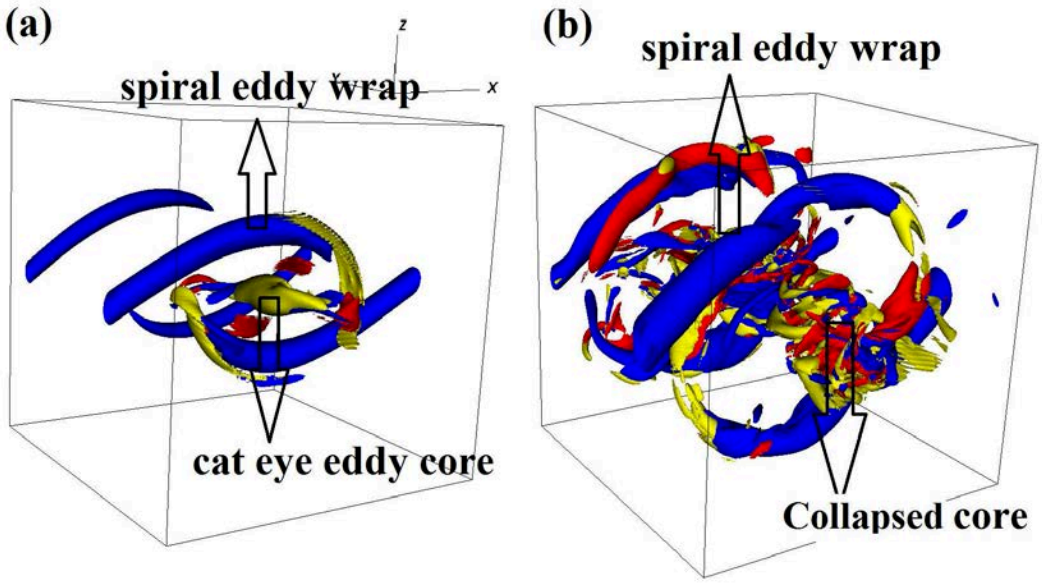

Fig. 4.8 Three dimensional contours of positive $\omega_x = 1.8893$ (red), negative $\omega_x = -1.8893$ (blue) and $\omega_y = 2.1592$ (yellow) for 'spanwise dominant' mode at (a) $t = 33$ and (b) at $t = 45$. The spanwise 'spiral eddy wrap' structures and streamwise 'cat eye' eddy core structures are marked in each subfigure respectively.

To give more specific details of how spanwise 'spiral eddy wrap' structures interact with streamwise 'cat eye' eddy structures, the contour plots of ω_x and ω_y in a vertical slice plane, which is the geometrical center plane of the spanwise eddy wrap structure, are produced from the obtained DNS results. For the KH instability case (at $\xi = 0$), this slice plane is the central vertical central plane at $y = 0.5L_y$, and for the CSS flow instability cases, it is the vertical slice plane determined by the initial point (0, y_i, 0) and the direction vector ($0.99\vec{i}$, $0.12\vec{j}$, $0.0\vec{k}$), rather than in the x direction, due to misaligned 'spiral' shape of spanwise eddy structures rotating around the streamwise 'cat eye' eddy cores in the x direction as shown in figure 4.7. For $\xi = 0.2$ and 0.5, $y_i = 0.25L_y$, and for $\xi = 0.8$, $y_i = 0.3125L_y$. Such vorticity contour plots are presented in figures 4.9 and 4.10 for $\xi = 0$, 0.2, 0.5, and 0.8, which correspond to the concentration contour plots (figures 4.3-4.6) as presented in the previous section.

Figures 4.9(a) and 4.9(b) present the contours of ω_x for the KH instability at $t = 30$, when the two-dimensional primary KH eddy core is about to form, and at $t = 60$, when the KH 'cat eye' eddy is developed and starts to expand in spanwise direction, respectively. At $t = 30$, the alternate positive and negative ω_x regions fill in the center 'core' regions (as marked in figure 4.9(a)), while the peripheral 'braid' regions (as marked in figure 4.9(a)) are filled with positive ω_x, which is in contrast to the CSS flow cases, as will be described below.

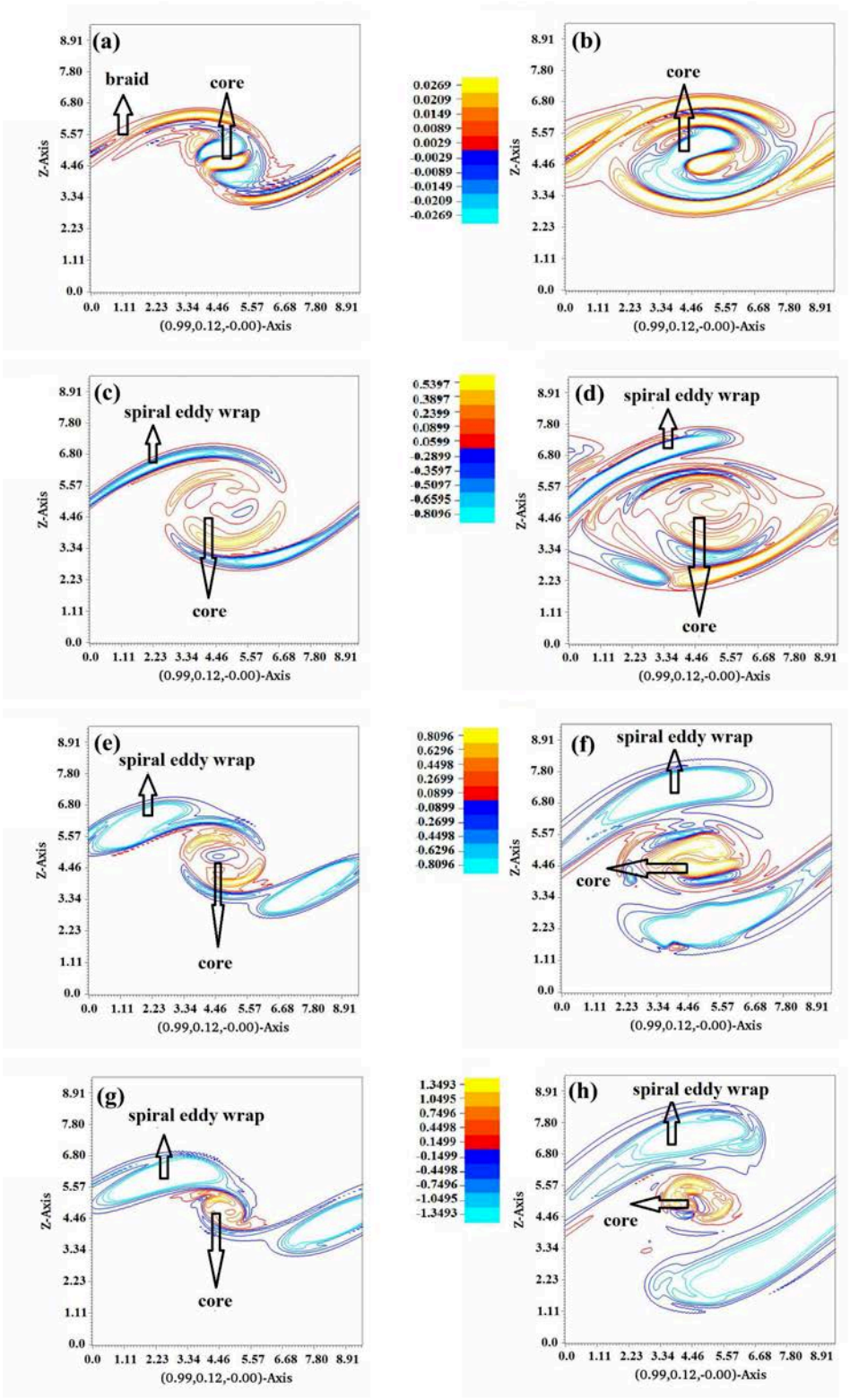

Fig. 4.9 Contours of ω_x in a vertical slice plane for the KH instability in the $\xi = 0$ case at (*a*) $t = 30$ and (*b*) $t = 60$ and for the CSS flow instability in the $\xi = 0.2$ case at (*c*) $t = 37$ and (*d*) $t = 55$, in the $\xi = 0.5$ case at (*e*) $t = 33$ and (*f*) $t = 44$, and in the $\xi = 0.8$ case at (*g*) $t = 30$ and (*h*) $t = 38$, respectively. The cold (hot) color denotes a negative (positive) ω_x.

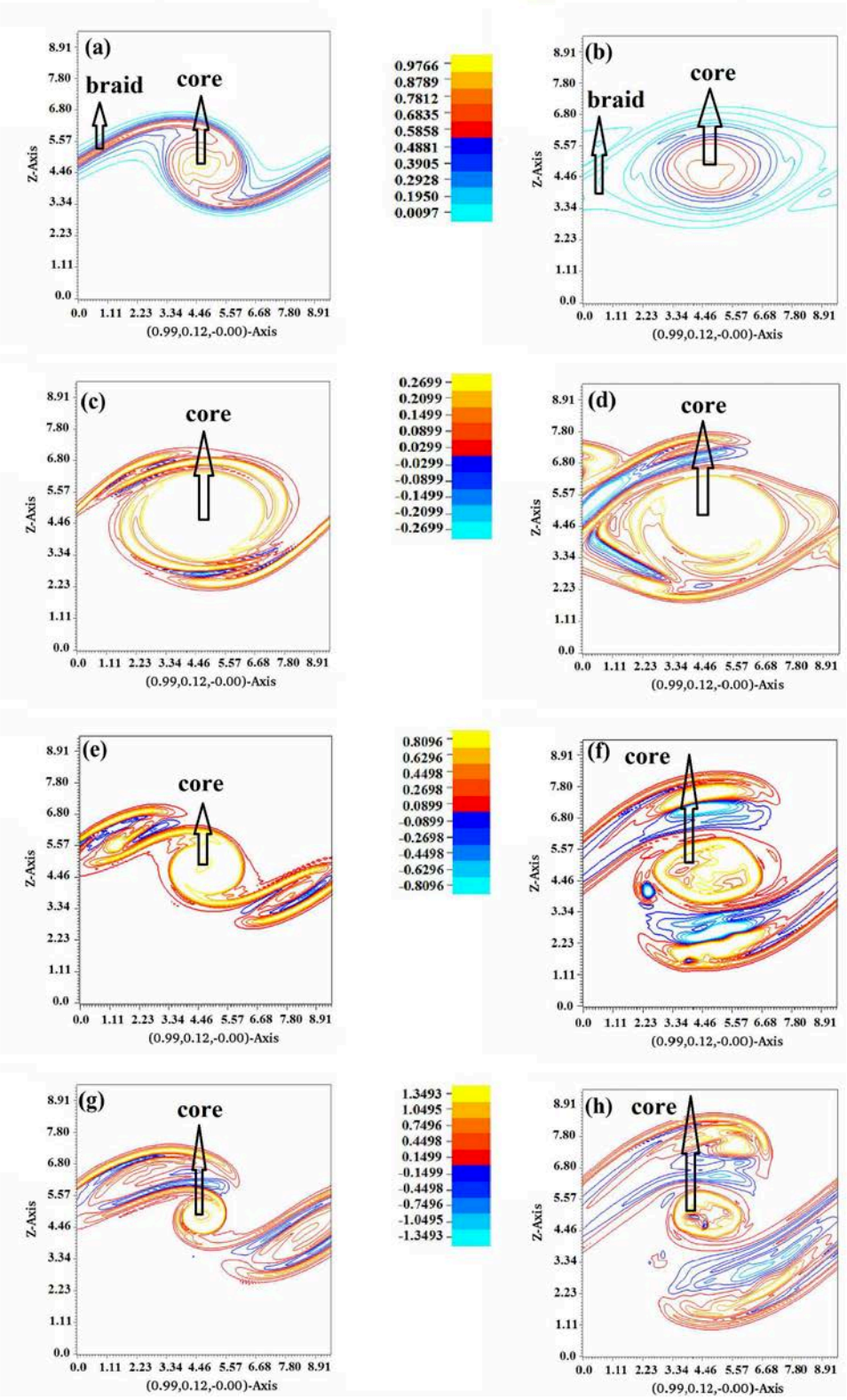

Fig. 4.10 Contours of ω_y in a vertical slice plane for the KH instability in the $\xi = 0$ case at (*a*) $t = 30$ and (*b*) $t = 60$ and for the CSS flow instability in the $\xi = 0.2$ case at (*c*) $t = 37$ and (*d*) $t = 55$, in the $\xi = 0.5$ case at (*e*) $t = 33$ and (*f*) $t = 44$, and in the $\xi = 0.8$ case at (*g*) $t = 30$ and (*h*) $t = 38$, respectively. The cold (hot) color denotes a negative (positive) ω_y.

The alternate positive/negative ω_x regions further develop into a noticeable 'cat eye' shape around $t = 44$ (not shown here) and start to expand their sizes at about $t = 60$ as exhibited in figure 4.9(b). At this stage, the expanding parts of the 'cat eye' eddy, which are identified as the top left and bottom right parts close to the braid regions, are also of positive ω_x.

Figures 4.9(c) and 4.9(d) show the ω_x structures in the 'streamwise-dominant' CSS flow instability corresponding to the concentration plot in figure 4.4. Even though they have a similar appearance in the concentration plots, the KH flow instability with $\xi = 0$ and the 'streamwise-dominant' CSS flow instability with $\xi = 0.2$ have quite different primary flow ω_x structures. In the $\xi = 0.2$ case, ω_x in the braid regions is negative, as shown in figures 4.9(c) and 4.9(d), whereas in the $\xi = 0$ case it is positive as shown in figures 4.9(a) and 4.9(b). The negative ω_x in the braid regions in the $\xi = 0.2$ case represents the weak spanwise 'spiral eddy wrap' as observed in the concentration plot in figure 4.4 and in figure 4.7. In addition, it is observed that the area of the negative ω_x regions at the eddy center is significantly decreased as ξ increases from 0 to 0.2, as if the negative ω_x is transferred from the eddy center to the braid regions. As a result of the braid regions where negative ω_x fills in, the expanding area of the 'cat eye' eddy in the $\xi = 0.2$ case becomes negative ω_x regions as shown 'spiral eddy wrap' regions of figures 4.9(d).

Figures 4.9(e) and 4.9(f) present the ω_x structures in a 'balanced' CSS flow instability at $\xi = 0.5$, which corresponds to the concentration plot in figure 4.5 and in figure 4.7. When compared to the $\xi = 0.2$ case, it is found that the spanwise 'spiral eddy wrap' structures as marked in figures 4.9(e) further expands and forms a a large area of negative ω_x corresponding to the spanwise eddy in figure 4.7(b). At $t = 44$, as shown in figure 4.9(f), a less developed 'cat eye' appearance are observed compared to figure 4.9(b) and (d). At the same time, the spanwise 'spiral eddy wrap' further develop and enclose the entire streamwise 'core' structures. The growth of the 'eddy wrap' coincides with the suppressed 'cat eye' eddy in the $\xi = 0.5$ case, suggesting that as ξ increases from 0.2 to 0.5, energy is transferred from the streamwise eddy to the spanwise eddy.

Figures 4.9(g) and 4.9(h) show the ω_x structures in a 'spanwise-dominant' CSS flow instability, at $\xi = 0.8$, which corresponds to the concentration plot in figure 4.6. When compared to the $\xi = 0.5$ case, it is seen that the stronger spanwise eddy tube observed in figure 4.6, represented by the large top/bottom area of negative ω_x in figures 4.9(g) and 4.9(h), further suppresses the size of the streamwise 'cat eye' eddy core structures. At $t = 38$ when even spanwise 'spiral eddy wrap' is to be developed, the streamwise vortex core are still undeveloped as 'cat eye' shape are unclear compared to Figures 4.9(a) and (b), with only a little spot of negative ω_x seen at the center. Such a severely suppressed and unformed streamwise eddy core observed from the ω_x contour plot correspond to the

'internal collapse' mechanism illustrated in figure 4.8. Similar ω_x structures are also found for other 'spanwise-dominant' CSS flow instability cases, with ξ in the range from 0.7 to 1.0, which correspond to the similar internal collapses observed in the concentration plots for the $0.7 \leq \xi \leq 1.0$ cases.

Figure 4.10 presents the corresponding contour plots of the spanwise vorticity ω_y for the same ξ cases on the same slice planes as those in figure 4.9. The progressive evolution events with increasing ξ involving the spanwise 'spiral eddy wrap' and the streamwise 'cat eye' eddy are basically similar to those presented in the ω_x plot in figures 4.9. It is noted that both positive and negative ω_y appear when $\xi > 0.2$, indicating that the spanwise vortex structures originating from the braid regions only exist in the CSS flows, which are different from the KH flow where only positive ω_y appears. Such alternative regions of positive and negative ω_y imply the strong stretching effects that deform the primary coherent structures. The stretching effects are mainly found at two locations; the first one is at the outer layer of the spanwise 'spiral eddy wrap', implying that the spanwise structures entrain the surrounding fluids to achieve its expansions; and the second one is at the periphery of the streamwise vorticity core, suggesting that the stretching effects could lead to energy transfer from the central 'cat eye' eddy to the wrapped spanwise 'spiral eddy wrap'. As ξ increases, both regions of alternative positive and negative ω_y grow quickly, suggesting that more energy transfer might occur. On the other hand, the decreasing size of streamwise 'cat eye' eddy along with its less and less developed eddy cores with increasing ξ appears more clear in ω_y slice plots than those ω_x slice plots of figure 4.9.

4.3.3 Kinetic energy budget

To further examine the dynamics of the coherent structures illustrated in previous sections, the statistical information about the velocity field is also obtained from the DNS simulations, inspired by the method employed in [19]. To do so, the perturbation velocity $\mathbf{u}'$ is defined below based on the horizontal plane average of the velocity,

$$\mathbf{u}'(x, y, z, t) = \mathbf{u} - \langle \mathbf{u} \rangle_{xy} \tag{4.23}$$

where the operator $\langle f \rangle_{xy}$ is the horizontal plane average of quantity f, which is calculated by

$$\langle f \rangle_{xy} = \frac{1}{L_x L_y} \int_0^{L_y} \int_0^{L_x} f(x, y, z, t) dx dy,$$

in which the subscript 'xy' denotes the average over the horizontal $x-y$ plane. Similarly, a single subscript letter denotes the average over the axis it represents, *e.g.* $\langle f \rangle_y$ represents the

average of f over y across the domain, *i.e.* ,

$$\langle f \rangle_y = \frac{1}{L_y} \int_0^{L_y} f(x, y, z, t) dy.$$

The perturbation velocity $\mathbf{u}'$ can be further divided into the spanwise averaged part and the remaining three-dimensional part, in order to isolate the kinetic energies of the streamwise and the rest structures, respectively. Similarly, the streamwise averaged perturbation velocity is able to isolate the kinetic energies of the spanwise structures as well. The spanwise and streamwise averaged perturbation velocity is defined as,

$$\mathbf{u}_{kh}(x, z, t) = \langle \mathbf{u} - \langle \mathbf{u} \rangle_{xy} \rangle_y, \mathbf{u}_{cs}(x, z, t) = \langle \mathbf{u} - \langle \mathbf{u} \rangle_{xy} \rangle_x, \tag{4.24}$$

in which the subscript 'kh', inherited from [19], means that, after the spanwise average, the dominant part of u_kh should come from the streamwise KH eddy. Similarly, the subscript 'cs' indicates the dominant part of u_cs should come from the spanwise CSS flow structures. Deducting $\mathbf{u}_{kh}$ from the perturbation velocity $\mathbf{u}'$ gives the followingremaining three-dimensional part of the perturbation velocity,

$$\mathbf{u}_{3d}(x, y, z, t) = \mathbf{u} - \langle \mathbf{u} \rangle_{xy} - \mathbf{u}_{kh}, \tag{4.25}$$

where the subscript '$3d$' denotes the perturbation velocity remaining in the spanwise direction. Accordingly, the corresponding kinetic energies based on the decomposed velocities represented by (4.23)-(4.25), which are made dimensionless by $(\Delta u_0)^2$, can be defined as follows,

$$\mathbf{K}'_{\mathbf{u}} = \langle \mathbf{u}' \cdot \mathbf{u}'/2 \rangle_{xyz}, \tag{4.26}$$

$$\mathbf{K}_{kh} = \langle \mathbf{u}_{kh} \cdot \mathbf{u}_{kh}/2 \rangle_{xz}, \tag{4.27}$$

$$\mathbf{K}_{cs} = \langle \mathbf{u}_{cs} \cdot \mathbf{u}_{cs}/2 \rangle_{xz}, \tag{4.28}$$

$$\mathbf{K}_{3d} = \langle \mathbf{u}_{3d} \cdot \mathbf{u}_{3d}/2 \rangle_{xyz}, \tag{4.29}$$

and the total kinetic energy, $\mathbf{K}_{all}$, and the horizontal plane average kinetic energy, $\mathbf{K}_{av}$, both also made dimensionless by $(\Delta u_0)^2$, are,

$$\mathbf{K}_{all} = \langle [u^2 + v^2 + w^2]/2 \rangle_{xyz}, \tag{4.30}$$

$$\mathbf{K}_{av} = \langle \langle \mathbf{u} \rangle_{xy} \cdot \langle \mathbf{u} \rangle_{xy}/2 \rangle_z. \tag{4.31}$$

The related kinetic energy budget is then,

$$\mathbf{K}_{all} = \mathbf{K}_{av} + \mathbf{K_u}' = \mathbf{K}_{av} + \mathbf{K}_{kh} + \mathbf{K}_{3d}. \tag{4.32}$$

The numerical errors associated with the DNS in the determination of the kinetic energy budget (4.32) are obtained for all DNS runs, and it was found that the relative errors obtained by $\mathbf{K}_{all} - \mathbf{K}_{av} - \mathbf{K}_{kh} - \mathbf{K}_{3d}$ are around 1% of the initial total kinetic energy, indicating that the division of $\mathbf{K}'$ is sufficiently accurate.

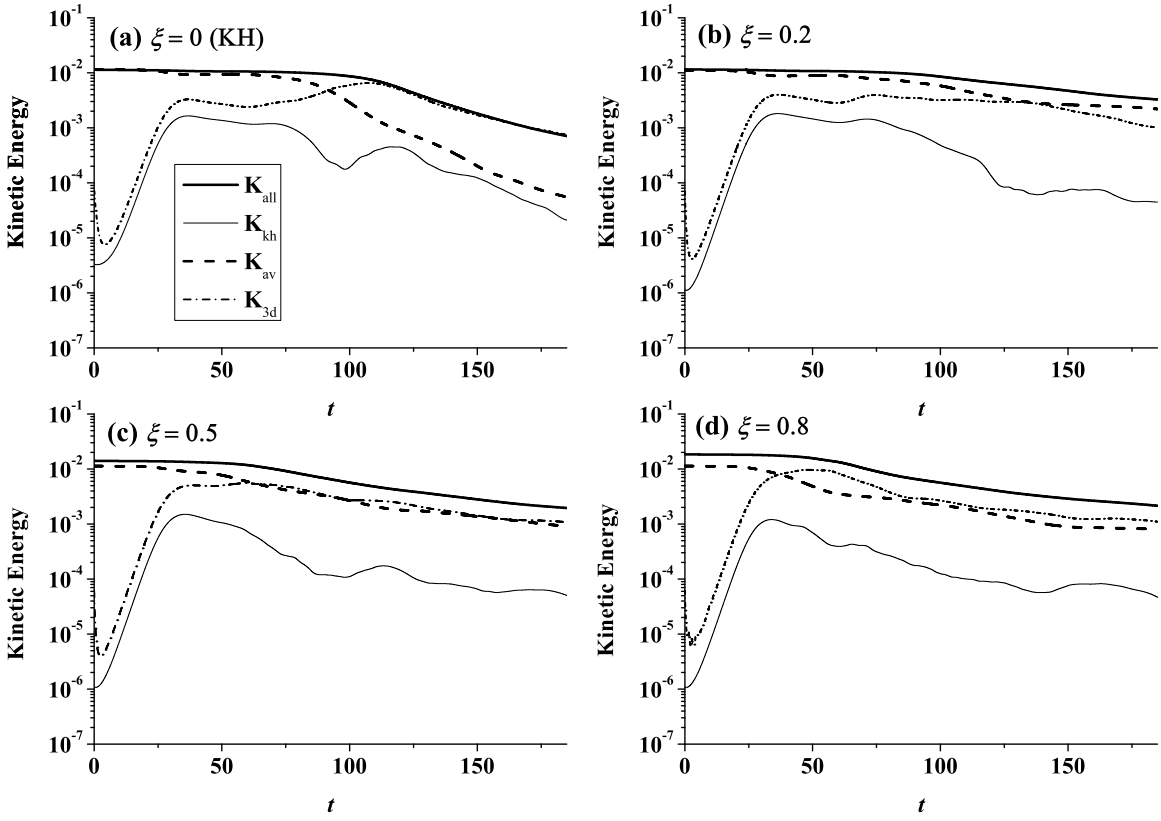

Fig. 4.11 Time series of the total kinetic energy $\mathbf{K}_{all}$, the horizontal plane average kinetic energy $\mathbf{K}_{av}$, the primary KH eddy kinetic energy $\mathbf{K}_{kh}$, the primary spanwise kinetic energy $\mathbf{K}_{cs}$ and the spanwise averaged kinetic energy $\mathbf{K}_{3d}$ in the cases of (a) $\xi = 0$, (b) $\xi = 0.2$, (c) $\xi = 0.5$ and (d) $\xi = 0.8$, respectively.

Figure 4.11 presents the time series of $\mathbf{K}_{all}$, $\mathbf{K}_{av}$, $\mathbf{K}_{kh}$ and $\mathbf{K}_{3d}$ for the KH instability with $\xi = 0$ and the CSS flow instability with $\xi = 0.2$, 0.5 and 0.8. All four kinetic energy terms here are components of conserved divisions of total kinetic energy 4.32. The difference between $\mathbf{K}_{all}$ and $\mathbf{K}_{av}$ is the total perturbation kinetic energy $\mathbf{K}'_{\mathbf{u}}$, which is an indicator of the turbulence in the flow. It is seen from figure 4.11(a) that the gap between $\mathbf{K}_{all}$ and $\mathbf{K}_{av}$ in the

$\xi = 0$ case enlarges at about $t = 74$, a time close to the formation of 'hatched cup' core as shown in figure 4.7, then gradually increases upto one order. It is noted that after the onset of turbulence at $t \approx 74$, $\mathbf{K}_{3d}$ increases to be at the same magnitude as $\mathbf{K}_{all}$ at $t \approx 110$, indicating that the the three-dimensionalization of the KH mode at this saturation stage provides almost all of the turbulent kinetic energy. For $\xi \neq 0$ cases as shown in figures 4.11(b)-(d), the gap between $\mathbf{K}_{all}$ and $\mathbf{K}_{av}$ is significantly smaller than that for the $\xi = 0$ case, indicating that the velocity/kinetic energy field is more organized as the total perturbation kinetic energy $\mathbf{K}'_{\mathbf{u}}$ is smaller. The reduced gap between $\mathbf{K}_{all}$ and $\mathbf{K}_{av}$ is the consequence of the spanwise 'eddy wrap' structures for $\xi > 0$, which include more coherent features than the secondary instability of the KH mode with $\xi = 0$.

From the onset of the 'hatched cup' core structures, at around $t = 74$ for the $\xi = 0$ case as shown in figure 4.11(a), it is seen that the gap between the decreasing $\mathbf{K}_{kh}$ and the increasing $\mathbf{K}_{3d}$ increases, indicating the kinetic energy transfer within 'cat eye' eddy structure are from the streamwise to the spanwise direction. For the $\xi = 0.2$ case as shown in figure 4.11(b), $\mathbf{K}_{kh}$ and $\mathbf{K}_{3d}$ together with their difference behave in a similar fashion, as the spanwise 'spiral eddy wrap' structures for this case are relatively weak. For the $\xi = 0.5$ and $\xi = 0.8$ cases, as shown in figures 4.11(c) and 4.11(d) respectively, the divergence between the decreasing $\mathbf{K}_{kh}$ and the increasing $\mathbf{K}_{3d}$ occurs earlier than that in the $\xi = 0$ case, with the gap between $\mathbf{K}_{kh}$ and $\mathbf{K}_{3d}$ at the divergence instant increasing from $\xi = 0.5$ to $\xi = 0.8$. The larger gaps between $\mathbf{K}_{kh}$ and $\mathbf{K}_{3d}$ in the divergence sections for the $\xi = 0.5$ and $\xi = 0.8$ cases coincide with the enhanced spanwise 'spiral eddy wrap' structures.

As 4.28 defined $\mathbf{K}_{cs}$ in the similar statistical way as $\mathbf{K}_{kh}$, it will be more useful to compare the time series of $\mathbf{K}_{kh}$ and $\mathbf{K}_{cs}$, as shown in figure 4.12 including $\xi = 0$, 0.2, 0.5 and 0.8 cases corresponding to those in the previous sections. The initializations of spanwise coherent structures shown in figure 4.3.2 are denoted by annotations in each subfigure. For the KH instability shown in figure 4.12(a), there are actually two peaks for $\mathbf{K}_{kh}$. According to our observations of concentration structures, the first peak at $t \approx 30 - 35$ and the secondary peak at $t \approx 45 - 50$ of $\mathbf{K}_{kh}$ curves indicates the streamwise rolling-up and subsequent formation of a clear 'cat eye' shape of streamwise eddy structures. The 'hatched cup' eddy core structures shown in figure 4.7(a) start to form at about $t = 60$ when $\mathbf{K}_{cs}$ becomes comparable to decreasing $\mathbf{K}_{kh}$. At $t \approx 80 - 86$ when the $\mathbf{K}_{cs}$ reach its peak, a complete 'hatched cup' shape has developed as shown in figure 4.7(a), followed by the saturation and breakdown of entire three-dimensional structures.

When a weak cross shear is introduced, in addition to the appearances of weak spanwise 'spiral eddy wrap' structures, the durations of coherent structures are extended in the 'streamwise dominant' mode as shown figure 4.12(b). Two peaks of $\mathbf{K}_{kh}$ curves are also

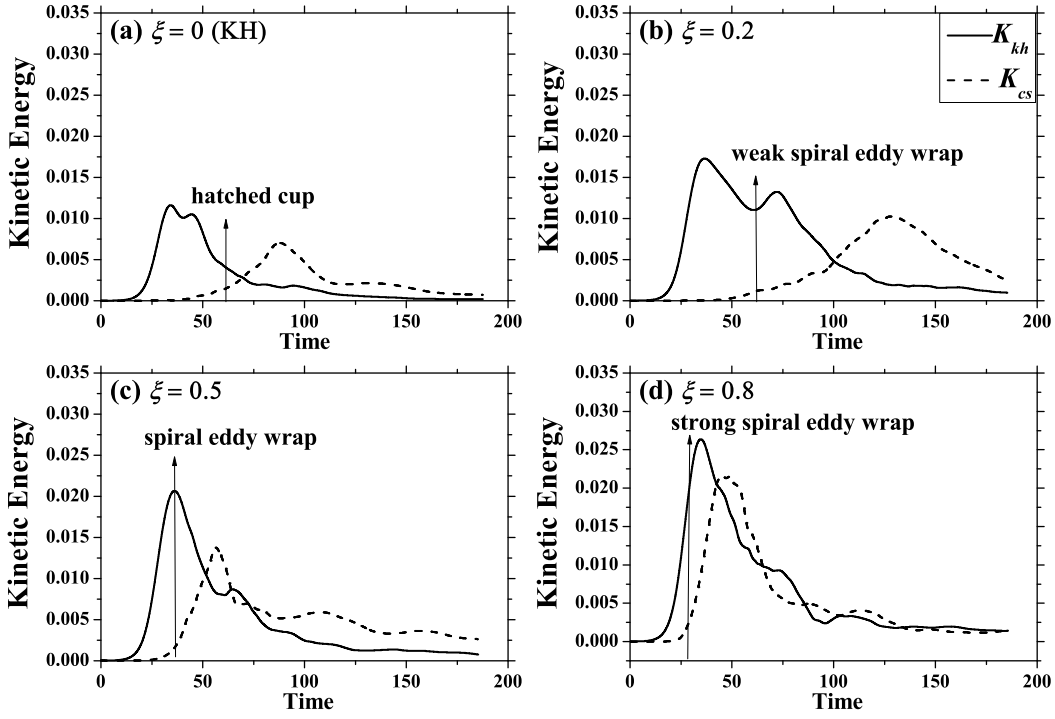

Fig. 4.12 Time series of the $\mathbf{K}_{kh}$ (solid curves) and $\mathbf{K}_{3d}$ (dash curves) and in the cases of (*a*) $\xi = 0$, (*b*) $\xi = 0.2$, (*c*) $\xi = 0.5$, and (*d*) $\xi = 0.8$, respectively. The formation of spanwise coherent structures are marked in each sub-figure, respectively.

observed in $\xi = 0.2$ cases, while compared to figure 4.12(a) the second peak occur at $t = 75$, 20 non-dimensional time units longer than the second peak of PSS flow case, therefore suggesting a extended developing period of streamwise 'cat eye' eddy in the 'streamwise dominant' mode. Meanwhile, $\mathbf{K}_{cs}$ begin to increase at $t \approx 50$, the same time when $\mathbf{K}_{cs}$ start to grow in figure 4.12(a). Yet, the spanwise flow structures in $\xi = 0.2$ become weak spanwise 'spiral eddy wrap' as shown in figure 4.4(*a*). The peak of $\mathbf{K}_{cs}$ occur at $t \approx 125 - 130$, 45-51 non-dimensional time units later than the PSS flow.

For 'balanced mode' where spanwise 'spiral eddy wrap' structures are clearly observed more comparable to streamwise 'cat eye' eddy, the evolution history of $\mathbf{K}_{kh}$ and $\mathbf{K}_{cs}$ start to interact with each other, as shown in figure 4.12(c). The most noticeable features of figure 4.12(c) is the peak of $\mathbf{K}_{cs}$ at $t \approx 55 - 60$ appear earlier than the second peak of $\mathbf{K}_{kh}$ at $t \approx 70 - 75$, indicating the formations of spanwise'spiral eddy wrap' are prior to the formations of streamwise'cat eye' shape eddy core. Our observations of flow structures

further confirm this point. Moreover, the magnitude of second peak of $\mathbf{K}_{kh}$ decrease from about 0.0125 at $\xi = 0.2$ to about 0.0075 at $\xi = 0.5$ case, implying the streamwise 'cat eye' eddy structures are less developed after the streamwise rolling-up event. Meanwhile, the peak of $\mathbf{K}_{cs}$ in $\xi = 0.5$ case further is significantly preceded from $t \approx 75$ at $\xi = 0.2$ case to $t = 60$. The coincidence between precede peak of $\mathbf{K}_{cs}$ and degrading second peak of $\mathbf{K}_{kh}$ suggest that enhancing spanwise 'spiral eddy wrap' suppress the prevent streamwise 'cat eye' eddy from further development.

In 'spanwise dominant' mode, the drastic suppressions from spanwise 'spiral eddy wrap' structures at last lead to 'internal collapse' mechanisms as shown in figure 4.8. Corresponding to 'internal collapse' in figure 4.12(d) the second peak of $\mathbf{K}_{kh}$ decay into turning point at $t \approx 75$ with magnitude of 0.01, which is only 4 percent of maximum $\mathbf{K}_{kh}$ of 0.027 at $t \approx 25 - 30$. On the contrary, remarkably increasing magnitude of $\mathbf{K}_{cs}$ at $\xi = 0.8$ are observed, with the peak magnitude now reach 0.020, nearly 80 percent of the maximum of $\mathbf{K}_{kh}$. In addition, the peak of $\mathbf{K}_{cs}$ occur very early at $t \approx 50$, when the streamwise roll-up has just developed, suggest a prompt transition to turbulence process, as predicted by linear stability analysis in 3.

Based on figure 4.12, it is noticed that in the CSS flow the the development of streawmwise flow structures always coincide with the growth of spanwise flow structures, suggesting there must be certain energy transfer occur between streamwise and spanwise flow structures. As shown in 4.5, the major contributions to energy flux in total and turbulence kinetic energy budget, during the formations of primary flow structures, depend on the rate of kinetic energy $DK_{\mathbf{all}}/Dt$, $DK'_{\mathbf{u}}/Dt$ and shear production S. The energy dissipation rate ε' only play significant role after the breakdown of coherent flow structures. On the other hand, the buoyancy B always plays insignificant roles through the entire evolution history of coherent structures of CSS flow. Therefore, the main energy transfer during the formation of primary coherent structures stage are mainly the kinetic energy transfer.

As $\mathbf{K_u}' = \mathbf{K}_{kh} + \mathbf{K}_{3d}$ always holds, to investigate the difference between $\mathbf{K}_{3d} - \mathbf{K}_{kh}$, especially the ratio $\mathbf{K}_{3d} - \mathbf{K}_{kh}/\mathbf{K_u}'$, will help to further identify the kinetic energy transfer between streamwise and spanwise coherent structures. Therefore, to further study the impact of ξ on the kinetic energy transfer between the streamwise and spanwise coherent structures, the time series of kinetic energy differences $\mathbf{K}_{3d} - \mathbf{K}_{kh}$ for ξ over $0 \leq \xi \leq 1.0$ are shown in figure 4.13. For the PSS flow case denoted by black solid curves in figure 4.13 , two peak regions of $\mathbf{K}_{3d} - \mathbf{K}_{kh}$ curve are observed separately at $t = 25 - 80$ and $t = 100 - 150$. In the first peak region at $t = 25 - 80$, two peaks corresponding to streamwise 'rolling up' and developed 'cat eye' shape cores are observed in the same way as those the two peak of $\mathbf{K}_{kh}$ in figure 4.12(a), suggesting during this time period the behaviors of $\mathbf{K}_{3d} - \mathbf{K}_{kh}$ curve

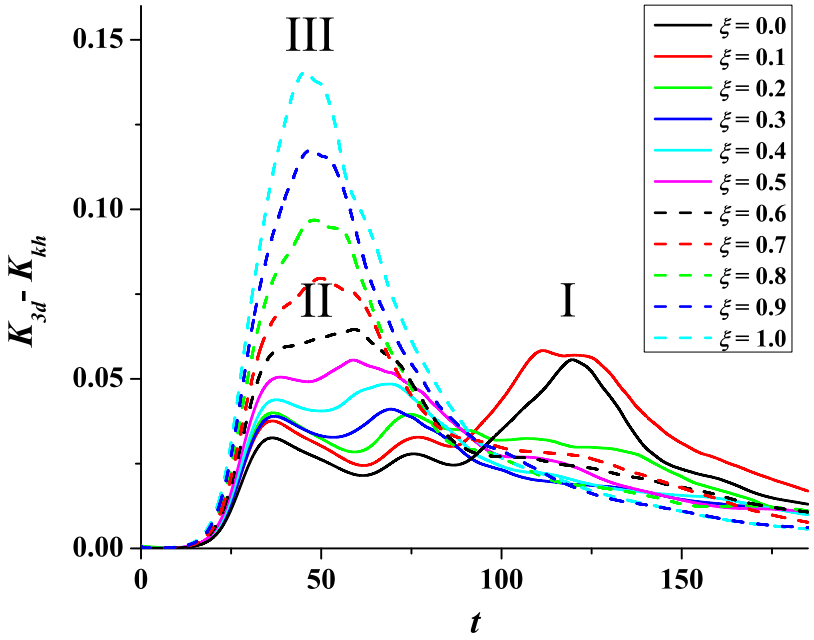

Fig. 4.13 Time series of the differences between the spanwise averaged kinetic energy $\mathbf{K}_{3d}$ and primary KH eddy kinetic energy $\mathbf{K}_{kh}$ for ξ over the range $0 \leq \xi \leq 1.0$.

follow the evolutions of primary KH 'cat eye' eddy structures. in the second peak region $t = 100 - 150$, only a single but maximum peak is observed as same as the peak of $\mathbf{K}_{cs}$ in figure 4.12(a), suggesting during this time period the $\mathbf{K}_{3d} - \mathbf{K}_{kh}$ curve reflect the evolutions of 'hatched cup' core structures. Thus, the $\mathbf{K}_{3d} - \mathbf{K}_{kh}$ curve is able to combine the features of time series of $\mathbf{K}_{kh}$ and $\mathbf{K}_{cs}$ shown in figure 4.12(a)

For the 'streamwise-dominant' mode denoted as 'I', the first peak regions with two peaks at $t = 25 - 80$ and the second peak regions at $t = 100 - 150$ are also observed. For the 'balanced' mode denoted as 'II', the only peak $\mathbf{K}_{3d} - \mathbf{K}_{kh}$ occurs at around $t = 55$ for $\xi = 0.5$ as an example when the spanwise 'spiral eddy wrap' structures coexist with the streamwise 'cat eye' structures, while the second peak regions exist in primary KH mode and 'streamwise dominant' mode disappear. For the 'spanwise-dominant' mode denoted as 'III', the similar single peak region is observed, with the maximum $\mathbf{K}_{3d} - \mathbf{K}_{kh}$ occurs at around $t = 45$ for $\xi = 0.8$ as an example, when the spanwise 'eddy wrap' structures suppress the streamwise 'cat eye' structures. The single peak regions observed in figure 4.13(c) and (d) follow the same single peak shape of $\mathbf{K}_{3d} - \mathbf{K}_{kh}$ curves in figure 4.12(c) and (d), therefore the time series of $\mathbf{K}_{3d} - \mathbf{K}_{kh}$ for strong cross shear cases can also capture the major kinetic energy features of coherent structures as same as $\mathbf{K}_{kh}$ and $\mathbf{K}_{cs}$.

Although the differences between the magnitude of the maximum peak for the 'balanced' mode, as indicated by 'II', and that for the 'streamwise-dominant' mode, as indicated by 'I', are very small, when ξ is increased to the range of the 'spanwise-dominant' mode as marked by 'III', the magnitude of the maximum peak rises rapidly and is more than twice of those for the 'streamwise-dominant' mode when ξ approaches 1. The increase in the magnitude of the maximum peak of $\mathbf{K}_{3d} - \mathbf{K}_{kh}$ with increasing ξ implies that more kinetic energy is transferred from the streamwise 'cat eye' eddy to the spanwise 'eddy wrap' structures as the cross shear becomes stronger. In addition, the maximum peaks for the 'balanced' mode appears to be more smooth and to fluctuate around the 'spanwise dominant' modes, as if the streamwise 'cat eye' eddy and the spanwise 'eddy wrap' structures compete with each other. Such fluctuations agree with the competitive features of the 'balanced' mode found in the time series of the perturbation kinetic energy as shown in figure 4.13. On the other hand, sharper maximum peaks for the 'spanwise dominant' modes shown in figure 4.13 with large positive and negative $\partial(\mathbf{K}_{3d} - \mathbf{K}_{kh})/\partial t$, suggesting that a strong kinetic energy transfer from the streamwise eddies to the spanwise eddies leads to a rapid saturation and then an equally rapid decay.

As the total perturbation kinetic energy $\mathbf{K}'_{\mathbf{u}}$ is different for each ξ case, it is necessary to introduce a non-dimensional parameter to represent the relative role of the kinetic energy transfer between the streamwise and the spanwise coherent structures. Such a dimensionless parameter, called the kinetic energy transfer ratio which is defined below, is proposed in this study,

$$\chi = \frac{\mathbf{K_{3d}} - \mathbf{K_{kh}}}{\mathbf{K'_u}} = \frac{\mathbf{K_{3d}} - \mathbf{K_{kh}}}{\mathbf{K_{3d}} + \mathbf{K_{kh}}}. \tag{4.33}$$

The time series of χ are plotted in figure 4.14 for all ξ cases considered, where the three CSS instability modes are presented in a more or less unified similar fashion. It is found from this figure that the time series of χ for $0 \leq \xi \leq 1.0$ in general involve three stages; the constant stage, the rapid growth stage and the asymptotic stage. The transition point between the constant stage and the rapid growth stage represents the onset of the kinetic energy transfer from the streamwise to the spanwise coherent structures, as $\partial(\mathbf{K}_{3d} - \mathbf{K}_{kh})/\partial t > 0$ for all ξ cases. Apparently, the spanwise 'eddy wrap' structures enable earlier transition to turbulence as the transition point between the constant stage and the rapid growth stage decreases with increasing ξ. It is further observed that the threshold of the kinetic energy transfer in the constant stage increases with increasing ξ. Interestingly, after the rapid growth stage the magnitudes of χ for all ξ cases converge to a unified value of about 0.9 in the asymptotic stage, in spite of different coherent structures and transitional paths to turbulence with varying ξ. The constant $\chi \approx 0.9$ at the asymptotic stage indicates that when they

collapse into turbulence there is little difference between a CSS flow and a PSS flow in terms of χ, perhaps due to statistically universal features of turbulence.

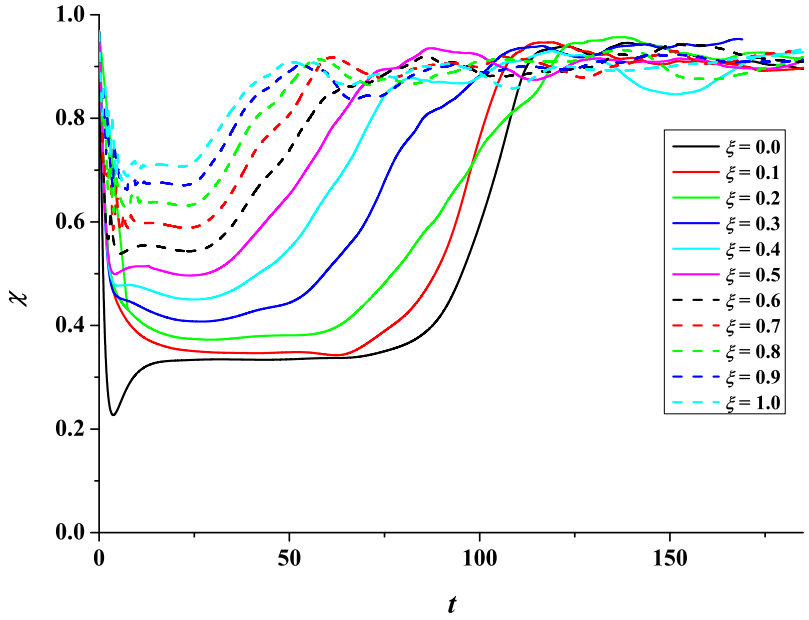

Fig. 4.14 Time series of χ for ξ over the range $0 \leq \xi \leq 1.0$.

4.3.4 Potential energy

In a sheared stratified flow where density varies in the vertical direction, the perturbed sheared flow will modify the background stratification, which reversely changes the shear dynamics by the local buoyancy induced by the local density displacement. Due to the interaction between the sheared dynamics and buoyancy, the potential energy will be transferred to the kinetic energy. As strong overturning or stirring might occur, the local denser fluid parcel will be brought upward but drop down soon due to the gravity. Thus, the potential energy involving overturning will transfer back to the kinetic energy in the form of the local buoyancy flux. With these, [42] recommended that the total potential energy P_{all} could be divided into the reversible or available potential energy P_{av} and the irreversible or background potential energy P_b, *i.e.* , the potential energy budget is,

$$P_{all} = P_{av} + P_b. \tag{4.34}$$

P_b is the potential energy created by reordering the local density parcels so that the reordered density will monotonically increase with the height, as proposed by [43]. The analysis of the

potential energy budget has been widely conducted in the studies of sheared stratified flow, such as [26, 30, 27, 33, 22, 20, 19, 23–25].

In this study, P_{all} and P_b are defined as,

$$P_{all} = -\langle bz \rangle_{xyz}, \quad P_b = -\langle b_r z \rangle_{xyz}, \tag{4.35}$$

where $b = g\Delta\rho/\rho_*$ is the buoyancy in which $\Delta\rho = \rho - \rho_*$ is the local density change with respect to the reference density ρ_* and b_r is the reordered buoyancy based on the reordered density ρ_r. Unlike some studies such as [19], ρ_* is selected as the minimum density in the domain as $\rho_* = \rho - \Delta\rho_0$ in this study. To obtain a reordered density field, each vertical $\phi(z)$ at each pair of (x,y) plane is treated as a one-dimensional column. For each vertical column, the one dimensional reordering techniques with the quick sort algorithm is conducted. Once all of the vertical density columns are reordered, the overall reordered density field is the congregation of all reodered density columns.

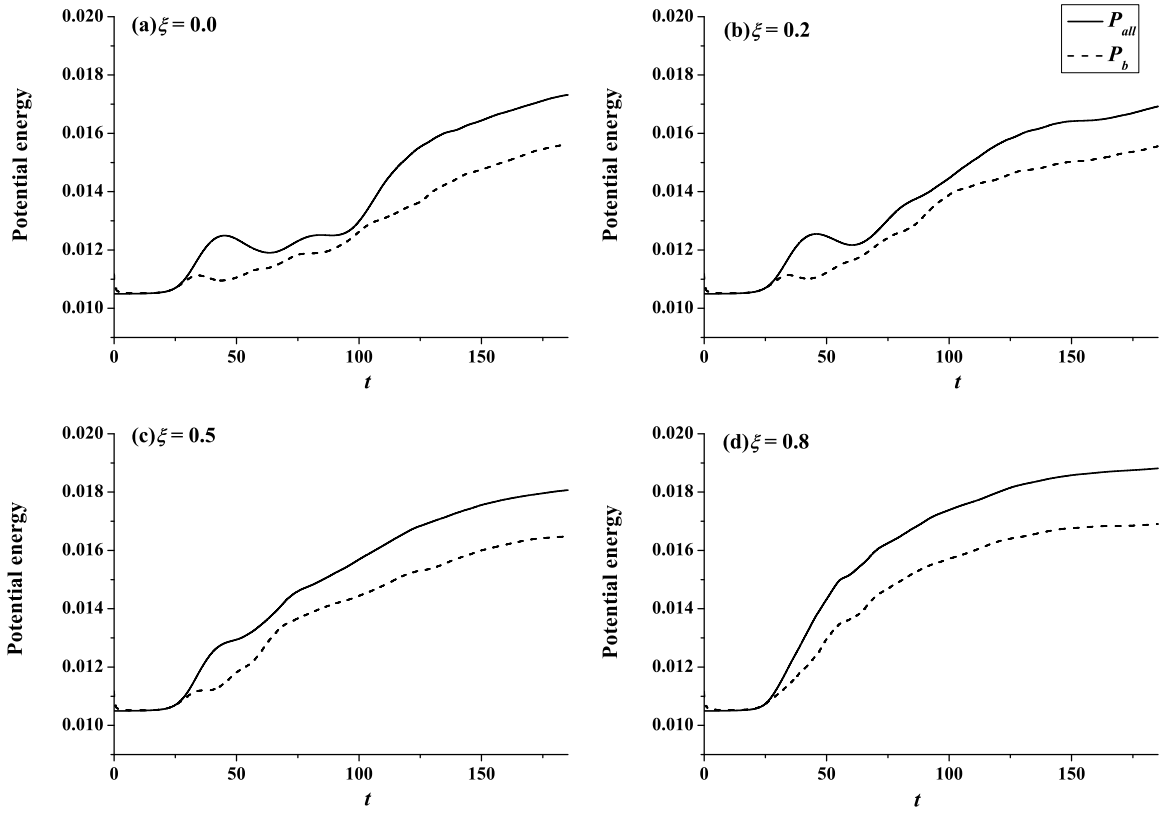

Fig. 4.15 Time series of P_{all} (solid line) and P_b (dash line) for (a) $\xi = 0$, (b) $\xi = 0.2$, (c) $\xi = 0.5$ and (d) $\xi = 0.8$.

Figure 4.15 presents the time series of P_{all} and P_b, which are made dimensionless by $(\Delta u_0)^2$, for $\xi = 0$, 0.2, 0.5 and 0.8 cases. The difference between P_{all} and P_b represents the available potential energy P_{av} that will be transferred to the kinetic energy in the form of the buoyancy flux. It is seen that at the early development stage, P_{av} is essentially zero for all ξ cases considered, indicating that there is no overturning. Subsequently, the P_{all} and P_b curves diverge, indicating that overturning occurs. The gap between the P_{all} and P_b curves varies with ξ. For the $\xi = 0$ and $\xi = 0.2$ cases, as shown in figures 4.15(a) and (b), there are two distinct periods with large gaps, representing two major P_{av} reservoirs. The first period, from $t = 31$ to around $t = 67$, corresponds to the development of the primary instability and the second one, from about $t = 103$ up to the whole turbulence stage, corresponds to the collapse of the entire coherent structures. According to the evolution history, the first gap period is the result of the 'cat eye' eddy structures, while the second gap period is the result of the chaotic turbulent flows that destroy the interfacial sheared/stratified layer and agitate the entire density field. The transitional, 'throat' region between these two gap periods relates to the three dimensionalization or transition to turbulence stage, where the length scale of flow dynamics gradually decreases yet the flow structures remain coherent. When the spanwise 'spiral eddy wrap' gradually becomes comparable to the streamwise KH eddy, as shown in figure 4.15(c), the 'throat' region shortens and becomes not very distinctive when compared to the $\xi = 0$ and $\xi = 0.2$ cases. The degrading 'throat' region agrees with the faster transition to turbulence for the case as observed in the previous sections. In the $\xi = 0.8$ case where the spanwise 'spiral eddy wrap' completely dominates, the gap between the P_{all} and P_b curves monotonically increases without a distinctive 'throat' region. This different behavior in potential energy in the $\xi = 0.8$ case is caused by the rapid transition to turbulence.

As shown in appendix 4.5, the buoyancy are insignificant in our CSS flow cases, so are the frequently used irreversible mixing flux M defined based on P_b budget as in [19]. Therefore,to further investigate the different dynamic features of the KH, 'streamwise dominant', 'balanced' and 'spanwise dominant' modes, the time series of the potential energy ratio P_b/P_{all} are presented in figure 4.16 for $0 \leq \xi \leq 1.0$. The smaller the P_b/P_{all} is, the larger the available potential energy reservoir is. With this dimensionless parameter, the characteristics of the potential energy associated with different instability modes can be more clearly seen, as shown in figure 4.16. For instance, the first and second gap periods as shown in figure 4.15(a) become two valleys in figure 4.16(a), whereas the 'throat' region in figure 4.15(a) converts to the fluctuating section in the middle above the $P_b/P_{all} = 0.95$ line in figure 4.16(a). For the 'streamwise dominant' mode with $0.1 \leq \xi \leq 0.3$ as shown in figure 4.16(b), the time series of the potential energy ratio are basically the same as those for $\xi = 0$, except for the later stage, from $t = 111$, where P_b/P_{all} increases slightly from 0.90 for $\xi = 0$ as shown in figure 4.16(a)

to 0.925 for $\xi = 0.2$ and 0.3 cases as shown in figure 4.16(b). For the 'balanced' mode as shown in figure 4.16(c), the fluctuating section for the secondary instability as shown in figure 4.16(b) reduces to a short peak region with only about 4 time units near $t = 74$, and the maximum P_b/P_{all} also reduces to 0.95. The much shorter duration of the transition to turbulence stage in the 'balanced' mode is consistent with the degradation of the 'throat' section as observed in figures 4.15(b) and (c) and the decreasing P_b/P_{all} suggests more available potential energy reservoir is created in the 'balanced' mode. For the 'spanwise dominant' mode, the features of P_b/P_{all} curves are essentially similar to those of the 'balanced' mode, with P_b/P_{all} at the secondary instability further reduced, from 0.95 to 0.925, implying that even more potential energy is available for stronger mixing in the subsequent turbulence stage. Note that the P_b/P_{all} (P_{av}/P_{all}) during the non-linear transition to turbulence stage at $t = 50-100$ decrease (increases) with ξ, corresponding to the increasing ε' with increasing ξ in figure 4.20 in appendix 4.5. Therefore, it seems that most of P_{av} transfer into turbulence energy dissipation rather than P_b as usually found in the PSS flow. Interestingly, over the whole range of $0 \leq \xi \leq 1.0$, P_b/P_{all} at the asymptotic stage approaches to 0.90, which is the same constant value found for χ in the asymptotical stage, possibly as a result of statistically universal features of turbulence as same as χ in the previous section. Therefore, P_b/P_{all} does not depend on ξ in the turbulence stage.

4.3.5 Mixedness

Another interesting issue for the CSS flow instability, that is also of significance to practical applications, is whether the mixing effect is improved when compared to the KH instability. A quantity called mixedness, M, introduced by [44] and defined below, is employed in this study as the measure to quantify the mixing effect,

$$M(z,t) = \frac{\int_0^{L_z} H(\rho-\rho_m)(\rho_b-\rho)dz + \int_0^{L_z} H(\rho_m-\rho)(\rho-\rho_t)dz}{\int_0^{L_z} H(\rho-\rho_m)(\rho_b-\rho_m)dz + \int_0^{L_z} H(\rho_m-\rho)(\rho_m-\rho_t)dz}, \tag{4.36}$$

where ρ_b, ρ_t and ρ_m are the densities at the bottom and top boundaries and at the middle interface, and the Heaviside step function $H(f)$ is defined as,

$$H(f) = \begin{cases} 1 & \text{for } f \geq 0, \\ 0 & \text{for } f < 0. \end{cases} \tag{4.37}$$

M represents the ratio between the densities with and without fluctuations, as the density fluctuation $(\rho - \rho_m)$ term in the denominator only defines the signs of constant $(\rho_b - \rho_m)$ and

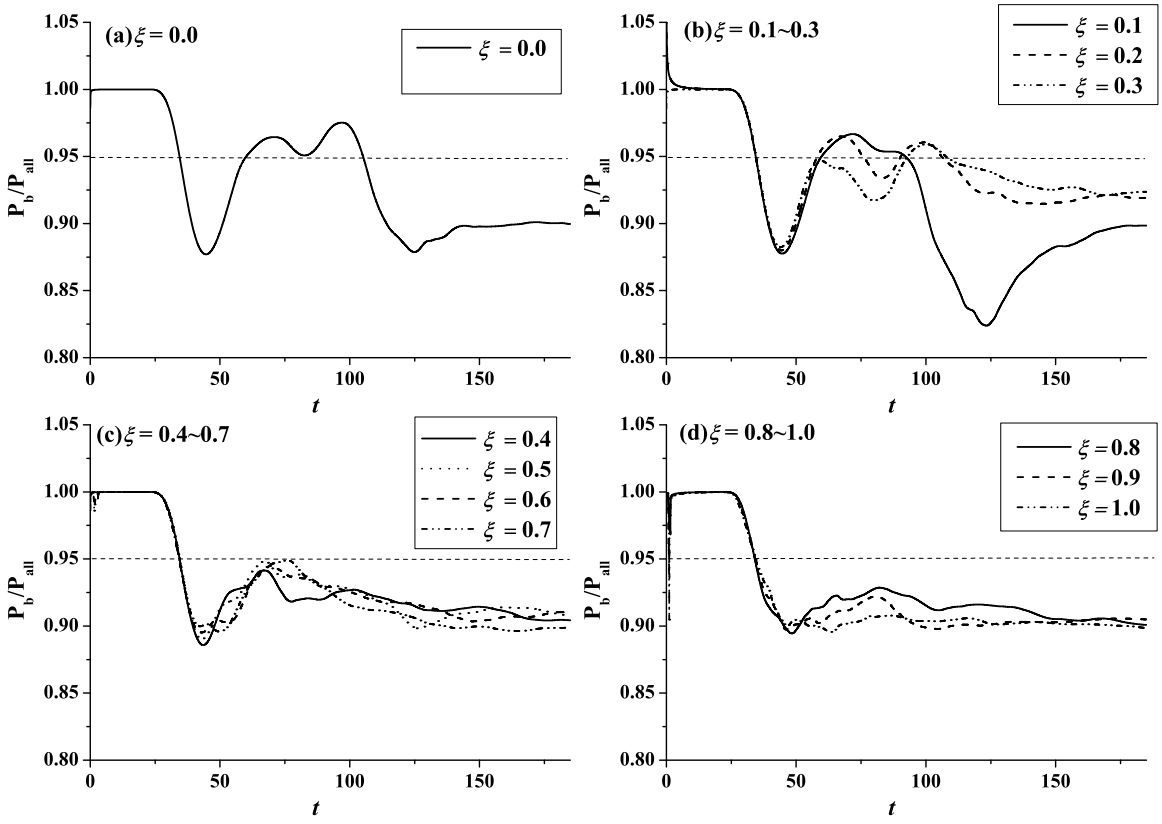

Fig. 4.16 Time series of the potential energy ratio P_b/P_{all} for (a) KH mode with $\xi = 0$, (b) 'streamwise dominant' mode with $0.1 \leq \xi \leq 0.3$, (c) 'balanced' mode with $0.4 \leq \xi \leq 0.6$, and (d) 'spanwise dominant' mode $0.17 \leq \xi \leq 1.0$.

$(\rho_m - \rho_t)$, but both the magnitudes and the signs of the density fluctuations are included in the numerator. The mixedness thickness, δ_θ, is then obtained by the integration of M, *i.e.* ,

$$\delta_\theta = \int_0^{L_z} M(z,t)dz. \tag{4.38}$$

Figure 4.17(a) presents the time series of δ_θ for ξ varying over the range $0 \leq \xi \leq 1.0$. For each ξ value, three development stages are observed for δ_θ; a short slow growth stage (when $t \lesssim 31$), a rapid growth stage (from $t \approx 31$ to $t \approx 130 \sim 150$), and finally an asymptotic stage (when $t \gtrsim 130 \sim 150$). In the slow growth stage, δ_θ is small and is essentially the same for all ξ values. The transition from the slow growth stage to the rapid one also occurs at almost the same instant for all ξ cases considered (at $t \approx 31$). In the rapid growth stage, δ_θ becomes quite significant, and in general increases with ξ, indicating that during this stage an increment in ξ will result in a very effective improvement in mixing. For example, at $t = 92$, the values of δ_θ at $\xi = 0.2$, 0.4, 0.6, 0.8, and 1.0 are about 1.32, 1.79, 1.82, 1.97,

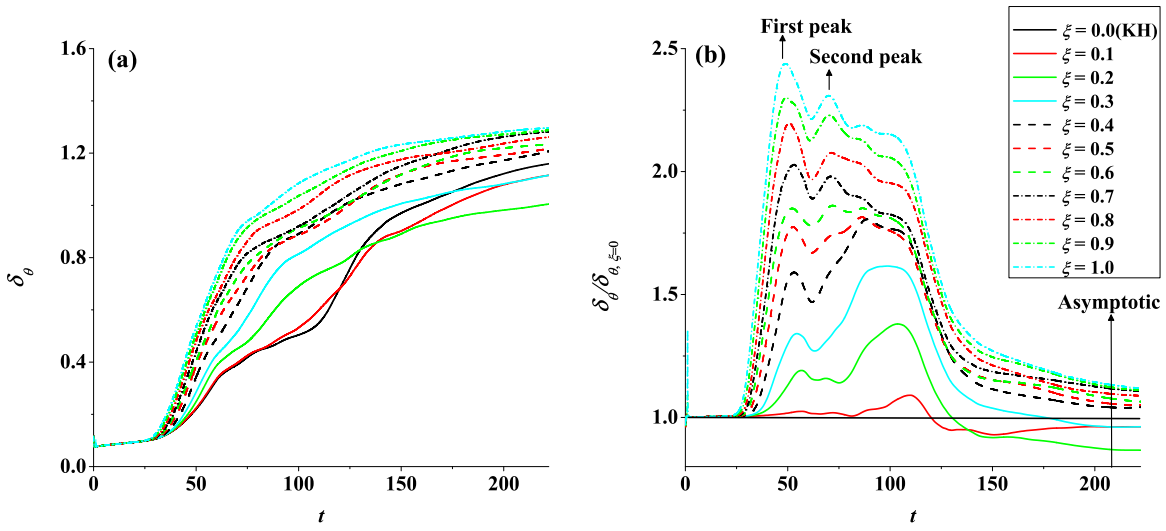

Fig. 4.17 Time series of the mixedness thickness δ_θ at $0 \leq \xi \leq 1.0$ in (a) dimensional form and (b) normalized form normalized by $\delta_{\theta,\xi=0}$, which is the δ_θ of the PSS flow with $\xi = 0$.

and 2.15, respectively, of the value of δ_θ at $\xi = 0$. Hence, it appears that the CSS flow instability is far more effective in terms of the mixing effect than the traditional KH instability during the rapid growth stage. This suggests that, at a certain stage of the flow instability (*i.e.* , at the rapid growth stage), the introduction of a spanwise velocity of a comparable magnitude can produce the spanwise eddy structures which will significantly improve the mixing effect. This is in line with the experimental observations by AV97 and numerical observations by LSY00. Nevertheless, there are large differences between the $\xi \lesssim 0.2$ cases and the $\xi > 0.2$ cases in terms of the transition from the rapid growth stage to the asymptotic stage, with the $\xi \leq 0.2$ cases commencing their asymptotic behavior at the time instants comparable to the KH instability, whereas the $\xi > 0.2$ cases commencing their asymptotic behavior much earlier. It is also observed that at the asymptotic stage introducing a spanwise basic flow does not always improve the mixing effect significantly and can even lead to a smaller δ_θ. For example, δ_θ at $\xi \leq 0.3$ is smaller than that at $\xi = 0$. After $t \approx 165$, there is little difference between the values of δ_θ for $\xi \geq 0.4$ cases, which indicates that introducing a large spanwise velocity has no obvious advantages in terms of the mixing effect at the asymptotic stage. Hence, the selection of the specific value of ξ to achieve the best mixing effect should be determined by whether the primary mixing (corresponding to the rapid growth stage) or turbulent mixing (corresponding to the asymptotic stage) being targeted by a specific application.

The results presented in figure 4.17(a) can be re-cast by normalizing δ_θ with $\delta_{\theta,\xi=0}$, which is for the KH instability case, as shown in figure 4.17(b). The improvement of the

mixing effect during the rapid growth stage associated with the introduction of a spanwise flow is very evident from this figure. It is seen that $\delta_\theta/\delta_{\theta,\xi=0}$ increases with increasing ξ at the whole rapid growth stage, with the maximum δ_θ at $\xi = 1.0$ nearly 2.50 that of δ_θ at $\xi = 0.0$. Even a small increment of ξ, from 0.0 to 0.2, will lead to a nearly 20% increase of δ_θ for almost the whole rapid growth stage. However, at the later asymptotic stage, the introduction of a larger spanwise velocity, or even any spanwise velocity at all, will have little advantage in terms of the mixing effect, as observed above.

In the water tank tilting experiments of AV97, the intensity of the basic cross sheared flows was controlled in terms of the percentage of the cross shear with respect to the main shear, which is exactly the same as ξ defined in this study. The time AV97 used was the ratio of the real time and the overturning time scale of the KH eddy $t_{kh} = \tilde{\alpha}/(\Delta u_0/2)$. In the current study, the dimensionless overturning time scale t_{kh} is about 3.7. With t/t_{kh}, it is possible to compare the current numerical results with the experimental results of AV97. In AV97, the initial record of the normalized mixedness thickness $\delta_\theta/\delta_{\theta,\xi=0}$ started from the first visible observation of the 'large-scale KH eddy' as reported by the authors. However, 'large-scale' is quite ambiguous because no precise criteria were specified in their work to define it. Thus it is very difficult to identify the same starting point for t/t_{kh} as that in AV97. To solve this problem, the current study artificially creates the coincidence of the times at the maximum $\delta_\theta/\delta_{\theta,\xi=0}$ between the experimental results of AV97 and the DNS results of the current study, and then uses this time for the maximum $\delta_\theta/\delta_{\theta,\xi=0}$ as the reference point for plotting the whole time series of the experimentally and numerically obtained $\delta_\theta/\delta_{\theta,\xi=0}$. The results are presented in figure 4.18, where the time series of the normalized mixedness thickness $\delta_\theta/\delta_{\theta,\xi=0}$ at $\xi = 0.2$, 0.25 and 0.3 obtained by the DNS simulation and that at $\xi = 0.25$ obtained by the experiments of AV97 are shown. In this figure, the original coordinate of t/t_{kh} of figure 26(b) of AV97 is also plotted at the top, where the zero point denotes the moment when the 'large-scale Kelvin-Helmholtz instability is first visible'. The numerical results in general agree well with the experimental results, over nearly the whole span of t/t_{kh}. The DNS curve for $\xi = 0.25$, which is the same cross shear ratio as used in the experiments of AV97, agrees very well with the experimental data until $t/t_{kh} \approx 18$, with a few experimental points fluctuating between the DNS curves for $\xi = 0.25$ and $\xi = 0.3$. In AV97, the cross shears were introduced by tilting the water tank once the KH eddy developed, and the momentum introduced from the initial tilting would inevitably modify the cross shears during the experiments, implying that $\xi = 0.25$ introduced at the beginning might fluctuate due to the imperfect experimental conditions, such as the water tank boundary. This could possibly be the main reason why the experimental data from AV97 fluctuate between the DNS curves for $\xi = 0.25$ and $\xi = 0.3$ at the later stage.

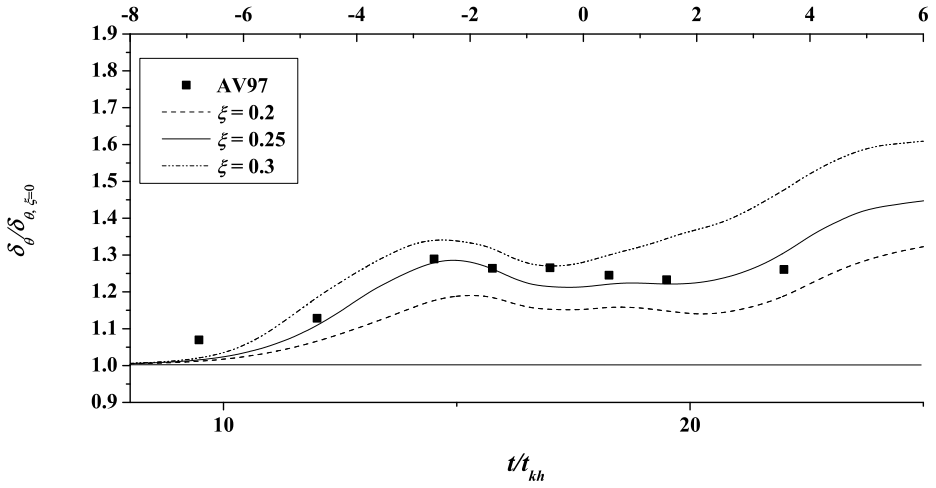

Fig. 4.18 Comparison between the time series of the normalized mixedness thickness $\delta_\theta/\delta_{\theta,\xi=0}$ at $\xi = 0.2$, $\xi = 0.25$ and $\xi = 0.3$ obtained by the DNS simulation and that obtained by the experiments of AV97 at $\xi = 0.25$. The horizontal black solid line denotes the KH instability case at $\xi = 0$.

4.4 Discussion and conclusions

Traditionally, the dynamics of turbulence transition in sheared stratified flows has been considered mainly through PSS flows. The general approach to investigate the transition to turbulence in two dimensional PSS flows has been through examining how a two-dimensional primary structures develop how subsequent three dimensionalization is achieved (with or without secondary instabilities)and how turbulence arises from the collapse of the developed three-dimensional structures. As more than one horizontal basic velocity components are introduced in a three dimensional CSS flow, the dynamics of turbulence transition in such a flow exhibits more complicated features, in that primary instability arises as three-dimensional coherent structures and could follow three dimensionalization routes even the all possibility of the secondary instabilities are suppressed. These different routes to turbulence along with different dynamic features are determined by the cross shear ratio ξ, a unique parameter for the CSS flow configuration.

A series of DNS were carried out to study the influence of ξ on the coherent structures of the CSS flow instability in a weakly stratified environment over the range $0 \leq \xi \leq 1.0$, with a clean setting to suppress all potential secondary instabilities based on previous experiences in the study of the PSS flow. The results demonstrate that the spanwise 'spiral eddy wrap' structures and the streamwise 'cat eye' eddy coexist in a CSS flow, and the interactions between them give rise to several distinctive flow instability modes leading to turbulence,

including the 'streamwise-dominant' mode with $0.1 \leq \xi \leq 0.3$, the 'balanced' mode with $0.4 \leq \xi \leq 0.6$, and the 'spanwise-dominant' mode with $0.7 \leq \xi \leq 1.0$. It is found that the prominent features in CSS flows are the spanwise 'spiral eddy wrap' structures, which have not been reported in the literature before. The analysis of the kinetic energy and potential budget in CSS flows reveals distinctively different dynamic features for the KH mode and the three CSS instability modes. In particular, the evolution history of $\mathbf{K}_{kh}$, $\mathbf{K}_{cs}$ and the kinetic energy difference $\mathbf{K}_{3d} - \mathbf{K}_{kh}$ demonstrates the significant kinetic energy variations and transfer from the streamwise KH instability to the spanwise 'eddy wrap' eddy structures in a CSS flow. The results also demonstrate that the evolution of the mixedness thickness in a CSS flow undergoes three distinct stages, *i.e.* , a short slow growth stage, a rapid growth stage, and an asymptotic stage. The mixing effect in CSS flows is found to be profound only in the rapid growth stage and increase with increasing ξ, but not significant in the other two growth stages, when compared to that in PSS flows where $\xi = 0$.

ξ introduced in this study is not only a parameter to describe the interaction between the two types of primary structures, but also has practical significance. In nature, the cross shear created by the spanwise flow can be either global or local. The intensity of local cross shear is approximately within $0 \leq \xi \leq 0.3$ based on the experimental records in AG97. Such an intensity of cross shear could be produced by different sources in nature and engineering. For instance, the weak cross shear could be produced by small tilting angle of oblique topography as simulated by the water tank experiment in AG97 and small angle between the velocities at the top and bottom flow layers in estuary system Despite different ways to introduce the cross shear, a good agreement between the DNS results in this study and the experimental results of AG97 at $\xi = 0.25$ was found, indicating that there are certain general features for the CSS flows with a local cross shear. These features might be similar to those found in the 'streamwise-dominant' mode in this study. Although there are no experimental reports for CSS flows with a large cross shear, for the CSS flows such as large-scale currents in ocean or atmospheric boundary layers, a 'balanced' or a 'spanwise-dominant' mode with $\xi > 0.3$ might also exist. Therefore, the CSS flow instability modes found in this study should be verified by further experimental works with stronger spanwise shears.

Over the whole range of ξ considered ($0 \leq \xi \leq 1$), the CSS flows are found to enhance the mixing effects in the rapid growth stage, which is in agreement with the experimental result of AG97 and the numerical results of LSY00. However, this study also demonstrated that the enhancement of the mixing effects through the introduction of the spanwise shear is not significant at the late asymptotic stage, which was not reported by AG97 and LSY00. Similarly, dynamic features in terms of the kinentic energy ratio χ and the potential energy ratio P_b/P_{all} are found to be different in the primary stage and in the turbulence (asymptotic)

stage for the three CSS instability modes. In the primary stage, χ and P_b/P_{all} are dependent on ξ, while in the asympototic stage, both χ and P_b/P_{all} approach a constant value of 0.9, implying that they are independent of ξ.

This chapter only conducted a preliminary study on the instability and coherent structures in CSS flows in a weakly stratified environment. The effect of stratification, in terms of Ri_0, will be studied in the next chapter. Nevertheless, it is apparent that much more further work must be done in order to obtain a better understanding of the instability and coherent structures in CSS flows to be significantly extended to cover more geophysical and industry settings in the future. For instance, only the CSS flow instability structures with a single wavelength are studied in this study. If the computational domain is extended to include multiple wavelengths, which is much closer to large scale geophysical and engineering scenarios, the instability structures may involve more complicated mechanisms such as the pairing between adjacent coherent structures.

4.5 Appendix: Kinetic energy budget test

The total kinetic energy budget is:

$$\frac{DK_{all}}{Dt} = B - \varepsilon. \tag{4.39}$$

where total energy dissipation rate ε and buoyancy flux B are defined as:

$$\varepsilon = 2\nu s_{ij}s_{ij}, \quad B = \langle b'w' \rangle_{xyz} \tag{4.40}$$

and

$$s_{ij} = \frac{\partial u_i}{\partial x_j} + \frac{\partial u_j}{\partial x_i} \tag{4.41}$$

Figure 4.19 shows the times series of total kinetic energy budget for $\xi = 0$, 0.2, 0.5 and 0.8, respectively. For four cases shown here, the total kinetic energy budget 4.39 are generally in closure. For other ξ cases investigated in this study, the closure of 4.39 are also found. Therefore, the DNS results in this study should be sufficiently accurate. Note that the contributions of buoyancy B is insignificant except the initiations of streamwsie rolling-up around $t = 25$ as shown in four ξ cases in figure 4.19 and other ξ cases not shown here. As a result, the balance of total kinetic energy are conserved by DK_{all}/Dt and ε. This satisfy the weakly stratified environment settings in this study, which aims to minimize the buoyancy

effects and emphasize the shear dynamics only. For the two major energy reservoirs, the evolution of kinetic energy will describe the energy features of coherent flow structures.

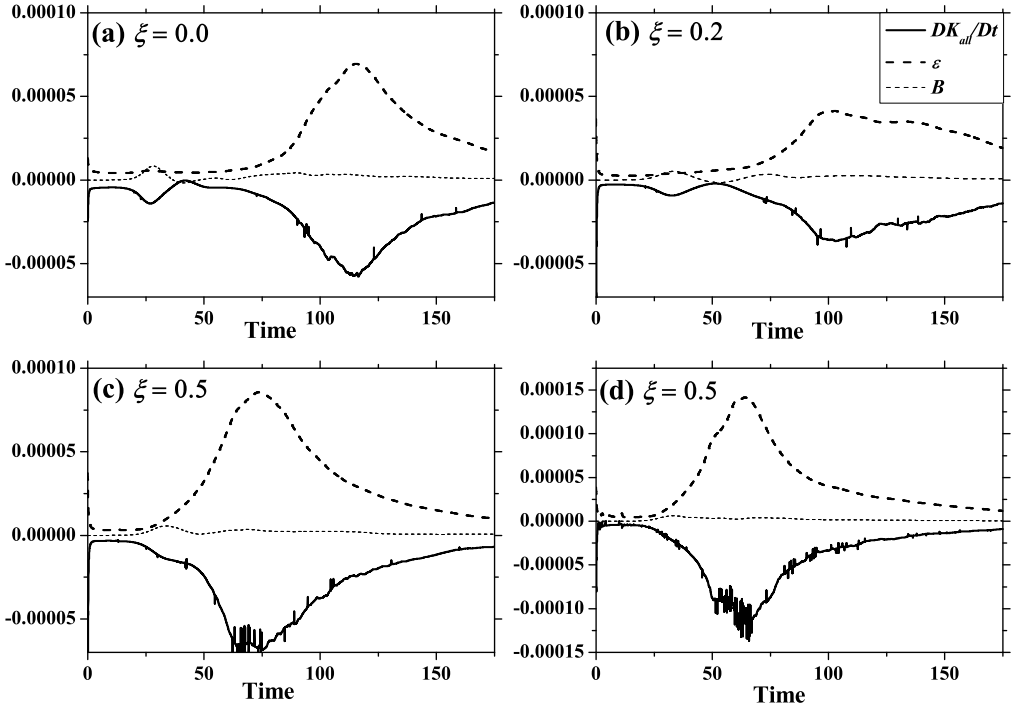

Fig. 4.19 Time series of total kinetic energy budget, where DK_{all}/Dt, B and ε are denoted by solid line, thick dash line and thin dash line, respectively

In addition to total kinetic energy budget 4.39, this study also examine the turbulence kinetic energy budget:

$$\frac{DK'_{\mathbf{u}}}{Dt} = S + B - \varepsilon' - \frac{\partial T}{\partial x_i}. \tag{4.42}$$

where the turbulence shear production, defined as:

$$S = -\langle u'_i u'_j \rangle_{xyz} \frac{\partial \langle u_i \rangle_{xyz}}{\partial x_j} \tag{4.43}$$

perturbation energy dissipation rate, defined as:

$$\varepsilon' = 2\nu s'_{ij} s'_{ij}, \quad s'_{ij} = \frac{\partial u'_i}{\partial x_j} + \frac{\partial u'_j}{\partial x_i} \tag{4.44}$$

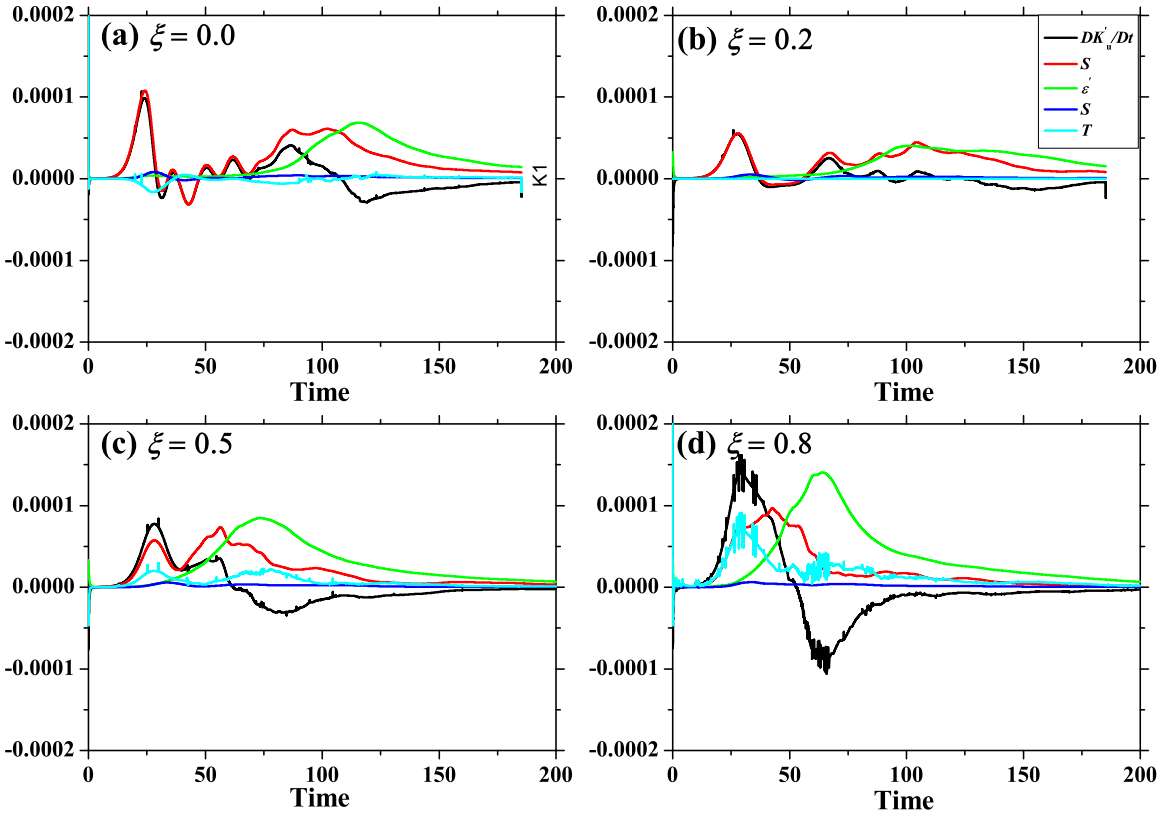

Fig. 4.20 Time series of turbulence kinetic energy budget, where DK_{per}/Dt,S,ε', B and T are denoted by different lines as shown in the legend, respectively

and turbulence kinetic energy transport. defined as:

$$T_i = \frac{1}{2}\langle u_i' u_j' u_j' \rangle_{xyz} + \langle u_i' u' \rangle_{xyz} - \frac{2}{Re_0}\langle u_j' s_{ij}' \rangle_{xyz} \tag{4.45}$$

Figure 4.20 shows the time series of $\frac{DK_{\mathbf{u}}'}{Dt}$, S,B,ε' and $\frac{\partial T}{\partial x_i}$ in turbulence kinetic energy budget for $\xi = 0$, 0.2, 0.5 and 0.8, respectively. As same as the total kinetic energy budget, the turbulence kinetic energy budget 4.42 keep closure for all cases of DNS runs. Similar to total kinetic energy budget, the buoyancy B play insignificant role. It is observed in figure 4.20 that during the formation of primary coherent structures before ε' become significant, nearly all of the $DK_{\mathbf{u}}'/Dt$ come from S, suggesting that the shear dynamics in terms of S dominate in the formation of primary coherent structures. As ε' start to increase to the peaks, the primary coherent structures generally become saturated and begin to breakdown into turbulent state. Based on dominance of kinetic energy terms in kinetic energy budget 4.39 and 4.42, the main

energy transfer sources during the formation of primary coherent structures are the kinetic energy transfer, rather than buoyancy and energy dissipation.

References

[1] PELTIER, J. S. & DAN, S. H. 2003 *Stability and Transition in Shear Flows: Chapter 9 Transition to Turbulence*. Springer.

[2] MOHAMED, G. H. 2000 *Flow Control: Passive, Active and Reactive Flow Management* . Cambridge University Press.

[3] FERNANDO H. J. S. 1991 Turbulent mixing in stratified fluids. *Annu. Rev. Fluid Mech.* **23**, 455–493.

[4] IVEY, G. N., WINTERS K. B. & KOSEFF J. R. 2008 Density stratification, turbulence, but how much mixing? *Annu. Rev. Fluid Mech.* **40**, 169–184.

[5] TAYLOR, G. I. 1931 Effect of variation in density on the stability of superposed streams of fluid. *Proc. Roy. Soc. London Ser. A.* **132**, 499–523.

[6] GOLDSTEIN, S. 1931 On the stability of superposed streams of fluids of different densities. *Proc. Roy. Soc. London Ser. A.* **132**, 524–548.

[7] MILES, J. W. 1961 On the stability of heterogeneous shear flows. *J. Fluid Mech.* **10**(4), 496–508.

[8] HOWARD, L. N. 1961 Note on a paper of John W. Miles. *J. Fluid Mech.* **10**(4), 509–512.

[9] HAZEL, P. 1972 Numerical studies of the stability of inviscid stratified shear flows. *J. Fluid Mech.* **51**, 39–61.

[10] HOLMBOE, J. 1962 On the behavior of symmetric waves in stratified shear layers. *Geophys. Publ.* **24**, 67–113.

[11] CORCOS, G. M. & SHERMAN, F. S. 1984 The mixing layer: deterministic models of a turbulent flow. Part 1. Introduction and the two-dimensional flow. *J. Fluid Mech.* **139**, 29–65.

[12] CORCOS, G. M. & LIN, S. J. 1984 The mixing layer: deterministic models of a turbulent flow. Part 2. The origin of the three-dimensional motion. *J. Fluid Mech.* **139**, 67–95.

[13] LIN, S. J & CORCOS, G. M. 1984 The mixing layer: deterministic models of a turbulent flow. Part 3. The effect of plane strain on the dynamics of streamwise vortices. *J. Fluid Mech.* **141**, 139–178.

[14] ROGERS, M. M. & MOSER, R. D. 1992 The three-dimensional evolution of a plane mixing layer: the Kelvin-Helmholtz rollup. *J. Fluid Mech.* **243**, 183–226.

[15] MOSER, R. D. & ROGERS, M. M. 1993 The three-dimensional evolution of a plane mixing layer: pairing and transition to turbulence. *J. Fluid Mech.* **247**, 275–320.

[16] THORPE, S. A. 1973 Turbulence in stably stratified fluids: a review of laboratory experiments. *Bound. Layer Meteorol.* **5**, 95–119.

[17] THORPE, S. A. 1985 Laboratory observations of secondary structures in Kelvin-Helmholtz billows and consequences for ocean mixing. *Geophys. Astrophys. Fluid Dyn.* **34**, 175–199.

[18] KLAASSEN, G. P. & PELTIER, W. R. 1989 The role of transverse secondary instabilities in the evolution of free shear layers. *J. Fluid Mech.* **202**, 367–402.

[19] CAULFIELD, C. P. & PELTIER, W. R. 2000 The anatomy of the mixing transition in homogeneous and stratified free shear layers *J. Fluid Mech.* **413**, 1–47.

[20] PELTIER, W. R. & CAULFIELD, C. P. 2003 Mixing efficiency in stratified shear flows. *Annu. Rev. Fluid Mech.* **35**, 135–167.

[21] STAQUET, C 1995 Two-dimensional secondary instabilities in a strongly stratied shear layer. *J. Fluid Mech.* **296**, 73–126.

[22] SMYTH, W. D. 2003 Secondary Kelvin-Helmholtz instability in weakly stratified shear flow. *J. Fluid Mech.* **487**, 67–98.

[23] MASHAYEK, A. & PELTIER, W. R. 2012a The 'zoo' of secondary instabilities precursory to stratified shear flow transtion. Part 1. Shear aligned convection, pairing, and braid instabilities. *J. Fluid Mech.* **708**, 5–44.

[24] MASHAYEK, A.& PELTIER, W. R. 2013 Shear-induced mixing in geophysical flows: does the route to turbulence matter to its efficiency? *J. Fluid Mech.* **725**, 216–261.

[25] MASHAYEK, A., CAULFIELD, P. & PELTIER, W. R. 2013 Time-dependent, non-monotonic mixing in stratified turbulent shear flows: implications for oceanographic estimates of buoyancy flux *J. Fluid Mech.* **736**, 570–593.

[26] SMYTH, W. D. & MOUM, D. J. 2000a Anisotropy of turbulence in stably stratified mixing layers. *Phys. Fluids* **12**, 1343–1362.

[27] SMYTH, W. D., MOUM, D. J. & CALDWELL, D. 2001 The efficiency of mixing in turbulent patches: Inferences from direct simulations and microstructure observations. *J. Phys. Oceanogr.* **31**, 1969–1992.

[28] PRASTOWO, T., GRIFFITHS, R. W., HUGHES, G. O., & HOGG, A. M. 2008 Mixing efficiency in controlled exchange flows. *J. Fluid Mech.* **600**, 235-244.

[29] MASHAYEK, A. & PELTIER, W. R. 2012b The 'zoo' of secondary instabilities precursory to stratified shear flow transition. Part 2. The influence of stratication. *J. Fluid Mech.* **708**, 45–70.

[30] SMYTH, W. D. & MOUM, D. J. 2000b Length scales of turbulence in stably stratified mixing layers. *Phys. Fluids* **12**, 1327–1342.

[31] LIN, J., SHAO, X. & YU, Z. 2000 Numerical research on coherent structures in a mixing layer with cross-shear. *Acta Aeronautica et Astronautica Sinic* **21**(1), 13–20.

[32] ATSAVAPRANEE, P. & GHARIB, M. 1997 Structures in stratified plane mixing layers and the effects of cross-shear. *J. Fluid Mech.* **342**, 53–86.

[33] SMYTH, W. D. & WINTER, K. B. 2002 Turbulence and mixing in Holmboe waves. *J. Phys. Oceanogr.* **33**, 694–711.

[34] KIRKPATRICK, M. P. 2013 *The PUFFIN Manual: An Engineering and Environmental Fluid Dynamics Simulation Model*, The University of Sydney.

[35] VAN DER VORST, H. A. 1992 Bi-CGSTAB: A fast and smoothly converging variant of Bi-CG for the solution of nonsymmetric linear systems. *SIAM J. Sci. and Stat. Comput.* **13**, 631-644.

[36] PRESS, W. H., TEUKOLSKY, S. A., VETTERLING, W. T. & FLANNERY, B. P. 2007 *Numerical Recipes: The Art of Scientific Computing.* (3rd Edition), Cambridge University Press.

[37] RANGA-DINESH, K. K. J., KIRKPATRICK, M. P. & JENKINS, K. W. 2009 Identification and analysis of instability in non-premixed swirling flames using LES. *Combustion Theory & Modelling* **13**, 947–971.

[38] RANGA-DINESH, K. K. J., KIRKPATRICK, M. P. & JENKINS, K. W. 2010 Investigation of the influence of swirl on a confined coannular swirl jet. *Computers & Fluids* **39**, 756–767.

[39] KIRKPATRICK, M. P., ARMFIELD S. W. & WILLIAMSON, N. 2012 Shear driven purging of negatively buoyant fluid from trapezoidal cavities and depressions. *Phys. Fluid.* **24**, 025106.

[40] DITTKO, K., KIRKPATRICK M. P. & ARMFIELD, S.W. 2013 Three dimensional simulation of natural convection in a reservoir sidearm. *Phys. Fluid.* **25**, 025105.

[41] XIAO, Y., LIN, W., ARMFIELD, S. W., KIRKPATRICK. M. P. & HE, Y. 2014 Hydrodynmaic stability analysis on inviscid cross sheared stratified flows. in *Proc. 19th Australasian Fluid Mech. Conf.*, 8-11 December, 2014, Melbourne, Australia, paper no 82.

[42] WINTERS, K., LOMBARD, P., RILEY, J., & D'ASARO, E. A. 1995 Available potential energy and mixing in densitystratified fluids. *J. Fluid Mech.* **289**, 115-128.

[43] THORPE, S. A. 1977 Turbulence and mixing in a Scottish loch. *Philos. Trans. R. Soc. London Ser. A* **286**, 125–181.

[44] KONRAD, J. H. 1976 An experimental investigation of mixing in two-dimensional turbulent shear flows with applications to diffusion-limited chemical reactions. PhD thesis, California Institue of Technology.

[45] SQUIRE, H. B. 1933 On the stability of three-dimensional disturbances of viscous flow between parallel walls. *Proc. Roy. Soc. London Ser. A.* **142**, 621–628.

[46] DRAZIN, P. G. & REID, W. H. 2004 *Hydrodynamic Stability* (second edition). Cambridge University Press.

[47] MOLER, C. B. & STEWART, G. W. 1973 An algorithm for generalzied matrix eigenvalue problems. *SIAM J. Numer. Anal.* **10**, 241–256.

Chapter 5

Stratification effects on turbulent mixing of CSS flow

Some results of this chapter are presented in the following publication:

1. XIAO, Y., LIN, W., MCCORMARC, J., Y. HE, ARMFIELD, S. W. & KIRKPATRICK, M. P. 2015 Turbulent mixing in cross sheared stratified flow. in *Proceedings of the International Symposium on Turbulence and Shear Flow Phenomena (TSFP-9)*, 30 June - 3 July 2015, Melbourne, Australia, Paper ID: 4C-5.

5.1 Introduction

To further understand the dynamic features especially the mixing effects improved by the CSS flow, this chapter extends the work presented in the previous chapter, from weakly stratified environment with the bulk Richardson number $Ri_0 = 0.01$ to stronger stratified environments with $Ri_0 = 0.01 \sim 0.20$, over the range of $\xi = 0 \sim 1.0$ so that a complete map of dynamics and mixing of CSS flow can be described in a wide $[\xi - Ri_0]$ space. Two major questions will be answered; firstly, are dynamic features found in weakly stratified environment described in the previous chapter the general signatures of the CSS flow instability in a wide of stratified environments? secondly, does the intensity of the background stratification quantified by Ri_0 have the same influences on CSS flow as that in PSS flow?

To answer these two questions, the governing parameter group G which represent the mixing effects and energy transfer, as will be described subsequently, will be studied as functions of ξ and Ri in this chapter. More specifically, G includes mixedness thickness introduced by Konrad [1], subdivisions of kinetic energy budget developed by Caulfield & Peltier [2], potential energy budget introduced by Winter et al. [3] and other new parameters

used to describe the dynamics of CSS flow. However, only the first two are addressed in this chapter.

As these three parameters G, ξ and Ri are involved in this study, the parameter space is inherently three-dimensional. In order to simplify the analysis and clarify the influences of ξ or Ri, all parameters included in the governing parameter group G will be normalized with two configurations; (a) G is normalized by $G_{\xi=0.0}$, which is the value of G at $\xi = 0$ (that is, the PSS flow case), and (b) G is normalized by $G_{Ri=0.01}$, which is the value of G at $Ri = 0.01$. Configuration (a) aims to take ξ as the main parameter to describe the features of CSS flow with Ri as a subordinate parameter, while Configuration (b) aims to play the inverse role. In Configuration (a), three CSS instability modes found in the previous chapter will be further studied to check if they are general modes in CSS flow in strong stratified environments as well. In Configuration (b), the influence of background stratification in terms of Ri on the behaviors of flow dynamics will be investigated. For the main parameter in each configuration, a sufficient number of values will be selected, with only a few typical values for the subordinate parameters. Together with Configurations (a) and (b), the dynamic map of CSS flow in the $[\xi, Ri]$ space will be revealed in terms of a number of correlations of $G \sim \xi$ and $G \sim Ri$, along with typical features in coherent structures in the $[\xi, Ri]$ space.

5.2 Methodology

The governing equations for DNS are the continuity, Navier-Stokes, and density equations for incompressible flows with the Boussinesq approximation, which are written in the Cartesian coordinates (x, y and z) as follow:

$$\nabla \cdot \mathbf{u} = \mathbf{0} \tag{5.1}$$

$$\frac{\partial \mathbf{u}}{\partial t} + \mathbf{u} \cdot \nabla \mathbf{u} = -\nabla \frac{p}{\bar{\rho}} + g \frac{\rho - \bar{\rho}}{\bar{\rho}} \vec{k} + \nu \nabla^2 \mathbf{u} \tag{5.2}$$

$$\frac{\partial \rho}{\partial t} + \mathbf{u} \cdot \nabla \rho = \kappa \nabla^2 \rho \tag{5.3}$$

where $\mathbf{u}$ is the dimensional velocity vector, whose components in the x, y, z directions are u, v, w, t is time, p is pressure, ρ is density, ν and κ are the kinematic viscosity and thermal diffusivity of fluid, g is the gravitational acceleration, and $\bar{\rho}$ is a reference density with a value of 1027 kg/m^3. In the DNS, $\nu = 9.95 \times 10^{-7}$ m^2/s is used.

The differential operator ∇ is $\nabla = (\partial/\partial x)\vec{i} + (\partial/\partial y)\vec{j} + (\partial/\partial z)\vec{k}$, where $\vec{i}$, $\vec{j}$ and $\vec{k}$ represent the unit vector in x, y and z directions. The Laplacian operator ∇^2 is $\nabla^2 = (\partial^2/\partial x^2)\vec{i} + (\partial^2/\partial y^2)\vec{j} + (\partial^2/\partial z^2)\vec{k}$. The following typical velocity and density profiles of

free shear flow are set up as the initial basic flow state:

$$\phi_0 = \Delta\phi_0 tanh[\frac{2}{\delta_s}(z-\frac{1}{2}L_z)], \tag{5.4}$$

in which ϕ represents *u, v,* ρ, the subscript '0' indicates the initial value of the physical property, Δu_0 and $\Delta\rho_0$ are the velocity and density changes across the initial sheared/stratified layer which has the initial thickness of δ_s, and L_z is the vertical extent of the domain under consideration. ξ is the cross shear ratio which represents the relative magnitude of the cross shear stresses in the spanwise direction compared to that in the streamwise direction and is defined as,

$$\xi = \frac{\Delta v_0}{\Delta u_0}.$$

To promote the coherent structures more efficiently, the following perturbations are imposed on the initial conditions, (5.4), aiming to excite the primary and secondary instabilities,

$$\begin{aligned}\phi_{pri} = \quad & -0.02\Delta u_0 cos(\frac{2\pi x}{L_x})sech[\frac{2}{\delta_s}(z-\frac{1}{2}L_z)] \\ & \times tanh[\frac{2}{\delta_s}(z-\frac{1}{2}L_z)],\end{aligned} \tag{5.5}$$

$$\phi_{sec} = A_\phi \Delta u_0\{1-|tanh[\frac{2}{\delta_s}(z-\frac{1}{2}L_z)]|\}r_\phi(x,y,z), \tag{5.6}$$

where the subscripts *pri* and *sec* denote the perturbation quantities for exciting the primary and secondary instabilities, respectively, r_ϕ is a random number between -1 and 1, A_ϕ is the amplitude coefficient for the secondary instability perturbations. For *u*, *v*, and ρ, A_ϕ are selected as 0.1, 0.1, and 0.5, respectively. As predicted by Xiao, et al. [4], the primary instability mode in CSS flows is a stationary mode usually corresponding to vortex structures, and the velocity shear will therefore be the predominant source to excite the primary instability. Accordingly, '*pri*' perturbations are only imposed on the two basic velocity components *u* and *v*, not on ρ. The initial field of a quantity will be the sum of the background profile, the primary perturbation, plus the secondary perturbation if applicable.

The periodic boundary conditions are applied in the horizontal directions. At the top and bottom boundaries, the impermeable condition is set for *w* and the zero flux boundary conditions are set for *u*, *v*, and ρ.

A reliable numerical code, PUFFIN, developed by Kirkpatrick [5], one of the current authors, is used to perform the DNS. The governing equations (5.1)-(5.3) are discretized in space using a finite volume formulation on a uniform, staggered, Cartesian grid. The advection terms in both the momentum and scalar transport equations used a 4th-order central

difference scheme, while all other spatial derivatives are discretised using a second-order central difference scheme. The second order Adams-Bashforth and Crank-Nicolson schemes are used for the time advancement. The CFL number criterion is used to make sure the simulation is stable, with the minimum and maximum limits of 0.3 and 0.4, respectively. The discretised momentum and scalar equations are solved by the Gauss-Seidel method. The pressure correction equation is solved by the BICGSTAB solver with a modified strongly implicit preconditioner. The code is parallelized using Message Passing Interface (MPI).

The dimensions of the computational domain are set based on the stability analysis results of Xiao, et al. [4]. L_x is choosen as $L_x = (2\pi/\alpha)(\delta_s/2)$ which is the one wavelength of the instability mode, in which α is the wavenumber corresponding to the most unstable mode. α is selected as 1/3 based on the stability analysis of Xiao, et al. [4]. L_y and L_z are set to be equal to L_x to prevent the boundary intervention when coherent structures in the CSS flow become more expansive at $\xi > 0.5$. δ_s is set as 0.1795 m. The number of cells in the x, y and z directions are set as $256 \times 256 \times 128$, which is sufficient to capture the necessary features of the primary coherent structures.

The dimensionless parameters dictating the stability of flow are the initial bulk Reynolds number, *Re*, the initial bulk Richardson number, *Ri*, and the Prandlt number, *Pr*, defined as follows,

$$Re = \frac{\Delta u_0 \delta_s}{\nu}, \quad Ri = \frac{g\Delta\rho_0\delta_s}{\bar{\rho}(\Delta u_0)^2}, \quad Pr = \frac{\nu}{\kappa}.$$

As this study aims to investigate the primary coherent structures of CSS flow, *Re* is therefore selected as 1200, in the common range ($1000 \sim 2000$) for laboratory flows. $Pr = 1$ is used for all simulations. *Ri* will vary from 0.01 to 0.2 and ξ will vary from 0 to 1.

5.3 Coherent Structures

The typical evolution history of CSS flow structures leading to turbulence is demonstrated in figure 5.1, where the three-dimensional plots of the concentration c at four representative moments of the CSS flow instability evolution obtained by DNS are shown for the $\xi = 0.5$ case at $Ri = 0.01$. c is defined as:

$$c = \frac{\rho - \rho_1}{\rho_2 - \rho_1} \tag{5.7}$$

where ρ is the local density, $\rho_1 (= \bar{\rho} - 0.5\Delta\rho_0)$ and $\rho_2 (= \bar{\rho} + 0.5\Delta\rho_0)$ are the initial densities at the top and bottom boundaries. During the primary instability stage, when $t = 1000$ s as shown in figure 5.1(a), three spanwise eddies are observed. It seems that the bodies of spanwise eddies, especially the largest one close to the $y = 0$ plane, not only extend across the computational domain, but also wrap over the developing body of the 'cat eye' eddy.

Therefore, unique spanwise 'eddy wrap' coherent structures are the prominent features of the CSS flow instability. Furthermore, the spanwise 'eddy wrap' and the streamwise 'cat eye' eddy structures continue to grow as shown in figure 5.1(b), followed subsequently by the commencement of the decay of the 'cat eye' eddy structures at about t =1600 s while the weaker spanwise eddies still expand as shown in figure 5.1(c). At t =2000 s, as shown in figure 5.1(d), the entire coherent structure collapses and a chaotic turbulent flow state appears.

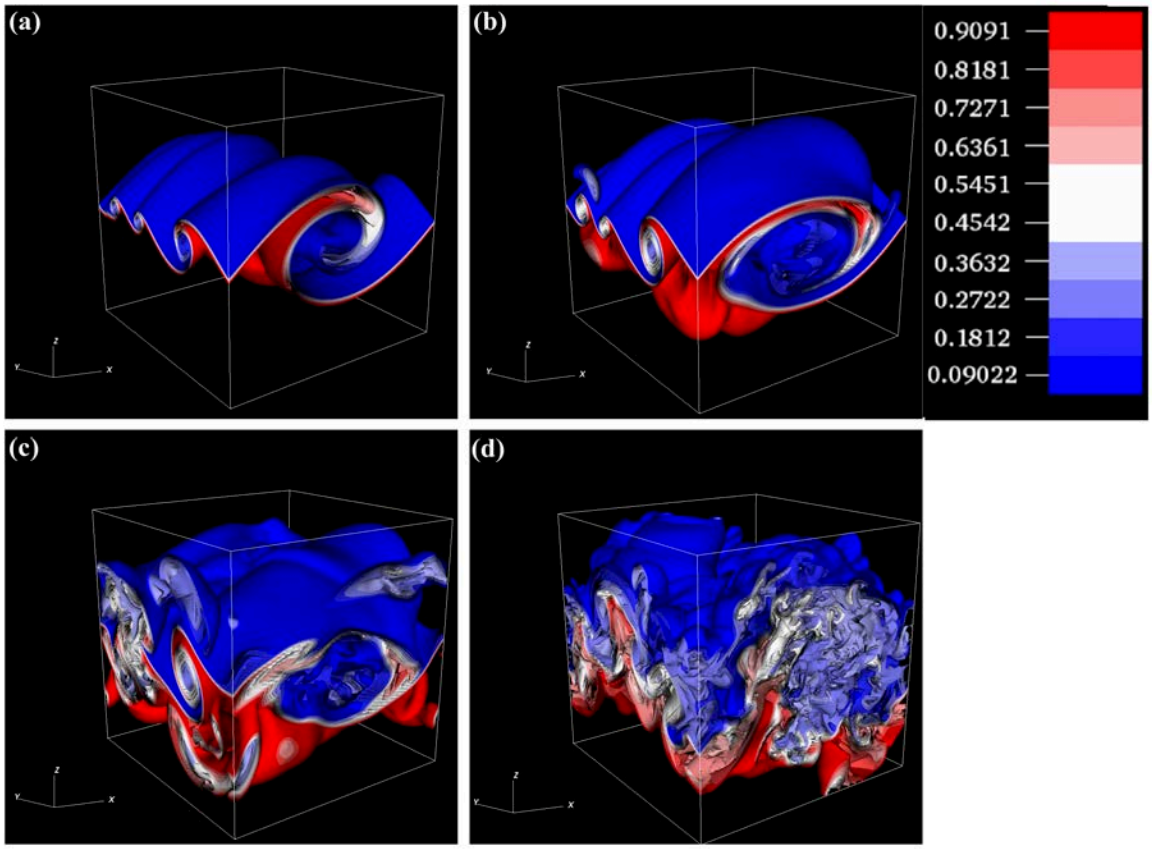

Fig. 5.1 Contours of concentration c for the CSS flow instability in the $\xi = 0.5$ and $Ri = 0.01$ case: (a) the primary eddy wrap structure at $t = 1000$ s; (b) the collapse of the streamwise eddy and the growth of the spanwise eddy at $t = 1380$ s; (c) the collapse of the streamwise eddies and the entire coherent structure at $t = 1600$ s; and (d) the decay into turbulence at $t = 2000$ s.

When ξ changes, the evolution of the CSS flow structures basically follows in a similar fashion to that shown in figure 5.1. However, different appearances of the coherent structures are observed for different ξ values during the primary and secondary instability stages as shown in figure 5.2. The different coherent structures at different ξ values can be categorized

as three types; a 'streamwise dominant mode' with $\xi = 0.1 - 0.3$, a 'balance mode' with $\xi = 0.4 - 0.6$, and a 'spanwise dominant mode' with $\xi = 0.7 - 1.0$. The typical coherent structures for these three different modes are exhibited in figure 5.2(b) to figure 5.2(d), respectively. Also included in the figure is the typical 'cat eye' eddy structures for the 'KH' mode for PSS flow with $\xi = 0.0$ for comparison, as shown in figure 5.2(a). For the 'KH' mode, there is no overturning in the spanwise direction. As a weak cross shear with $\xi = 0.2$ is introduced, as shown in figure 5.2(b), several small spanwise 'eddy spots' are observed at the braid region of the streamwise 'cat eye' eddy. As ξ is further increaset to 0.5, the spanwise 'eddy spots' evolve into a 'eddy wrap' as shown in figure 5.2(c), where the 'cat eye' features become ambiguous at the center of the streawmwise eddy structures. At $\xi = 0.8$, as shown in figure 5.2(d), the enlarging spanwise 'eddy wrap' structure seems to suppress the streamwise 'cat eye' and lead to an internal collapse of the streamwise eddy structure from its center.

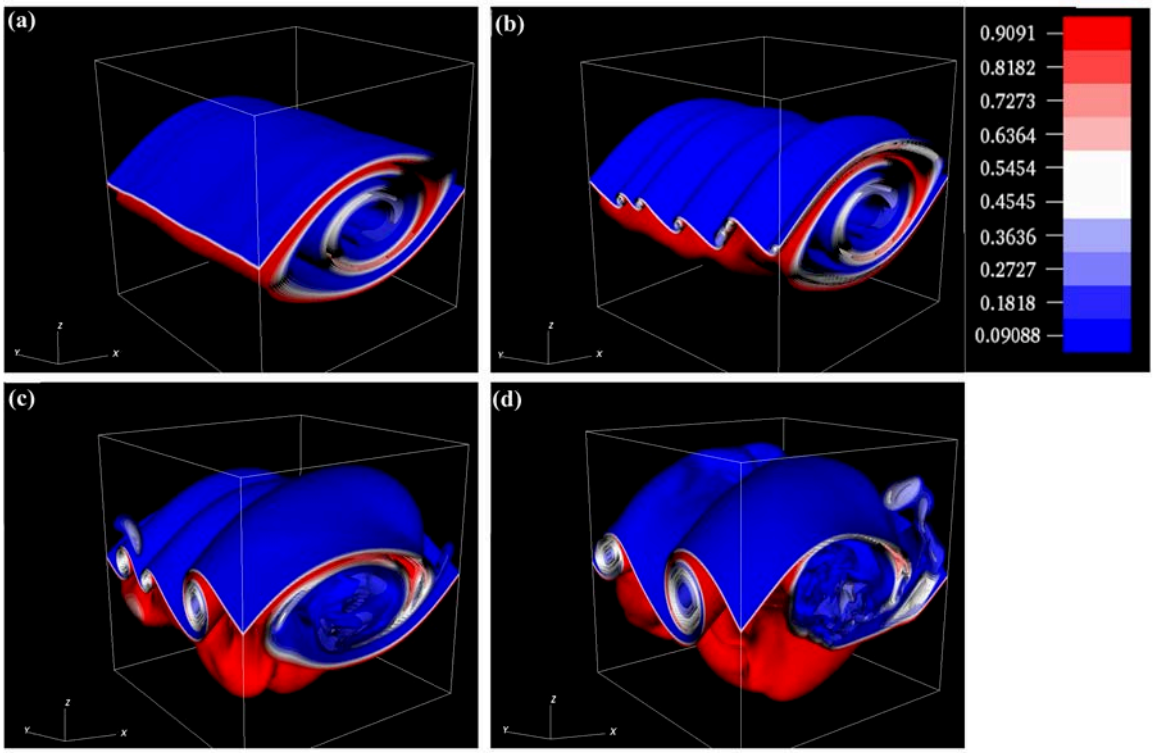

Fig. 5.2 Contours of concentration c of the CSS flow at $Ri = 0.01$ with (a) the 'KH' mode for PSS flow with $\xi = 0.0$ at $t = 1380$ s, (b) the 'streamwise dominant' mode for CSS flow with $\xi = 0.2$ at $t = 1200$ s, (c) the 'balanced mode' for CSS flow with $\xi = 0.5$ at $t = 1380$ s, and (d) the 'spanwise dominant mode' for CSS flow with $\xi = 0.8$ at $t = 1200$ s.

If the background stratification becomes stronger as Ri increases, the coherent structures observed in the weakly stratified environment as shown in figure 5.1 will more or less

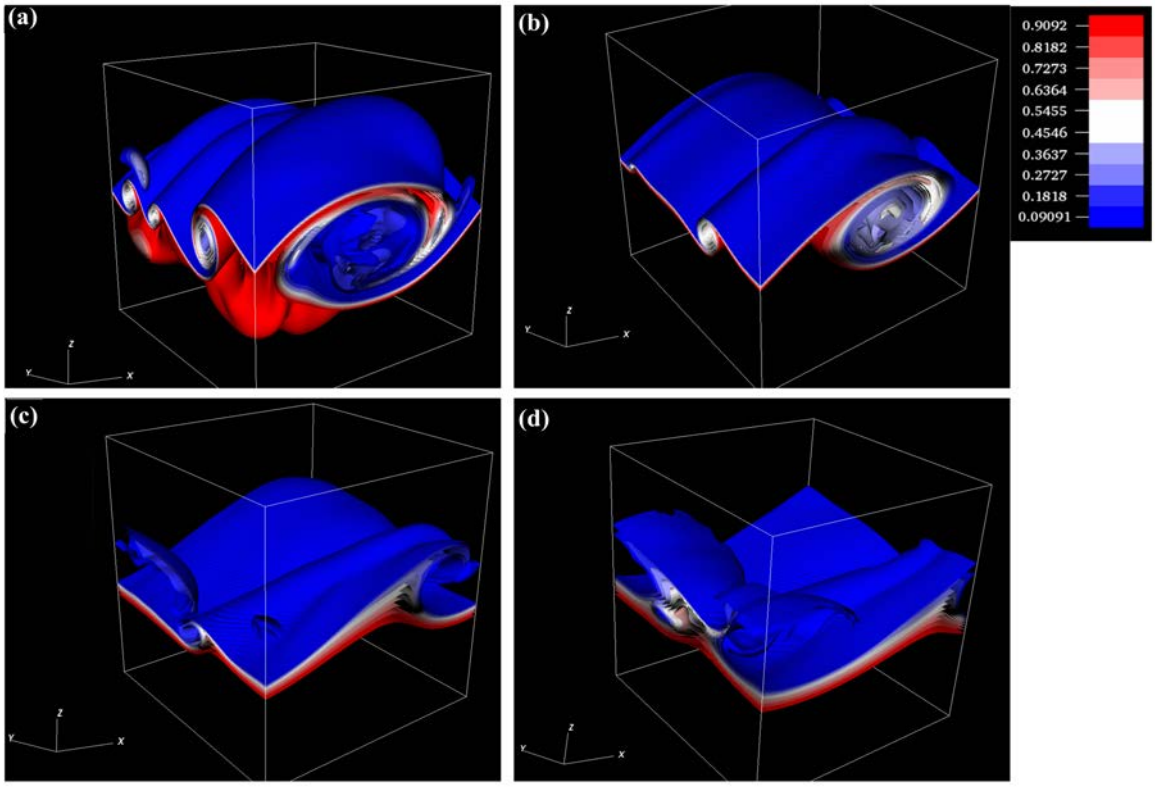

Fig. 5.3 Contours of concentration c of CSS flow at ξ=0.5 with (a) Ri =0.01 at t =1380 s, (b) Ri =0.05 at t =1500 s, (c) Ri =0.15 at t =1250 s, and (d) Ri =0.20 at t =1500 s.

be suppressed, as demonstrated in figure 5.3 which shows the different primary coherent structures of CSS flow at different Ri values but with a fixed $\xi = 0.5$. When Ri is increased from 0.01 to 0.05, as shown in figure 5.3(a) and figure 5.3(b), both the streamwise 'cat eye' eddy and the spanwise 'eddy wrap' eddy structures seem to be compressed towards the eddy core, as the size of the coherent eddy structures diminishes while the concentrations c at the eddy cores increase from $0.01 \sim 0.18$ as shown by blue contour to $0.45 \sim 0.55$ as shown by white contour. At $Ri = 0.15$, as shown in figure 5.3(c), both the streamwise and spanwise eddy structures degrade into overturning structures, whose sizes further decrease when compared to the $Ri = 0.05$ case. At $Ri = 0.2$, as shown in figure 5.3(d), the spanwise overturning structures further decay into wave-featured structures due to a stronger background stratification, while on the other hand the spanwise overturning seems to reversely grow stronger, suggesting a complicated mechanisms in strongly stratified environments.

As coherent structures in the CSS flow display strong eddy features, it is very helpful to further examine the vorticity contour plots corresponding to the c contour plots. Figure 5.4 shows the slice plot of the streamwise vorticity contours at Ri =0.01 with different ξ values.

The streamwise vorticity is defined as:

$$\omega_x = \frac{\partial w}{\partial y} - \frac{\partial v}{\partial z}. \tag{5.8}$$

For the KH instability case (at $\xi = 0$), this slice plane is the vertical central plane at $y = 0.5L_y$, and for the CSS flow instability cases, it is the vertical slice plane determined by the initial point (0, y_i, 0) and the direction vector ($0.99\vec{i}$, $0.12\vec{j}$, $0.0\vec{k}$), rather than in the x direction, due to the slight misalignment of the symmetry axis of the spanwise eddy wrap structure with the x direction. For $\xi = 0.2$ and 0.5, $y_i = 0.25L_y$, and for $\xi = 0.8$, $y_i = 0.3125L_y$.

For the 'KH' mode as shown in figure 5.4(a), the positive and negative ω_x regions alternatively fill in the 'cat eye' eddy core area, while in the braid region only positive ω_x exists. As cross shear is introduced, negative ω_x representing the spanwise vorticity tube appears in the braid regions as well. At $\xi = 0.2$, as shown in figure 5.4(b), the negative ω_x in the braid regions is still very weak, which corresponds to the weak appearances of spanwise eddies shown in figure 5.2(b). At ξ =0.5, as shown in figure 5.4(c), the significant spanwise 'eddy wrap' structures are represented by large negative ω_x regions surround the central 'cat eye' eddy core, where positive ω_x dominates. Compared to the 'KH' mode and the 'streamwise dominant' mode, the sizes of the central 'cat eye' eddies in the ω_x plot are smaller, indicating that the expanding spanwise 'eddy wrap' structures largely suppress the streamwise eddy structures. A complete domination of the spanwise 'eddy wrap' occurs for the 'spanwise dominant mode' as shown in figure 5.4(d), where only a small positive ω_x spot survives in the center. The significantly degrading 'cat eye' structures shown in figure 5.4(d) supports the observations from figure 5.2(d) that the streamwise eddy structures collapse from its core.

The influence of *Ri* is also examined with the ω_x plots as shown in figure 5.5 for $\xi = 0.5$ and four *Ri* values which are the same as those in figure 5.3. As *Ri* increases to 0.05, the spanwise 'eddy wrap' structures reduce to thin and extended eddy tubes, as shown in figure 5.5(b). The streamwise 'cat eye' eddies at the center of the domain are compressed as a result of the enhanced background stratification so that a more evident 'cat eye' shape is observed when compared to that in figure 5.5(a). As *Ri* is further increased, the entire coherent structures start to propagate across the periodic streamwise boundaries. When *Ri* =0.15, the size of streamwise 'cat' eye eddy further decreases as shown in figure 5.5(c) and at *Ri*=0.20 the eddy structures are totally replaced by the propagating wave-featured structures seen in figure 5.5(d), where the spanwise wave structures grow larger compared to a small spanwise overturning structure in figure 5.5(c). The growing spanwise wave

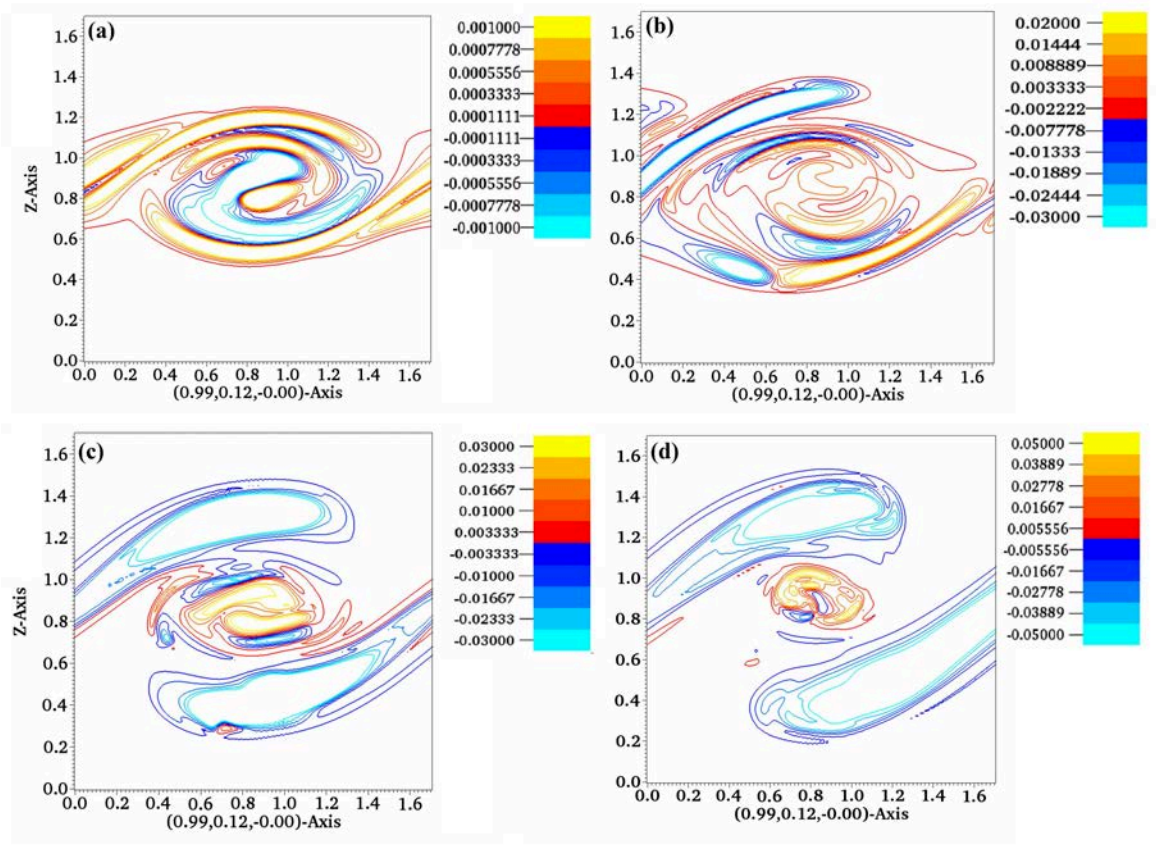

Fig. 5.4 Contours of ω_x in a vertical slice plane for CSS flow in a weakly stratified environment at $Ri = 0.01$ with (a) $\xi = 0.0$ at $t = 1600$ s, (b) $\xi = 0.2$ at $t = 1500$ s, (c) $\xi = 0.5$ at $t = 1200$ s, and (d) $\xi = 0.8$ at $t = 1050$ s. The cold(hot) color denotes a negative(positive) ω_x.

structures suggest that more complicated mechanisms might be involved in CSS flow with large background stratifications.

5.4 Mixedness thickness δ_θ

A quantity called mixedness, M, introduced by Konrad [1] and defined below, is employed in this study as the measure to quantify the mixing effects,

$$M(t,z) = \frac{\int_0^{L_z} H(\rho-\rho_m)(\rho_b-\rho) + \int_0^{L_z} H(\rho_m-\rho)(\rho-\rho_t)}{\int_0^{L_z} H(\rho-\rho_m)(\rho_b-\rho_m) + \int_0^{L_z} H(\rho_m-\rho)(\rho_m-\rho_t)} \tag{5.9}$$

where ρ_b, ρ_t and ρ_m are densities at the bottom and top boundaries and at the mid interface and the Heaviside step function is defined: $H(f) = 1$ for $f \geq 0$ and $H(f) = 0$ for $f < 0$. M is

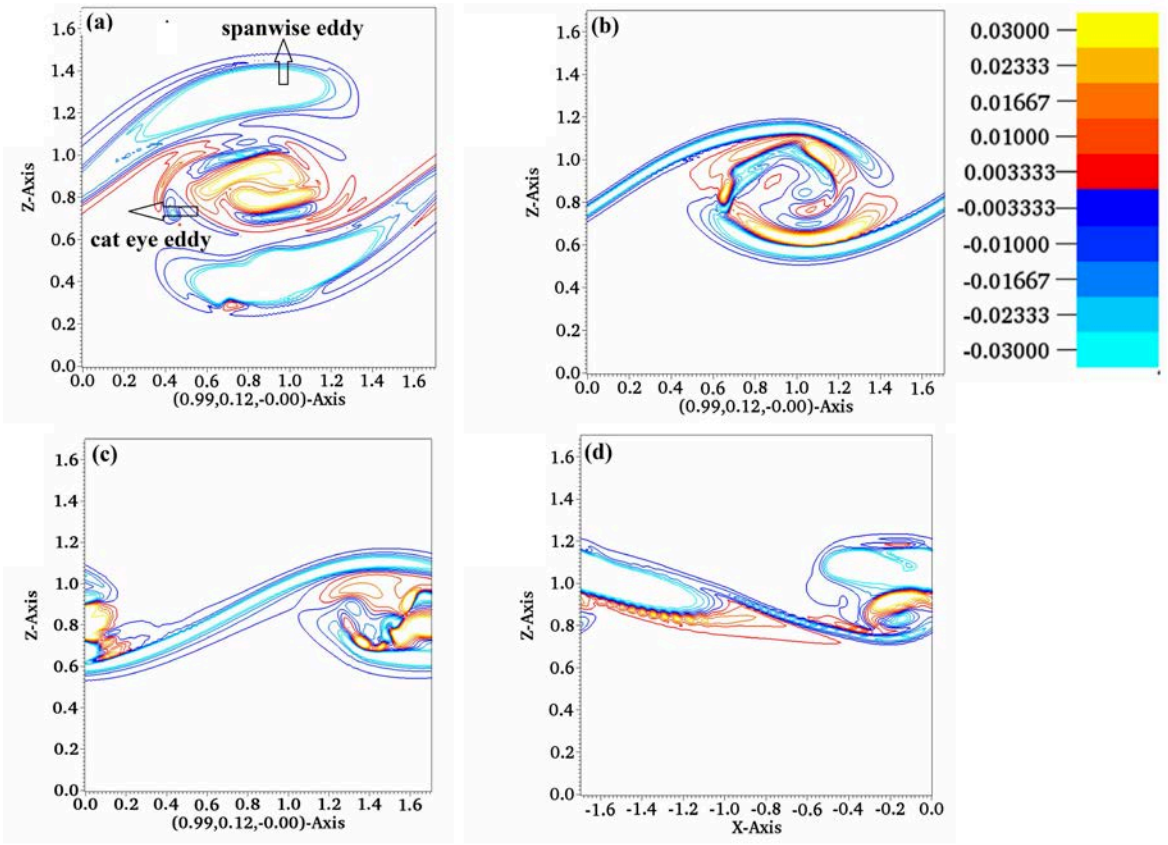

Fig. 5.5 Contours of ω_x in a vertical slice plane for CSS flow with $\xi = 0.5$ and at (a) Ri=0.01 at $t = 1200$ s, (b) Ri=0.05 at $t = 1500$ s, (c) Ri=0.15 at $t = 1250$ s, and (d) Ri=0.2 at $t = 1500$ s. The cold(hot) color denotes a negative(positive) ω_x.

the ratio between the densities with and without fluctuation effects, as the density fluctuation $(\rho - \rho_m)$ term at the denominator of the fraction only defines the sign of the constants $(\rho_b - \rho_m)$ and $(\rho_m - \rho_t)$, but both the magnitude and the sign of density fluctuations are included in the numerator of the fraction. The integration of M is the mixedness thickness δ_θ defined as follows

$$\delta_\theta = \int_0^{L_z} M(t, y) dz \tag{5.10}$$

δ_θ is a physical parameter to indicate how much fluid is absorbed by the central stratified layer due to turbulent mixing.

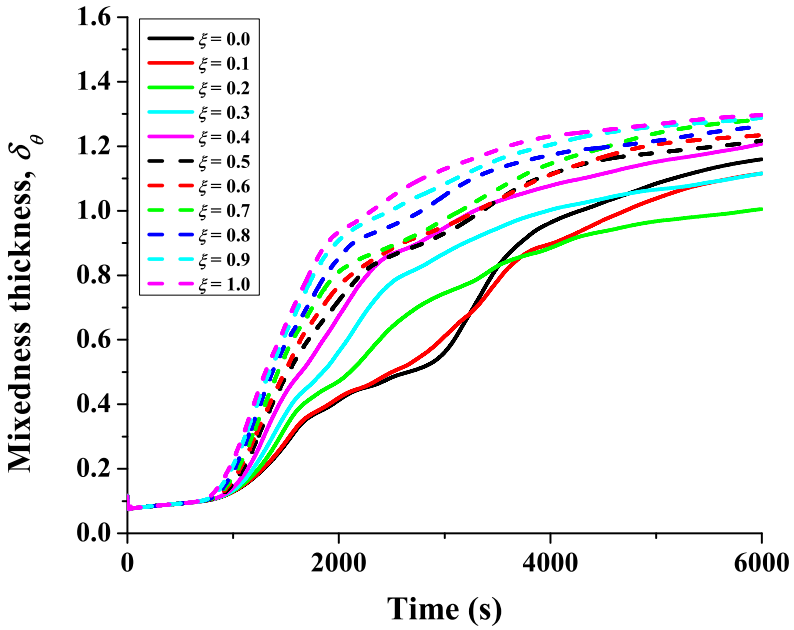

Fig. 5.6 Time series of δ_θ at $Ri = 0.01$ with ξ varying over the range of $0 \leq \xi \leq 1.0$.

5.4.1 Mixedness thickness normalized by $\delta_{\theta,\xi=0}$

Figure 5.6 presents the time series of δ_θ for ξ varying over the range $0 \leq \xi \leq 1.0$ in weakly stratified environment at $Ri_0 = 0.01$. For each ξ value, three development stages are observed for δ_θ; a short slow growth stage (when time is less than about 1000 s), a rapid growth stage (when time is in the range of about 1000 s to 3000 s) and finally an asymptotic stage (when time is beyond approximately 3000 s). In the slow growth stage, the values of δ_θ are very small for all ξ values and all of them almost overlap. In the rapid growth stage, the magnitude of δ_θ increases monotonically and significantly with increasing ξ, indicating effective improvement in mixing. Thus, during the rapid growth stage, the CSS flow instability is far more effective in terms of the mixing effect than the traditional KH instability. This is in line with the experimental observations by Atsavapranee and Gharib [6] (referred to "AV97" hereafter) and Lin, Shao and Yu [7]. Nonetheless, it is observed that the CSS flow has no obvious advantages in terms of the mixing effect at the asymptotic stage, as there is little difference between the values of δ_θ for $\xi \geq 0.4$ cases.

When δ_θ is normalized by $\delta_{\theta,\xi=0}$, where $\delta_{\theta,\xi=0}$ is the value of the PSS flow, two peaks are clearly shown in Fig. 5.7 and are marked as the "first peak" and the "second peak", which indicate the developed primary instability and the saturation of the coherent structures

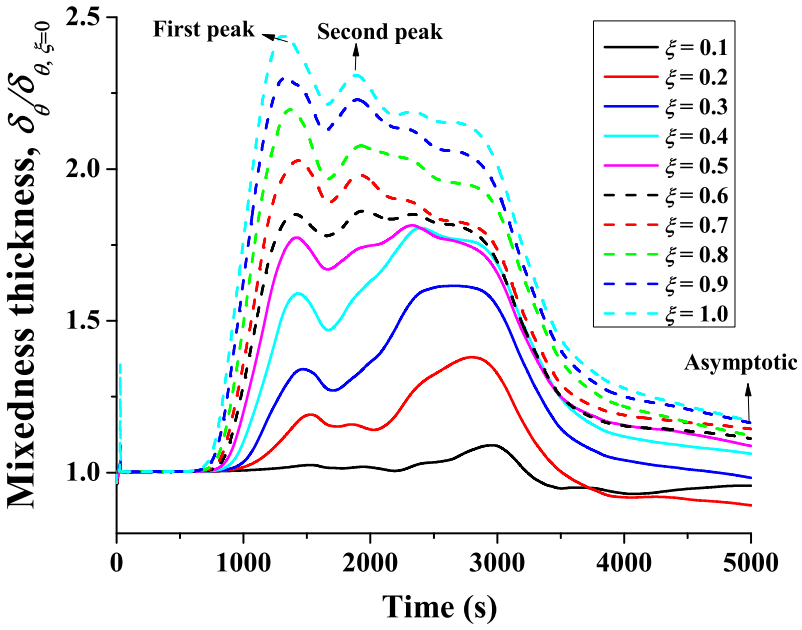

Fig. 5.7 Time series of the normalized mixedness thickness $\delta_\theta/\delta_{\theta,\xi=0}$ at $Ri = 0.01$ with ξ varying over the range of $0 \leq \xi \leq 1.0$.

respectively. Two peaks found in the time series of $\delta_\theta/\delta_{\theta,\xi=0}$ at different ξ reflect the results of the normalization factor $\delta_{\theta,\xi=0}$, in which the primary instability and the secondary instability are distinct from each other, as seen in Fig. 5.6. Similar to Fig. 5.6, asymptotic stages are found in Fig. 5.7 where at different ξ values δ_θ is not so significant compared to those at the primary(second) instability stage as marked by "first(second) peak".

With appearances of two peaks, the differences among three CSS instability modes as described in the previous chapter are more obvious in the time series of $\delta_\theta/\delta_{\theta,\xi=0}$. For the "streamwise dominant" mode with $\xi = 0.1 \sim 0.3$, the second peak is significantly higher than the first peak, indicating that the mixing process is stronger at the saturation stage. This is physically reasonable because in the "streamwise dominant" mode, the streamwise "cat eye" eddy still dominates over the weak spanwise "eddy wrap" structures, therefore the expansion of the KH eddy contributes more to the spanwise saturation process. In the "balanced" mode with $\xi = 0.4 \sim 0.6$, the first peak catches up with the second, indicating that the primary and secondary instabilities achieve almost the same amount of mixing due to the gradually stronger spanwise eddy structures. In the "spanwise dominant" mode, the first peak overtakes the second peak and becomes the dominant factor in the turbulence mixing. This is because the streamwise KH eddy is strongly suppressed by the spanwise eddy as

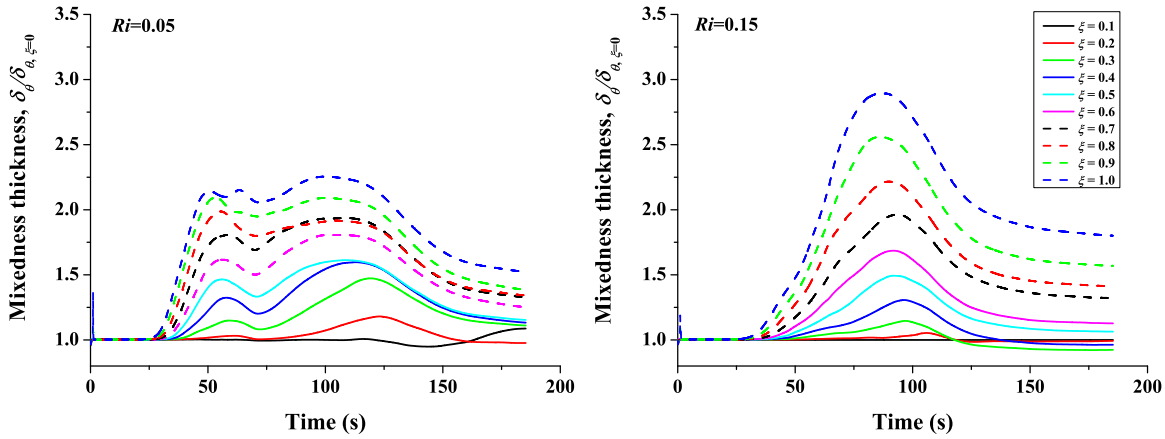

Fig. 5.8 Time series of $\delta_\theta/\delta_{\theta,\xi=0}$ (a) at $Ri = 0.05$ and (b) at $Ri = 0.15$ for ξ over the range of $\xi = 0 \sim 1.0$.

shown in Fig. 5.2(d) and Fig. 5.4(d). It is noted that the time span from the first peak to the second peak is decreasing with increasing ξ, indicating faster transition to turbulence in the CSS flow with increasing ξ.

As Ri further increases, the evolution of δ_θ is modified by the increasing background stratification. Two different modes are further observed for different Ri values, as shown in Fig. 5.8 where the time series of $\delta_\theta/\delta_{\theta,\xi=0}$ at $Ri = 0.05$ and $Ri = 0.15$ are presented over $\xi = 0 \sim 1.0$. There are two peaks at $Ri = 0.05$ but a single peak at $Ri = 0.15$. It is further found that the "two-peak" feature is also present in the time series of $\delta_\theta/\delta_{\theta,\xi=0}$ at $Ri \leq 0.05$ while the "single-peak" feature is also present in the time series of $\delta_\theta/\delta_{\theta,\xi=0.0}$ at $Ri > 0.05$. The single peak at higher Ri value occurs at the time when the saturation of the coherent structures commences before the turbulence stage (that is, onset of collapse). The disappearance of the first peak associated with the primary instability at higher Ri corresponds to the suppressed appearance of the primary coherent structures observed in Fig. 5.3(c).

It is further observed that compared to the $Ri = 0.01$ case as shown in Fig. 5.7, the behavior of the three CSS instability modes at higher Ri follows the similar pattern, except for $\xi = 1.0$ where the two primary peaks form with smaller magnitudes compared to that of the second peak. In addition, the second peak in the "streamwise dominant" mode with $\xi = 0.7 \sim 1.0$ at higher Ri generally happens later compared to that at the $Ri = 0.01$ case. The delayed second peaks in the "streamwise dominant" mode is because the development of the spanwise "eddy wrap" structures is suppressed in a stronger stratified environment, so that the quick collapse in the "streamwise dominant" mode found in $Ri = 0.01$ is postponed.

It is conjectured here that during the primary instability stage the major contributor to the mixing is in the braid regions of the KH mode. In the CSS flow, as cross shear is introduced, the original braid regions in the KH mode evolve into "eddy wrap" structures, which still play a significant role in the mixing process. As Ri increases, the "eddy wrap" structures are suppressed much more than the "cat eye" eddy, as shown in Fig. 5.5.

As time series of $\delta_\theta/\delta_{\theta,\xi=0}$ at different ξ values in Configuration (a) include three general milestones, *i.e.* , the primary peak, the secondary peak and the asymptotic stage, it is possible to correlate the values of $\delta_\theta/\delta_{\theta,\xi=0}$ at these three milestones with the corresponding ξ. Figure 5.9 presents the relations and correlations between $\delta_\theta/\delta_{\theta,\xi=0}$ at the primary/secondary peak(s) and ξ for different Ri values over $\xi = 0 \sim 1.0$. In both the $Ri = 0.01$ and $Ri = 0.05$ cases, as shown in Fig. 5.9(a) and Fig. 5.9(b), $\delta_\theta/\delta_{\theta,\xi=0}$ at the primary peak basically follows the linear relation with increasing ξ, except that at $\xi = 0.1$ in the $Ri = 0.05$ case. $\delta_\theta/\delta_{\theta,\xi=0}$ at the secondary peak in these two cases follows a cubic curve with ξ, implying that the dynamics in the secondary instability is more complicated than that in the primary instability. As discussed above, only the secondary peaks are found when $Ri > 0.05$. The relations and correlations between $\delta_\theta/\delta_{\theta,\xi=0}$ and ξ at the only secondary peak for higher Ri values are presented in Fig. 5.9(c). It is shown that in general a good linear relation is found between $\delta_\theta/\delta_{\theta,\xi=0}$ and ξ for the $Ri = 0.10$, 0.15 and 0.20 cases, except for the $\xi = 0.1$ points.

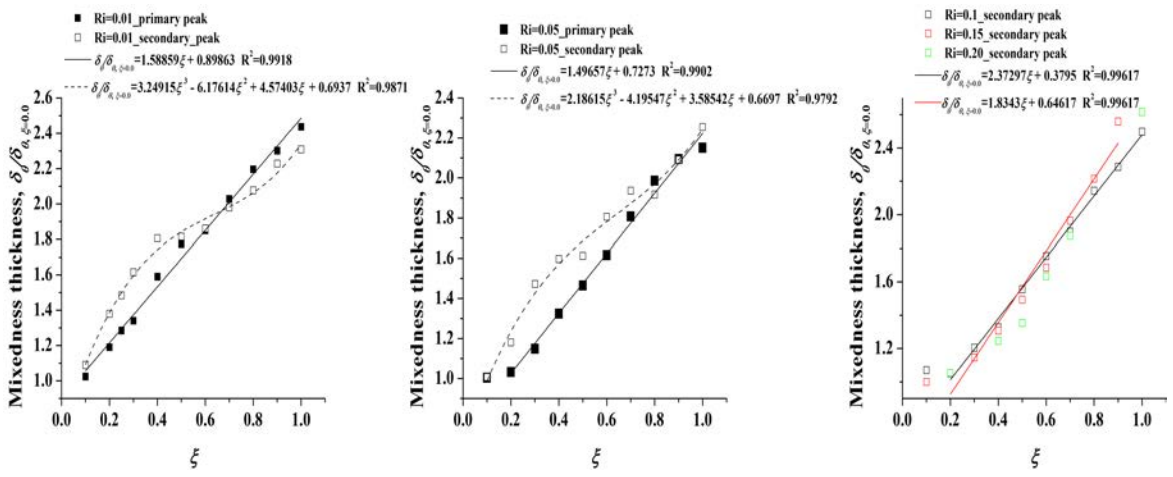

Fig. 5.9 Correlations between $\delta_\theta/\delta_{\theta,\xi=0}$ and ξ at the primary/secondary peak(s) for (a) $Ri = 0.01$, (b) $Ri = 0.05$, and (c) $Ri = 0.1$, 0.15 and 0.2.

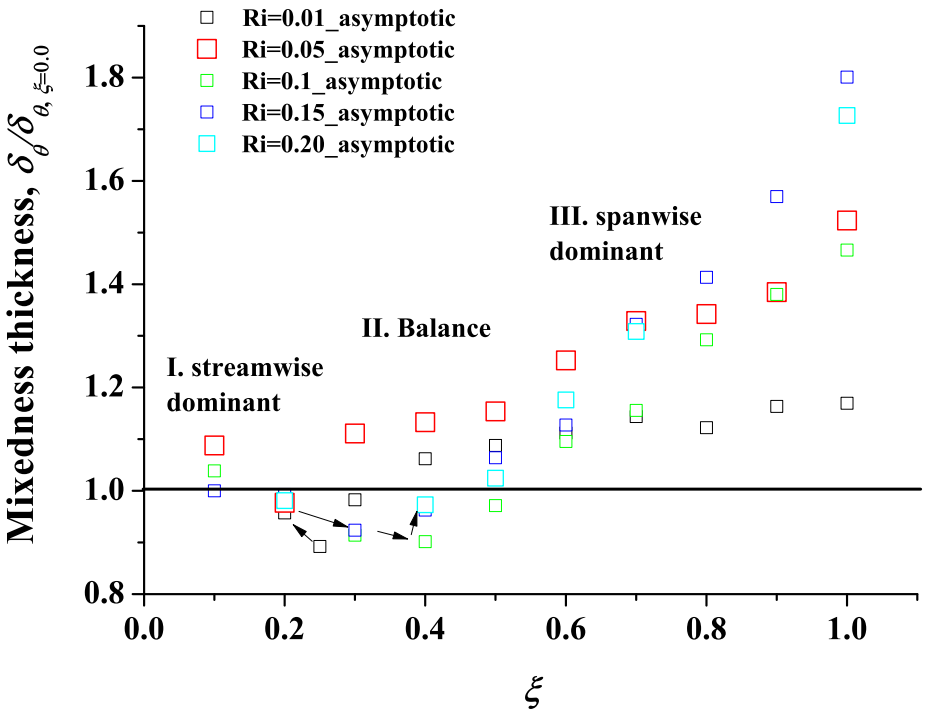

Fig. 5.10 The three CSS instability modes on the curve between $\delta_\theta/\delta_{\theta,\xi=0}$ and ξ at the asymptotic stage for different Ri cases in the range of $0.01 \leq Ri \leq 0.20$.

The relation between $\delta_\theta/\delta_{\theta,\xi=0}$ and ξ at the asymptotic stage are plotted in Fig. 5.10 for different Ri values. It is seen that the three CSS instability modes are well represented in the figure. At the asymptotic stage, the relation between $\delta_\theta/\delta_{\theta,\xi=0}$ and ξ is in general non-monotonic. For each Ri, when $\xi < 0.3$ (in the valley section), $\delta_\theta/\delta_{\theta,\xi=0}$ is less than 1, which represents the "streamwise dominant" mode. With the increase of ξ, the increasing section around $\delta_\theta/\delta_{\theta,\xi=0} = 1.0$ represents the "balanced" mode, and the further increasing of ξ gradually increases $\delta_\theta/\delta_{\theta,\xi=0}$ beyond 1, representing the "spanwise dominant" mode. The rationale to define the three CSS instability modes using $\delta_\theta/\delta_{\theta,\xi=0.0} = 1.0$ as the dividing point is because it is a symbolic value of the PSS flow, which only includes the streamwise velocity shear. If $\delta_\theta/\delta_{\theta,\xi=0}$ is around 1.0 for a CSS flow, the contributions of the streamwise structures to achieved mixing process are important.

Using $\delta_\theta/\delta_{\theta,\xi=0}$=1.0 as the criterion, it is found that in the $Ri = 0.01$ case, the three CSS instability modes exhibit weak differences as found in Fig. 5.7. Yet as Ri increases, the differences of $\delta_\theta/\delta_{\theta,\xi=0}$ among the three modes are more obvious, especially for the "spanwise dominant" mode where the gradients of $\delta_\theta/\delta_{\theta,\xi=0}$ against ξ apparently increase compared to the $Ri = 0.01$ case. As a result, $\delta_\theta/\delta_{\theta,\xi=0}$ at the "spanwise dominant" mode varies between 1.4 and 1.7 for Ri in the range of 0.05 to 0.20. Such large changes suggest

that the "spanwise dominant" mode would still improve the mixing effects at the turbulence stage even in a strong stratified environment.

In addition, the minimum $\delta_\theta/\delta_{\theta,\xi=0}$ at the asymptotic stage for different Ri cases are moving with increasing Ri, as indicated by the arrows in Fig. 5.10, so do the $\delta_\theta/\delta_{\theta,\xi=0.0}=1.0$ points for different Ri cases. This suggest that increasing Ri would increase the critical ξ where the "streamwise dominant" mode transits into the "balanced" mode.

5.4.2 Mixedness thickness normalized by $\delta_{\theta,Ri=0.01}$

If δ_θ is normalized by $\delta_{\theta,Ri=0.01}$, Ri will become the main parameter, whereas the typical ξ values representing the PSS flow ($\xi=0.0$), the "streamwise dominant" mode ($\xi=0.0\sim0.2$), the "balanced" mode ($\xi=0.2\sim0.5$), and the "spanwise dominant" mode ($\xi=0.5\sim1.0$), will be used as subordinate parameter to further examine the dynamic features of the three CSS instability modes at different Ri cases.

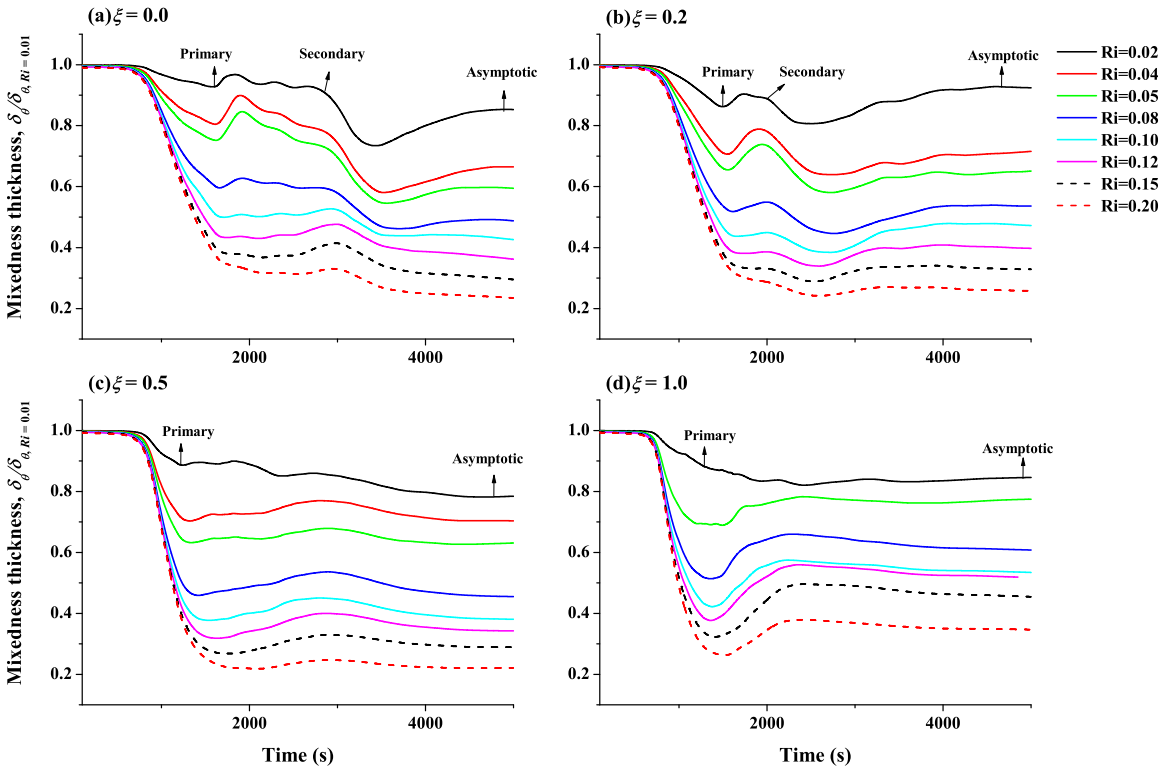

Fig. 5.11 Time series of $\delta_\theta/\delta_{\theta,Ri=0.01}$ for different Ri cases over $Ri=0.02\sim0.20$ at (a) $\xi=0.0$, (b) $\xi=0.2$, (c) $\xi=0.5$, and (d) $\xi=1.0$.

Figure 5.11 shows the time series of the normalized $\delta_\theta/\delta_{\theta,Ri=0.01}$ with Ri in the range of $Ri = 0.01 \sim 0.20$ at four ξ values, that is, $\xi = 0.0$ as the PSS flow, $\xi = 0.2$ as the "streamwise dominant" mode, $\xi = 0.5$ as the "balanced" mode, and $\xi = 1.0$ as the "spanwise dominant" mode. Compared to Fig. 5.8 where δ_θ is normalized by $\delta_{\theta,\xi=0}$, the time series of $\delta_\theta/\delta_{\theta,Ri=0.01}$ are in quite different shapes. This is because $\delta_\theta/\delta_{\theta,Ri=0.01}$ is the reflection of its denominator $\delta_{\theta,Ri=0.01}$ rather than $\delta_{\theta,\xi=0}$. It is found that for each of the four modes represented by different ξ values, increasing Ri in general weakens the mixing effects as $\delta_\theta/\delta_{\theta,Ri=0.01}$ decrease significantly. The time series of $\delta_\theta/\delta_{\theta,Ri=0.01}$ at different Ri values is parallel with each other in terms of the profile.

In the time series of $\delta_\theta/\delta_{\theta,Ri=0.01}$ representing all four CSS modes, it is seen that the end of the primary instability exhibits unanimously as a "valley" shape as marked in Fig. 5.11. The "valley" peak looks ambiguous most in the "balanced" mode, in which the streamwise and spanwise instabilities are equivalently strong during the primary stage. For the remaining CSS instability modes where dominance is rather one-sided, the "valley" shape during the primary stage looks more obvious. As $Ri > 0.10$, the "valley" point gradually decays into the turning point in the $\xi = 0.0$, 0.2 and 0.5 case, while in the $\xi = 1.0$ case, the "valley" shape is still clearly shown. In addition to the "valley", "peak" are found right after as marked in Fig. 5.11, with clear traces in the PSS flow and the "streamwise dominant" mode. Matching with the evolution of coherent structures, the peak indicates the onset of the secondary instability. As $\xi > 0.0$, the trails of the secondary instability are no longer found in $\delta_\theta/\delta_{\theta,Ri=0.01}$ time series.

$\delta_\theta/\delta_{\theta,Ri=0.01}$ at each primary instability described by the "valley" shape shown in Fig. 5.11 are collected and plotted against Ri in Fig. 5.12. For high Ri cases where only turning points instead of the "valley" is observed, $\delta_\theta/\delta_{\theta,Ri=0.01}$ is selected at these turning points. It is clear from this figure that all $\delta_\theta/\delta_{\theta,Ri=0.01}$ values at the primary instability fall approximately onto an asymptotically declining curve, suggesting that a general relation between $\delta_\theta/\delta_{\theta,Ri=0.01}$ and Ri exists for all four instability modes. Regression analysis gives the following two correlations,

$$\delta_\theta/\delta_{\theta,Ri=0.01} = 0.17829 Ri^{-0.39854} \tag{5.11}$$

$$\delta_\theta/\delta_{\theta,Ri=0.01} = 0.17828 + 0.92578 \times (1.04273 \times 10^{-6})^{Ri} \tag{5.12}$$

which are also presented in the figure. The power law correlations are used because in previous studies on the PSS flow the relations between mixing properties such as the entrainment

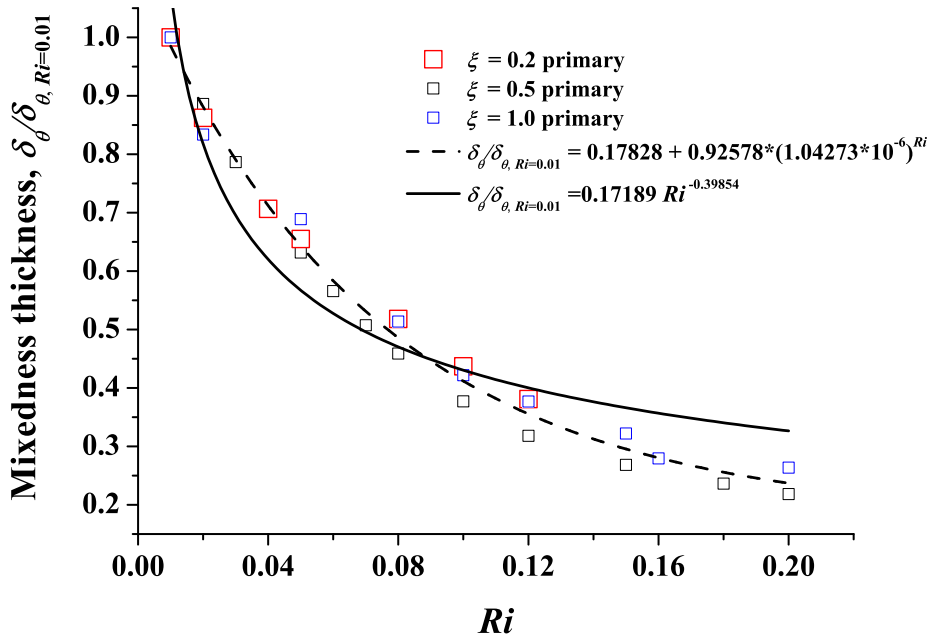

Fig. 5.12 Relation and correlation between $\delta_\theta/\delta_{\theta,Ri=0.01}$ at each primary instability and Ri for different ξ values.

ratio and Ri are in power law. Apparently, the exponential asymptotic function shows a better correlation outcome, with nearly all $\delta_\theta/\delta_{\theta,Ri=0.01}$ points fall near the correlated curve.

Similarly, $\delta_\theta/\delta_{\theta,Ri=0.01}$ at the asymptotic stage is also collected from Fig. 5.11 and plotted against Ri as shown in Fig. 5.13. The experimental results from AV97 and Koop and Browand [8] in normalized form $\delta_\theta/\delta_{\theta,Ri=0.01}$ are also shown in the figure. A gap is found between the experimental results and the DNS results, which increases substantially after $Ri = 0.03$. Such increasing gap mainly stems from the different length scales in the experiments and the DNS simulation. In the current DNS simulation, only a single wavelength of the instability mode is setup with periodical boundary conditions, while in the experiments of AV97 the water tank extends the length of several unstable mode units. Therefore the coupling between adjacent flow structures, such as pairing between two adjacent eddy structures, is unable to be produced in the current DNS study. Nevertheless,at small values of Ri ($Ri < 0.03$) where the length scale of unstable flow structures is larger due to less suppression from stratified flow, the experimental results and the current DNS results correlate very well. Good agreement between the DNS results and the experimental results of AV97 at $Ri = 0.01$ also suggests a better correlation between experimental results and the DNS results in weakly stratified flow.

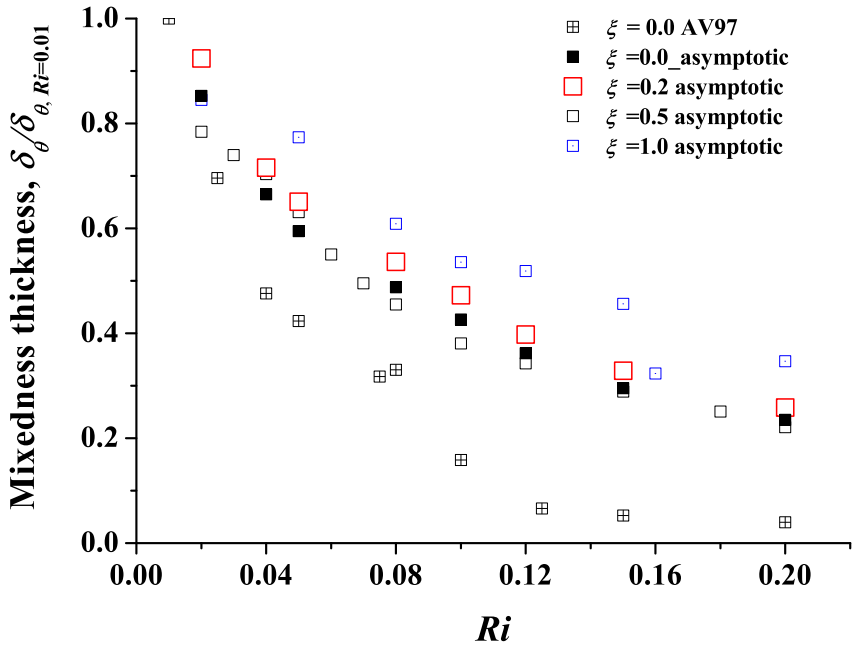

Fig. 5.13 Relation between $\delta_\theta/\delta_{\theta,Ri=0.01}$ at the asymptotic stageeach and Ri for different ξ values.

Similar to the correlations at the primary instability, power function and exponential function are also used to represent the relations between $\delta_\theta/\delta_{\theta,Ri=0.01}$ at the asymptotic stage and Ri. The obtained correlations, as shown in Fig. 5.14, are as follows,

$$\delta_\theta/\delta_{\theta,Ri=0.01} = 0.18902Ri^{-0.37468} \tag{5.13}$$

$$\delta_\theta/\delta_{\theta,Ri=0.01} = 0.22874 + 0.85318 \times (8.01364 \times 10^{-7})^{Ri} \tag{5.14}$$

for the DNS results and

$$\delta_\theta/\delta_{\theta,Ri=0.01} = 0.16393Ri^{-0.40542} \tag{5.15}$$

$$\delta_\theta/\delta_{\theta,Ri=0.01} = 0.0131 + 1.16979 \times (1.74621 \times 10^{-9})^{Ri} \tag{5.16}$$

for experimental results. It should be noted that strong deviations are found at $\xi = 1.0$, implying a different dynamic mechanisms occurring at high cross shear. The deviations of $\xi = 1.0$ echo the similar deviations found in Fig. 5.10 for the "spanwise dominant" mode, implying a different dynamic features of the "spanwise dominant" mode.

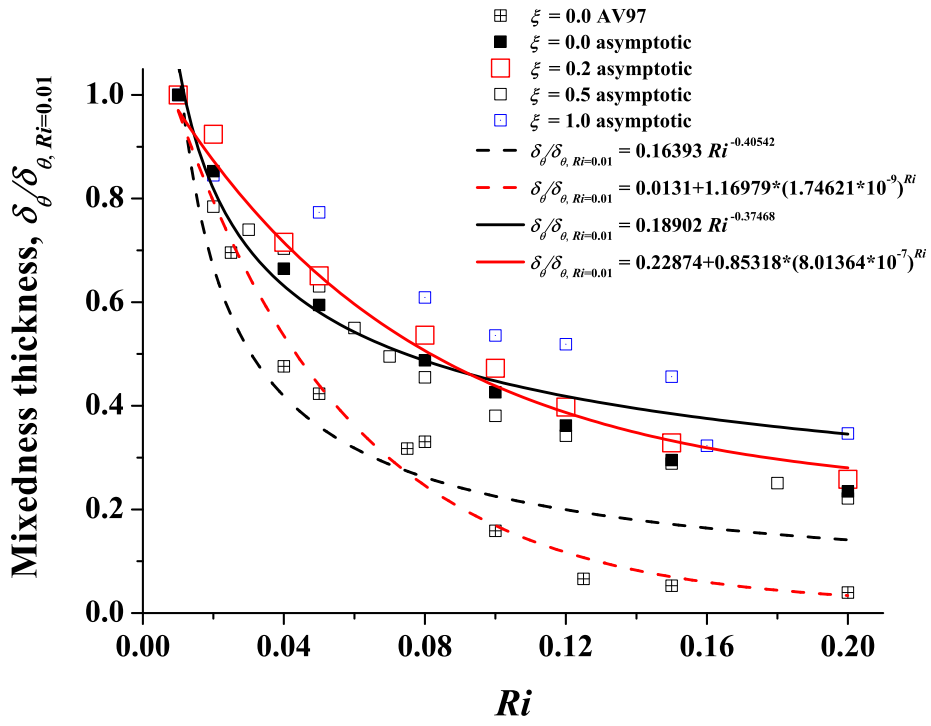

Fig. 5.14 Correlations between $\delta_\theta/\delta_{\theta,Ri=0.01}$ at the asymptotic stage and Ri for different ξ values in comparison with the experimental results of AV97.

5.4.3 Correlation for $\delta_\theta/\delta_{\theta,Ri=0.01}$ with combined ξ and Ri

A regression analysis of the DNS results gives the following correlation for δ_θ with combined ξ and Ri,

$$\delta_\theta = 1.4156 - 1.79549^x \tag{5.17}$$

$$\delta_\theta = -0.02233x^2 + 0.35687x - 0.2068 \tag{5.18}$$

where $x = Ri^{-0.454}\xi^{0.24563}$. Both correlations, which are in different forms, correlate the DNS results very well, although the power law one is slightly fitting better.

5.5 Kinetic energy budget

5.5.1 Definition

Based on the horizontal-plane statics, the perturbation velocity $\mathbf{u}'$ can be defined as,

$$\mathbf{u}'(x, y, z, t) = \mathbf{u} - \langle \mathbf{u} \rangle_{xy} \tag{5.19}$$

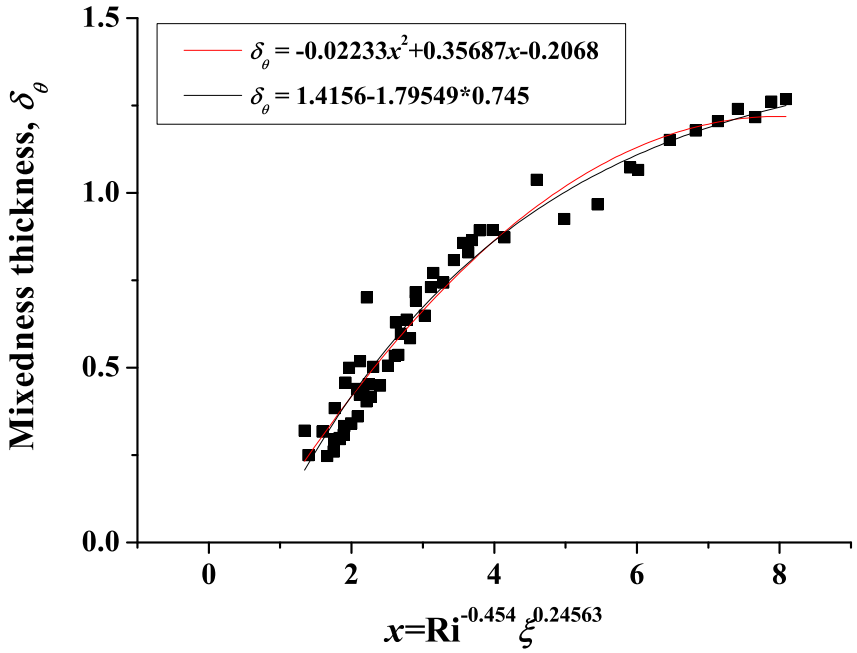

Fig. 5.15 Correlations between δ_θ and $x = Ri^{-0.454}\xi^{0.24563}$ obtained from the DNS results.

where the operator $\langle\rangle_{xy}$ is the horizontal plane average:

$$\langle f\rangle_{xy} = \frac{1}{L_x L_y}\int_0^{L_y}\int_0^{L_x} f(x,y,z,t)dxdy$$

in which the subscript "xy" denotes the average over the horizontal $x-y$ plane. Similarly a single subscript letter denotes the average over the axis where presents, *e.g.* $\langle f\rangle_y$ represents the average of f over y across the domain,

$$\langle f\rangle_y = \frac{1}{L_y}\int_0^{L_y} f(x,y,z,t)dy$$

Suggested by Caulfield and Peltiler [2], perturbation velocity $\mathbf{u}'$ can be further divided into the spanwise averaged part and the remaining three-dimensional part, so that the kinetic energies of the streamwise and the rest spanwise structures will be isolated separately. The spanwise averaged perturbation velocity is defined as,

$$\mathbf{u}_{kh}(x,z,t) = \langle \mathbf{u} - \langle \mathbf{u}\rangle_{xy}\rangle_x \tag{5.20}$$

where the subscript "*kh*", inherited from Caulfield and Peltier [2], indicates after the spanwise average the velocity field $\mathbf{u}_{kh}$ should predominantly represent those belong to the streamwise KH eddy. Further deducting $\mathbf{u}_{kh}$ from $\mathbf{u}'$ gives the following remaining three-dimensional part of the perturbation velocity,

$$\mathbf{u}_{3d}(x, y, z, t) = \mathbf{u} - \mathbf{u}_{kh} - \langle \mathbf{u} \rangle_{xy} \tag{5.21}$$

where the subscript "3*d*" denotes the perturbation velocity left in the spanwise direction. Accordingly, the corresponding kinetic energies based on the decomposed velocities represented by 5.19-5.21 are defined as follows,

$$\mathbf{K}' = \langle \mathbf{u}' \cdot \mathbf{u}'/2 \rangle_{xyz} \tag{5.22}$$

$$\mathbf{K}_{kh} = \langle \langle \mathbf{u} \rangle_{kh} \cdot \langle \mathbf{u} \rangle_{kh}/2 \rangle_{xz} \tag{5.23}$$

$$\mathbf{K}_{3d} = \langle \langle \mathbf{u} \rangle_{3d} \cdot \langle \mathbf{u} \rangle_{3d}/2 \rangle_{xyz} \tag{5.24}$$

and the total kinetic energy, $\mathbf{K}_{all}$, and the horizontal plane average kinetic energy, $\mathbf{K}_{av}$, are

$$\mathbf{K}_{all} = \langle [u^2 + v^2 + w^2]/2 \rangle_{xyz} \tag{5.25}$$

$$\mathbf{K}_{av} = \langle \langle \mathbf{u} \rangle_{xy} \cdot \langle \mathbf{u} \rangle_{xy}/2 \rangle_{z} \tag{5.26}$$

The related kinetic energy budget is then,

$$\mathbf{K}_{all} = \mathbf{K}_{av} + \mathbf{K}' = \mathbf{K}_{av} + \mathbf{K}_{kh} + \mathbf{K}_{3d} \tag{5.27}$$

The numerical errors associated with DNS in the determination of the kinetic energy budget (5.27) are checked and found at around 1% of the initial total kinetic energy, suggesting the division $\mathbf{K}'$ is sufficiently accurate. The difference between $\mathbf{K}_{kh}$ and $\mathbf{K}_{3d}$ also indicates the transfer of $\mathbf{K}'$ between the streamwise and spanwise structures, if kinetic energy budget is conserved well. If $\partial(\mathbf{K}_{3d} - \mathbf{K}_{kh})/\partial t > 0$, $\mathbf{K}'$ is transferred from the spanwise structures to the streamwise structures, and vice verse. Accordingly, the kinetic energy ratio, which is the ratio between $\mathbf{K}_{3d} - \mathbf{K}_{kh}$ and $\mathbf{K}'$, is defined as follows,

$$\chi = \frac{\mathbf{K}_{3d} - \mathbf{K}_{kh}}{\mathbf{K}'} = \frac{\mathbf{K}_{3d} - \mathbf{K}_{kh}}{\mathbf{K}_{3d} + \mathbf{K}_{kh}} \tag{5.28}$$

The kinetic energy ratio χ represents the proportion of $\mathbf{K}'$ involved in the kinetic energy transfer within the coherent structures.

5.5.2 Influences of ξ

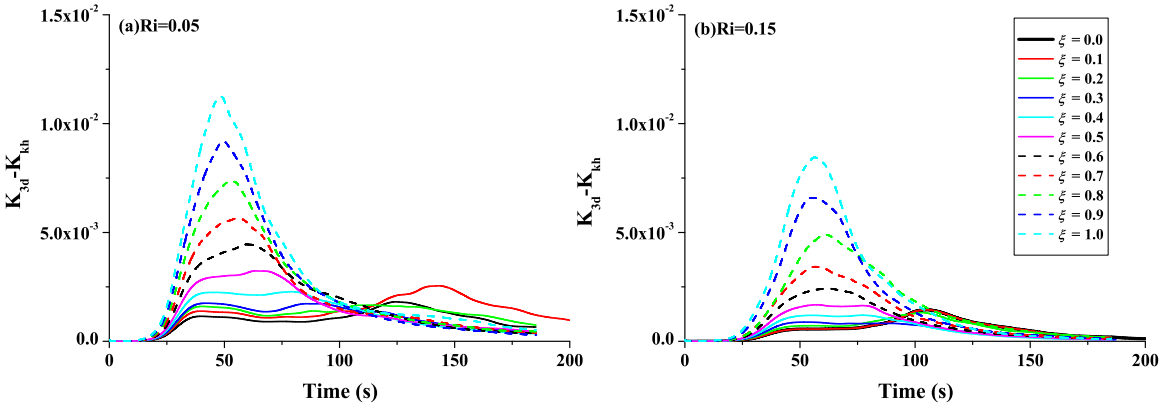

Fig. 5.16 Time series of $(\mathbf{K}_{3d} - \mathbf{K}_{kh})$ at (a) $Ri = 0.05$ and (b) $Ri = 0.15$ for different ξ values varying from 0 to 1.0.

Figure 5.16 shows the time series of $\mathbf{K}_{3d} - \mathbf{K}_{kh}$ at $Ri = 0.05$ and $Ri = 0.15$ for different ξ values over the range of $0 \leq \xi 1.0$. Similar shapes in the time series of $(\mathbf{K}_{3d} - \mathbf{K}_{kh})$ shown in this figure are also found in the $Ri \leq 0.10$ cases and in the $Ri > 0.10$ case as well. In the $Ri = 0.05$ case, as shown in Fig. 5.16(a), two peaks of $(\mathbf{K}_{3d} - \mathbf{K}_{kh})$ indicate that the climax of kinetic energy transfer are observed around $t = 50$ s (the first peak) and around 120 s (the second peak). The first peaks are observed for all ξ cases considered, whereas the second peaks are found only for the "streamwise dominant" mode with $\xi < 0.3$. The appearance of the second peak in the "streamwise dominant" mode agrees with its dynamic features, in that the coherent structures in the "streamwise dominant" mode saturated first in the streamwise direction then in the spanwise direction. For the "balanced" mode with $\xi = 0.4 - 0.6$, the second peak of in the time series of $(\mathbf{K}_{3d} - \mathbf{K}_{kh})$ disappears as a result of earlier decay caused by enhanced spanwise "eddy wrap" structures. Meanwhile, the first peak for the $\xi = 0.4 - 0.6$ cases postpones for $15 \sim 25$ s based on the maximum $(\mathbf{K}_{3d} - \mathbf{K}_{kh})$ and reaches around the same level of the secondary peak in the "streamwise dominant" mode with $\xi < 0.3$, therefore giving the "balanced" features more obvious in $(\mathbf{K}_{3d} - \mathbf{K}_{kh})$. As ξ further increases, the first peak of $(\mathbf{K}_{3d} - \mathbf{K}_{kh})$ further increases significantly and exceeds

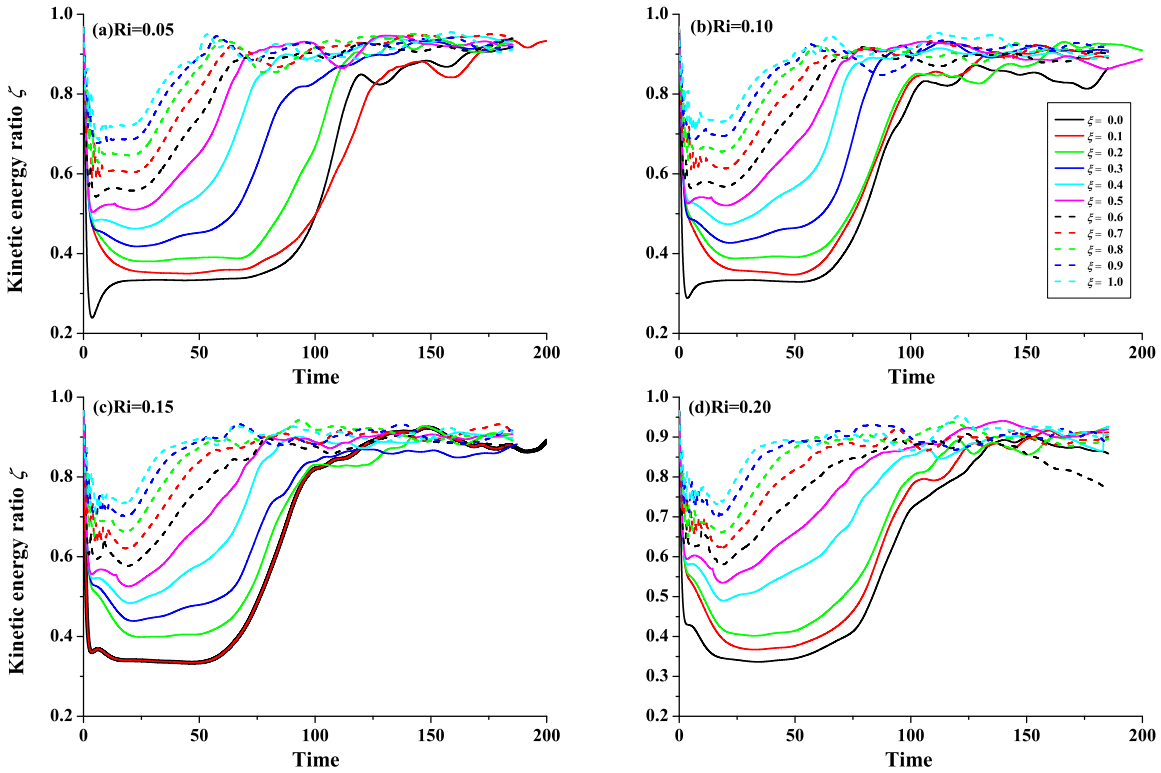

Fig. 5.17 Time series of the kinetic energy ratio χ at (a) $Ri = 0.05$, (b) $Ri = 0.1$, (c) $Ri = 0.15$, and (d) $Ri = 0.2$ for different ξ values varying from 0 to 1.0. (Note: in this figure ζ is used to denote the kinetic energy ratio instead of χ).

far beyond the maximum ($\mathbf{K}_{3d} - \mathbf{K}_{kh}$) found in the "streamwise dominant" and "balanced" modes, suggesting that the enhancing spanwise structures completely break the "balance" between the streamwise and spanwise structures and absorb more kinetic energy from the streamwise structures.

In the $Ri = 0.15$ case, a similar behavior in the time series of ($\mathbf{K}_{3d} - \mathbf{K}_{kh}$) is found, except the positions of the second peaks drop even to the declining branch of the time series for the $\xi = 0.7 - 1.0$ cases. The time for the second peak in the $Ri = 0.15$ case also happenes earlier, at about 110 s. In addition, the first peaks in the $Ri = 0.15$ case, as shown in Fig. 5.16(b), are lower than those in the $Ri = 0.05$ case, as shown in Fig. 5.16(a).

To further examine the proportion of kinetic energy transfer in terms of ($\mathbf{K}_{3d} - \mathbf{K}_{kh}$) related to the total perturbation kinetic energy $\mathbf{K}'$, the time series of kinetic energy ratio χ is presented in Fig. 5.17 for $Ri = 0.05$, 0.10, 0.15 and 0.20, where each case include plots at ξ varying from 0.0 to 1.0. It is seen that χ experiences a primary constant stage, a rapidly increasing stage and an asymptotic stage. The transitional points between the rapid

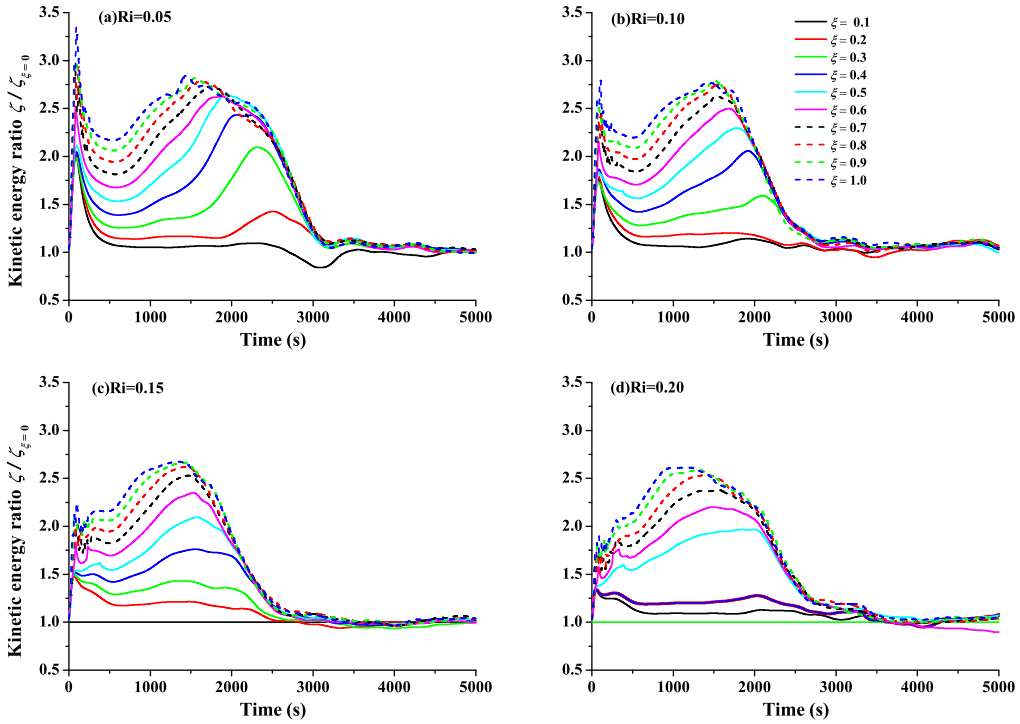

Fig. 5.18 Time series of $\chi/\chi_{\xi=0}$ at (a) $Ri = 0.05$, (b) $Ri = 0.1$, (c) $Ri = 0.15$, and (d) $Ri = 0.2$ for different ξ values varying from 0 to 1.0. (Note: in this figure ζ is used to denote the kinetic energy ratio instead of χ).

increasing stage and the asymptotic stage are displayed as the smooth turning point for the plots at $\xi < 0.5$ and the sharp peaks for the plots at $\xi \geq 0.5$. It is very interesting that in the asymptotic stage , when the coherent structures completely decay into turbulent state, a nearly universal value of $\chi \approx 0.9$ were found for all plots at all Ri values and ξ values, indicating a universal state where most of $\mathbf{K}'$ are included in the spanwise instability structures.

On the other hand, the moment of the primary peak (turning point) precedes with increasing ξ in the four Ri cases. To show the transitional points more clearly, the time series of χ normalized by $\chi_{\xi=0}$, which is χ at $\xi = 0$ (that is, the PSS flow), similar to the mixedness thickness δ_θ as described in the previous section, are presented in Fig. 5.18. In this figure, it is seen that the primary transitional peaks (the turning points) in Figure 5.16, which indicate the saturation of the coherent structures, all translated into the sharp peaks in Fig. 5.18. In addition, In each of the four Ri cases, the time series of $\chi/\chi_{\xi=0}$ merge together at the onset of the asymptotic stage, as such a merging point represents the onset of the turbulence stage.

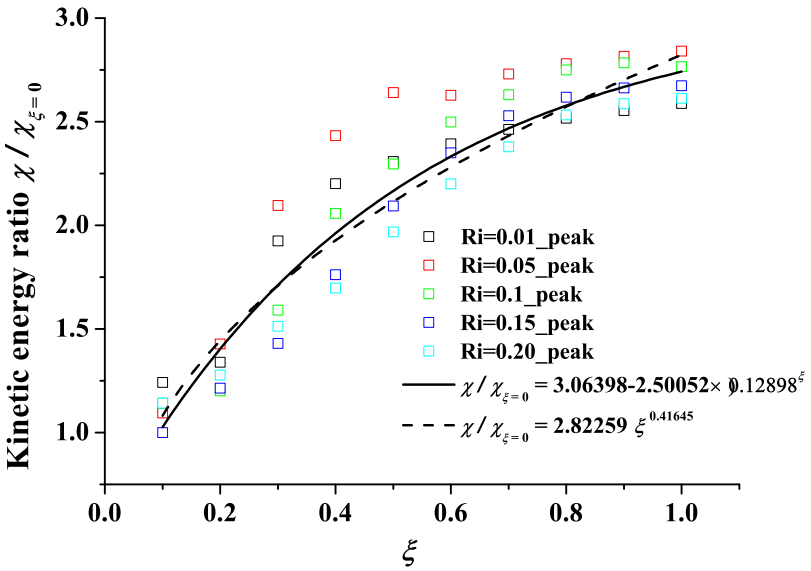

Fig. 5.19 Relation and correlations between the peak value of $\chi/\chi_{\xi=0}$ in its time series and ξ for four *Ri* cases.

The magnitudes of $\chi/\chi_{\xi=0}$ at each peak shown in Fig. 5.18, along with $Ri = 0.01$ cases, are plotted against ξ in Fig. 5.19. Generally, a monotonically increasing tendency is observed between the $\chi/\chi_{\xi=0}$ at peaks and ξ. After different trials, the best two correlation functions are chosen and their correlated results are:

$$\chi/\chi_{\xi=0} = 2.82259\xi^{0.41645} \tag{5.29}$$

$$\chi/\chi_{\xi=0} = 3.06398 - 2.50052 \times 0.12898^{\xi} \tag{5.30}$$

5.5.3 Influences of *Ri*

Similar to Figure 5.16, Figures 5.20 shows the time series of $(\mathbf{K}_{3d} - \mathbf{K}_{kh})$ at four modes observed before, $\xi = 0.0$ (the PSS flow), $\xi = 0.2$ (at the "streamwise dominant" mode), $\xi = 0.5$ (at the "balanced" mode), and $\xi = 1.0$ (at the "spanwise dominant" mode) for *Ri* varying from 0.01 to 0.2. Generally at all four modes, the magnitudes of $(\mathbf{K}_{3d} - \mathbf{K}_{kh})$ decrease with the increasing *Ri*, indicating the suppression from enhanced background stratifications

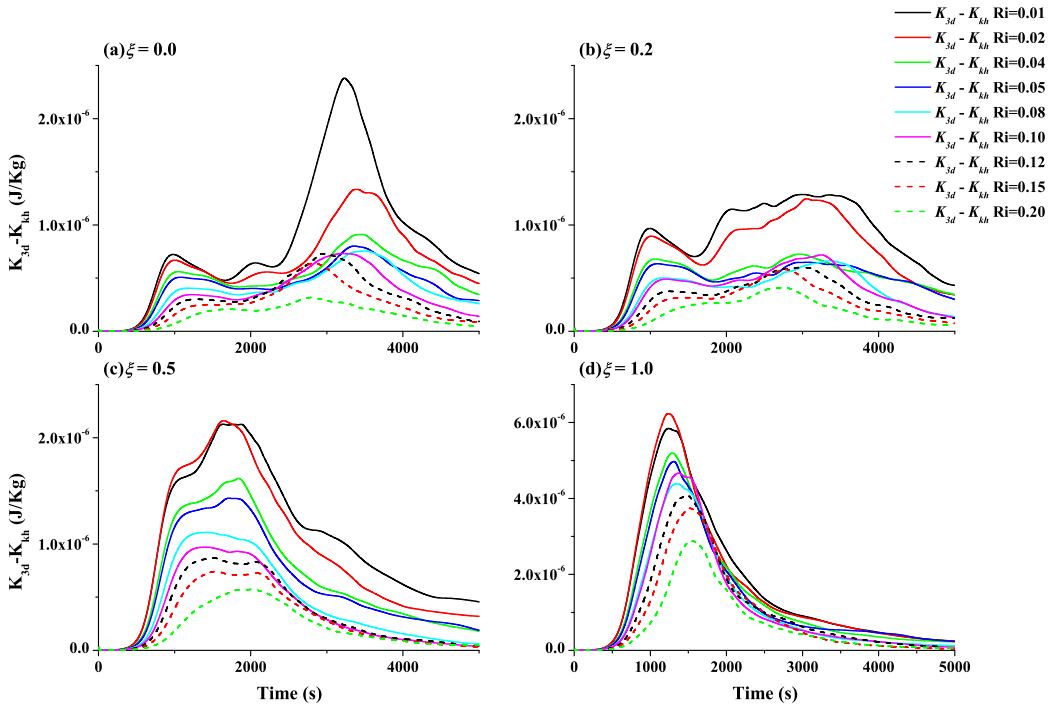

Fig. 5.20 Time series of $(\mathbf{K}_{3d} - \mathbf{K}_{kh})$ at (a) $\xi = 0.0$, (b) $\xi = 0.2$, (c) $\xi = 0.5$ and (d) $\xi = 1.0$ for different *Ri* values varying from 0.01 to 0.2.

on the developing coherent flows structures. In addition, the increased stratifcation in terms of increased *Ri* also lead to earlier decay of coherent structures. For the PSS flow (Figures 5.20(a)) and weak CSS flow cases (Figures 5.20(b)), the second peak at about $t \approx 3000$, which indicate the decay of flow coherent structures, occur earlier as *Ri* increases. For stronger CSS flow such as $\xi = 0.5$ and $\xi = 0.8$ cases, shown in Figures 5.20(c) and (d), the coherent flow structures collaspe much faster due to cross shear dynamics. Nevertheless, increased *Ri* still force the single peak to shift slighty backward in the time axis, suggesting a the decay of coherent structures occur a slightly earlier at stronger background stratification.

Figures 5.21 shows the time series of χ for corresponding cases in Figures 5.20. Similar to Fig. 5.17, χ also experience primary constant stage, a rapidly increasing stage and an asymptotic stage in Figures 5.21. Nevertheless, after normalized by $\mathbf{K}'$ the discrepancies among different *Ri* plot curves in Figures 5.20 gradually fade away, as in all ξ cases different plots at different *Ri* basically overlap. After all, χ itself indicates the role of kinetic energy budget, which is primarily determiend by turbulence shear dynamics rather than stratification. Moreover, the initial value of χ gradually increases with increased ξ, indicating the influences of enhanced spanwise flow structures as the initial cross shear increases. On the contrary, at the asympotitc stage, a relatively constant χ whose value is 0.9 are observed in all cases, which agrees the results presented in Fig. 5.17. Due to such overlap in figures 5.21, the

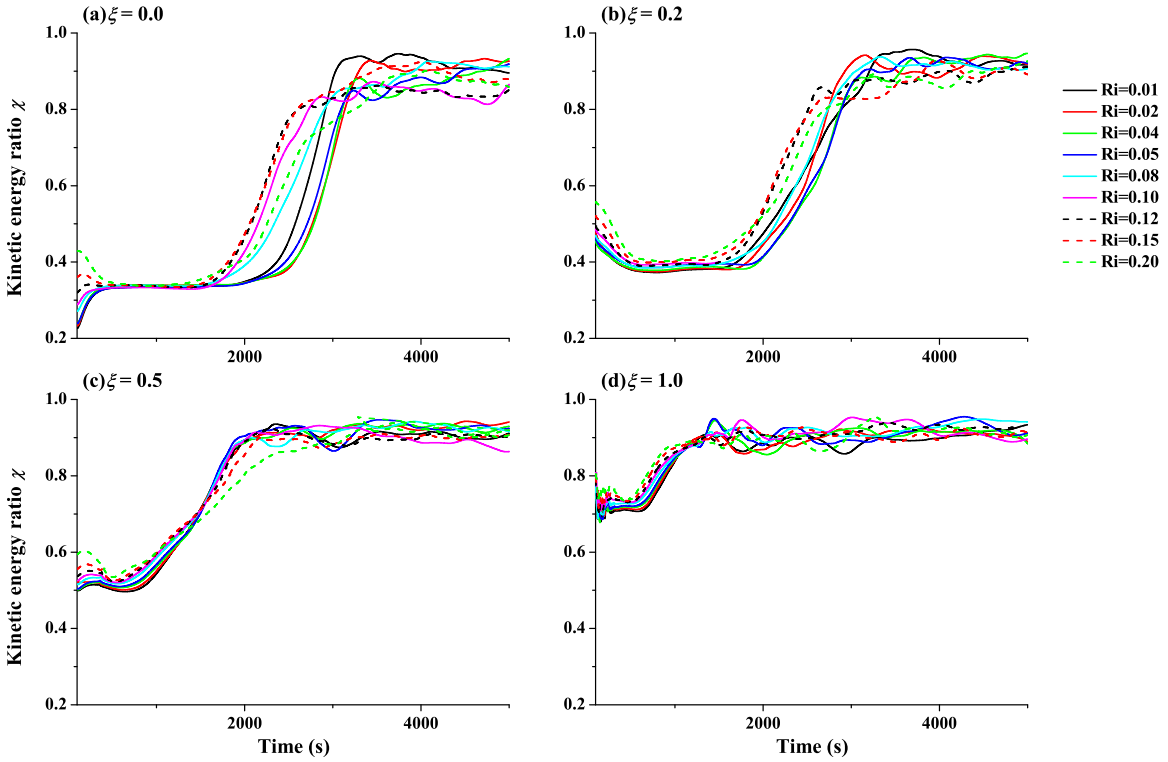

Fig. 5.21 Time series of $(\mathbf{K}_{3d} - \mathbf{K}_{kh})$ at (a) $\xi = 0.0$, (b) $\xi = 0.2$, (c) $\xi = 0.5$ and (d) $\xi = 1.0$ for different Ri values varying from 0.01 to 0.2.

time series of χ normalized by $\chi_{Ri=0.01}$ are found to fluctuate around unity, therefore it is unnecessary to plot them here. The results then show that,

$$\chi / \chi_{Ri=0.01} \sim 1.0$$

5.6 Conclusions

In this chapter, the stratification effects on turbulent mixing of the CSS flow, through changing the values of the bulk Richardson number Ri which represents the relative intensity of the background stratification with respect to the streamwise velocity shear, is investigated numerically for the CSS flow over the ranges of $\xi = 0 \sim 1$ and $Ri = 0.01 \sim 0.2$. As stronger background stratifications are introduced, the eddy-featured coherent structures are suppressed and ultimately downgraded to wave-like coherent structures.

The time series of the mixedness thickness δ_m for weakly stratified environments show significant increases of δ_m at the primary and secondary instability stages in CSS flow

compared to PSS flow. After normalization of δ_m by δ_m at ξ =0 for the PSS flow, two peaks appear in the times series of the normalized mixedness thickness $\delta_\theta/\delta_{\theta,\xi=0}$ as manifestations of primary and secondary instabilities. In the times series of $\delta_\theta/\delta_{\theta,\xi=0}$, the features of the three CSS flow instability modes are clearly identified by whether $\delta_\theta/\delta_{\theta,\xi=0}$ at the first peak (the primary instability stage) is more than, comparable to, or less than $\delta_\theta/\delta_{\theta,\xi=0}$ at the second peak (the secondary instability stage). Furthermore, as *Ri* increases up to 0.05, two peaks found in the time series of $\delta_\theta/\delta_{\theta,\xi=0}$ at $Ri = 0.01$ reduce to a single peak, which occurs at the time when the coherent structures saturate. Finally, it is also found that the normalized mixedness thickness $\delta_\theta/\delta_{\theta,Ri=0.01}$, which is normalized by δ_m at Ri =0.01, decreases as an exponential function of *Ri* at the turbulence stage.

The time series of the kinetic energy difference $\mathbf{K}_{3d} - \mathbf{K}_{kh}$ and kinetic energy ratio χ shows that, as ξ increases the kinetic energy involved in the transition to turbulence significantly increases exponentially. In addition, as *Ri* increases, the magnitude of $\mathbf{K}_{3d} - \mathbf{K}_{kh}$ and χ only decrease significantly near the primary peaks, which indicates the development of the primary flow structures. At asymptotic stage, however, the enhanced stratification in terms of increased *Ri* has no influences on kinetic energy budget, as constant value of $\chi = 0.9$ are found in all *Ri* cases.

References

[1] KONRAD, J. H. 1976 An experimental investigation of mixing in two-dimensional turbulent shear flows with applications to diffusion-limited chemical reactions. PhD thesis, California Institue of Technology.

[2] CAULFIELD, C. P. & PELTIER, W. R. 2000 The anatomy of the mixing transition in homogeneous and stratified free shear layers *J. Fluid Mech.* **413**, 1–47.

[3] WINTERS, K., LOMBARD, P., RILEY, J., & D'ASARO, E. A. 1995 Available potential energy and mixing in densitystratified fluids. *J. Fluid Mech.* **289**, 115-128.

[4] XIAO, Y., LIN, W., ARMFIELD, S.W., KIRKPATRICK, M.P., & HE, Y. 2014 Hydrodynmaic Linear Stability Analysis on Cross Sheared Stratified Flows. in *19th Australasian Fluid Mech. Conf.*, 8-11 December, 2014, Melbourne, Australia.

[5] KIRKPATRICK, M. P. 2013 *The PUFFIN Manual: An Engineering and Environmental Fluid Dynamics Simulation Model*, The University of Sydney.

[6] ATSAVAPRANEE, P. & GHARIB, M. 1997 Structures in stratified plane mixing layers and the effects of cross-shear. *J. Fluid Mech.* **342**, 53–86.

[7] LIN, J., SHAO, X. & YU, Z. 2000 Numerical research on coherent structures in a mixing layer with cross-shear. *Acta Aeronautica et Astronautica Sinic* **21**(1), 13–20.

[8] KOOP, C. G. & BROWAND, F. K. 1978 Instability and turbulence in a stratified fluid with shear. *J. Fluid Mech.* **93**, 135–159.

Chapter 6

Hydrodynamic stability analysis of SCBL flows in stratified environments

The results of this chapter are presented in the following publication:

1. XIAO, Y., LIN, W., Y. HE, ARMFIELD, S. W. & KIRKPATRICK, M. P. 2015 Hydrodynamic stability analysis of sheared convective boundary layer flows in stratified environments. in *Proceedings of the International Symposium on Turbulence and Shear Flow Phenomena (TSFP-9)*, 30 June - 3 July 2015, Melbourne, Australia, Paper ID: P-51.

6.1 Introduction

As a representative geographical flow, sheared stratified (SS) flow in which sheared flow motions occur in a stratified environment has received substantial studies in the past decades. However, in the geographical settings such as the planetary or oceanic boundary layers and engineering settings involving heat transfer from radiation or chemical reaction, the comparable thermally convective flows inevitably coexist with sheared stratified flow, together forming a complex flow configuration, namely the sheared convective boundary layer (SCBL). SCBL flows have significant importance for environmental issues, such as the mixing process of pollutants in atmospheric boundary layers, the heat and mass transfer in the upper ocean, and the mixing in large scale water bodies such as reservoirs, lakes and estuaries. The SCBL flows in fire-induced smoke transportation will potentially increase the fire hazards by changing flow patterns.

As pure thermally convective flows and pure sheared stratified flows have independent unstable modes, *i.e.* , the Rayleigh-Benard instability and shear stratified instability (*e.g.* , the

Kelvin-Helmholtz instability and Holmboe instability), the combination of the two basic flow configurations are expected to produce more interactive and complicated unstable modes and corresponding flow patterns. For instance, Raasch & Franke [1] used high resolution numerical simulation to find the transitional behaviour from a spoke-shape flow pattern in pure thermal convection to a band-like flow pattern in sheared thermal convection. Yang, et al. [2] observed experimentally a unique flow pattern near the interface in fire induced SCBL. Most recently, Stewart, Holmes & Lin [3] investigated the SCBL flows with two-dimensional direct numerical simulation and found that the Kelvin-Helmholtz instability and the Rayleigh-Benard instability coexist in some stratification conditions, where the presence of the penetrative convection modifies the original Kelvin-Helmholtz eddy structures. Their results also suggest that new unstable modes might occur in the SCBL flow settings, which motivates the current hydrodynamic stability analysis to examine the stability features of the SCBL flow.

This paper will study the hydrodynamics of SCBL flow by introducing an unstable stratification factor J_b into the Taylor-Goldstein equation that describes the hydrodynamics of shear stratified flow. This idea comes from the hydrodynamic study of two-layer thermal penetrative convective flows where a thermally convective region is capped by a stable stratified layer. The difference between the current SCBL flow and such two-layer penetrative convection is whether horizontal shear flow is present. By solving modified Taylor-Goldstein equations for SCBL flows, the instability features of the SCBL, including temporal growth rate and spatial perturbation structures, will be investigated, after a brief introduction of the numerical methodology.

6.2 Perturbation equations

Based on the Taylor-Goldstein equations for sheared stratified flow and by applying the Squire transformations as detailed in [4], the following perturbation equations, written in matrix form, have been derived by the current study,

$$\tilde{\sigma}\begin{bmatrix} \nabla_s^2 & \\ & I \end{bmatrix}\begin{bmatrix} \hat{w} \\ \tilde{b} \end{bmatrix} = \begin{bmatrix} -i\tilde{\alpha}(U\nabla_s^2 - U_{zz}) & \dfrac{\tilde{\alpha}^2}{Fr^2} \\ \tilde{N}^2 & -i\tilde{\alpha}U \end{bmatrix}\begin{bmatrix} \hat{w} \\ \tilde{b} \end{bmatrix} \tag{6.1}$$

where the subscript 'zz' denotes the second order differentiation with respect to z, ∇_s^2 is the Squire Laplacian operator defined as $\nabla_s^2 = D^2 - \tilde{\alpha}^2$, $D = \partial/\partial z$ is the differential operator for the perturbation properties, $\tilde{\alpha}$ is the Squire wavenumber, I is the identity matrix, $\tilde{\sigma}$ is the Squire temporal growth rate of the perturbations properties, $\hat{w}$ and $\tilde{b}$ ($\tilde{b} = \gamma\tilde{\theta}$) are

the vertical component of the velocity perturbation and the Squire buoyancy, $\tilde{\theta}$ is the Squire temperature, γ is the thermal expansion coefficient, and $\tilde{N}^2$ ($\tilde{N}^2 = \gamma\tilde{\theta}_z$) is the local Squire buoyancy Brunt-Väisälä frequency. For sheared stratified flows, the sheared layer thickness, the velocity and temperature changes across the sheared/stratified layer are usually selected as the characteristic length scale L, velocity scale $\Delta u_{*,0}$ and temperature scale $\Delta\theta_{*,0}$, respectively. $Fr = \Delta u_{*,0}/\sqrt{gL}$ is the Froude number where g is the gravitational acceleration.

Hazel [5] suggested that when the basic velocity and background stratification in the sheared/stratified layer are in the form of $\Delta u_{*,0} f(z_*)$ and $\Delta\theta_{*,0} f(z_*)$, where $f(z_*)$ is a hyperbolic function, and if $(\partial u/\partial z)|_{z=0} = 1$ and $(\partial\theta/\partial z)|_{z=0} = 1$, where $z = 0$ is the central line of the sheared/stratified layer, then the local Richardson number $Ri_g(z)$ is

$$Ri_g(z) = \frac{N_*^2(z_*)}{(\partial u_*/\partial z_*)^2} = J\frac{(\partial\theta/\partial z)}{(\partial u/\partial z)^2}, \tag{6.2}$$

in which $J = g\gamma\Delta\theta_{*,0}L/\Delta u_{*,0}^2 = (g\gamma\Delta\theta_{*,0}/L)(L/\Delta u_{*,0})^2$. Here the bulk temperature gradient $\Delta\theta_{*,0}/L$ within the sheared/stratified layer is extracted. In practical stability analysis, J plays as an effective substitiute for Ri_g.

The SCBL flow system in this study is shown in figure 6.1, where the convective flow region with unstably linear stratification and the length scale L_b occurs at the bottom of the sheared stratified flow region with smooth tangential stratification and the length scale L. As the temperature at the bottom boundary $\theta_{b,*}$ is larger than the temperature $\theta_{1,*}$ the flows are unstable at $z_* < L_b$. However, when $z_* > L_b$, the flows are stably stratified as $\Delta\theta_{0,*} = \theta_{2,*} - \theta_{1,*} > 0$. In the convective flow region the bulk temperature gradient is $G_b = -\Delta\theta_{b,*}/L_b$, where the negative sign indicates that the temperature decreases with increasing height. Correspondingly, the bulk temperature gradient for the stably stratified layer is $G_s = \Delta\theta_{0,*}/L$, where the positive sign indicates that the temperature increases with increasing height.

In penetrative convection problems where a thermal convection region is capped by a stably stratified layer, Whitehead & Chen [6] and Sun [7] introduced a stability factor S by replacing the bulk temperature gradient in the Rayleigh number with the bulk temperature gradient in the top stably stratified layer. Inspired by this method, in the current SCBL flow, we replace the bulk temperature gradient G_s in J with G_b in the convective flow region $z < L_b$ and define the unstable stratification factor $J_{b,*}$ for SCBL flow as

$$J_b = -\frac{g\gamma\Delta\theta_{b,*}}{L_b}\left(\frac{L}{\Delta u_{*,0}}\right)^2 = g\gamma G_b\left(\frac{L}{\Delta u_{*,0}}\right)^2 = \frac{G_b}{G_s}J, \tag{6.3}$$

so that when $z > L_b$, $N_*^2 = J(\partial\theta/\partial z)$ and when $z < L_b$ $N_*^2 = J_b(\partial\theta/\partial z)$ in (6.2). It is noted that J_b and J have the opposite signs, indicating unstable and stable background stratification, respectively. Therefore, while solving (6.1), N_*^2 will become a piecewise function depending on if $z > L_b$ or $z < L_b$.

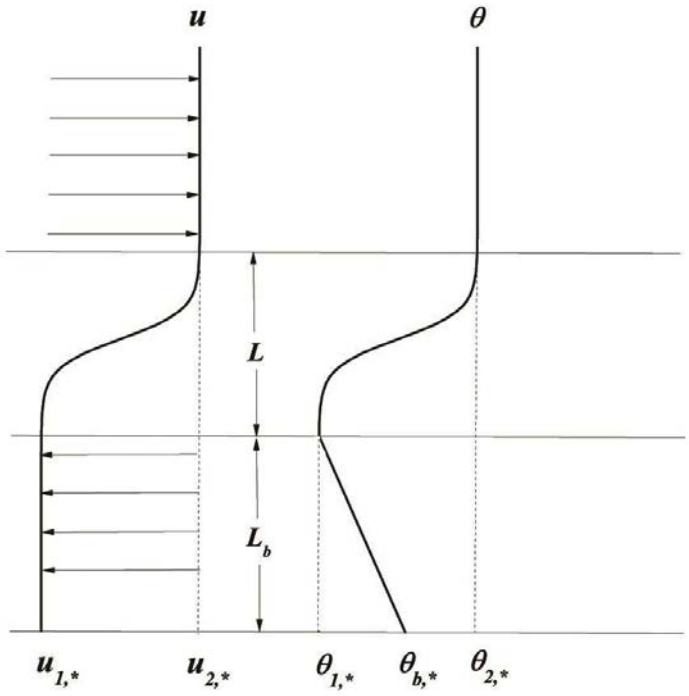

Fig. 6.1 The SCBL flow configuration under consideration and the background velocity and stratification profiles.

6.3 Methodology

The temporal mode of (6.1), where α is a real number and c is a complex number, is solved in this study. It should be noted that the real part of the temporal growth rate, $\tilde{\sigma} = i\tilde{\alpha}c$, of the perturbation is only determined by the imaginary part of the complex wave speed c, for the wavenumber $\tilde{\alpha}$ is fixed as a real number.

Matrix methods are used to solve the eigenvalue problems formed by discretising the perturbation equations (6.1) with uniform grid and using the second-order central difference scheme. The QZ algorithm developed by Moler & Stewart[8], which is integrated in the

LAPACK routine CGGEV, is used as the complex eigenvalue solver. The robustness of the QZ algorithm in hydrodynamic stability analysis has been demonstrated in some recent studies, such as Smyth, Moum & Nash [9], Liu, Thorpe & Smyth [10], and Thorpe, Smyth & Li [11].

The boundary conditions $\hat{w} = \tilde{b} = 0$ are applied at both the top and the bottom boundaries. The dimensionless vertical coordinate z varies between -5 and 5, where z is made dimensionless by δ_s, giving the computational domain a size ten times that of δ_s, where the characteristic length δ_s is selected as one half of the sheared layer thickness. The length scale for the unstable stratified layer is $L_b = 3\delta_s$, which allows the unstable stratified layer to be adjacent to the central shear stratified layer. Based on (6.3), when $\Delta\theta_{*,0} = \Delta\theta_{*,b}$, $J_b = G_b = (1/3)J$. Thus, this study will change J_b in the way that J_b/J will be the factor of 1/3.

6.4 Results

6.4.1 Growth Rate $\tilde{\sigma}$

Figure 6.2 shows the contours of the real part of the temporal growth rate $\tilde{\sigma}$ in the $J - \tilde{\alpha}$ plane for different unstable stratifications in terms of J_b. In figure 6.2(a) where $J_b = 0$ which represents that no convective flux exists, the unstable hemi-ellipse regions over $\tilde{\sigma} = 0 \sim 1$, in which the imaginary part of $\tilde{\sigma}$ (Im[$\tilde{\sigma}$]) is found to be zero, correspond to the stationary Kelvin-Helmholtz instability mode in SS flow as marked by 'SS'. The shapes of the KH mode regions are similar to the numerical results from Hazel [5], where the critical stratification factor J_{cr} occurs at a corresponding critical wavenumber $\tilde{\alpha}_{cr} = 0.5$. As $J_b \neq 0$ when a convective flux is introduced, the other large unstable region where Im[$\tilde{\sigma}$]$\neq 0$ appears, as marked by 'RB' in figure 6.2(b) and figure 6.2(c). In figure 6.2(b), the 'RB' region interacts with the 'SS' region at $\tilde{\alpha} \approx 0.8$. In figure 6.2(c) when J_b is one thrid of J, the intersection points move to the small wavenumber range $\tilde{\alpha} \approx 0.25$ and the two contour curves of $\tilde{\alpha} = 0.2$ merge together at $\tilde{\alpha} = 0.45 \sim 0.8$. Inside this merging region, part of the $\tilde{\sigma} = 0.01$ contour, which was in the 'SS' region, is overwhelmed by the $\tilde{\sigma} = 0.02$ contour of the 'RB' region.

To further study the interactions between the two instability regions, figure 6.3 shows Re[$\tilde{\sigma}$] plotted against J at the critical wavenumber $\tilde{\alpha}_{cr} = 0.5$ for a series of J_b/J ratios. This figure can be considered as a vertical slice plot of figure 6.2 at $\tilde{\alpha} = 0.5$. The Im[$\tilde{\sigma}$]$= 0$ solutions for the 'SS' mode and the Im[$\tilde{\sigma}$]$\neq 0$ solutions for the 'RB' mode are denoted by dashed and solid curves, respectively. It is found that as different J_b/J are applied, the 'SS' curve retains its original shape at $J_b = 0$ although different 'RB' curves are obtained.

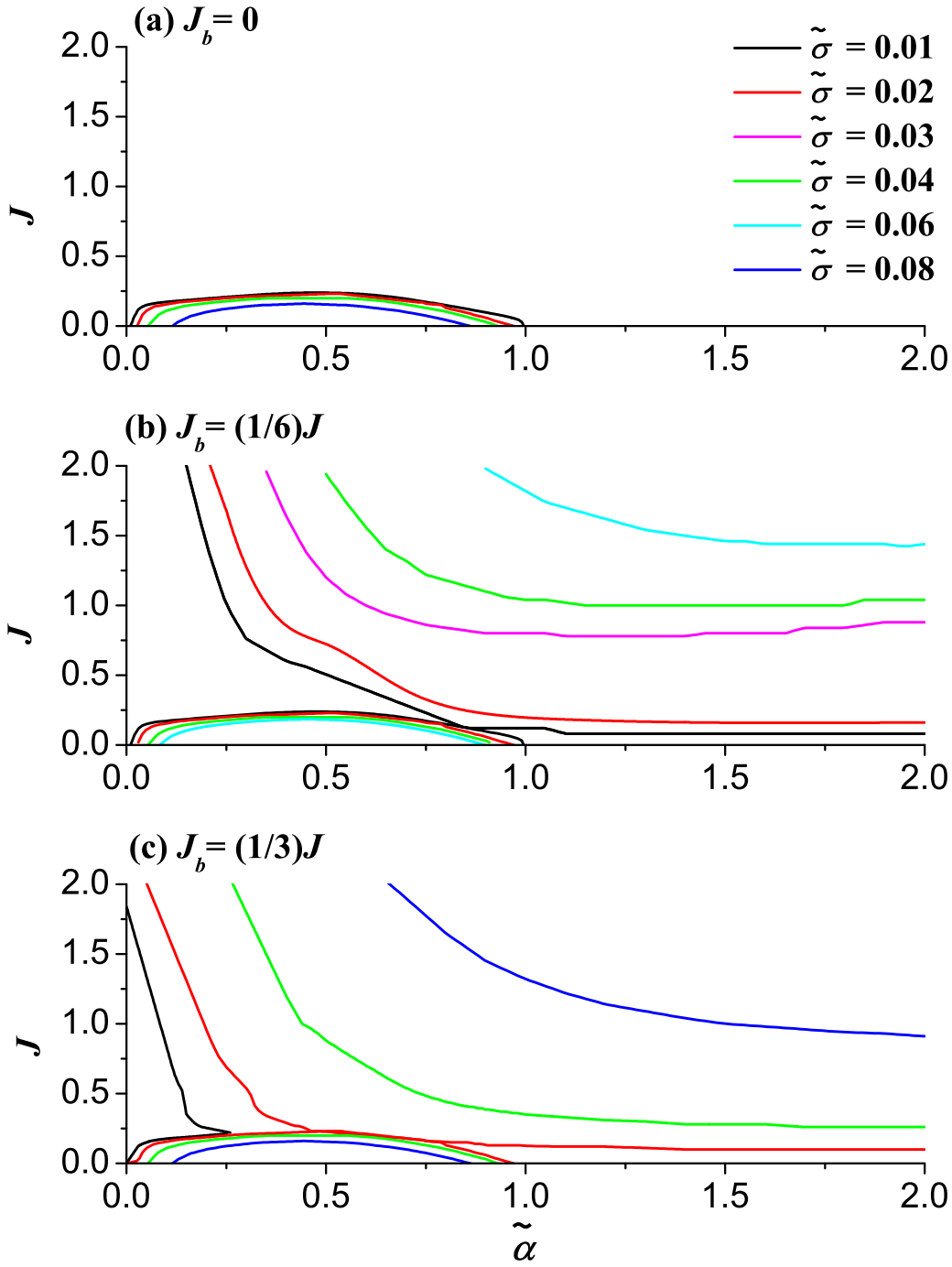

Fig. 6.2 Contour plots of the real part of temporal growth rate $\tilde{\sigma}$ in the J versus Squire wavenumber $\tilde{\alpha}$ plane with (a) $J_b = 0$, (b)$J_b = (1/6)J$ and (c) $J_b = (1/3)J$. The magnitudes of $\tilde{\sigma}$ are denoted by curves in different colors.

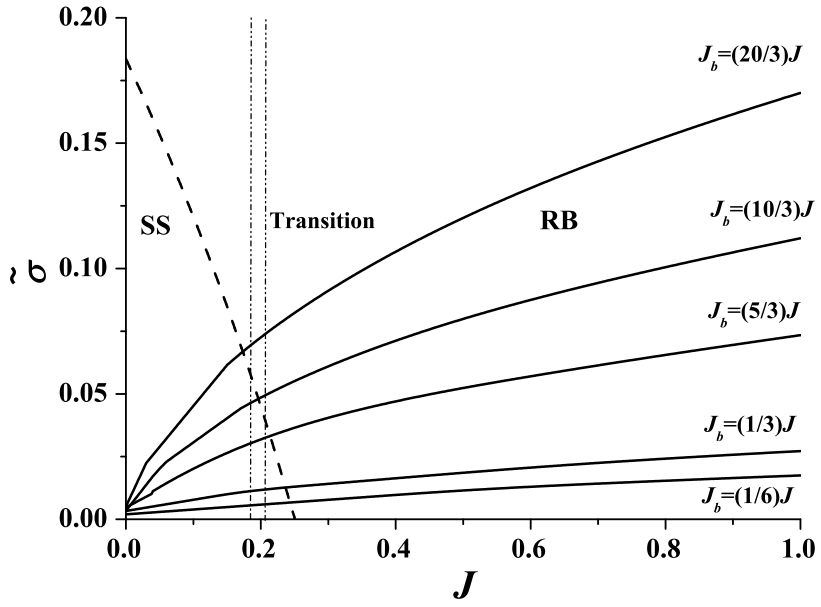

Fig. 6.3 Calculated real part of the temporal growth rate $\tilde{\sigma}$ plotted against J at $\tilde{\alpha} = 0.5$. The results in the SS and RB unstable regiosn are denoted by the dashed and solid curves, respectively.

Therefore, the 'SS' mode is independent of the 'RB' mode. As the 'SS' mode branch decreases quickly with increasing J and the 'RB' mode branch increases gradually with increasing J, the two branches intersect near the critical stratification factor $J = 0.25$ for SS flow. Near the intersection point, as Re$[\tilde{\sigma}]$ in the 'RB' mode is comparable to that in the 'SS' mode, a narrow transition region where both 'SS' and 'RB' have equal influence is created. As J_b/J increases, the 'RB' mode curves gradually rise upwards and cap the 'SS' mode curves, thereby moving the intersection point upwards as well. As a result, some unstable regions which were in the 'SS' mode are replaced by the 'RB' mode, *e.g.* , $J = 0.20 \sim 0.25$ belong to the 'SS' region for $J_b < (10/3)J$ but belong to the 'RB' for $J_b > (10/3)J$.

Figure 6.4 shows the dispersion relations between Re$[\tilde{\sigma}]$ and wavenumber $\tilde{\alpha}$ at $J = 0.2$. It can be considered as a horizontal slice plot of figure 6.2 at $J = 0.2$. Similar to the $J \sim \tilde{\sigma}$ plot in figure 6.3, the dispersion curves for the 'SS' and the 'RB' modes are represented by dashed and solid curves, respectively. Different from figure 6.3, two intersection points between the 'SS' mode dispersion curve and each 'RB' mode dispersion curve are found at small wavenumber range and large wavenumber range respectively, forming two transitional regions in the $\tilde{\alpha} \sim \tilde{\sigma}$ plane. As J_b increases, the 'RB' dispersion curves gradually rise based on their common origin point and move the two intersection points to larger Re$[\tilde{\sigma}]$. Consequently, more and more the 'SS' mode dispersion curve is dominated by the 'RB'

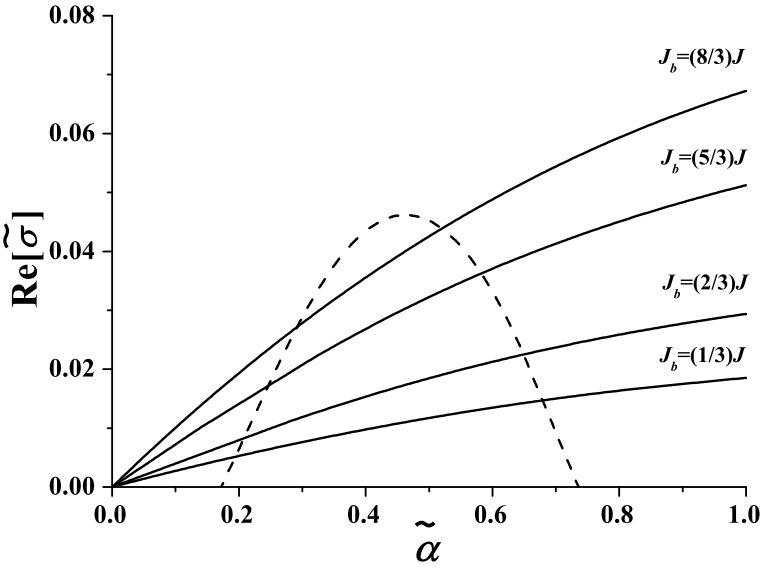

Fig. 6.4 Calculated real part of the temporal growth rate $\tilde{\sigma}$ plotted against $\tilde{\alpha}$ at $J = 0.2$. The results in the SS and RB unstable regiosn are denoted by the dashed and solid curves, respectively.

mode dispersion curve, *e.g.* when $J_b = (8/3)J$ most parts of the 'SS' dispersion curve are covered by the 'RB' curves.

To quantify how the 'RB' mode gradually overwhelms the 'SS' mode as J_b increases, figure 6.5 shows Re$[\tilde{\sigma}]$ plotted against the stratification ratio J_b/J for both the 'SS' and the 'RB' modes at $\tilde{\alpha} = 0.5$ and $J = 0.2$. As both J and $\tilde{\alpha}$ are fixed, Re$[\tilde{\sigma}]$ for the 'SS' mode is constant at 0.045. On the other hand, Re$[\tilde{\sigma}]$ for the 'RB' mode increases with increasing J_b/J in a parabolic fashion, with the following correlation,

$$Re[\tilde{\sigma}]_{RB} = -0.00124(\frac{J_b}{J})^2 + 0.01625(\frac{J_b}{J}) + 0.00837, \tag{6.4}$$

where the subscript 'RB' indicates that the growth rate belongs to the 'RB' mode. It is noted that the 'RB' mode curve and the 'SS' mode curve intersect at $J_b/J = 3$, which indicates a critical transition stratification condition from the 'SS' mode to the 'RB' mode.

6.4.2 Eigenfunctions

Based on figures 6.3 and 6.5, the eigenfunctions for buoyancy perturbation b', vertical velocity perturbation w' in (6.1) and their product, and buoyancy flux perturbation $B' = \theta' w'$

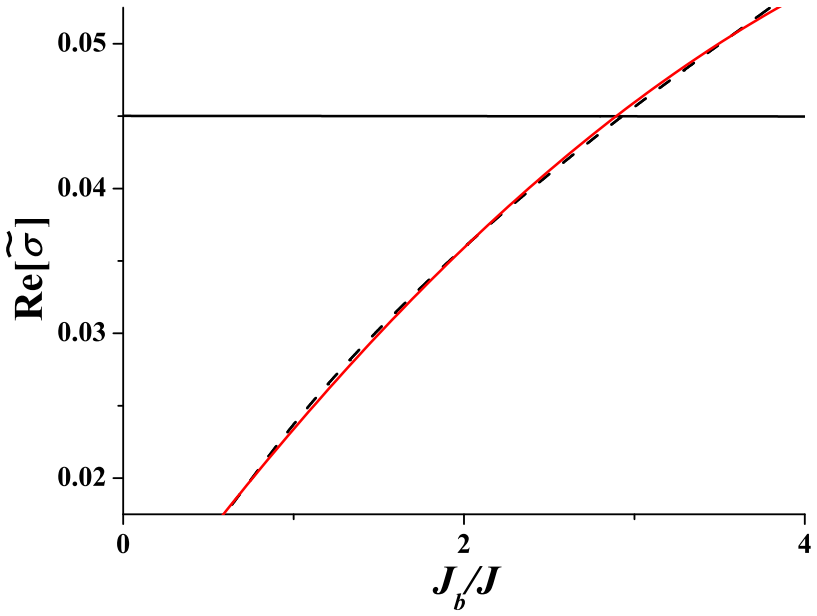

Fig. 6.5 Calculated real part of the temporal growth rate $\tilde{\sigma}$ plotted against the stratification ratio J_b/J at $J = 0.2$ and $\tilde{\alpha} = 0.5$. The results in the SS and RB unstable regiosn are denoted by the dashed and solid curves, respectively. The parabolic correlation for the RB mode plot is denoted by the red solid curve.

are studied at the critical wavenumber $\tilde{\alpha} = 0.5$ and stratification ratio $J_b/J = 3$, which is the intersection point found in figure 6.5. Three typical J values are selected at $J = 0.1$ where the 'SS' mode dominates, at $J = 0.2$ where the transition from the 'SS' mode to the 'RB' mode occurs, and at $J = 1.0$ where the 'RB' mode dominates. For $J = 0.2$, the Re$[\tilde{\sigma}]$ for the 'SS' and 'RB' modes are very close to each other, therefore the eigenfunctions for both modes are shown.

Figure 6.6 shows the calculated eigenfunctions for b' at $\tilde{\alpha}_{cr} = 0.5$ and $J_b/J = 3$ but with three typical J values as discussed above. The solid and the dashed curves represent the real and the imaginary parts of b', which correspond to the amplitude and the phase of b', respectively. At $J = 0.1$ where the 'SS' mode dominates, b' concentrated on the initial central shear/stratified layer, despite slight deviations of phase (dashed curve) due to weakly convective flow induced by the bottom unstable stratified layer. As J increases to 0.2, for the 'RB' mode as shown in figure 6.6(b), b' varies drastically near $z = -2$, which is the vertical height of the interface between the initial stable and unstable stratified layer. For the 'SS' mode as shown figure 6.6(c), the variation of b' remains at the central shear layer but its amplitude becomes positive compared to the negative one as shown in figure 6.6(a). As J increases to 1.0 where the 'RB' mode dominates, the absolute magnitude of the phase

change (dashed curve) evolves to be larger than the amplitude change (solid curve) of b' at $z = -2$. Meanwhile, the amplitude variation along z in figure 6.6(d) keeps a similar profile to that shown in figure 6.6(b), and also shows a similar b' profile to that Sun [7] where only penetrative convection occurs.

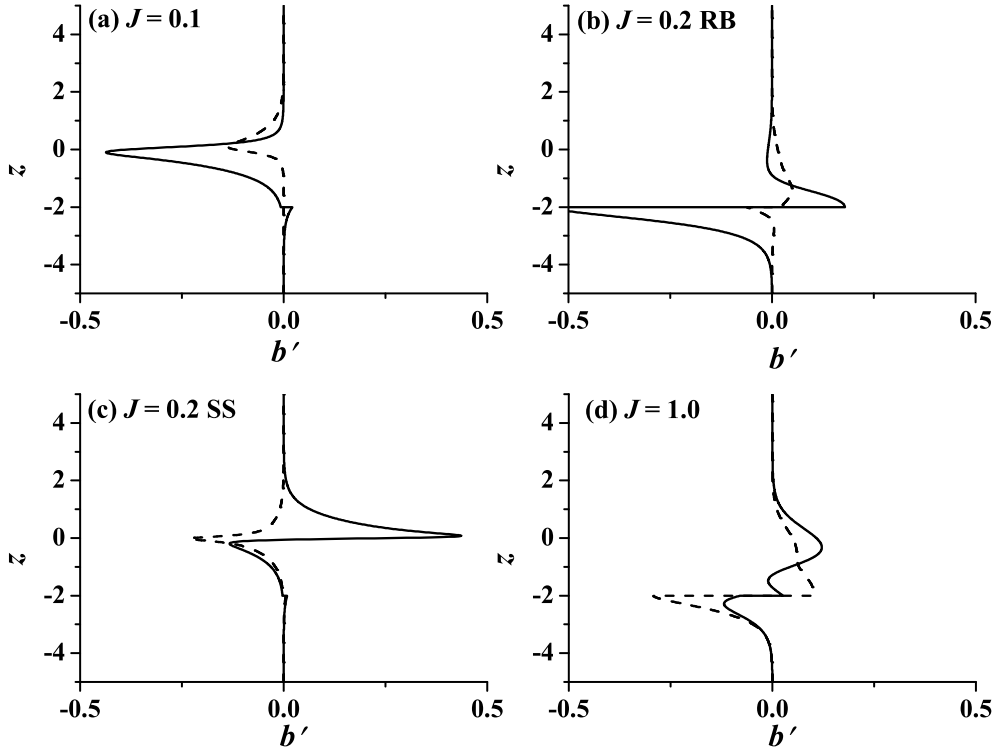

Fig. 6.6 Calculated eigenfunctions of the buoyancy b' at $\tilde{\alpha} = 0.5$ with (a) J=0.1, (b) J=0.2 for the RB branch, (c) J=0.2 for the SS branch, and (d) J=1.0. The solid and dashed curves represent the amplitude and the phase, respectively.

Figure 6.7 shows the calculated eigenfunctions for w' at $\tilde{\alpha}_{cr} = 0.5$ and $J_b/J = 3$ but with three typical J corresponding to figure 6.6. At $J = 0.1$, the central line of amplitude of w' is located slightly above the center of the initial shear layer ($z = 0$), as a result of weak convection flow due to a small J_b. At $J = 0.2$, the strong variation section of w' starts from the bottom of the domain for both the 'SS' and 'RB' modes. For the 'RB' mode, as shown in figure 6.6(b), the profile of the amplitude of w' changes remarkably at $z = -5 \sim -1$, indicating that most of w' originate from the bottom convective flow rather than from the initial shear layer which extends from $z = -1 \sim 1$. For the 'SS' mode as shown in figure 6.6(c), although the amplitude of w' starts to vary from the bottom of the domain, the maximum w' still occurs within the initial shear layer where $z = -1 \sim 1$. At

$J = 1.0$ where the 'RB' completely dominates, w' shows strong propagative features as the magnitude of phase is larger than the magnitude of amplitude.

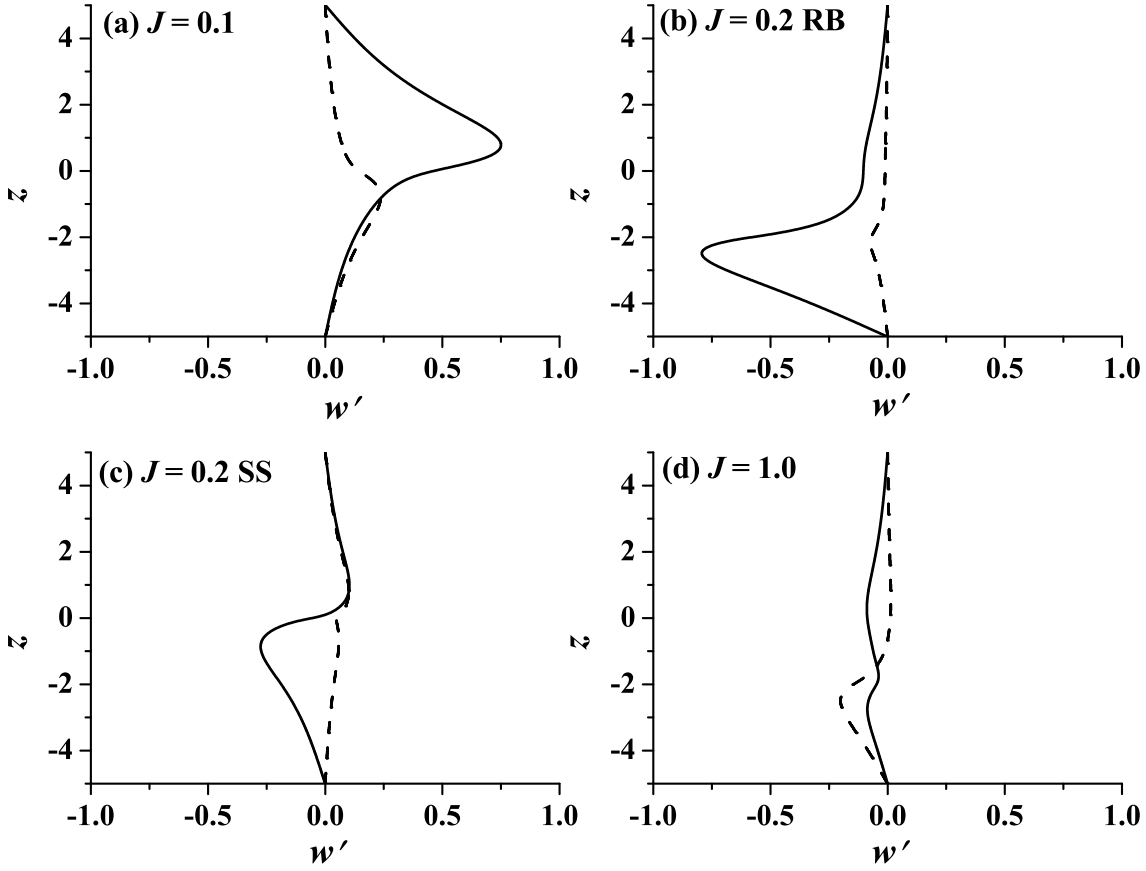

Fig. 6.7 Calculated eigenfunctions of the vertical velocity perturbation b' at $\tilde{\alpha} = 0.5$ with (a) J=0.1, (b) J=0.2 for the RB branch, (c) J=0.2 for the SS branch, and (d) J=1.0. The solid and dashed curves represent the amplitude and the phase, respectively.

Figure 6.8 shows the calculated eigenfunctions for the buoyancy flux perturbation $B' = b'w'$ at $\tilde{\alpha}_{cr} = 0.5$ and $J_b/J = 3$ but with three typical J corresponding to figures 6.6 and 6.7. At $J = 0.1$, the buoyancy flux perturbation is formed on the initial shear layer at the center of the domain. As J increases to 0.2, significant differences are found between the 'SS' and 'RB' modes. For the 'RB' mode, as shown in figure 6.8(b), strong buoyancy flux perturbation occurs near the interface at $z = -2$, with intense and positive magnitude of amplitude compared to figure 6.8(a). For the 'SS' mode as shown in figure 6.8(c), although the variations of B' occur mainly in the initial shear layer, such variations appear very weak as the magnitude of the amplitude and phase significantly decrease compared to figure 6.8(a) and 6.8(b). At $J = 1.0$, the buoyancy flux perturbations are almost negligible. The transitional behaviors of B' from the 'SS' mode to the 'RB' mode suggests that as unstable stratification

increases, the buoyancy flux generated from the bottom thermal boundary will gradually smooth out the buoyancy flux perturbations generated by the central shear stratified layer and eventially dominates in the entire domain.

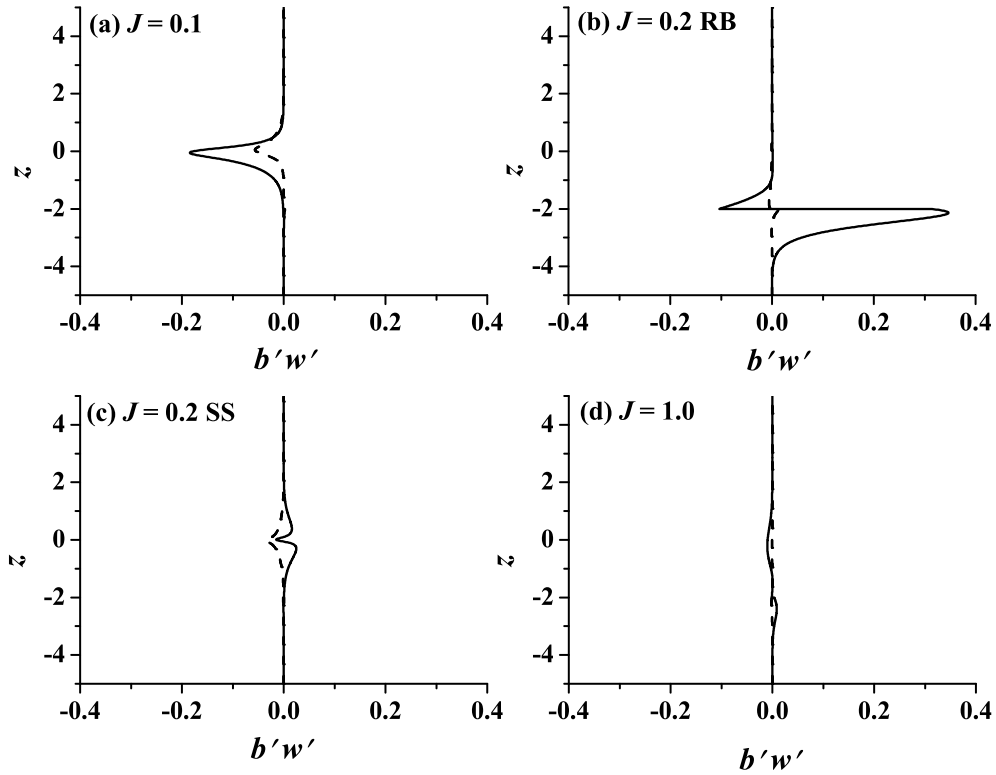

Fig. 6.8 Calculated eigenfunctions of the buoyancy flux $b'w'$ at $\tilde{\alpha} = 0.5$ with (a) J=0.1, (b) J=0.2 for the RB branch, (c) J=0.2 for the SS branch, and (d) J=1.0. The solid and dashed curves represent the amplitude and the phase, respectively.

6.5 Conclusions

The influences of the bottom thermal convection region, in terms of an unstable stratification factor J_b, are added to the Taylor-Goldstein equations to describe the stability features of the sheared convective boundary layer (SCBL) flow. As J_b is introduced into the Taylor-Goldstein equation system, new unstable regions indicating thermal instability are found above the critical stratification factor $J = 0.25$, for the shear stratified flow, in the $J - \tilde{\alpha}$ plane, in addition to the semicircle instability region of the classic sheared stratified flow at $J < 0.25$. As the stratification ratio J_b/J further increases, the thermal unstable region expands and gradually merges with the shear stratified unstable regions. In the $J \sim \tilde{\sigma}$ and

$\tilde{\alpha} \sim \tilde{\sigma}$ planes, increasing J_b expands the thermal unstable regions and accordingly leads to domination of the thermal unstable mode over the shear stratified unstable mode. It is further found that the temporal growth rate of the thermal unstable mode increases in a parabolic fashion with the stratification ratio J_b/J and gradually approaches, intersects and at last overwhelms the temporal growth rate of the shear stratified mode, leading to a transition from shear stratified dominant SCBL mode to thermal convection dominant SCBL mode. The critical transition condition for SCBL flow is found at $J_b/J = 3$ and $\tilde{\alpha} = 0.5$. The analysis of the eigenfunctions of the buoyancy perturbation b', vertical velocity perturbation w' and buoyancy flux perturbation $B' = b'w'$ shows distinctively different spatial perturbation structures for the shear stratified dominant mode, transitional mode and the thermal dominant mode.

References

[1] Raasch S. and Franke T. Structure and formation of dust devil-like vortices in the atmospheric boundary layer: A high-resolution numerical study. *J. Geophy. Res.* **116**, D16120, 2011.

[2] Yang D., Hu L. H., Hou R., et al. Experimental study on buoyant flow stratification induced by a fire in a horizontal channel. *App. Therm. Eng.*, **30**: 872-878, 2010

[3] Stewart N., Holmes D. and Lin W. Direct Numeric Simulation of Sheared Convective Boundar y Layer Mixing and Entrainment. *19the Australian Fluid Mechanics Conference*, Royal Melbourne Institute of Technology, Melbourne, Australia, December 8-11, 2015

[4] Drazin P. G. and Reid W. H. *Hydrodynamic Stability (second edition)* .Cambridge University Press, 2004.

[5] Hazel, P., Numerical Studies of the Stability of Inviscid Stratified Shear Flows, *J. Fluid Mech.*, **51**, 1972, 39–61.

[6] Whitehead J. A. and Chen M. M. Thermal instability and convection of a thin fluid layer bounded by a stable stratification. *J. Fluid Mech.*. **40**: 549-576.

[7] Sun Y. W. Linear stability of penetrative convection. *J. Atmos. Sci*. **33**: 1911-1920.

[8] Moler, C. B. and Stewart, G. W. An algorithm for generalzied matrix eigenvalue problems. *SIAM J. Numer. Anal*. **10**, 1973, 241–256

[9] Smyth, W. D., Moum, D. J. & Nash, J. D. Narrowband, high-frequency oscillations at the equator. Part II: Properties of shear instabilities. *J. Phys. Oceanogr*. **41**, 2011, 412–428.

[10] Liu, Z., Thorpe, S. A. and Smyth, W. D. Instability and hydraulics of turbulent stratified shear flows. *J. Fluid Mech.* **695**, 2012, 235–256.

[11] Thorpe, S. A., Smyth, W. D. and Li, L. The effect of small viscosity and diffusivity on the marginal stability of stably stratified shear flows. *J. Fluid Mech.* **731**, 2013, 461–476.

Chapter 7

Conclusions and future work

This thesis develops a linear stability analysis system for general cross shear flow, obtains preliminary linear stability analysis results of several fundamental cross shear flow configurations, and studies the non-linear evolution of cross shear stratified flows under a wide range conditions. The main conclusions of this thesis are summarized below.

A linear stability analysis is carried out in this study on the cross shear stratified (CSS) flow, where the streamwise and spanwise basic sheared flows interact with each other in a stratified environment. New linear perturbation equations are derived to describe the infinitesimal stability of an inviscid cross sheared stratified flow. A new governing parameter, cross shear ratio ξ, is introduced, which represents the relative extent of the cross shear. With the hyperbolic velocity profile used, another governing parameter, cross shear thickness ratio R_s, is introduced to indicate the relative length scale of the cross shear layer. By obtaining the eigenvalues of the new linear perturbation equations with matrix methods, the effects of ξ and R_s on the stability boundary, temporal growth rate and transition from stationary mode to propagative mode for several CSS flow configurations are investigated. It is found that for all CSS flow configurations considered, both ξ and R_s significantly expand the stability boundary, increase the temporal growth rate and postpone the transition from the stationary mode to the propagative mode to stronger stratification conditions. The relations between two CSS flow controlling parameters and wavenumber, stratification conditions along with temporal growth rate are made and quantified.

The primary instability and coherent structures of cross sheared stratified (CSS) flows, in which the horizontal streamwise and spanwise basic sheared flow components interact with each other in a stratified environment, are studied by direct numerical simulation with the introduction of perturbations. The influence of ξ on the coherent structures of the CSS flow instability in a weakly stratified environment is examined by DNS over the range $0 \leq \xi \leq 1.0$. The results demonstrate that there are three distinct CSS flow primary instability modes: the

"streamwise-dominant" mode with $0.1 \leq \xi \leq 0.3$, the "balanced" mode with $0.4 \leq \xi \leq 0.6$, and the "spanwise-dominant" mode with $0.7 \leq \xi \leq 1.0$. The characteristics of the coherent structures in these three modes are described in terms of the density concentration, the spanwise and streamwise vorticities. It is found that the prominent features of these three instability modes are the coexisting of the spanwise "spiral eddy wrap" structures and the streamwise "cat eye" eddy structures, which have been indirectly mentioned in a previous study. These primary coherent structures are further studied in terms of kinetic energy and potential energy budget. Distinctively different dynamic features are identified for the Kelvin-Helmholtz (KH) mode and these three CSS instability modes, particularly in terms of the kinetic energy difference and the potential energy ratio. It is found that the energy transfer from the streamwise KH instability to the spanwise "eddy wrap" eddy structures increases as ξ increases. Finally the mixing effect of the CSS flows is examined in terms of the mixedness thickness, and it is found that the evolution of the mixedness thickness in a CSS flow undergoes three distinct stages: a short slow growth stage, a rapid growth stage, and an asymptotic stage. The mixing effect in CSS flows is found to be significant only in the rapid growth stage and increases with increasing ξ, but not significant in the other two growth stages, when compared to that in parallel sheared stratified flows where $\xi = 0$. An excellent agreement between DNS results in this study and the available previous experimental results in terms of mixedness thickness are obtained.

The stratification effects on turbulent mixing of CSS flow, through changing the values of the bulk Richardson number Ri which represents the relative intensity of the background stratification with respect to the mainstream velocity shear, is investigated with direct numerical simulation for the CSS flow over the ranges of $\xi = 0 \sim 1$ and $Ri = 0.01 \sim 0.2$. It is found that for stronger background stratifications with increased Ri values, the eddy-featured coherent structures observed for the CSS flows in a weakly stratified environment are suppressed and progressively decay into the wave-like structures. The analysis of the mixedness thickness and kinetic energy budget shows that there are some distinct differences of the coherent structures and turbulent mixing in strong stratified environments compared to weakly stratified environment and demonstrates that normalized mixedness thickness in strong stratified environments decreases as an exponential function of increasing Ri at the turbulence stage.

Hydrodynamic stability analysis is also carried out on sheared convective boundary layer flow, in which both sheared stratified flow and thermally convective flow coexist. The linear unstable stratification for the thermal convective flow region is included in the Taylor-Goldstein equations in terms of an unstable factor J_b in parallel with a stable stratification factor J. New unstable regions corresponding to the thermally convective instability are found

above the pure sheared stratified flow regions in the wavenumber $\tilde{\alpha}$ versus stratification factor J plane. As the stratification ratio J_b/J increases, the unstable regions of thermal convection gradually approach and dominate the shear stratified unstable regions. The transition from shear stratified unstable mode to thermal convection unstable mode is also observed in the temporal growth rate $\tilde{\sigma}$ versus J plane and in the $\tilde{\sigma}$ versus $\tilde{\alpha}$ plane. The eigenfunctions of buoyancy, vertical velocity and buoyancy flux perturbations for sheared stratified dominant mode, the transitional mode and the thermal convection dominant mode in SCBL flow configuration are also discussed.

This study is basically a preliminary study on CSS flows in stratified environments and only some primary results on the dynamics of the flows are obtained. It raises more questions than answered, which will ensue further work on the topic. for example, the expansion of the coherent structures and turbulent mixing in CSS flows over a much wide range of Ri values, the further detailed investigation on the instability, coherent structures, turbulent mixing in convective sheared flows and sheared convective boundary layers, the various energy transfer mechanism responsible for the onset of instability, coherent structures and turbulent mixing in cross sheared flows under various stratified backgrounds, just to mention a few.

The main issues, limitations and challenges for further studies of CSS flow are considered as:

1. The expansion of computational domain involve more complicated secondary coherent flow structures and their interactions within. For KH instability, there is a single primary two-dimensional streamwise roll-up structure, while for the CSS instability there are three types of primary instabilities, in other word, three primary branches are ready to bifurcate into more sub secondary branches. Even though KH instability has relatively simple two dimensional primary structures, a group of secondary instabilities have been found in previous investigations on KH instability, once the computational domain includes two or more wavelength. Considering the rich dynamics in pairing of KH instability, it is expected that each CSS primary instability branch might also have a potential hierarchy of dependent secondary instabilities once domain sizes extended to more than two wavelengths.

2. The expansion of computational domain requires substantial even formidable computational resources. Apparently, for three-dimensional numerical simulation, a simple expansion of 1 mesh/grid in the spanwise direction y would lead to the increase of mesh/grid number of $x \times z$. To investigate computational domain of 4-8 wavelengths of coherent structure may require an extensive period for even a single run for the direct numerical simulation. Therefore, before operating such a huge numerical experiment

for the CSS flow, sufficient preliminary stability analysis and basic understanding of flow dynamics based on 1-2 wavelength DNS results are desperately needed.

3. The laboratory method to create cross shear meets more challenges. As reviewed in chapter 1, the only recorded experimental method to create cross shear is by tilting a water tank in spanwise direction. Nevertheless, the tilting can only produce a limited range of cross shear in just a few seconds. A better solution to create a wide range of cross shear in a long during is also needed for the future experimental investigations.